THE AUSTIN CHALK/EAGLE FORD FIELD LABORATORY (ACEFFL)

DOE Award No.: DE-FE0031579

Final Report

Project Period (April 1, 2018 – December 31, 2023)

Submitted by:

A. Daniel Hill

A. D. Hill

Signature

Texas A&M University
DUN's Number: 191510239

3116 TAMU
College Station, TX77843
danhill@tamu.edu

Prepared for:
United States Department of Energy
National Energy Technology Laboratory

Project Title: **THE AUSTIN CHALK/EAGLE FORD FIELD LABORATORY (ACEFFL)**

Type of Report: **Final Scientific/Technical Report**

Reporting Period Start Date: **April 01, 2018**

Reporting Period End Date: **December 31, 2023**

Principal Author: **Dr. Dan Hill, Principal Investigator**

Date Report was Issued: **March 31, 2024**

DOE Award Number: **DE-FE0031579**

Name and Address of Submitting Organizations:
Texas A&M University
Dan Hill
3116 TAMU, College Station, TX77843
danhill@tamu,edu , 979-8452278

Authors:
Texas A&M University
Dan Hill, Ding Zhu, George Moridis, Akhil Datta-Gupta, Sara Abedi

SM Energy
Erich Kerr

Lawrence Berkeley National Laboratory
Julia Correa, Avinash Nayak, Stanislav Glubokovskikh, Linqing Luo, Todd Wood

Rice University
Jonathan Ajo-Franklin, Xiaoyu (Rosie) Zhu, Yuanyuan Ma, Feng Cheng

Sandford University
Mark Zoback, Arjun Kohli

University of California, Berkeley
Kenichi Soga, Jaewon Saw

Class VI Solutions Inc.
Barry Freifeld

Acknowledgements

The authors acknowledge the Department of Energy's Office of Fossil Energy and the National Energy Technology Laboratory for financial support of this project through the award "The Eagle Ford Shale Laboratory: A Field Study of the Stimulated Reservoir Volume, Detailed Fracture Characteristics, and EOR Potential," Award No. DE-FE0031579. Funding for LBNL was provided through the U.S. DOE, Assistant Secretary for Fossil Energy and Carbon Management, Office of Fossil Energy and Carbon Management, under contract No. DE-AC02-05CH11231. The authors wish to acknowledge the contributions of Lawrence Berkeley National Laboratory's Geosciences Measurement Facility (gmf.lbl.gov) and its support of custom instrumentation solutions for earth, energy, and environmental science discovery.

The authors also thank Erich Kerr and all of his colleagues at SM Energy for providing the field site and immeasurable help in carrying out all of the field activities that were the heart of this project. We also express our greatest appreciation to NETL program manager, Joe Renk III, for his unwavering support for the project.

TABLE OF CONTENTS

Executive Summary

This project, led by Texas A&M University, developed a science-based field laboratory in the Austin Chalk/Eagle Ford Shale Formation to determine the stimulated reservoir volume created by the fracturing of multiple wells. Utilizing newly developed monitoring solutions, the team delivered comprehensive high-quality field data on the extent and morphologies of productive fractures created from these wells. Advanced field monitoring was complemented by laboratory testing on cores and drill cuttings, and coupled modeling for design, prediction, calibration, and code validation. The Austin Chalk/Eagle Ford Field Laboratory (ACEFFL) was hosted by SM Energy, which provided access to the wells of opportunity.

The optical fibers installed in two of the six project wells were the key sensors used in the comprehensive fracture diagnostic measurements applied in ACEFFL. However, numerous other measurements and methods were also applied. The fracture diagnostic methods applied included DAS and DTS measurements for interpreting flow allocation, Low-frequency DAS monitoring for frac-hit detection and fracture propagation measurement, Sealed wellbore pressure response, Downhole pressure gauges, Diagnostic Fracture Injection Tests (DFITs), Downhole video for perforation erosion monitoring, Tracers, Microseismic mapping with surface geophone array, Microseismic mapping with downhole DAS fiber, Active seismic monitoring from SOV sources to map fracture network, and Production logging.

To maximize the information gained about optimal hydraulic fracturing methods, treating conditions were varied over a wide range of conditions in virtually every fracture stage pumped in the two wells equipped with fiber.

Numerous supporting laboratory and modeling studies were also conducted. These included modeling of active seismic responses, interpretation of fractures created by modeling of DTS/DAS responses, interpretation of fracture propagation of low frequency DAS signals, laboratory measurement of low frequency DAS responses the propagating fractures, analysis of production logs, modeling of sealed wellbore pressure responses, modeling of stress profiles and fracture height growth, modeling of near-wellbore fracture initiation and growth, geomechanical measurements of rock properties of cores and cuttings, and reservoir simulation and history matching using hundreds of fractures determined from DTS/DAS interpretation.

From all of these studies, a comprehensive mapping of the created fractures at the field site was created and corroborated by subsequent production performance.

1. Project Overview

1.1 Project Objectives

This project, led by Texas A&M University, developed a science-based field laboratory in the Austin Chalk/Eagle Ford Shale Formation to determine the stimulated reservoir volume created by the fracturing of multiple wells. Utilizing newly developed monitoring solutions, the team delivered comprehensive high-quality field data on the extent and morphologies of productive fractures created from these wells. Advanced field monitoring was complemented by laboratory testing on cores and drill cuttings, and coupled modeling for design, prediction, calibration, and code validation. The Austin Chalk/Eagle Ford Field Laboratory was hosted by SM Energy, which provided access to the wells of opportunity.

The ultimate objective of the Austin Chalk/Eagle Ford Field Laboratory Project was to improve the effectiveness of shale oil production by providing new scientific knowledge and new monitoring technology for both initial stimulation/production as well as longer term production after fracture stimulation. The project has provided key insights into the fracture stimulation processes and developed new methodologies and operational experience for optimized production of oil from fractured unconventional reservoirs, an end result that allows for more production from fewer new wells with less material and energy use. While aspects of the proposed project were site-specific to the Austin Chalk/Eagle Ford formation, there are many realistic and practical learnings that apply to other unconventional plays, or even apply to other subsurface applications such as unconventional gas recovery and geologic carbon sequestration and storage.

SM Energy is the field operator that hosted the field site for the Austin Chalk/Eagle Ford Field Laboratory led by Texas A&M University (TAMU) to conduct a science-based field laboratory project in the Austin Chalk/Eagle Ford Formation. Utilizing newly developed and integrated monitoring solutions, the project team delivered comprehensive high-quality field data to improve scientific knowledge of unconventional reservoir stimulation with the most advanced hydraulic fracturing being applied. Multistage hydraulic fracturing of six producing wells was monitored using DTS/DAS fiber optic cables in two of the wells, downhole pressure gauges, and surface seismic sources and receivers for active seismic interrogation and microseismic mapping. Other supporting measurements that were made include openhole fracture imaging logs, oil and water-soluble tracers added to some of the fracture fluid, downhole video imaging of perforations before and after fracturing, and production logs run in some of the wells after production began. In two of the wells, fracturing conditions were varied stage by stage to determine the effects of parameters like fracture fluid volume, proppant type and amount, fracture fluid characteristics, and perforating conditions on the created fracture system. Field monitoring was complemented by laboratory testing on cores and drill cuttings, and coupled modeling for design, prediction, calibration, optimization, and code validation.

SM Energy, the site host, conducted these activities as part of the field laboratory:

1. Drilling and multistage fracture stimulation of six new wells
2. Running a fracture imaging log on one of the wells
3. Installation of fiber optic cables and surface equipment on two of the wells

4. Installation of downhole pressure gauges in some of the new wells, and in some previously drilled wells near the new wells
5. Installation of surface orbital vibrators (SOVs) for active seismic sources
6. Installation of a surface array of geophones for microseismic monitoring
7. Injection of oil and soluble chemical tracers in some stages of the fracture treatments
8. Running downhole video cameras before and after fracturing to image perforations in one of the wells
9. Running production logs in one or more of the wells after they were placed on production.

The ultimate objective of the Austin Chalk/Eagle Ford Field Laboratory Project was to help improve the effectiveness of oil production in unconventional reservoirs by providing new scientific knowledge and new monitoring technology. The main scientific/technical objectives of the proposed project were:

- Build and test surface active seismic monitoring with fiber optics in observation wells with DAS and SOVs to conduct: (1) real-time monitoring of fracture propagation and stimulated volume for multiple horizontal wells, and (2) time-lapse seismic monitoring of reservoir changes during production.
- Test distributed temperature sensing (DTS), distributed acoustic sensing (DAS) and distributed strain sensing (DSS) with fiber optic technology and develop protocols for field application.
- Assess spatially and temporally resolved production characteristics and explore relationship with stimulated fracture characteristics by DFIT, openhole logging, production logging, and tracer technology.
- Understand rock mechanical properties and reservoir fluid properties and their effects on stimulation efficiency through coring, core analysis and drill cuttings analysis.
- Develop forward and inverse modeling to calibrate simulation models using all monitored data.

1.2 Revision of Field Experimental Plans

The original field host was WildHorse Resource Development. The acquisition of WildHorse Resource Development (former subcontractor to the project and site lease holder) by Chesapeake Energy Corporation, which was announced on October 30, 2018, led to a change in the industry partner for the project. The acquisition officially closed on February 1, 2019, at which point Chesapeake Energy Corporation became the new industry partner and original Eagle Ford Site Laboratory (EFSL) field test site operator. This transition in industry partners caused delays in the performance of field test site activities planned during this period of performance (BP1). After 10 months of tremendous effort, the EFSL team at Texas A&M, along with representatives from the EFSL project partner organizations (LBNL and Stanford), and the field host of the project, Chesapeake, reached the conclusion that the partnership had to be terminated due to the lack of common technical interests. In August 2019, the EFSL team negotiated with INPEX Eagle Ford, LLC, for the possibility of having INPEX as the field site host, and INPEX submitted a letter of intent to provide the host site for the project. At that time, INPEX intended to begin drilling and completing wells for the project in January 2020. However, even with INPEX's enthusiastic interest in collaboration, during the COVID-19 pandemic and economic downturn, the project was postponed repeatedly, and finally, INPEX announced to withdraw as the site host in January 2021. The current potential site host, SM Energy, had a science plan for field tests of fracture stimulation that was in-place and well-aligned with the scope and objectives of the EFSL project. SM Energy had wells/pad for testing already selected and they fit the testing goal defined by the research team perfectly. The mutual interests led to the agreement that SM Energy would be the new field host for the project.

The subcontract with SM Energy making them the host operator was fully executed on July 7, 2021 after months of negotiations. Planning for the field experimentation began immediately.

1.3 Reason for the changes to the project

The proposed changes to the project were necessitated by the withdrawal of INPEX Corporation as the host operator. The research team was fortunate to get in contact with SM Energy and agree on a collaborative project to monitor the hydraulic fracture stimulation of 6 new wells to be landed in the Austin Chalk formation, just above the Eagle Ford formation. The main changes to the project were:

- SM Energy will host the project at a 6-well site in Webb County, Texas
- Target formation is changed from Eagle Ford to Austin Chalk/Eagle Ford

The original proposed project had three phases; Phase I – refracture, Phase II – new fractures, and Phase II – EOR. Because SM Energy has the field test pad setup that directly fits the main activates in Phase II, monitoring fracturing in newly-drilled wells, the project team conducted Phase II of the original proposal first, and made it as one-phase project in this revision.

The new proposed research was similar to Phase II of the original proposal, but instead of monitoring 2 new production wells as previously planned, in the SM Energy project, the project team monitored the fracture treatments of 6 new producing wells. In addition, 2 of the horizontal wells were be equipped with fiber optic cables, not just one as previously planned.

1.4 Chronology of Field Activities

The project activities conducted in the field occurred in 2021 and the first quarter of 2022. A chronology of these activities is:

Drilling and Casing Installation, fiber installation in 2 wells,	July-September, 2021
Data Acquisition trailer set up on site	October, 2021
Surface Orbital Vibrators (SOVs) installed	August-September, 2021
SOVs tested	October and November, 2021
Hydraulic fracturing operations on 6 wells	December 2021, January, 2022
Start of production	March, 2022
Downhole video run	March, 2022
Production log run	May, 2022

The timeline for the field activities is shown in Figure 1.1.

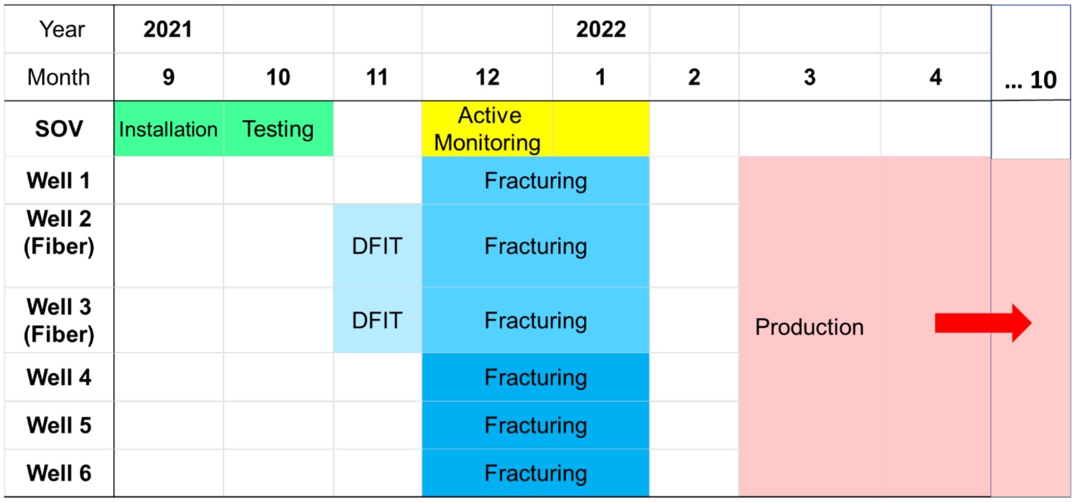

Year	2021				2022				
Month	9	10	11	12	1	2	3	4	... 10
SOV	Installation	Testing		Active Monitoring					
Well 1				Fracturing			Production →		
Well 2 (Fiber)			DFIT	Fracturing					
Well 3 (Fiber)			DFIT	Fracturing					
Well 4				Fracturing					
Well 5				Fracturing					
Well 6				Fracturing					

Figure 1.1 Timeline of ACEFFL field activities

1.5 Site Description

The field location for the project was SM Energy's Briscoe Ranch lease in Webb County, Texas, shown as the star on the map of the Eagle Ford trend in south Texas (Fig. 1.2). The test site consisted of 6 parallel horizontal wells drilled from 2 pad sites as shown in the aerial photograph (Fig. 1.3). Each horizontal lateral was 7000 – 8000 feet long. The gun barrel view of the wells (Fig. 1.4) shows the relative horizontal spacing between the wells (not to scale), and that two of the wells were lower than the other four wells. The wells colored red in this figure were the wells equipped with optical fibers.

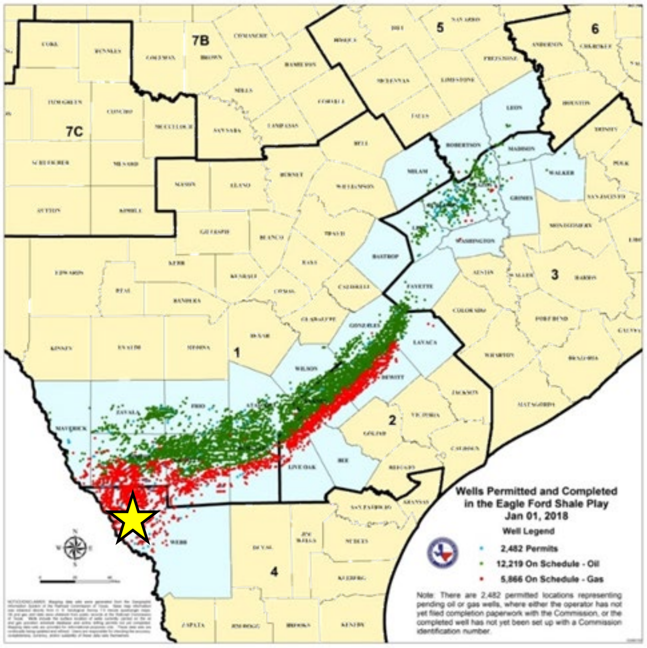

Figure 1.2 ACEFFL field test location.

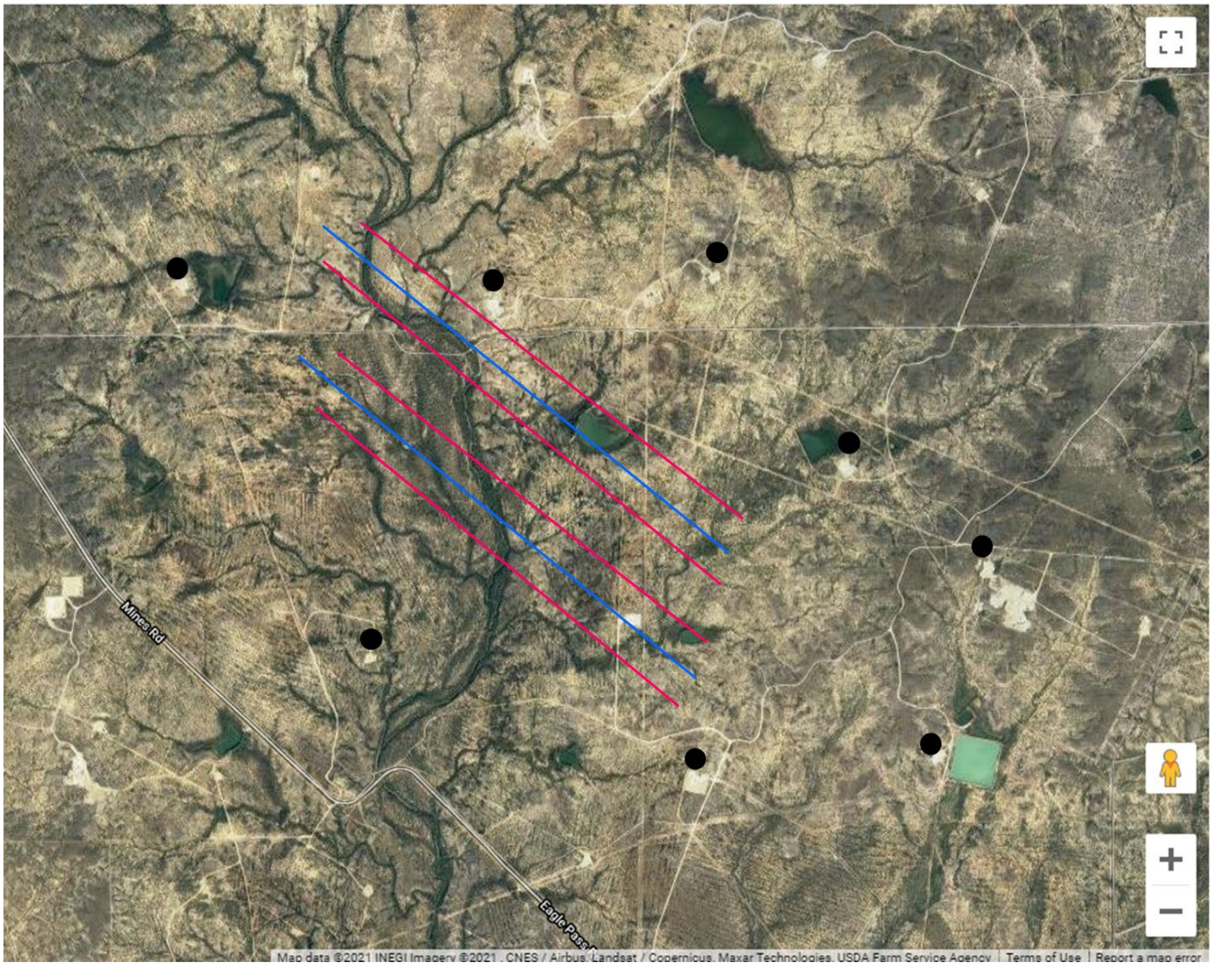

Figure 1.3 Aerial view of the ACEFFL field site, showing the trajectories of the 6 horizontal wells.

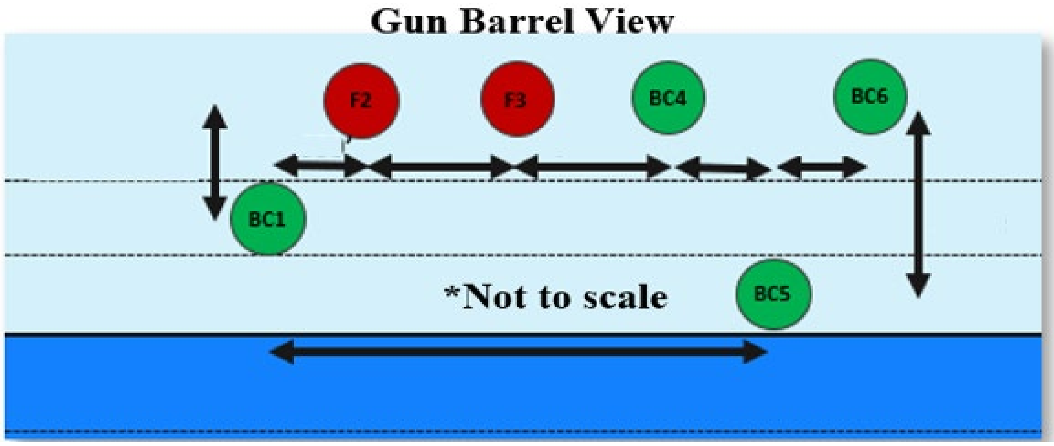

Figure 1.4 Gun barrel view of test well layout.

A large array of geophones was also installed in the field to acquire microseismic responses throughout all fracturing treatments. These were arranged in a star pattern over the well region as shown in Figure 1.5.

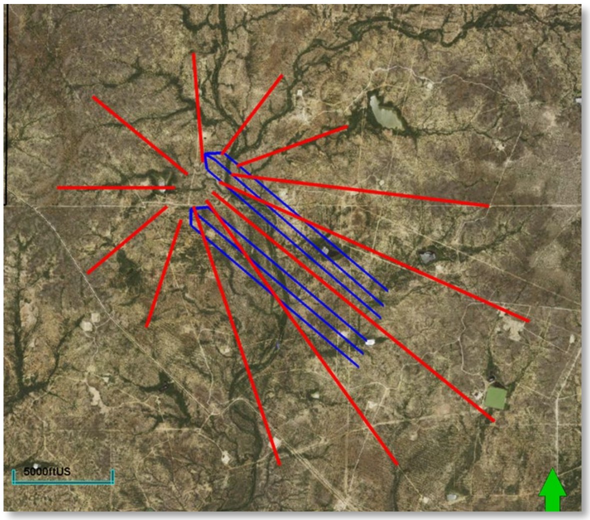

Figure 1.5 Microseismic Star Array of geophones.

2. Surface Orbital Vibrators (SOVs) for Fracture Monitoring and Diagnosis

2.1 Introduction of SOV

A unique aspect of the ACEFFL field experimentation was the use of surface orbital vibrators (SOVs) as seismic sources for active seismic imaging of the subsurface region being hydraulically fracture. An SOV is a large motor with an asymmetric flywheel attached to the motor shaft so that the rotation of the shaft causes vibrations. The motor is firmly coupled to a large cement block that is acoustically coupled to the surrounding ground so that the vibrations are transmitted into the earth.

In the ACEFFL project, 5 SOV sites were built over the trajectories of the horizontal wells (The seismic signals created by the SOVs were received by the DAS cables in the two fiber-equipped wells. Each site had 2 or 3 SOVs of different motor sizes. Auxiliary equipment at each SOV site included a generator to provide power to the motors, equipment to receive control signals and transmit data, and solar panels to power electronics.

Fracture Diagnostics Methods Applied in ACEFFL are:

The optical fibers installed in two of the six project wells were the key sensors used in the comprehensive fracture diagnostic measurements applied in ACEFFL. However, numerous other measurements and methods were also applied. The fracture diagnostic methods applied included:

1. DAS and DTS measurements for interpreting flow allocation
2. Low-frequency DAS monitoring for frac-hit detection and fracture propagation measurement
3. Sealed wellbore pressure response
4. Downhole pressure gauges

5. Diagnostic Fracture Injection Tests (DFITs)
6. Downhole video for perforation erosion monitoring
7. Tracers
8. Microseismic mapping with surface geophone array
9. Microseismic mapping with downhole DAS fiber
10. Active seismic monitoring from SOV sources to map fracture network
11. Production logging

To maximize the information gained about optimal hydraulic fracturing methods, treating conditions were varied over a wide range of conditions in virtually every fracture stage pumped in the two wells equipped with fiber. Table 2.1 summarizes the fracture designs tested in the study.

Table 2.1 Fracture Treatment Designs

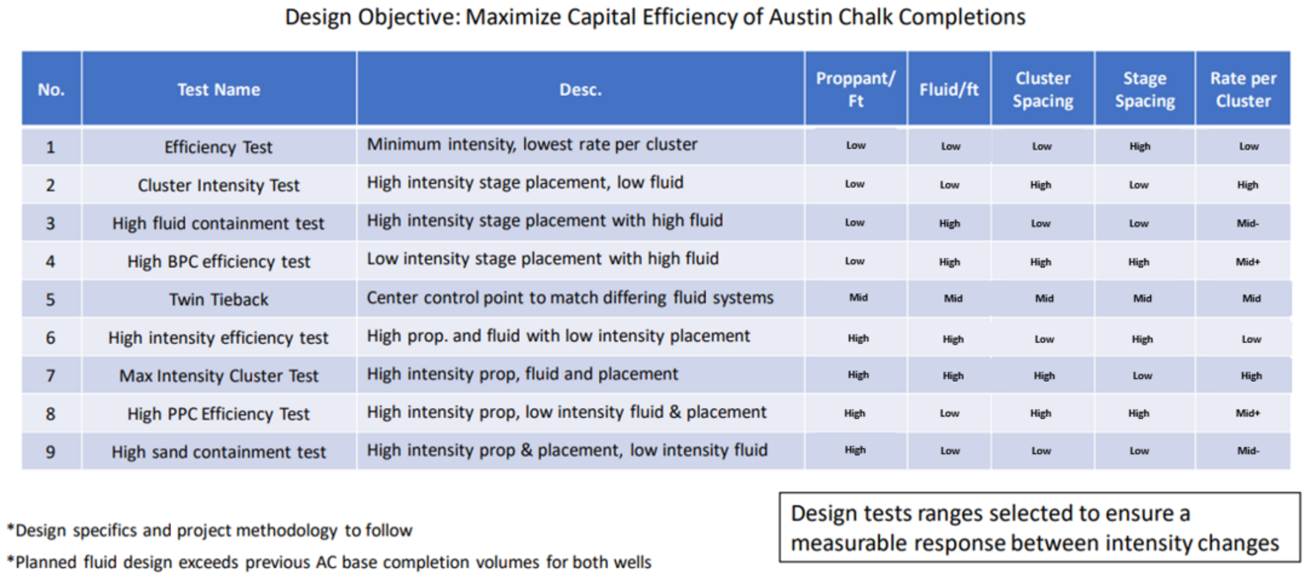

Design Objective: Maximize Capital Efficiency of Austin Chalk Completions

No.	Test Name	Desc.	Proppant/ Ft	Fluid/ft	Cluster Spacing	Stage Spacing	Rate per Cluster
1	Efficiency Test	Minimum intensity, lowest rate per cluster	Low	Low	Low	High	Low
2	Cluster Intensity Test	High intensity stage placement, low fluid	Low	Low	High	Low	High
3	High fluid containment test	High intensity stage placement with high fluid	Low	High	Low	Low	Mid-
4	High BPC efficiency test	Low intensity stage placement with high fluid	Low	High	High	High	Mid+
5	Twin Tieback	Center control point to match differing fluid systems	Mid	Mid	Mid	Mid	Mid
6	High intensity efficiency test	High prop. and fluid with low intensity placement	High	High	Low	High	Low
7	Max Intensity Cluster Test	High intensity prop, fluid and placement	High	High	High	Low	High
8	High PPC Efficiency Test	High intensity prop, low intensity fluid & placement	High	Low	High	High	Mid+
9	High sand containment test	High intensity prop & placement, low intensity fluid	High	Low	Low	Low	Mid-

*Design specifics and project methodology to follow

*Planned fluid design exceeds previous AC base completion volumes for both wells

Design tests ranges selected to ensure a measurable response between intensity changes

2.2 Background of SOV

The Austin Chalk/Eagle Ford Field Laboratory (ACEFFL) project aims to improve scientific knowledge of unconventional oil producing formations during stimulation and production through state-of-the art monitoring technologies with the ultimate objective to improve effectiveness of production with time. For this, we will use distributed fiber-optic sensing to perform continuous measurements of dynamic strain, static strain, and temperature, through the techniques called Distributed Acoustic Sensing (DAS), Distributed Strain Sensing (DSS) and Distributed Temperature Sensing (DTS), respectively. Additionally, we will deploy unique permanent seismic sources called Surface Orbital Vibrator (SOV) for continuous and autonomous time-lapse Vertical Seismic Profiling (VSP). SOV sources are ideal for continuous monitoring as they offer high desirable repeatability for time-lapse measurements. The SOV source can also be remotely operated and offers a low acquisition footprint.

LBNL plans to conduct semi-permanent seismic sensing during fracture stimulation. Our objective is to use changes in subsurface seismic properties (e.g. P & S wave velocity, attenuation, and anisotropy) to effectively map the stimulated volume, which we believe is possible even in regions which exhibit minimal microseismicity, and also monitor the long-term changes in reservoir properties as production commences. The LBNL team proposes the application of the SOVs and fiber-optics permanent monitoring for understanding seismic and aseismic processes happening with stimulation and consequent fracturing of the target formation. Such processes can potentially affect the long-term fluid production, though they are not always picked up by conventional microseismic monitoring.

The project will apply advanced monitoring technology to a six-well development in South Texas. The six wells will be drilled approximately parallel and will be landed in the Austin Chalk formation. The inner two wells were drilled first and equipped with permanently installed fiber optic cables for DTS/DSS/DAS acquisition, so they are ready prior to hydraulic fracturing conducted in the other four wells. DOE funding is used to implement advanced monitoring instrumentation and measurements to characterize the propped fracture system created.

This report is part of LBNL's deliverables to the Department of Energy (DOE). LBNL's tasks in this project involves:

1. *Evaluation of existing data;*

This task aims to analyze existing data in the proposed location that will serve as the basis for a detailed design of the active seismic array. We will use available sonic log and density log data along with existing seismic data to produce a representative velocity model as the basis for forward modeling of the seismic receiver array.

2. *Design of SOV deployment;*

The forward seismic model from Task 1 will be used as the basis for the design of the SOV deployment. We designed a five-source deployment along the lateral of the wells. Each source location was selected to provide good coupling of the direct P arrival along different sections of the lateral.

3. *Installation of SOV seismic sources;*

This task aims to install the SOV seismic sources at the proposed locations. The installation of the sources will require each a 10 x 10 x 10 ft concrete block as the base for the SOV motor. Each source also includes a control board to be installed nearby the motor.

4. *Monitoring of before, during and after fracturing;*

We plan to acquire seismic data using the fiber-optic cables already installed in the wells by the operator. The fiber-optic cables will be connected to a DAS interrogator unit. DAS data will be acquired continuously along the vertical and lateral sections of the well. Additionally, we plan to acquire DTS and DSS data using the same cable. In total, two single-mode fibers and one multi-mode fiber will be used for the fiber-optics sensing acquisition. DTS/DAS/DSS data will be acquired before, during and after fracturing operations, in continuous mode.

The SOV sources will be programmed to run every day for a period of approximately 2 to 3 hours, generating signals from 10 to 80 Hz. The DAS acquisition will record active seismic data generated from the SOV sources during the source operation times. Outside the SOV operating times, DAS will record passive seismic data.

5. Analysis of monitoring data from active DAS/SOV acquisition and passive seismic;

The fracturing process will be monitored using a combination of active and passive seismic measurement techniques. The active seismic source array using the SOVs as the seismic signal will be utilized to measure changes in P and S wave velocities as well as attenuation in the stimulated zone as a function of time during sequential stages. The SOV source signal will be recorded on DAS. In addition to the SOV signal, microseismic events will be tracked using both in-well DAS and surface 3C geophones. The combination of active source seismic and microseismic measurements will provide improved constraints on both aperture changes in the existing fracture network as well as shear-related fracture network expansion. Additionally, dynamic extensional strain changes along the well resulting from fracture opening and closing will be recorded with the DSS system.

2.3 Equipment Installation and Acquisition

2.3.1 Permanent seismic sources with Surface Orbital Vibrators

The SOV source design was developed at LBNL and piloted at several locations (CO2CRC Otway Project, Victoria Australia, Archer Daniels Midland, Decatur IL, and for a DOD SERDP project in Fairbanks AK), from near surface monitoring applications to CO_2 storage (Correa et al., 2021). SOVs consist of common AC induction motors driving eccentric weights to generate acoustic signals at the ground surface (Figure 2.1). SOVs produce vibrations as an effect of the rotation of the eccentric weights, which produces a compressional wave and vertical and horizontally polarized shear waves (Figure 2.1) (Daley and Cox, 2001). One can adjust the eccentric weights to vary the maximum force of the source providing that one keeps the force and rotational speed within the bearing capacity of the motor. The force of the source increases as the frequency squared of the SOVs rotational velocity. With their low capital and operating cost and high output force, SOVs are a good alternative to common seismic sources for permanent reservoir monitoring.

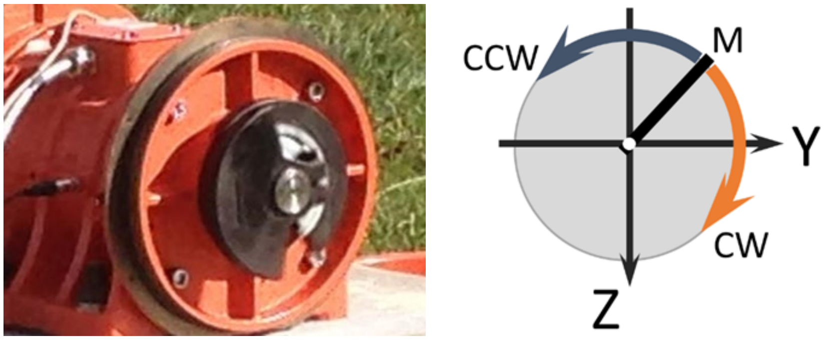

Figure 2.1 Surface Orbital Vibrator showing eccentric weights (left). Diagram demonstrating the rotation of the eccentric weights to clockwise (CW) direction and counter-clockwise (CCW) direction, which results in horizontal Y and vertical Z force (right).

SOV motors, motor controllers, generators and seismic digitizers were installed and commissioned between October 12, 2021 and October 27, 2021 at the Bryce Canyon well site. This activity was conducted by scientists and engineers from LBNL and Class VI Solutions, Inc. with support from SM-Energy, LARM Electrical and SOS field contractors. SM-Energy supervised the installation of the SOV foundations and beginning on October 12 the SOV motors were torqued to the foundations in preparation for operation (Figure 2.2). Electricians proceeded to wire the DCA45 generators to the motor controllers, and connect the motor controllers to the three-phase SOV motors.

Figure 2.3 shows SOV5, which is the easternmost location out of the five SOV stations. The major system components are identified as the seismic digitizer, motor controllers, cellular modem, generator, and SOV motors. The seismic digitizer is solar powered and electrically isolated from the rest of the installation. The digitizer contains a Raspberry PI computer which provides oversight of the operation of the SOV and records the pilot 3C geophone that is located beneath the SOV motors. The motor controllers contain variable frequency drives that control the sweep of the SOV motors using commands generated by the Raspberry PI computer. External communication is provided by a Sierra Wireless RV55 series cellular gateway modem. A DCA45 diesel generator is remotely operated so that it only operates when the SOV motors are running. SOV1, SOV3, and SOV5 have three motors with force outputs of 23 T-f, 15 T-f, and 10 T-f. SOV2 and SOV4 have two motors with force outputs of 15 T-f and 10T-f.

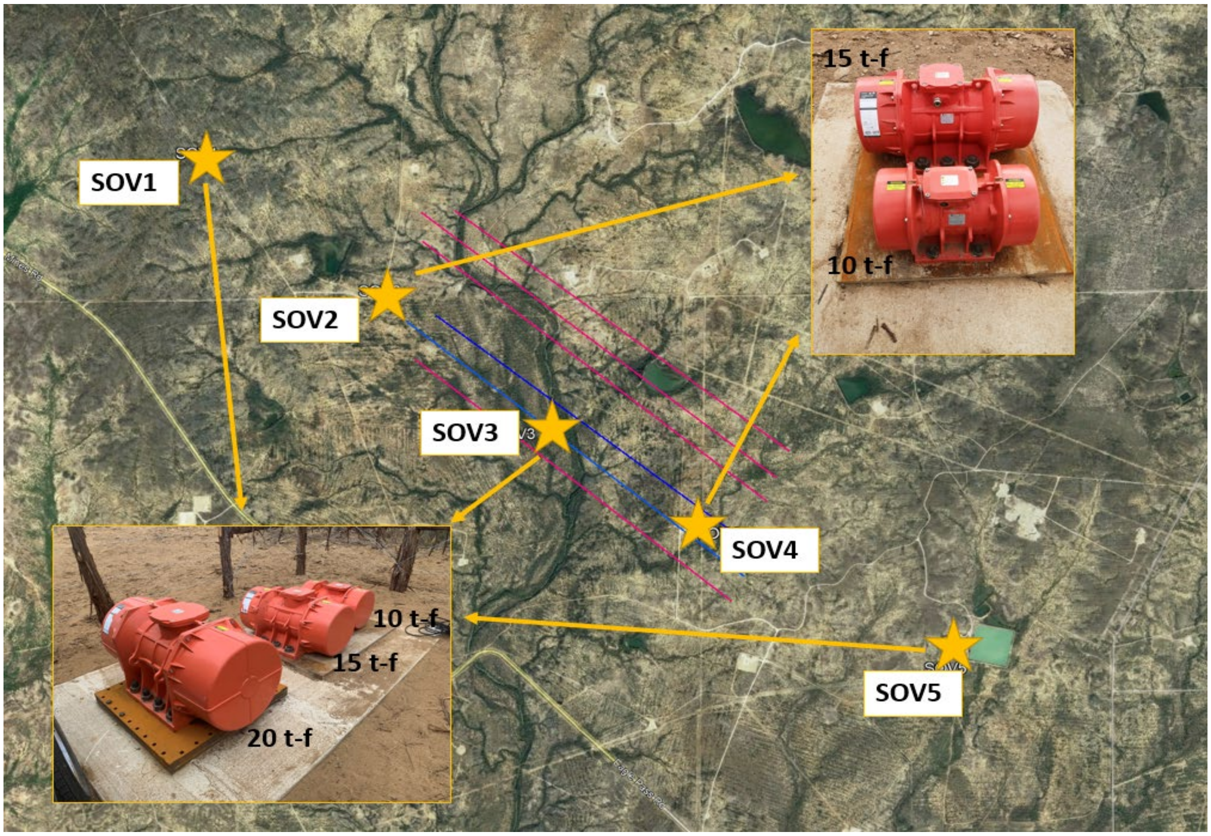

Figure 2.2 SOV source locations and the motor sizes in each location. The blue wells correspond to the fiber wells, 1F and 2F.

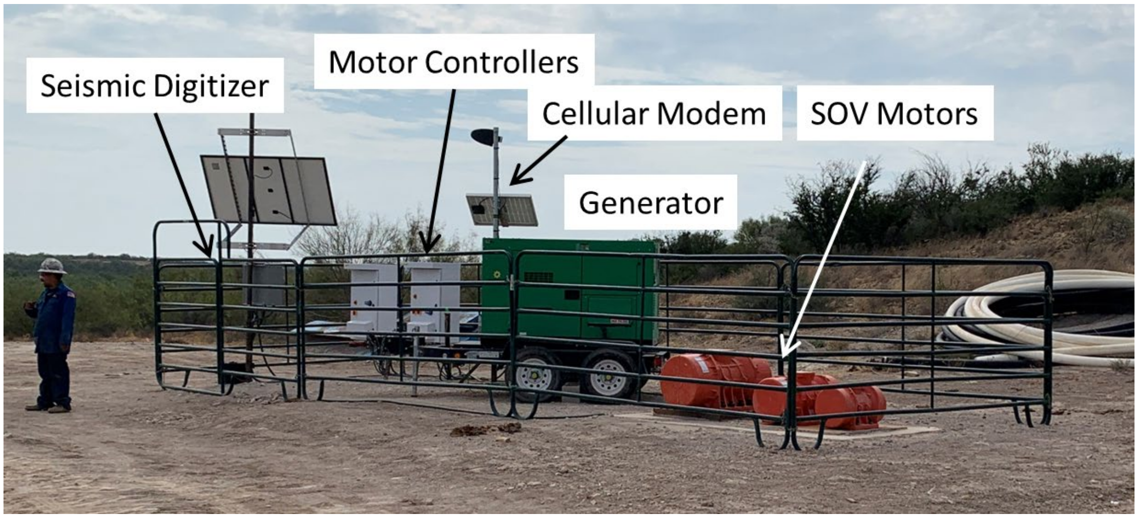

Figure 2.3 SOV5 showing the major system components: seismic digitizer, motor controllers, cellular modem, DCA45 generator and three different sized SOV motors.

Repair of SOV2 Foundation

On November 16, it was discovered that the SOV2 small motor had sheared it's M27 holddown bolts, left the foundation and was still running adjacent to the foundation pad. The generator was shut down and SOV2 was LOTO'd (Locked Out and Tagged Out of service). The other SOVs were taken out of service temporarily until the foundations could be inspected and the source of the problem determined.

Figure 2.4 shows SOV2 foundation with large amounts of cracking around the perimeter of the mounting plate. One edge of the steel plate revealed a large void, where concrete had not filled in under the plate. SOV foundations were inspected on November 18 and November 19. As this was the first foundation installed and the temperature was greater than 100F it was concluded that the placement of already hydrating concrete resulted in a weak foundation with large voids. Figure 5 shows a close up of some of the concrete at SOV2 revealing large vuggs.

Figure 2.4 Degradation of the SOV2 foundation. Note that the small motor has sheared the hold-down bolts and is located beside the concrete pad. The above picture shows a large void under the steel plate and a significant degradation of the concrete around the plate.

Figure 2.5 Close inspection of the SOV2 foundation revealed that the concrete had begun hydrating prior to placement, and large voids and vuggs were observed.

Figure 2.6(a) shows the rebar cage installed to repair SOV2 and Figure 2.6(b) shows SOV2 after the concrete was placed. Concrete break tests were conducted to verify that the concrete achieved a strength of 3500 psi after 21 days of curing, with the concrete mix having a designed ultimate strength of 4000 psi.

Figure 2.6 (a) Rebar cage installed during the repair of SOV2, and (b) SOV2 after placement of concrete.

Replacement of Seismic Digitizers

After several weeks of operation, the SOVs geophone noise was observed to be steadily increasing. The Measurement Computing MCC-172 data acquisition units closest to the SOV motors at SOV1, SOV2 and SOV3 were the units that were degrading the most, and SOV4 and SOV5 digitizers exhibited lower noise levels. It was decided to replace the MCC-172 units with Webdaq 504 digitizers, which were used successfully during other SOV projects and after initial testing they showed to be less susceptible to vibration. The Raspberry PI software was modified to switch the data collection from the MCC172s to the new Webdaq units (Figure 2.7). The replacement of all the seismic digitizers was conducted on December 2 and 3, 2021.

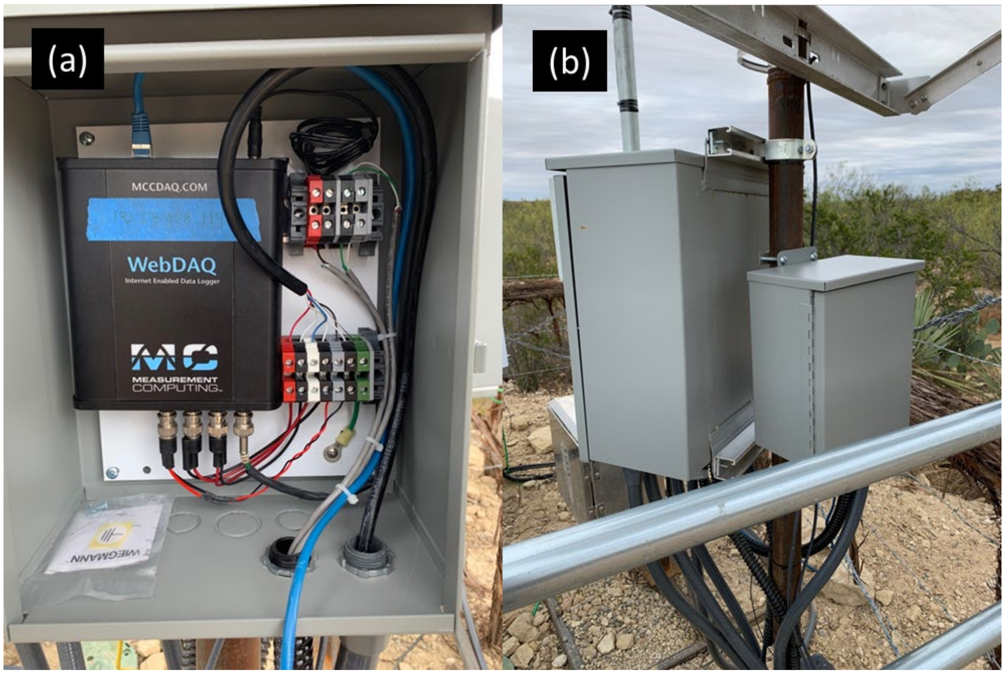

Figure 2.7(a) Webdaq 504 digitizer and interface terminals designed to replace the existing MCC-172 digitizers. (b) SOV1 existing seismic digitizer installing with the new Webdaq504 enclosure installed on the same mounting pole. Raspberry PI software was modified to operate the system.

2.3.2 Dynamic strain sensing with DAS

The Distributed Fiber Optic Sensing (DFOS) techniques utilize the phase shift of backscattered laser energy to detect changes in strain along the fiber. Distributed Acoustic Sensing (DAS) uses Rayleigh scattering to predominantly capture acoustic information along the fiber. We use two Silixa Carina interrogator units, each connected to a Constellation fiber in the 1F and 2F wells, to record the dynamic strain data with DAS. The data was recorded continuously, saved every 30 s, with 10 meters gauge length, 1 m spatial sampling, and 1kHz output time sampling. The dynamic strain sensing with DAS was used to acquire active seismic data with the SOV sources as well as used for microseismic detection and low-frequency DAS.

During the November 2021 field period, numerous SOV/DAS datasets were collected during a field trial, prior to the injection. The objective of the field trial in November was to test the deployed acquisition equipment and evaluate data quality. To check the data quality, we first apply a standard data processing workflow to the SOV/DAS VSP dataset. The data processing workflow consists of time window alignment between SOV sweeps and DAS time series, SOV signature removal by using a water-level regularized deconvolution algorithm, and subsequently multiple sweeps stacking. Figure 2.8 shows the shot gathers acquired during the initial field trial for each SOV location in 1F well.

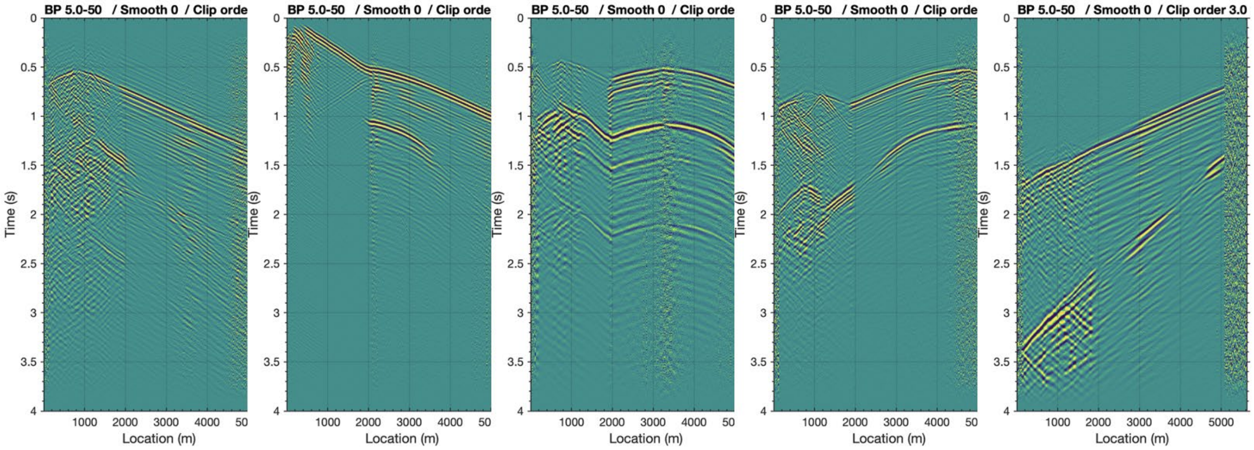

Figure 2.8 Stacked SOV/DAS seismic wavefield after source signature removal. From left to right, five shot gathers show results from SOV1, SOV2, SOV3, SOV4 and SOV5, respectively.

Signal-to-noise ratio (SNR) has also been employed on all stacked wavefields for the November 2021 field test. Figure 2.9 shows the details about the SNR calculation in this case and the SNR distributions of various SOVs arrays along two wells. All datasets show high data quality above 30 dB. SOV2 presents the best quality SNR (it is the closest location to the wellhead), with the vertical portion of the well exhibiting a SNR of 60 dB. After the initial trial, we concluded that the data acquired by the DAS/SOV showed satisfactory quality for subsequent monitoring of stimulation. The passive DAS data would also be used for microseismic detection and low-frequency DAS analysis.

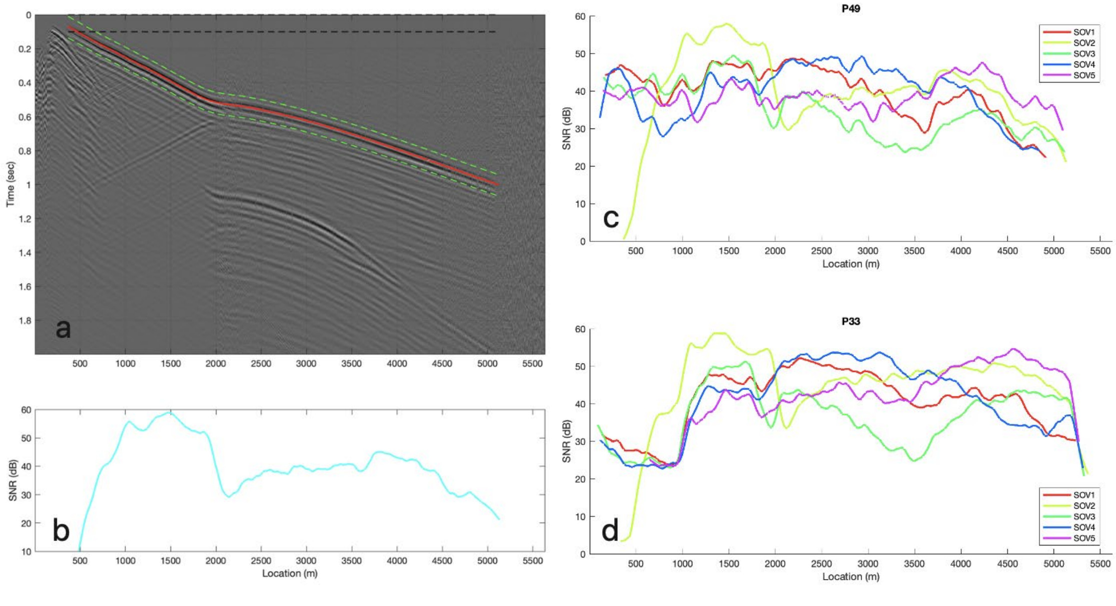

Figure 2.9 SNR QC for first dataset collected in November, 2021. a shows the signal window and noise window; b shows the measured SNR for SOV2 in a; c and d display all SNR distribution along the cable for five SOVs and two wells.

2.3.3 Static strain sensing with DSS

Interrogator design

In the oil and gas industry, Raman scattering-based distributed temperature sensing dominates distributed fiber optic sensing (DFOS). However, it can only measure temperature and requires regular calibration due to power loss along the optical fiber. Because it uses multimode fiber, the sensing distance and spatial resolution are also limited. Comparing Raman scattering-based DFOS to Brillouin scattering-based DFOS, the latter is an emerging technology that reads strain and temperature simultaneously by detecting the Brillouin scattering spectral shift in the frequency domain. Therefore, it does not require regular calibration and can be continuously used for a long time.

For the currently available BOTDR, the signal is obtained using the analog frequency sweeping method, which employs a band-pass filter and records the power of the filtered signal at every read-out point along the fiber. The spectrum is then plotted by shifting the filter to other frequencies until the entire bands are individually swept. The discrete spectrum is fitted by applying a Lorentzian, polynomial, or parabolic function to evaluate the center frequency at the peak power of the spectrum.

The shift in Brillouin backscattering spectra, strain, and temperature change are correlated as shown in the following equation:

$$\Delta\nu_B = C_{\epsilon,B}\,\Delta\epsilon + C_{T,B}\,\Delta T \tag{2.1}$$

Here, $\Delta\nu_B$ represents the frequency shift in Brillouin backscattering spectra, $C_{\epsilon,B}$ is the strain coefficient for Brillouin backscattering, $C_{T,B}$ is the temperature coefficient for Brillouin backscattering, $\Delta\epsilon$ is the strain change, and ΔT is the temperature change. The coefficients do not change with the interrogation system. The strain coefficient is usually 500 MHz/% and the temperature coefficient is usually 1 MHz/℃.

Compared to BOTDR, the BOTDA system requires access at two ends in the field. This is nearly impossible for a deep well, as it necessitates a return fiber from the bottom to the top. Not only does this double the cost of the optical fiber cable, but it also increases the chance of fiber breakage. In this project, we propose using the BOTDR system to monitor strain and temperature to investigate the integrity of the natural gas storage well.

In this project, we designed a BOTDR system based on a typical heterodyne detection architecture, as illustrated in Figure 2.10. An ultra-narrow-line-width laser with a wavelength of 1550.12 nm served as the light source. After passing through a 99/1 coupler, a portion of the continuous-wave (CW) light was modulated by a semiconductor optical amplifier (SOA) with the pulse generated by a controlling module. The control module adjusted the pulse width, ranging from 10 ns to 100 ns, thereby controlling the spatial resolution from 1 m to 10 m. The current input to the SOA was controlled to adjust the output pulsed light peak power. The pulsed light was then amplified by an Erbium-doped fiber amplifier (EDFA) and circulated into the fiber under test to generate the Brillouin backscattered signal. This signal was heterodyned with the reference CW light in the reference branch B and then down-converted to the radio frequency (RF) range using a wideband photodetector (PD). The signal was further down-converted to the intermediate frequency (IF) range (100-600 MHz), which was digitized in the time domain by an analog-to-digital converter (ADC) and processed using the Short-Time Fourier Transform (STFT) signal processing algorithm to obtain the frequency peaks along the fiber under test.

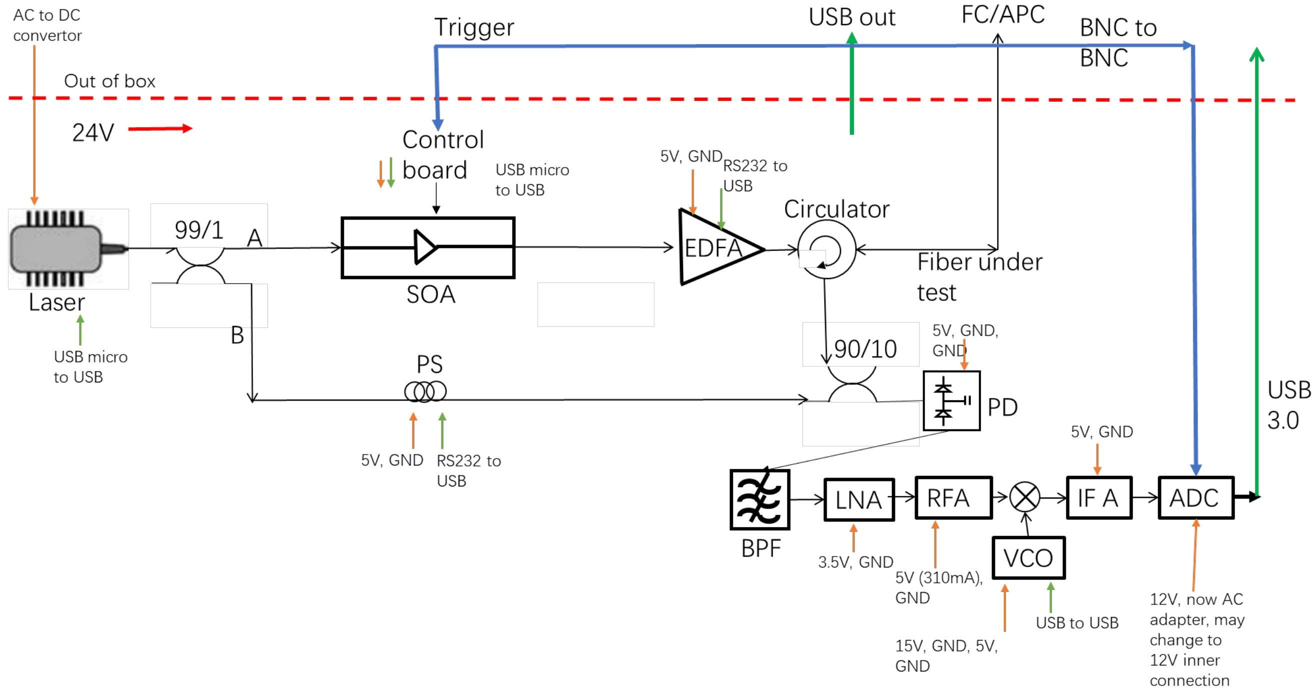

Figure 2.10 The schematic of the STFT-BOTDR architecture. SOA: Semiconductor optical amplifier; EDFA: Erbium-doped fiber amplifier; PS: Polarization scrambler; PD: photodetector; BPF: Bandpass filter; LNA: Low noise amplifier; RFA: Radio frequency amplifier; VCO: Voltage controller oscillator; IF A: Intermediate frequency amplifier; ADC: Analogue to digital converter. FC/APC is a type of fiber connectors; BNC is a type of electrical wire connectors; RS232, USB or USB 3.0 are three types of communication protocols, GND is electrical ground, AC is alternating current, DC is direct current.

In our prototype design, the DFT was implemented using the STFT. The STFT offers a time-frequency analysis method, representing the frequency power spectrum within a short time window within a long data stream. It is based on the fundamental continuous time-frequency analysis tool of classical Fourier analysis, which asserts that any signal can be decomposed into a set of sinusoidal signals with different frequencies and amplitudes (James, 2011).

$$X(f) = \int_{-\infty}^{\infty} x(t) e^{-j2\pi f t} dt \qquad (2.2)$$

The inversion transform can be written as:

$$x(t) = \int_{-\infty}^{\infty} X(f) e^{j2\pi ft} df \qquad (2.3)$$

In discrete time, the data is broken into frames, and the transform can be expressed as:

$$X_k = \sum_{n=0}^{N-1} x_n e^{-2\pi ikn/N}, k \in \boldsymbol{Z} \qquad (2.4)$$

The inverse transform is written as:

$$x_n = \frac{1}{N} \sum_{k=0}^{N-1} X_k e^{2\pi ikn/N}, n \in \boldsymbol{Z} \qquad (2.5)$$

The Short-Time Fourier Transform (STFT) determines the sinusoidal frequency and phase information within a localized section of a signal as the signal changes over time. The signal is analyzed within a time section defined by a window frame on the original signal. The signal is segmented into equal-length sections using the window, and these segments are then processed to obtain the Fourier Transform and Fourier spectrum.

The computation for the discrete time STFT (DT-STFT) is expressed as (Durak & Arikan, 2003):

By utilizing the STFT, the Brillouin frequency shift can be calculated and applied for strain and temperature monitoring.

$$\mathrm{STFT}\{x[n]\}(m, \omega) \equiv X(m, \omega) = \sum_{n=-\infty}^{\infty} x[n] \omega[n-m] e^{-j\omega n} \qquad (2.6)$$

Interrogator development

The system was initially assembled on the bench, as depicted by the blue circle in Figure 2.11. Each component underwent testing and optimization before assembly. Subsequently, the components were integrated into a two-layer 19” rack enclosure.

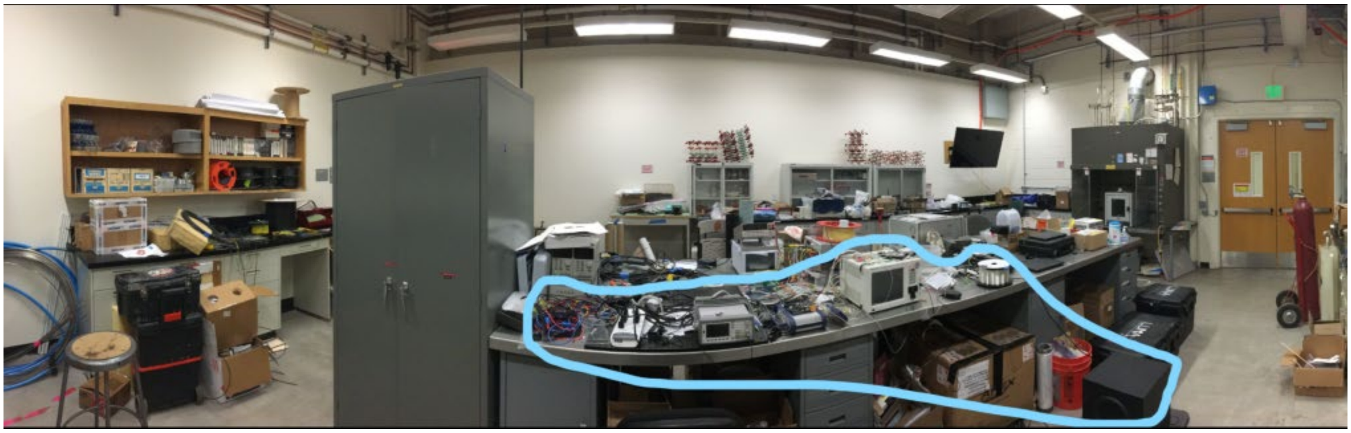

Figure 2.11 Bench version of home-made STFT-BOTDR interrogator shown in the blue circled.

The electronics and power components are housed in the lower layer of the enclosure, as illustrated in Figure 2.12. This layer encompasses power distribution boards (bottom left), a digitizer (bottom right), power adapters (middle), and electronics for the radio frequency downconverter (top left). The 110V voltage was converted to the voltages required by each component. Sufficient space was allocated for airflow and heat dissipation.

The upper layer, as shown in Figure 2.13, incorporates an optical amplifier, a laser, a polarization scrambler, and a semiconductor optical amplifier. This layer encompasses all optics and optical fiber connections, all of which are driven by low voltage. The controlling USB connectors were linked to a USB hub for external connections. The optical fibers were organized to be neater than depicted in Figure 13.

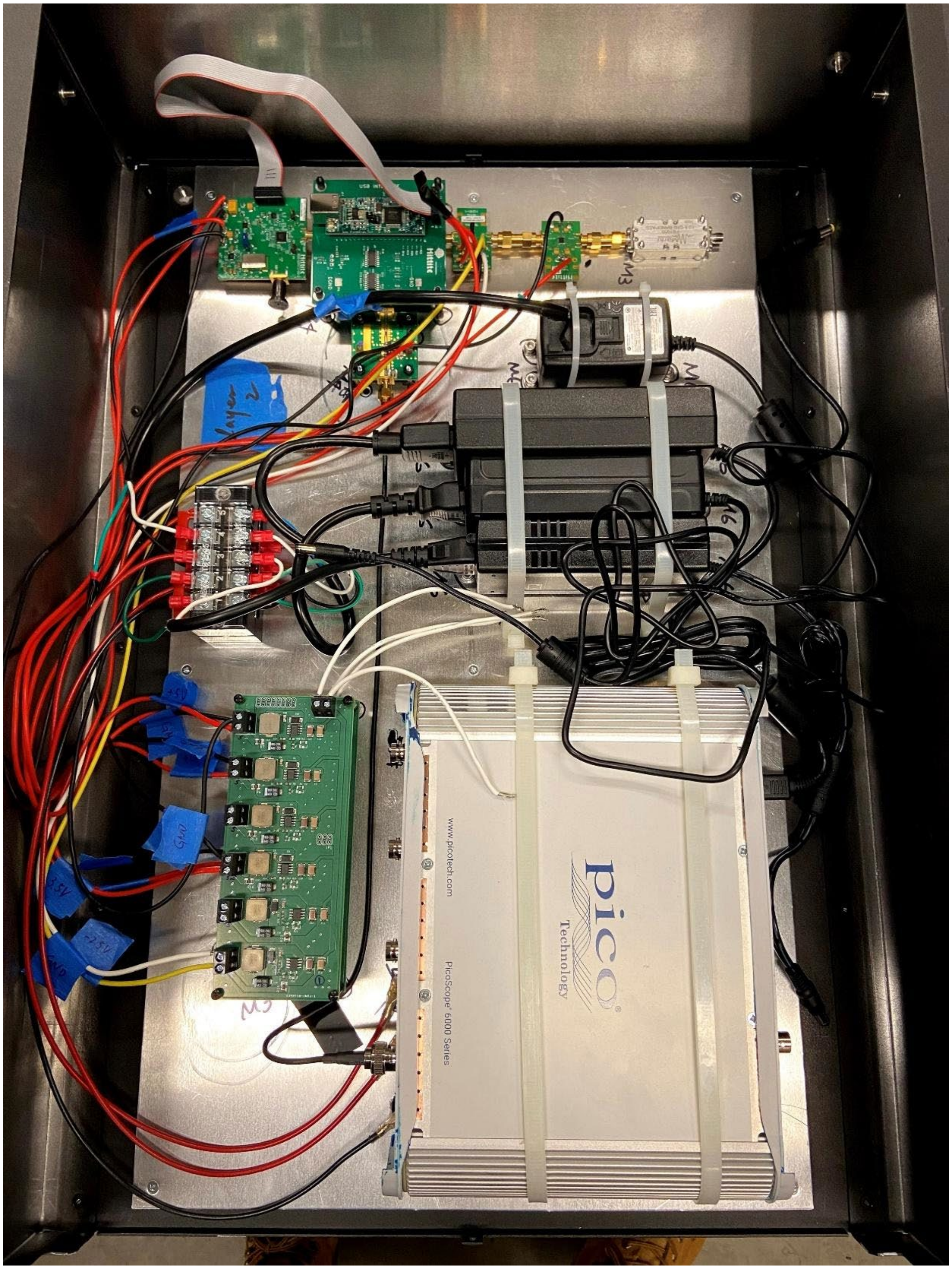

Figure 2.12 The lower layer of the enclosure. This layer includes power distribution boards (bottom left), digitizer (bottom right), power adapters (middle), electronics for radio frequency down convertor (top left).

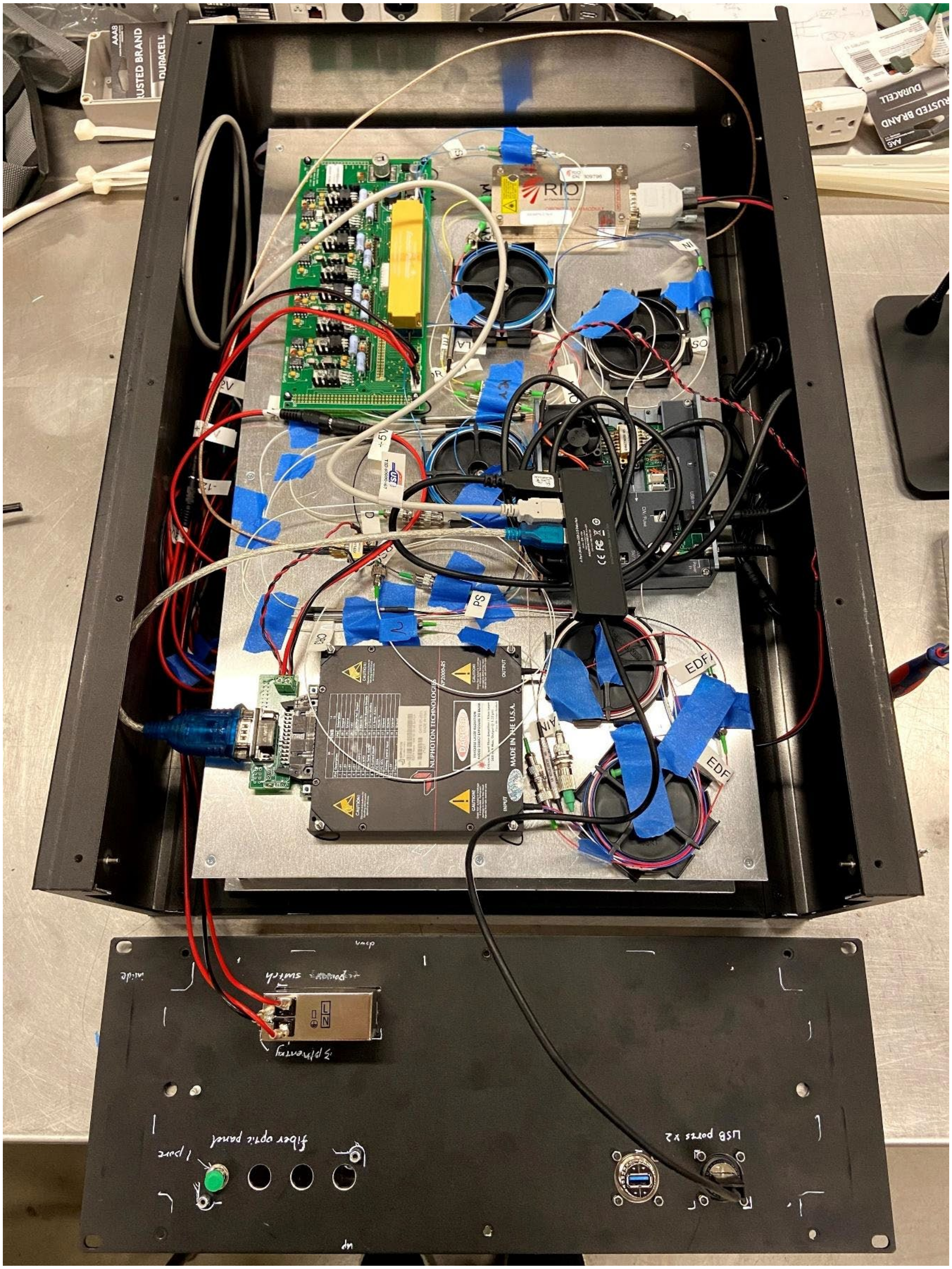

Figure 2.13 The upper layer and back of the front panel (black panel) of the interrogator. The upper layer includes optical amplifier, semiconductor optical amplifier and its controller, laser and polarization scrambler.

After the two layers were assembled, a front panel was added to the enclosure. The front panel, displayed in Figure 2.14, features an FC/APC connector, a power switch, and USB connectors. The FC/APC connector connects to the fiber under test. Subsequently, an optical switch, specifically a 1*2 switch was incorporated into the FC/APC connector after the enclosure was set up at PG&E McDonald Island. This optical switch allows the interrogator to be connected to one of the two channels at any given time. It is controlled by non-latch voltage, and a software program developed by us is used to control the switch.

The front panel also hosts a power switch at the bottom left, connecting to the external 110 V power supply. Two USB connectors are present—one for the digitizer to transmit data to the control computer, and the other for controlling all the components within the interrogator.

Figure 2.14 illustrates the front panel of the enclosure, which includes the FC/APC connector, power switch, and USB connectors.

Figure 2.14 The front panel of the enclosure. This front panel includes FC/APC connector, power switch and USB connectors.

The data is transmitted to the local computer and analyzed locally. Processed strain/temperature profiles are saved locally and synchronized to the cloud, enabling researchers to monitor the borehole from their offices. After testing the interrogator, the system was set up at PG&E McDonald Island for real-time monitoring of strain and temperature in a natural gas storage well.

Interrogator test: Heat dissipation test

The STFT-BOTDR underwent a heat dissipation test, running continuously for several days to assess its stability before fans were added to the enclosure. Three thermal couples were strategically placed at different locations, and the measured temperature data from these couples were shared on the cloud for real-time monitoring with a reading interval set to 1 minute.

- Temperature Sensor 11408593: Placed outside the interrogator to measure the room environment temperature change.

- Temperature Sensor 1140859A: Positioned on the upper layer to measure the temperature in proximity to the upper layer within the enclosure.

- Temperature Sensor 1140853A: Located on the lower layer to measure the temperature in proximity to the lower layer within the enclosure.

Figure 2.15 illustrates a two-day temperature reading from the three thermal couples during continuous operation of the interrogator. The readings showed that the temperature inside the enclosure consistently stayed approximately 16 ℃ higher than the room temperature. Based on this observation, even if the room temperature reaches 40 ℃, the temperature inside the enclosure would remain below 60 ℃, which is acceptable for onsite measurement. This indicates that the enclosure should not encounter issues running continuously onsite, especially with the assistance of an air conditioner.

To further ensure that the heat dissipation meets temperature requirements, six 12V fans were added to the enclosure to expel heat (Figure 2.16).

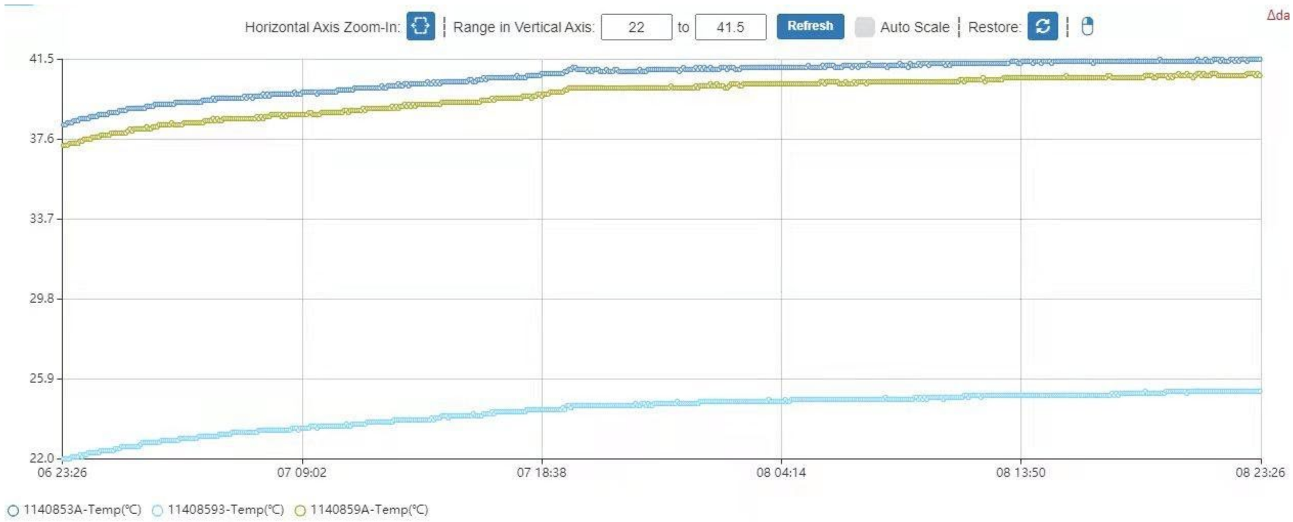

Figure 2.15 An illustration of two days temperature readings from the three temperature sensors. 1140853A was put on the lower layer inside the enclosure. 11408593 was put out of the enclosure. 1140859A was put on the upper layer inside the enclosure.

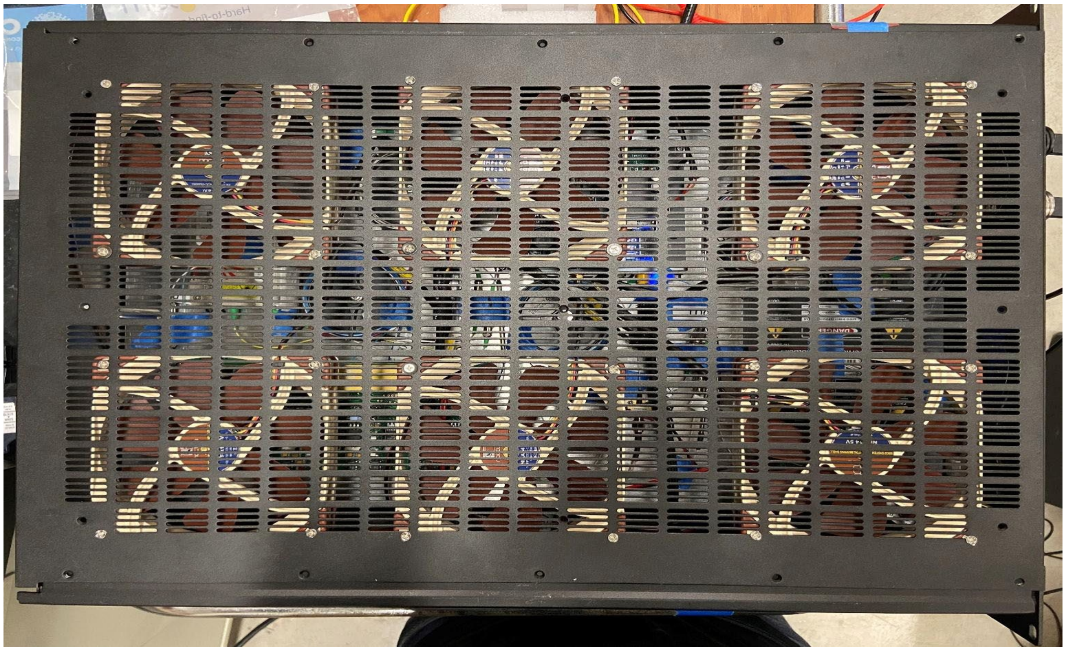

Figure 2.16 The STFT-BOTDR interrogator enclosure with 6 of 12V fans (view from the top). The fans are used to blow the heat out.

Interrogator test: Sensitivity

For Distributed Fiber Optic Sensing (DFOS), four critical specifications influence system selection: spatial resolution, readout, sensing distance, and accuracy.

- Spatial Resolution: This is the minimum distance over which the system accurately indicates the value of the measurands. In time domain modulation techniques, spatial resolution is determined by pulse width. For our system, pulse width can vary from 10 ns to 100 ns, corresponding to spatial resolutions between 1 m and 10 m.

- Readout (Sampling Interval): Also known as the sampling interval, it is the distance between two points of measurement data. In our system, readout can be as small as 2 cm, with the flexibility to decimate to 10-50 cm to reduce data size if storage limitations apply.

- Sensing Distance: This is the maximum distance the power of light can be transmitted until the scattered light no longer maintains the required signal-to-noise ratio for spatial resolution and accuracy at the end of the fiber. The distance, known as fiber length for the Fiber Under Test (FUT), is limited by the transmitted light's power. Optical power budget calculations for each sensing cable determine the distance a DFOS can cover.

- Accuracy: Accuracy is the smallest difference in measurands observable from the measurement output. It is influenced by random error, system error, noise, readout, and spatial resolution, especially in events with rapid temporal transitions or narrow spatial widths. In this report, accuracy was measured by taking the standard deviation at specific locations under the assumption of no strain or temperature variation.

Figure 2.17 illustrates a sensing distance test using a 10 km single-mode fiber (SMF) assumed to have no strain or temperature variation. Different pulse widths were tested, showing that the system could not read Brillouin scattering when the spatial resolution was less than 1 m. As the pulse width increased to 20 ns (2 m spatial resolution), the system successfully read the Brillouin scattering signal even at the end of the 10 km fiber.

In this test, accuracy was measured by the standard deviation at different locations, resulting in values such as 1.08 MHz at 200 m, 1.93 MHz at 4400 m, and 2.47 MHz at 8600 m. Given the borehole's depth of about 1600 m in this project, the sensing distance and accuracy at 1600 m were sufficient to meet monitoring requirements.

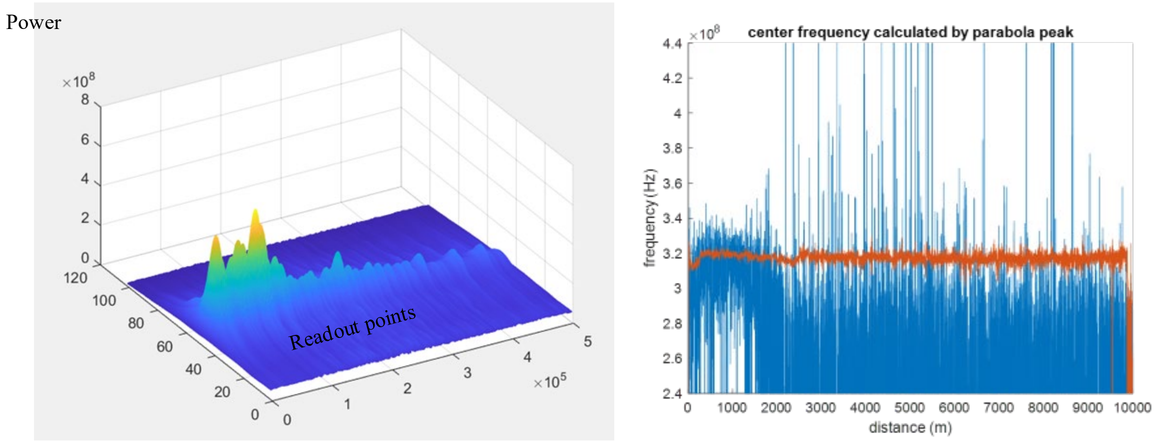

Figure 2.17 The sensing distance test 1 :10km single mode fiber (SMF). Left: the Brillouin scattering spectrum along the 10km fiber when the spatial resolution is 2 m. Right: the peak Brillouin scattering frequency profile along the 10km SMF fiber. The blue line is when the pulse width is less than 10 ns which does not have good reading result, and the red line is when pulse width is 20 ns which shows the good result through the whole optical fiber. Left spectrum is the red line at the right.

To assess the system's capability to detect strain or temperature changes (resolution), water bath tests were conducted to evaluate the interrogator's performance. In the first test, some parts of the optical fiber were immersed in water, which was heated in a tank, as shown in Figure 2.18. The 1m and 2m sections were 0.9mm fiber optic cable, and the 10m section was 8mm fiber optic cable. The optical fiber was heated from 25 to 60 °C, and the results are shown in Figure 19. The two ramps between 65 to 75 m represent the 1m and 2m sections in the water. The ramp between 115 to 125 m is the 10m section in the water. The left figure shows the Brillouin scattering frequency shift when the temperature changed from 25 °C to 60 °C, whereas the optical fibers that were out of the water tub remained at 0 frequency change.

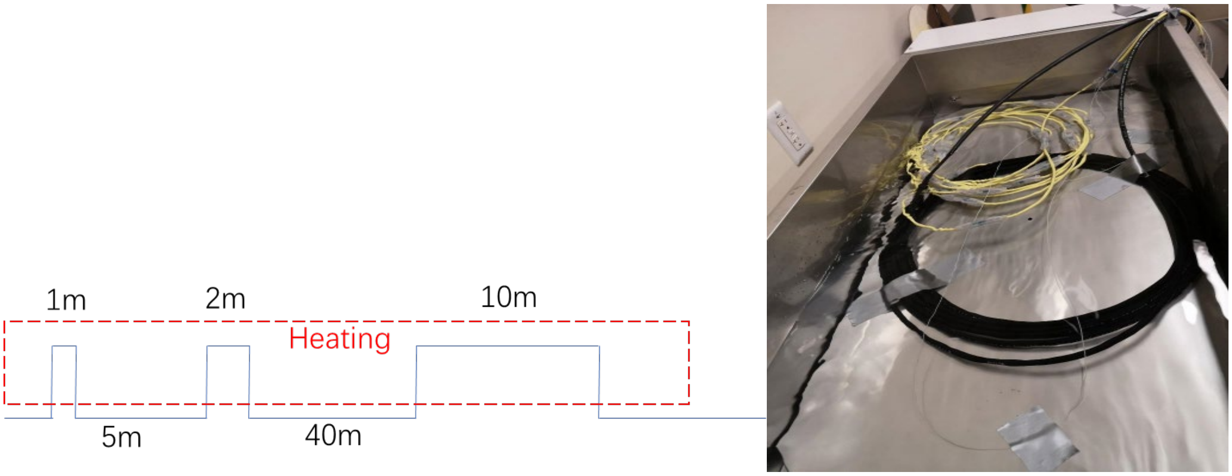

Figure 2.18 The water bath test setup for the temperature change test. 1 m, 2 m and 10 m sections of optical fiber was merged in the water to be heated with accurate temperature control. The length between 1 m and 2 m is about 5m and the length between 2 m to 10 m is about 40m.

The right figure in Figure 2.19 displays the Brillouin scattering frequency shift profile when the temperature was at 53, 54, 56, and 60 ℃. The variations in these readings demonstrate its capability to identify a 1 ℃ change. The accuracy of the readings ranges between 0.8 to 1.2 MHz, depending on the optical fiber length.

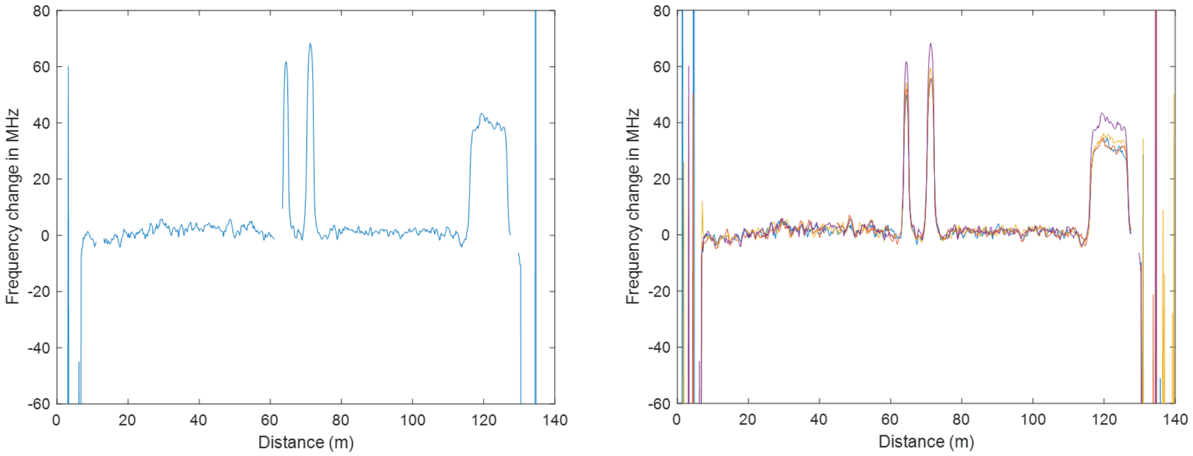

Figure 2.19 The testing result for the water bath test with water temperature changed from 25 to 60 ℃. Heated section was 1 m and 2 m at about 65m and 10 m at about 115 m. Left figure shows the Brillouin frequency shift profile when the temperature was 60 ℃ with 25 ℃ reference. Right figure shows the Brillouin frequency shift profiles when temperatures were 53, 54, 56, 60 ℃ with 25 ℃ reference.

In general, the interrogator has a specification shown in Table 2.2.

Table 2.2 The specification of the homemade STFT-BOTDR

Spatial resolution	1 to 10m
Readout	2cm to 50cm
Sensing distance	Up to 10km
Accuracy	0.8 to 1.2MHz below 2km 2MHz at about 5km 2.5MHz at about 10km Note: 500 MHz/% or 1 MHz/℃
Channel	2 channels (possible for more channels)

Interrogator deployment and data collection

After the optical fiber cable was successfully installed, the LBNL team set up a home-made interrogator for distributed fiber optic strain sensing (DSS) based on Brillouin scattering. This interrogator reads strain and temperature simultaneously, resulting in combined strain and temperature information in the readings. Temperature compensation is necessary during the data processing to ensure accurate results. Figure 2.20 shows the system.

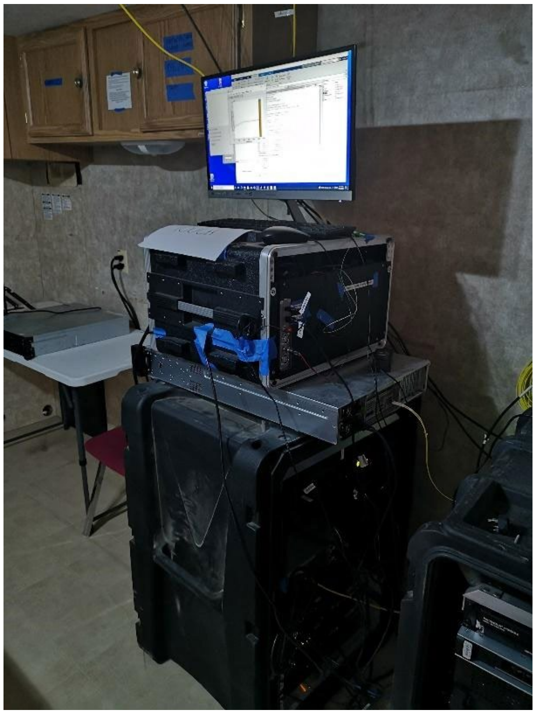

Figure 2.20 The interrogator used for distributed fiber optic strain sensing.

The single-mode fibers in the optical fiber cable from wells 1F and 2F were connected to the interrogator using FC/APC connections. Since the two single-mode fibers have different core characteristics, they exhibit different Brillouin scattering frequency shifts (BFS). The interrogator was adjusted to accommodate the BFS for both single-mode fibers, and the output power and other settings were optimized based on the power loss and power budget for the installed fibers. Subsequently, several readings were taken for both 1F and 2F to ensure the parametric setup worked.

Initially, measurements were focused on well 2F for about a month due to an interesting bump in the measured profile. However, it was discovered that there was a significant power drop at around 14,600 feet, resulting in reduced resolution at the bottom of the well. Consequently, in December, the fiber connected to the interrogator was switched to well 1F. The interrogator recorded data with a 20-minute measurement frequency, 0.4m data interval, and approximately 3m spatial resolution. The data was saved locally and shared with the QNAP. Regular processing of the data was conducted to assess the system's performance.

The following figures (Figures 2.21-2.24) display some example profiles, including the reading profiles for well 2F in November, the reading profiles from December 22 to January 20 for well 1F, the raw Brillouin scattering frequency shift of well 1F, and the strain and temperature changes in well 1F since December 22.

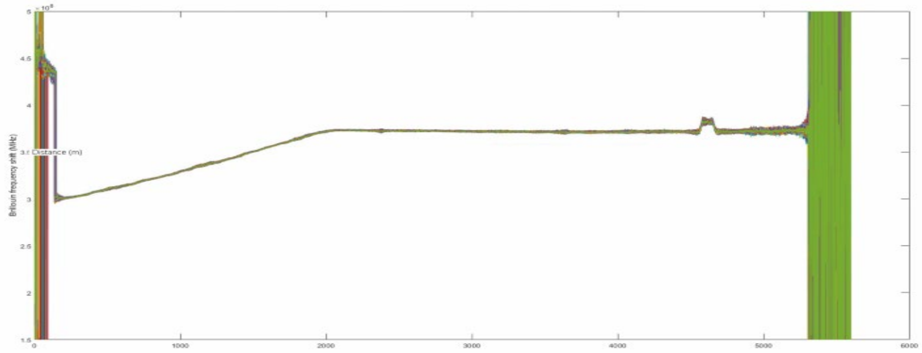

Figure 2.21 The reading profile of 2F.

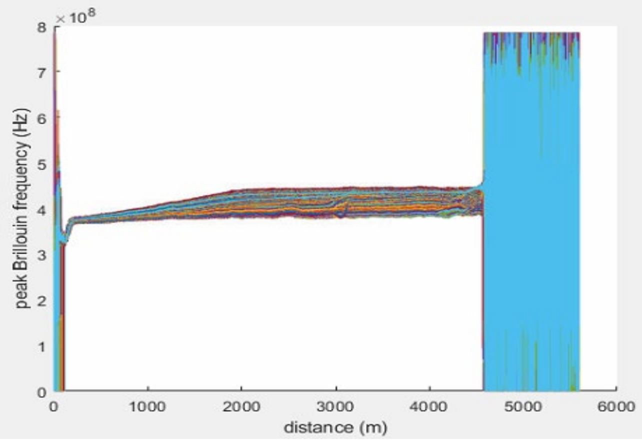

Figure 2.22 The reading profiles following December 22.

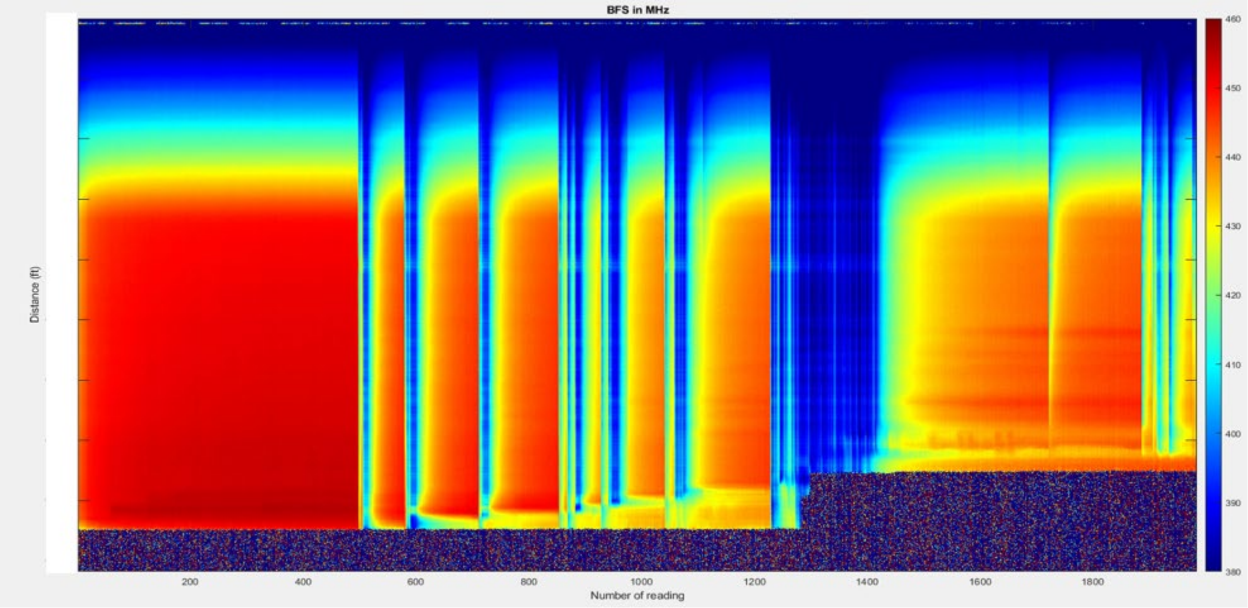

Figure 23: The raw Brillouin frequency shift readings for DSS of 1F after December 22.

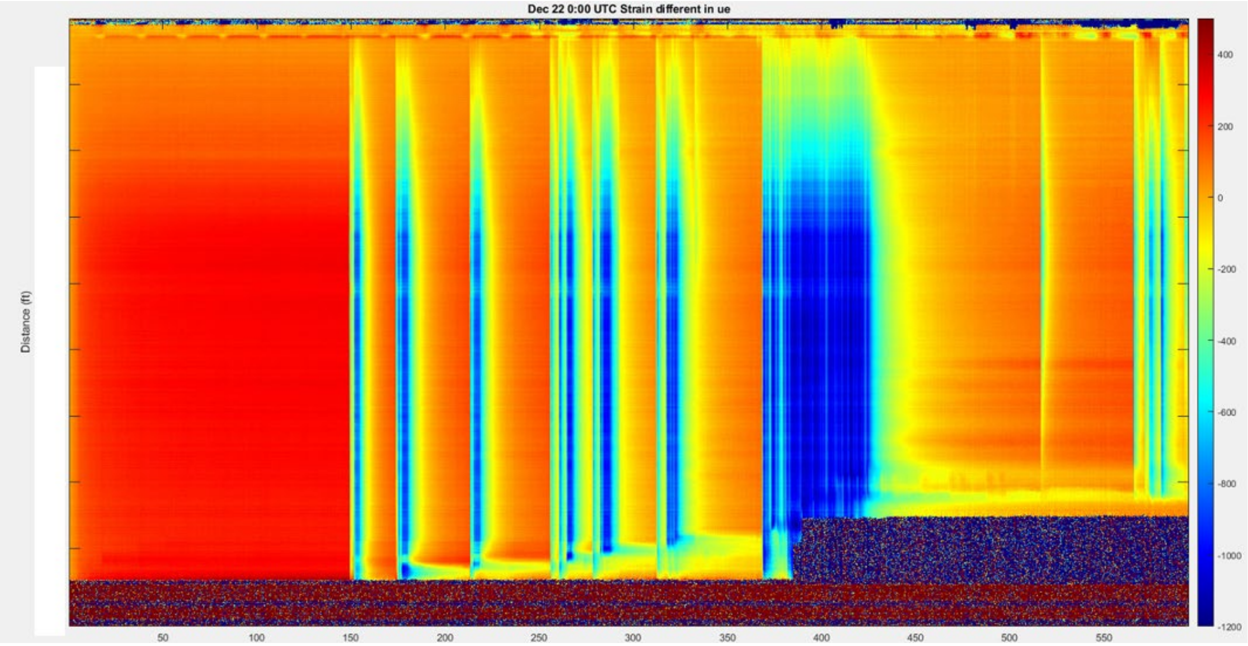

Figure 24: The strain and temperature change readings for DSS of 1F after December 22.

2.4 Data processing and edge computing

We developed an on-site data processing flow to generate data products as well as quality control plots in a rapid manner after the daily acquisition. In total, we acquired approximately 1 Tb of data daily, therefore, it was important to develop an automated flow that could “sort” through the large amount of data and provide insightful information of the daily fiber-optic datasets. The objective of the on-site processing flow was to (1) streamline and accelerate the processing of the large amount of data and provide a quick assessment of the quality and information containing the data, (2) generate smaller datasets or data products that could be transferable over the internet for further in-house processing.

Figure 2.25 illustrates the data stream, from the interrogator units and SOVs, to the data storage and processing server. The rapid quasi-real-time processing flow provides data products of the daily raw data as well as quality control plots to assess information such as frequency range and time series of the SOV sweep, as well as provide particular insights daily, such as temperature changes along the well and low-frequency strain.

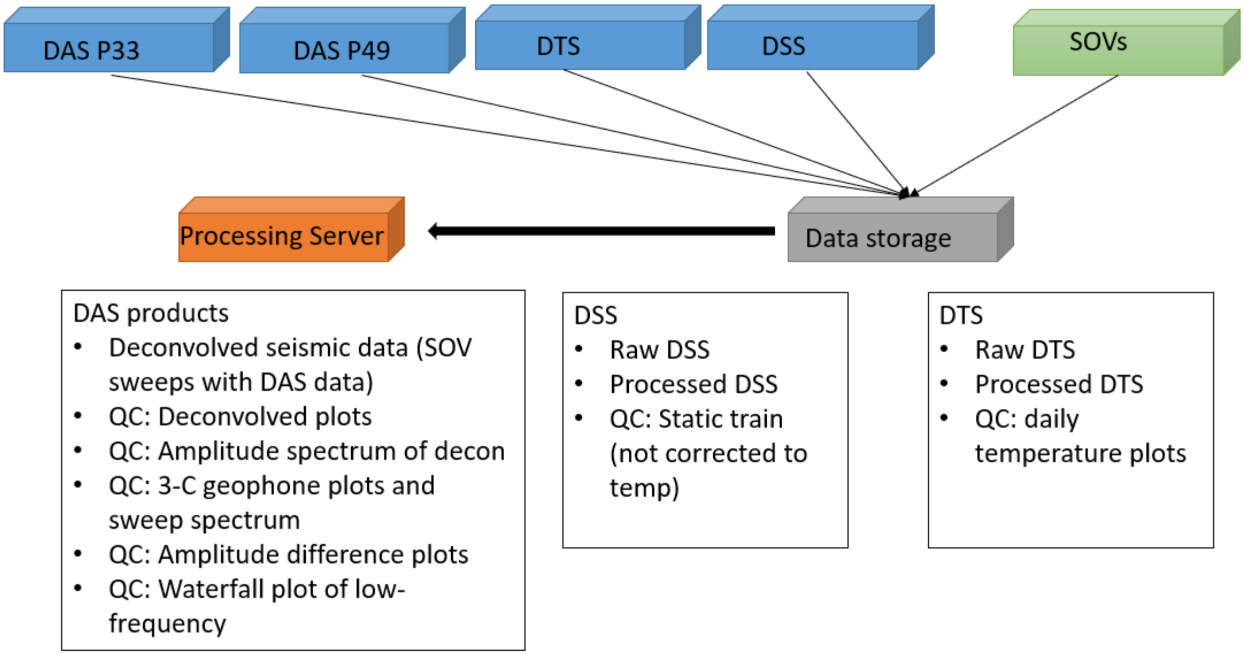

Figure 2.25 Diagram of the on-site data stream. After acquisition of the data from each field equipment, the data is then stored in 200 Tb data storage units, which are then read by the processing server to generate the pre-processed data and QC plots.

2.4.1 DAS/SOV

The raw DAS data is also processed as a conventional VSP survey to generate a series of seismic gathers for each SOV sweep acquired. For this processing flow, given that the DAS data is acquired continuously, we first match the DAS GPS time to each sweep start time. After matching the correct start time of the sweep to the DAS data, we deconvolve the DAS signal with the sweep signal. Deconvolution is preferred in this case in comparison with cross-correlation because it minimizes the effect of correlation side-lobes caused by the unbalanced frequency spectrum of the pilot sweep, as the amplitude of the signal is proportional to frequency squared. Plots of the seismic gathers and sweeps are saved for quality control. Figure 2.26 provides an example of one of the QC plots generated from the DAS/SOV data processing stream. The figure shows the time series of the near-field geophone at SOV5 location recording a 150 s sweep, as well as the frequency information of the sweep signal.

After the data products are generated, they are automatically uploaded to the cloud. We should note that the processing steps reduce data volume by close to two orders of magnitude, thus allowing transfer even at sites with bandwidth limited telemetry links. The subsequent phases of the seismic data processing are done in-house. After obtaining the deconvolved sweeps, each 10-sweep cycle is stacked, resulting in one VSP gather per hour for each source position (this was the acquisition schedule during stimulation). The stacked VSP gathers go through a noise attenuation flow consisting of applying a band-pass filter of 5 to 80 Hz, followed by a 2D spatial filter to remove the common-mode noise caused by ambient vibrations in the vicinity of the DAS interrogator. An additional 2D spatial filter is applied after sorting the data to the receiver domain to minimize the effect of noisy traces caused by disturbance in the well due to stimulation and surface activities.

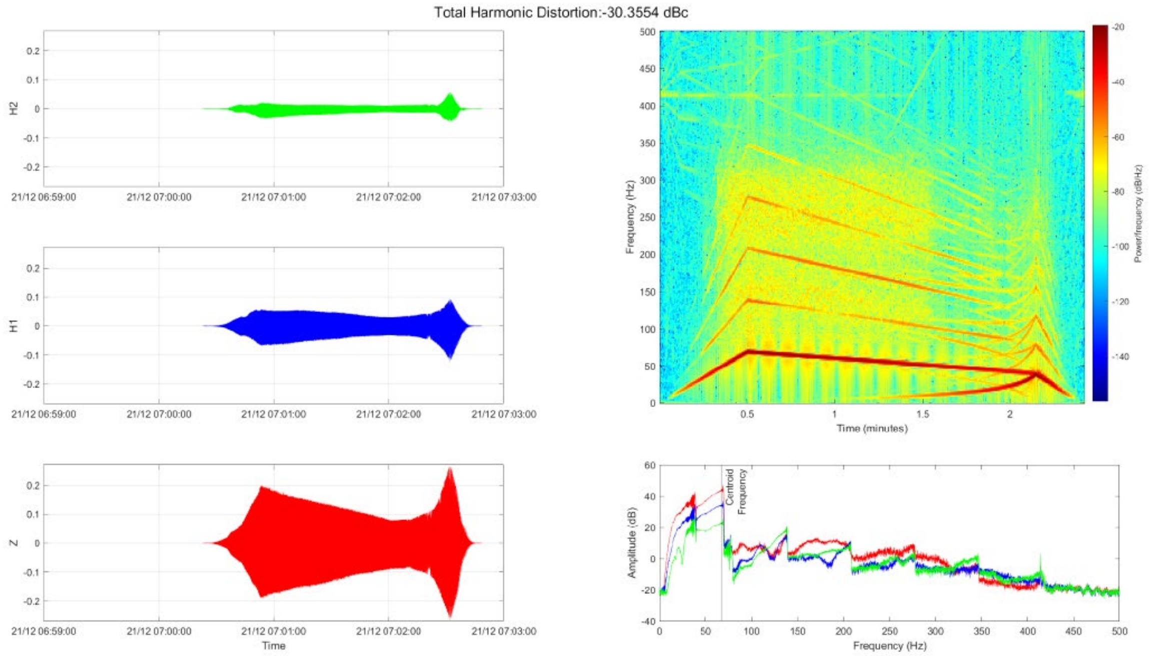

Figure 2.26 Example of a quality control plot showing the sweep response. On the left, the three-component time series of the near-field geophone recording of the sweeps is plotted; on the top right, the frequency spectrum of time of the vertical component of the geophone; on the bottom right, the amplitude spectrum of the three geophone components.

2.4.2 Low-frequency DAS

We established an automated workflow to estimate the low-frequency (LF) component of the DAS data (LF-DAS). LF-DAS strain-rate and strain signals have been observed to be helpful in monitoring the formation, growth and propagation of fractures and estimate fracture characteristics (length, height, width) in other studies. In this workflow, the raw DAS data for the horizontal section of the wells under treatment are read in segments of 4.8 hours and decimated to 5 Hz. The segments of decimated data are distributed in the cloud. This minimally processed dataset (only decimated) is easily transferred over the internet every day and can be used for further analysis and interpretation. We further remove common mode noise from the decimated strain-rate data by subtracting the median value over all channels for each time sample. Next, plots are prepared to display both strain-rate and strain (strain-rate integrated to strain) for a range of frequency passbands and clipping levels for quality control and monitoring purposes and distributed to other researchers (for example, Figure 2.27).

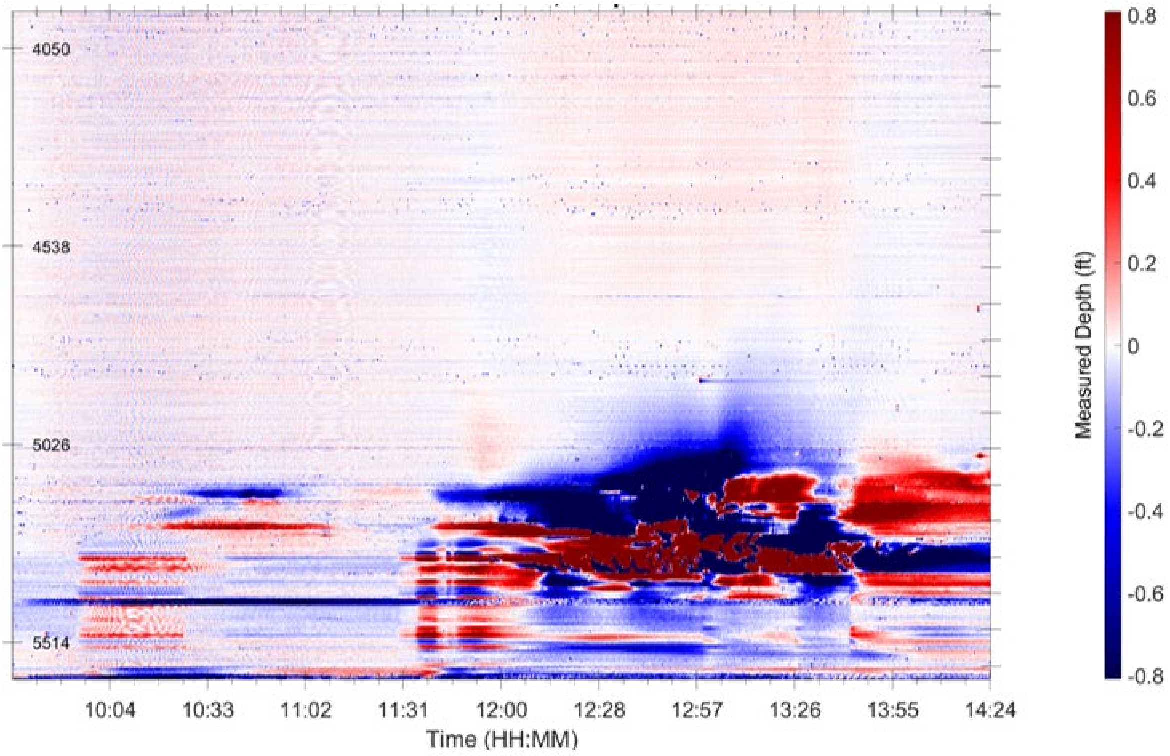

Figure 2.27 LF-DAS (strain-rate) recorded at well 1F, low-pass filtered at 0.1 Hz. The recorded strains are in response to the treatment of adjoining well 2F (stage 7). The regions in red are extending and regions in blue are compressing.

2.4.3 Microseismic events

Numerous microseismic events were detected during the hydraulic fracturing operations at wells 1F, 2F and 1H (Figure 2.28, for example). The catalog of microseismic events induced during the hydraulic fracturing operations was developed by Microseismic Inc. (MSI) using a dense surface geophone array. However, the data quality for surface instruments typically suffers from near-surface noise, thereby preventing the detection of smaller events. Downhole DAS deployed in the horizontal section of wells recorded high quality signals from the microseismic events, being very close to the seismic sources. We therefore establish a workflow to detect, locate and estimate magnitudes of the microseismic events using the downhole DAS data. This workflow was performed in-house after data acquisition.

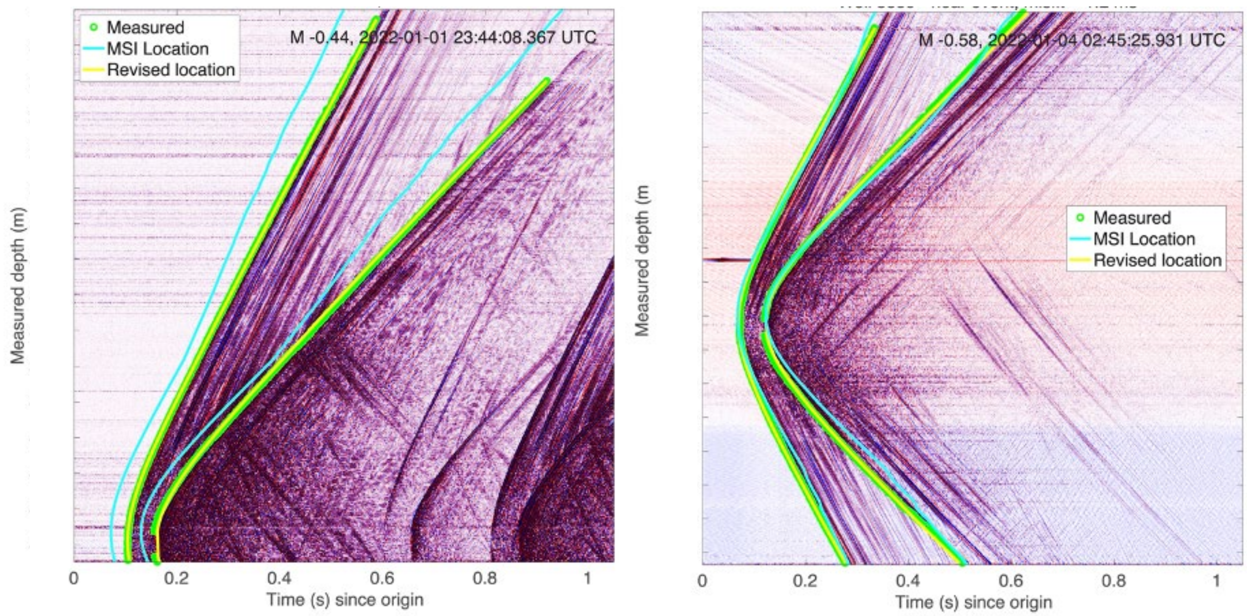

Figure 2.28 DAS record section of an example microseismic event - left: well 1F, right: well 2F. Green circles are measured arrival times. Cyan curves are the predicted arrival times for the original location and the velocity model. Yellow curves are the predicted arrival times for the revised location and the uniform velocity model.

2.4.4 Distributed Temperature Sensing (DTS)

We established a simple automatic processing workflow for the DTS data at wells 1F and 2F. The product of this workflow is a series of quality control plots like shown in Figure 2.29 that show three temperature traces with depth for given times (left side) and two waterfall plots. The top waterfall plot shows absolute temperature with time while the bottom one shows the instantaneous change in temperature with time. The bottom-most panel shows two time series for the specified depths.

We also set up automatic data transfers between the local storage from the XT-DTS to the LBNL network-attached storage on-site in Texas. From there, the data are transferred to LBNL servers and disseminated to project collaborators in the cloud. Multi-mode fibers in each of the two wells were interrogated by Silixa XT-DTS units.

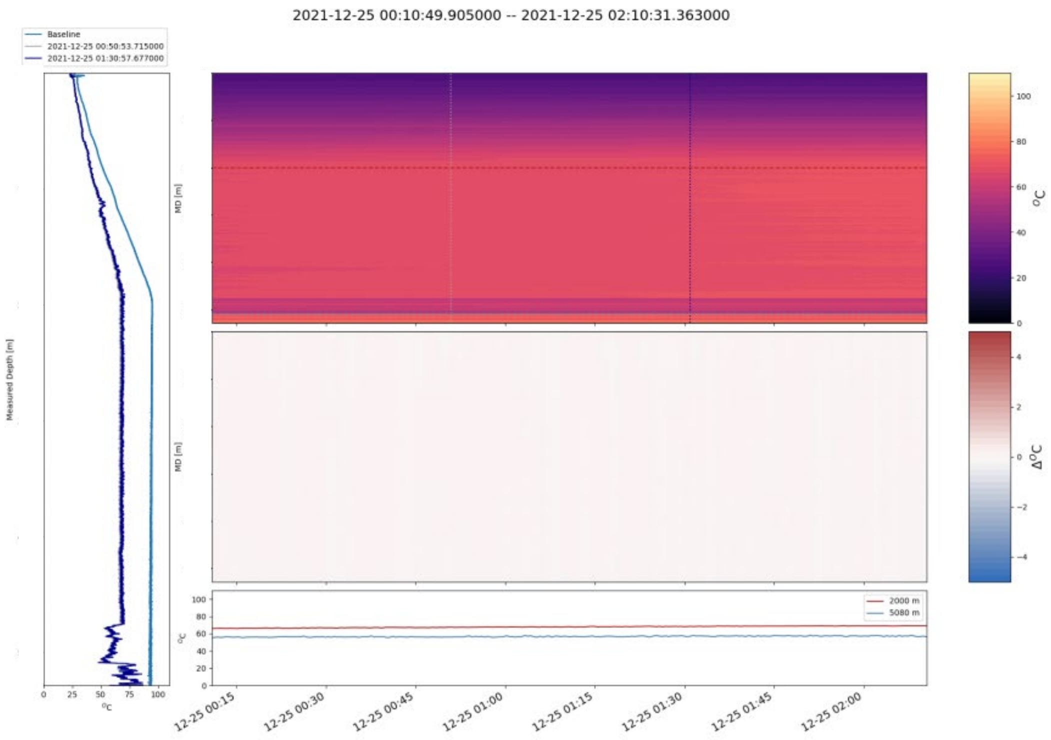

Figure 2.29 Temperature plot of the pre-processed DTS data.

2.4.5 Distributed Static Sensing (DSS)

After the optical fiber cable was successfully installed, LBNL team set up a home-made interrogator for the distributed fiber optic strain sensing (DSS) based on Brillouin scattering (Figure 2.20) during the November 2021 field trial. This interrogator reads strain and temperature changes at the same time. Therefore, the readings combine the strain and temperature information. The readings need to be temperature compensated in the data processing.

The single mode fibers in the optical fiber cable from well 1F and 2F were connected to the interrogator with FC/APC connection (during stimulation, only 1F was connected to the DSS). The two SMF fibers have different core characteristics therefore they have different Brillouin scattering frequency shift (BFS). The interrogator was adjusted to fit the BFS for both SMF fibers. Then the output power and other settings of the interrogator were optimized based on the power loss and power budget for the installed fibers. After that, several readings were taken for both 1F and 2F to make sure the parametric setup worked.

At the beginning, the 2F was selected and measured for about one month because it had an interesting bump in the measured profile (Figure 2.30). However, it was found that there was a large power drop at about 14600 ft, leading to a worse resolution at the bottom of the well. Then the fiber connected to the interrogator was switched to 1F in December (Figure 2.31). The interrogator read with 20 min measurement frequency with 0.4m data interval and about 3m spatial resolution. The data was saved locally and shared to the QNAP. The data was then regularly processed to check the performance of the system. The following figures shows some example figures, including the reading profiles for the 2F in November (Figure 31); the reading profiles from Dec 22 to now of 1F (Figure 32); the raw Brillouin scattering frequency shift of the 1F (Figure 2.32); the strain and temperature changes in the 1F since Dec 22 (Figure 2.33).

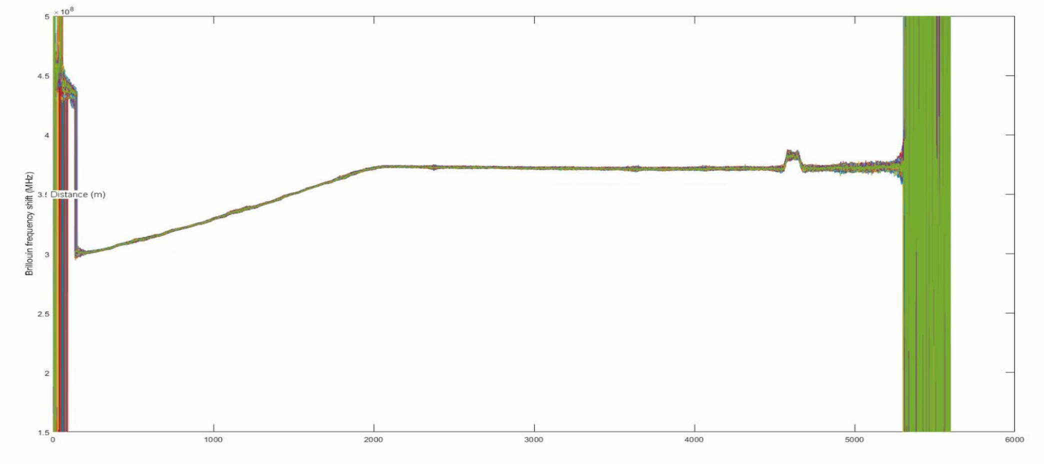

Figure 2.30 The reading profile of 2F.

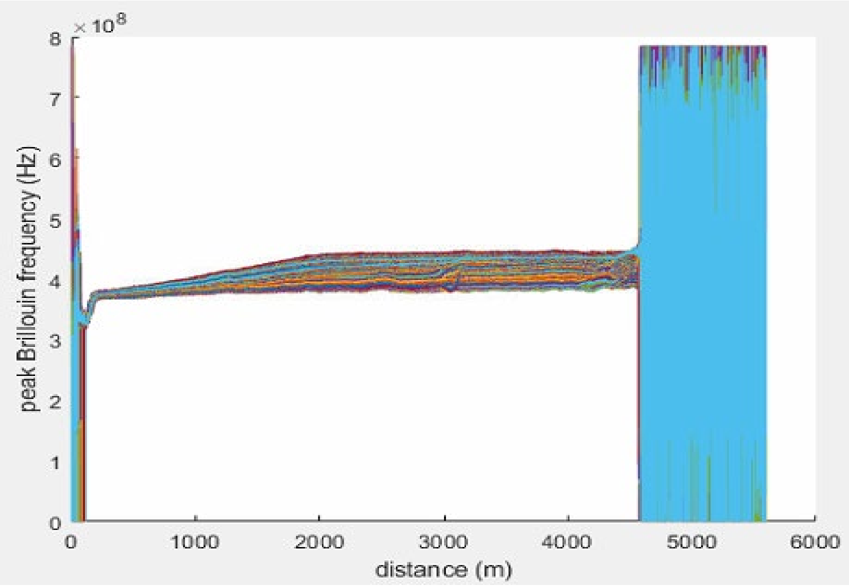

Figure 2.31 The reading profiles from Dec 22 to now of 1F.

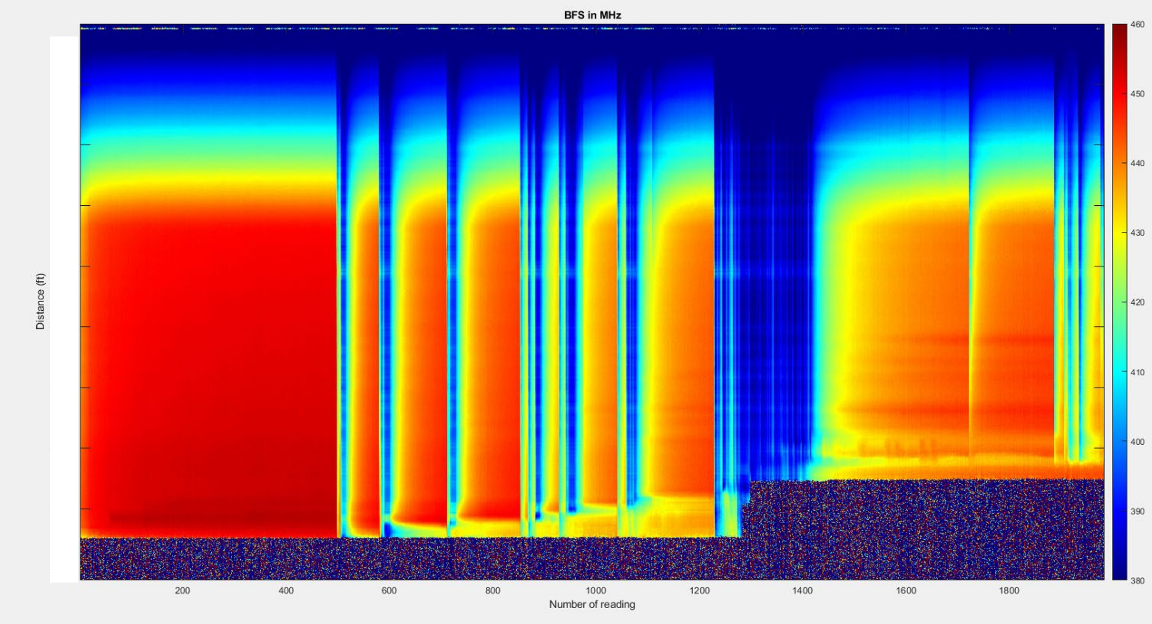

Figure 2.32 The raw Brillouin frequency shift readings for DSS of 1F after Dec 22.

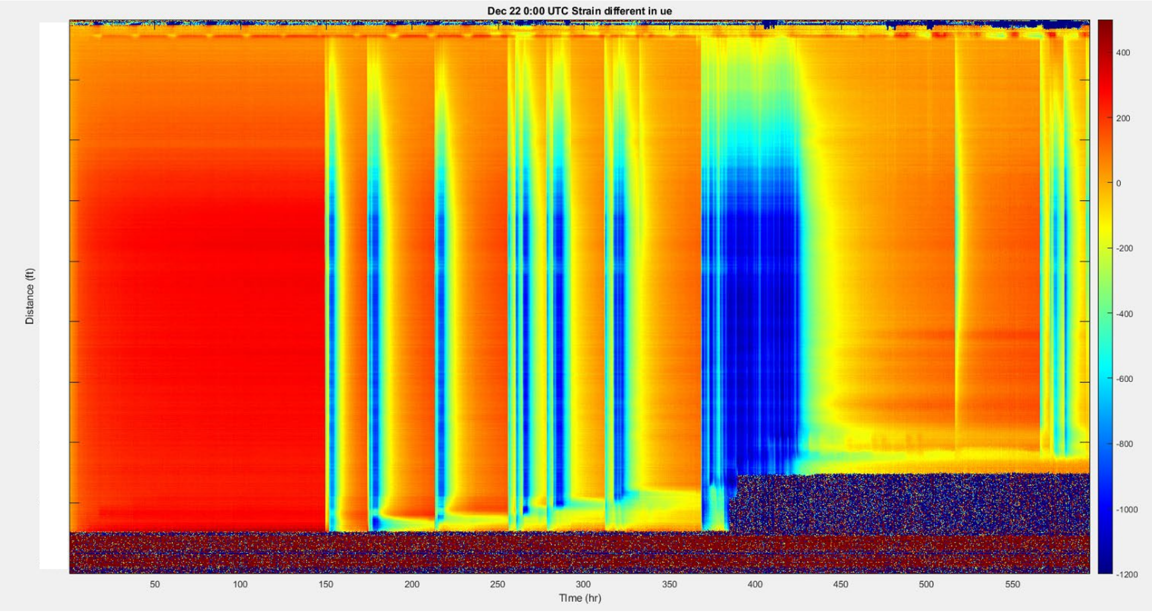

Figure 2.33 The strain+temperature change readings for DSS of 1F after Dec 22.

2.5 Fiber-optics Data Analysis during Stimulation

We acquired continuous fiber-optics (DTS, DAS, DSS) data for the stimulation period. After approximately one month of operations, the fiber was damaged which stopped us from monitoring during production. Below we describe the results for the continuous DAS measurements and DSS during stimulation.

The results in this section were published in Zhu et al. 2023, Saw et al., 2023, Ma et al. 2024, Correa et al. 2024, Glubokovskikh et al. 2024, Nayak et al. 2024.

2.5.1 DAS/SOV

DAS/SOV timelapse data analysis

For the analysis of the timelapse DAS/SOV data, we focus on the first nine days of stimulation (Figure 2.34). Figure 2.34 shows the full running schedule for the SOV, and in this analysis we focus on the time highlighted in gray. During the first nine days, SOV3 and SOV5 were running every hour, for 30 minutes straight, for a total of 10 sweeps each round. The two locations were chosen due to their optimum position in relation to the stimulation along the toe of the well, as SOV3 and SOV5 would shoot wave paths across both sides of the newly formed fractures. During the first nine days, well 1F mostly served as a monitor while 2F was being fracked.

Figure 2.35 shows the shot gathered after a band pass filter up from 10 to 70 Hz and two passes of 2D spatial filter to remove common-mode noise from the DAS interrogator vibration. Figure 2.36 has an additional pass of a 2D spatial filter, this time in the receiver domain, to remove the burst noise in the traces that appear randomly in Figure 2.36. Note that the data in Figure 2.36 appears significantly smoother after the removal of the burst noise. To isolate the scattering events due to fracturing, we remove the first breaks, seen in Figure 2.37 (first break picks are displayed in red). Note that, after the removal of the first breaks, the scattering events are more visible, appearing with time and disappearing as the stages are completed. The scattering anomalies appear to be seen by the DAS/SOV data for several days, when they disappear. To our knowledge, this is the first time scattering from fractures is recorded on VSP data at every hour, showing unprecedented time snapshots on fracture dynamics. This information can be used to understand the fracture compliance and permeability as it can suggest the time each fracture stays opened.

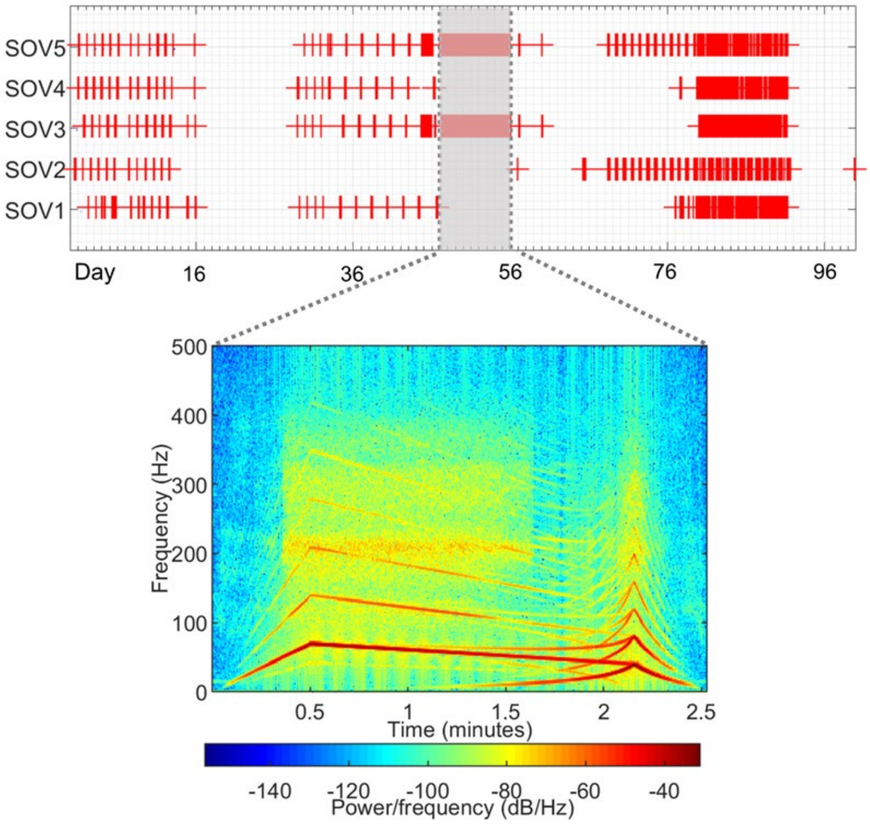

Figure 2.34 The top plot shows the time of operation for each SOV since the start of the continuous acquisition, before stimulation; the gray area represents the nine days of continuous hourly operation on SOV3 and SOV5 during stimulation. The bottom plot shows the frequency spectrum of the SOV sweep during the nine days of acquisition.

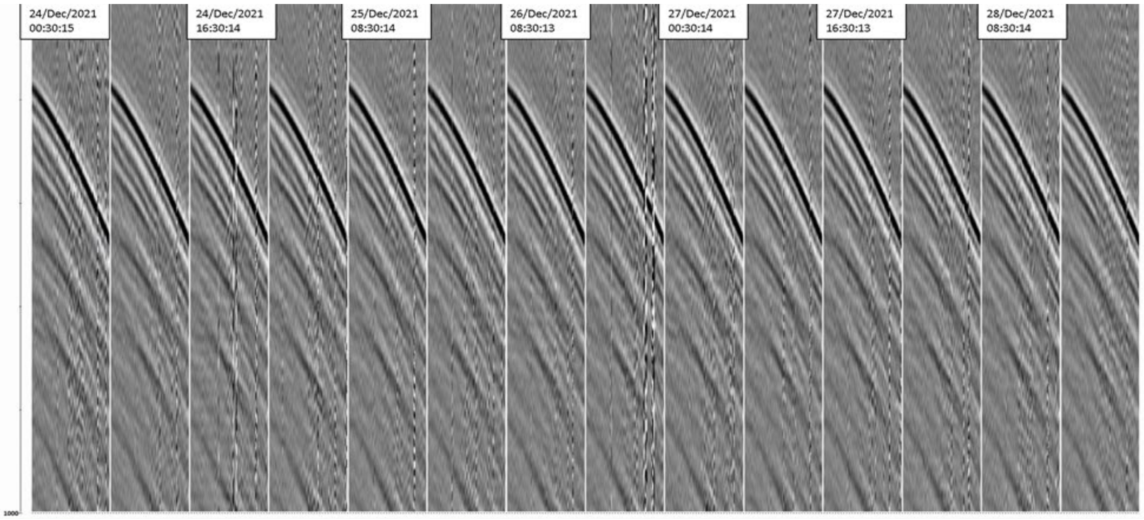

Figure 2.35 Shot gather acquired with DAS in 1F well and SOV3, from the 24th of December at 00:30:15 UTC until the 28th of December at 16:30:13 UTC. Data has had a bandpass filter and 2D spatial filter applied. The x-axis displays measured depth in meters while the y-axis displays time in milliseconds.

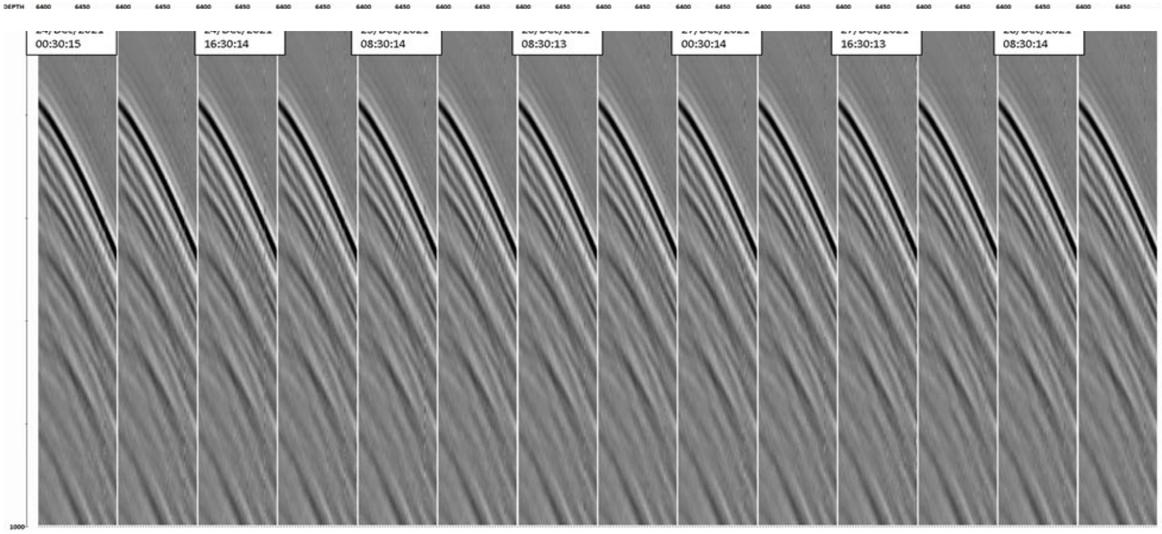

Figure 2.36 Shot gather acquired with DAS in 1F well and SOV3, from the 24th of December at 00:30:15 UTC until the 28th of December at 16:30:13 UTC. Data has had 2D spatial filter applied in the receiver domain using the output shown in Figure 1. The x-axis displays measured depth in meters while the y-axis displays time in milliseconds.

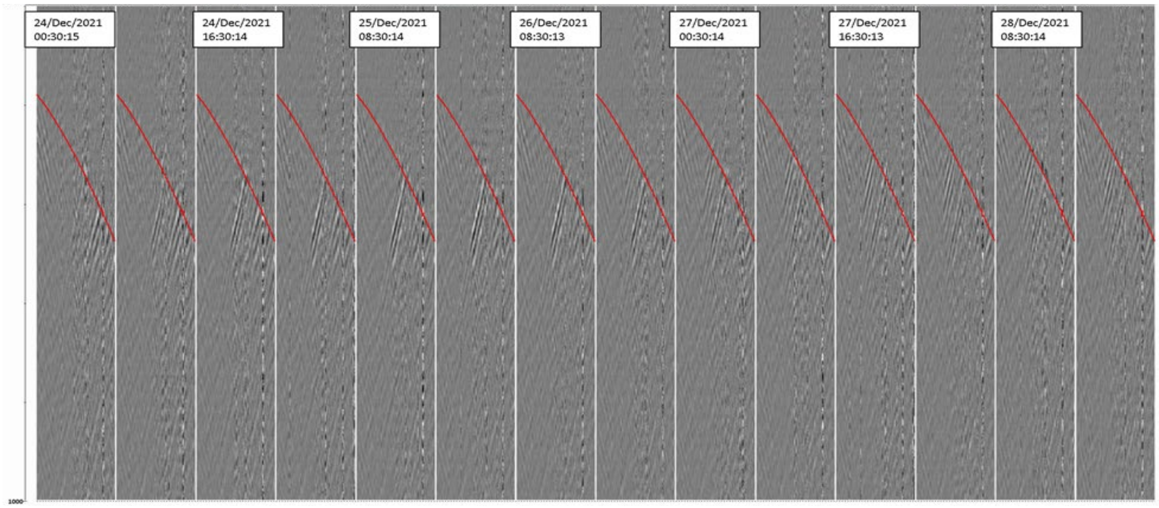

Figure 2.37 Shot gather acquired with DAS in 1F well and SOV3, from the 24th of December at 00:30:15 UTC until the 28th of December at 16:30:13 UTC. Data has the first breaks removed, using as input the data in Figure 2. First break picks are displayed in red. The x-axis displays measured depth in meters while the y-axis displays time in milliseconds.

To understand the dynamics of fracture behavior through the seismic measurements, we analyze the variations in fracture reflectivity over time. To compute this parameter, we use fully-processed shot gathers after baseline subtraction (acquired before stimulation on the 20th of December), and flatten the reflections along the time coordinate. After flattening, a top mute is applied above the first break and a bottom mute is applied 100 ms after the first break. Each one hour flattened snapshot is then stacked into one single trace. The time-depth relationship obtained from the VSP is used to convert the relative time to depth.

Figure 2.38a shows the evolution over time of the SOV/DAS fracture scattering amplitudes in Well 1F, as Well 2F is undergoing treatment, where each wiggle represents the amplitude of the scattered events at each hour. Figure 2.38b shows the simultaneously acquired LFDAS data, where blue indicates compressive strain and red indicates extension. Hydraulic fractures initiated from Well 2F and intersecting Well 1F show up as frac-hit patterns in LFDAS, where we can observe extension strain at the tip of a fracture, and compression of its sides (Zhu et al., 2023). Figure 2.38c shows the pressure in the treating well, Well 2F, acquired with a wellhead pressure gauge; each increase in pressure marks the start of a fracturing stage.

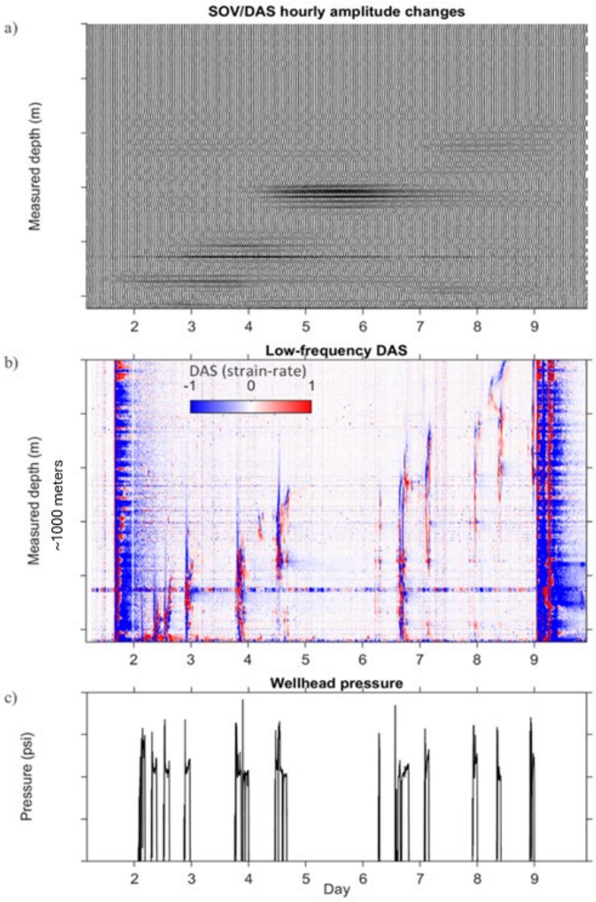

Figure 2.38 (a) Stacked hourly amplitudes from the scattered energy along the nine days of continuous operation as recorded in Well 3. (b) LFDAS as recorded in Well 3. (c) The wellhead pressure is displayed for the treating well, Well 2F. The increase of the scattered amplitudes in Well 1Fcorrelates well with the pressure increase as treatment starts in Well 2F. The LFDAS anomaly indicates frac-hits from the treating well to the monitor well. Note the SOV/DAS amplitudes decay slowly with time after the end of each stage. Figure from Correa et al. 2024.

Quality Control

We calculate the RMS amplitude difference of all the datasets acquired for 1F and SOV3. The RMS amplitude can show changes associated with fluid substitution in the rock frame. To calculate the RMS amplitude, we use a 10 ms window around the first break. The difference is taken from the RMS amplitude of the baseline, acquired on the 20th of December, with each respective consecutive dataset. The RMS amplitude difference for 1F well (Figure 2.39) shows a clear amplitude anomaly towards the toe of the well (yellow anomalies), which follow stage depths occurring in 2F (blue dots). This suggests DAS/SOV3 in 1F is sensitive to the fracturing occurring in the stimulated well.

A series of quality control plots can be generated to ensure the above signatures are not related to any noise happening on the surface or even within the well. Signal-to-noise ratio (SNR) and normal-root-mean-square (NRMS) plots can be helpful to indicate sections of the well that can be "trusted", where the signal is strong and repeatable. Figure 2.40 shows the SNR for the 1F using SOV3, for all the datasets acquired for this well-source pair. The yellow sections indicate high SNR, reaching 30 dB. For this well-source pair, high SNR data is present along the toe and heel sections, with low SNR along the middle of the lateral. This happens as a result of the angular sensitivity of DAS (less sensitive to P wave arriving perpendicular to the fiber axis). Along the toe, where we see the amplitude anomaly feature in 1F, the SNR is high, indicating that these are datasets with relatively low noise.

Additionally, NRMS can indicate sections along the well where the data is repeatable, meaning it replicates well the baseline data (in this case, the baseline is acquired on the 20th of December). A general "rule-of-thumb" considers NRMS values below 40% repeatable. Figure 2.41 shows the NRMS value for 1F and SOV3 is mostly below 40% for the toe area. Therefore, both quality control plots, RMS and NRMS, indicate that the amplitude signature seen on Figure 4 is an event related to the fracturing in 2F.

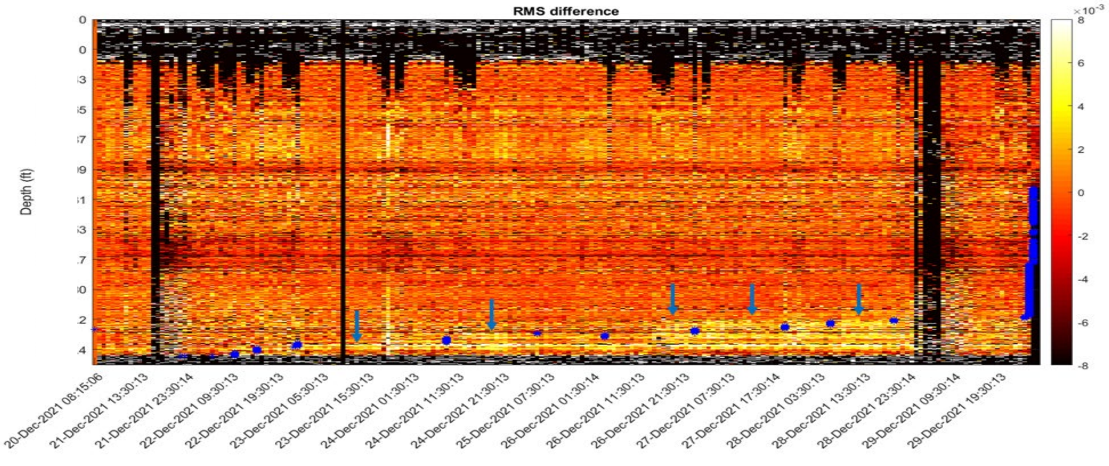

Figure 2.39 RMS amplitude difference of the P direct arrival for all the data acquired with DAS in 1F using SOV3. The difference indicates the changes in comparison with the baseline survey, acquired on the 20th of December. The blue dots indicate the time and location of stages occurring in 2F. The blue arrow indicate the area where there is an increase in amplitude, which seems to follow the stages occurring in the adjacent well.

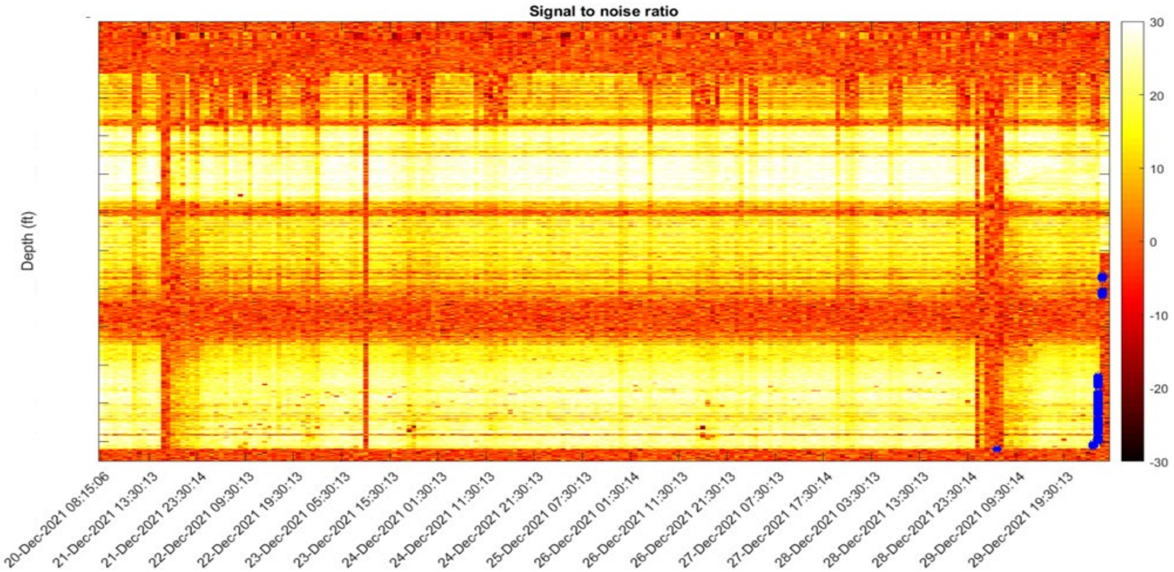

Figure 2.40 Signal to noise ratio calculated for all DAS data acquired in 1F with SOV3. SNR is displayed in decibels (dB).

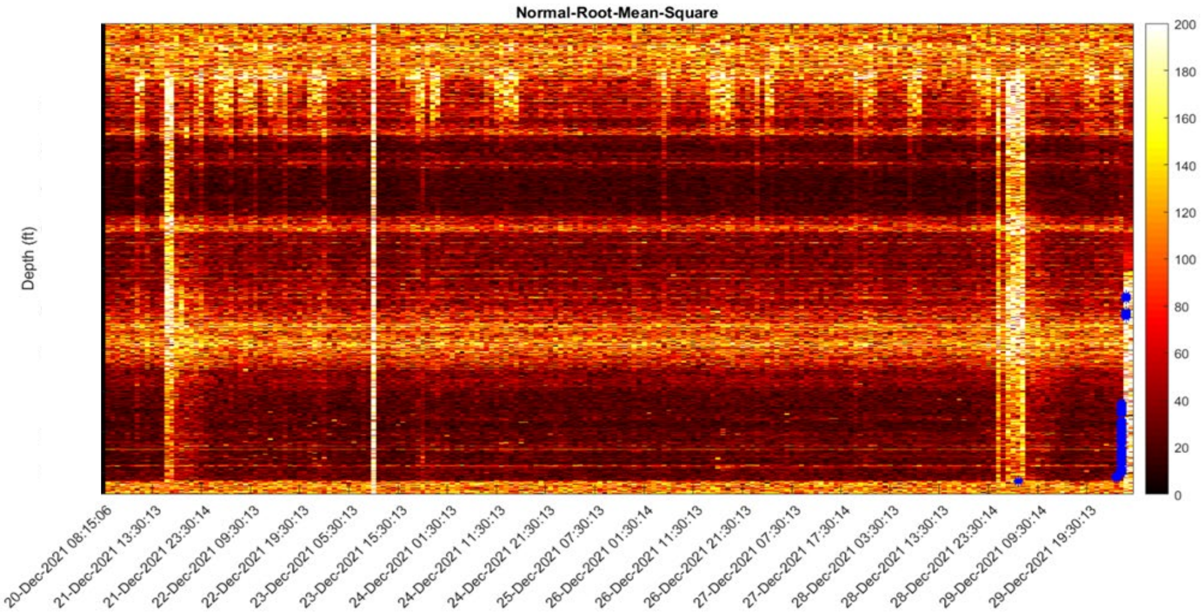

Figure 2.41 NRMS repeatability values for all DAS data acquired in 1F well with SOV3. Value below 40% are considered repeatable. NRMS is displayed in percentage (%).

Quantitative interpretation of seismic scattering on fractures

The SOV/DAS monitoring data contain scattered seismic waves on fracture planes distributed along the borehole. Reflectivity of these fractures varies with time and has a clear correlation with the fluid injections into the stimulation well. A rigorous interpretation of the seismic anomalies and strain anomalies requires application of sophisticated rock physics models of an individual fracture.

Although the presented data set is extremely rich in terms of the subsurface characterization, we still may not unambiguously constrain the geometry of the fractures and their permeability. It will require a comprehensive, almost forensic, rock physics analysis of the seismic anomalies in combination with the strain-rates and microseismic clusters. We mentioned the likely candidates to explain the observed data: fracture opening, deposition of stiff clusters of interconnected proppant grains, contacting asperities on the fracture surfaces, vertical and lateral growth of the existing fractures, and formation of the new fractures in-between the existing ones. Typically, VSP interpretation only considers the last aspect and pore pressure effects. In reality, all of these processes affect the seismic response simultaneously and may not be decoupled. Therefore, we believe that for our field experiment, the standard approaches to the analysis of fracture scattering (Binder et al., 2020; Titov et al., 2021) may be an oversimplification. One must rely on sophisticated coupled geomechanical simulations to estimate the hydromechanical fracture properties based on the pressurization/relaxation times and number of fracture hits. Such estimates would aid a robust prediction of the performance of stimulated reservoirs.

This section discusses some hydromechanical processes, which may explain the observed signals and provide some insights into the process of fracture activation.

Qualitative analysis of the evolution of the fracture reflectivity

In the previous section, we described the anomalies detected by the LF-DAS and the seismic scattering in the SOV/DAS data. Although the geophysical signals induced by reservoir stimulation operations vary for different depth intervals, the data reveal a repeated pattern:

- Phase 1: seismic scattering appears along the entire segment of the fiber-optic cable, around the time of a borehole operation that manifests itself by a strong strain anomaly on the first day.
- Phase 2: the strength of the seismic signals decreases in the parts of the reservoir that are located further away from the toe and are not reactivated by the fluid injections.
- Phase 3: the apparent changes of the seismic reflectivity are consistently preceded by bursts of strain-rate, which indicate an onset of reservoir stimulation.
- Phase 4: finally, the seismic anomaly gradually fades away once the stimulation stages progress toward the heel.
- Phase 5: the seismic amplitudes flatten out after another strain anomaly extended through the entire borehole.

To explain the origin of Phases 1-4, we rely on the linear slip model of fracture deformation (Schoenberg, 1980; Schoenberg and Sayers, 1995). Due to high compliance of fractures, propagating seismic waves become discontinuous across the fractures; the waves induce a significant displacement of the opposite surfaces of the fracture. The size of the displacement discontinuity depends on the moduli of the fracture-filling material, the fracture aperture (Fehler, 1982; Oelke et al., 2013), and the contacts between the fracture surfaces (Glubokovskikh et al., 2016; Sayers & Kachanov, 1991). Thus, we expect to see a strong response from a pressurized or hydropropped fracture, which is wide open, has only a few small contacts, and contains proppant grains suspended in fracturing fluid without direct load-bearing contact. Otherwise, contacting asperities at fracture surfaces and dense proppant packs transmit the normal and tangential displacements through the narrow fracture in a stress-dependent manner. At higher effective stress states, the propped fracture may have a minimal seismic contrast with the surrounding formation. We hypothesize that Phase 2 corresponds to pressure dissipation inside fractures opened on the first day of the treatment of the stimulation well and a corresponding increase in normal stress across the fracture plane. In the interval 4900-5020 m, Phase 2 is absent, because this interval remains pressurized, as it is close to the first stimulation stage (the first stage happens before the time frame displayed at a section of the toe without fiber). Once the fracturing operations approach a particular interval, the fracture-associated reflectivity slowly increases due to hydraulic connectivity with adjacent fracturing operations, until the interval is stimulated directly and existing fractures are pressurized again (Phase 3). After that, the pressure dissipates and the proppant is slowly loaded within the fracture, effectively reducing the impedance contrast visible to seismic waves (Phase 4 and Phase 5).

The interpretation above ignores the fact that fractures may grow during stimulation. Each fracture patch will contribute to the observed scattered amplitudes depending on its position and orientation relative to the receiving fiber-optic cable, and thus fracture configuration plays an important role in the observed seismic amplitudes. In general, a larger fracture produces a stronger response than a smaller fracture with the same compliance. Also, fractures that intersect the monitoring borehole laterally and have sufficient height above the borehole will produce strong response

The last aspect that we discuss here has to do with the limited seismic resolution of the SOV/DAS data. The dominant seismic wavelength is around 100 m, which implies that seismic scattering from adjacent fractures, separated by less than 25 m, are indistinguishable. Thus, some of the changes of the scattering amplitudes may correspond to strain-rate anomalies produced by new hydraulic fractures that propagated from the stimulation well to the observation well, parallel to the ones that were activated by earlier fluid injections.

Seismic scattering amplitudes versus offset

In addition to the change of reflectivity, we may derive some useful conclusions about the fracture activation from the pre-stack seismograms – prior to the corridor stacking. Figure 2.42a shows a 'reflected' PS-wave in the difference seismogram acquire at day 5 of the continuous monitoring. Its spectral characteristics change with the offset to the fracture set due to the diffraction effects that play an important role at distances comparable with the fracture height (Figure 2.42b-c). Strong P-to-S reflection R_{PS} and transmission T_{PS} coefficients at the surface of weak fractures is anticipated for the steep incidence angles that we have for SOV-3 and the toe region the observation well, around 60° (Fehler, 1982; Oelke et al., 2013). However, P-to-P reflection R_{PP} should have considerable strength as well. Part of the reason that PP-waves are barely visible is the sensitivity of DAS. It is linearly proportional to k_{ax} - projection of the wave vector on the fiber. For the given incidence angles and seismic properties of the subsurface (Table 1), the receivers are almost three times more sensitive to the PS-waves than to PP-waves. For individual fractures we may realistically have $R_{\mathrm{PP}} \sim 0.5R_{\mathrm{PS}}$, so the reflected PP-wave is six times weaker than PS-wave and may be well below the noise level.

Two other features of our data set are somewhat puzzling: negligible time delays of the direct P-wave and absence of a strong transmitted PS-wave. The former one has been the main seismic characteristic of the SRV produced by hydraulic fracturing (Binder et al., 2020; Meek et al., 2019; Zhao et al., 2021). The P-wave slow-down is interpreted as the overpressure, which opens micro-crack, fractures and expands pores in the formation (Binder et al., 2020). Binder et al. (2020);

Titov et al. (2021) reported strong transmitted PS-waves in their VSP data, which was caused by discrete low-velocity zones of ~ 20 m thickness. These zones, adjacent to major fractures, experienced stronger stiffness reduction than the rest of the SRV. Neither SOV-3 nor SOV-5 data contain strong T_{PS}. Which leads us to a hypothesis that the fluid injections in the stimulation well pressurized natural fractures, which have very weak hydraulic connectivity to the surrounding rocks causing extremely slow pressure relaxation. This will be our interpretation model for the quantitative analysis of the reflected signals.

Furthermore, the pre-stack records of the spectral analysis of the time-lapse events unanimously confirm that they are caused be scattering on fractures. We stack direct P-wave arrivals along lateral segment of the fiber Figure 2.43a, which is also shown in Figure 2.42d. The correlated waveform from SOV-3 contains a clear negative peak offset from the main one by 20 s (Figure 2.43b). The interference causes a clearly-recognizable notch in the spectrum at frequency ~40 Hz (Figure 2.43c), similar to a ghost wave in marine seismic data (Egorov et al., 2017). Most likely, the signal is a surface-related multiple produced by a strong near-surface reflection. Then, we see that the waveforms and amplitude spectra for the differentiated incident wavelet and stacked PS-wave reflection for the same seismic vintage are very similar (Figure 2.43d-e), as is expected for a thin layer reflection (Widess, 1973). The agreement is very good. We confirm again that the impact of the fracture pressurization on the matrix rock is minimal and the reservoir changes are confined to a very small vicinity of the fractures (a few centimeters at most). Otherwise, the propagating wave would experience significant scattering loss and attenuation within the fractured interval. Instead, the wavelet remains almost unchanged within the characterized interval. Finally, the scattered wavelet contains a relatively strong phase at the end of the waveform, which suggests that the observed signals are a result of interference of multiple fractures.

In the next section we will provide a more rigorous validation of these conclusions.

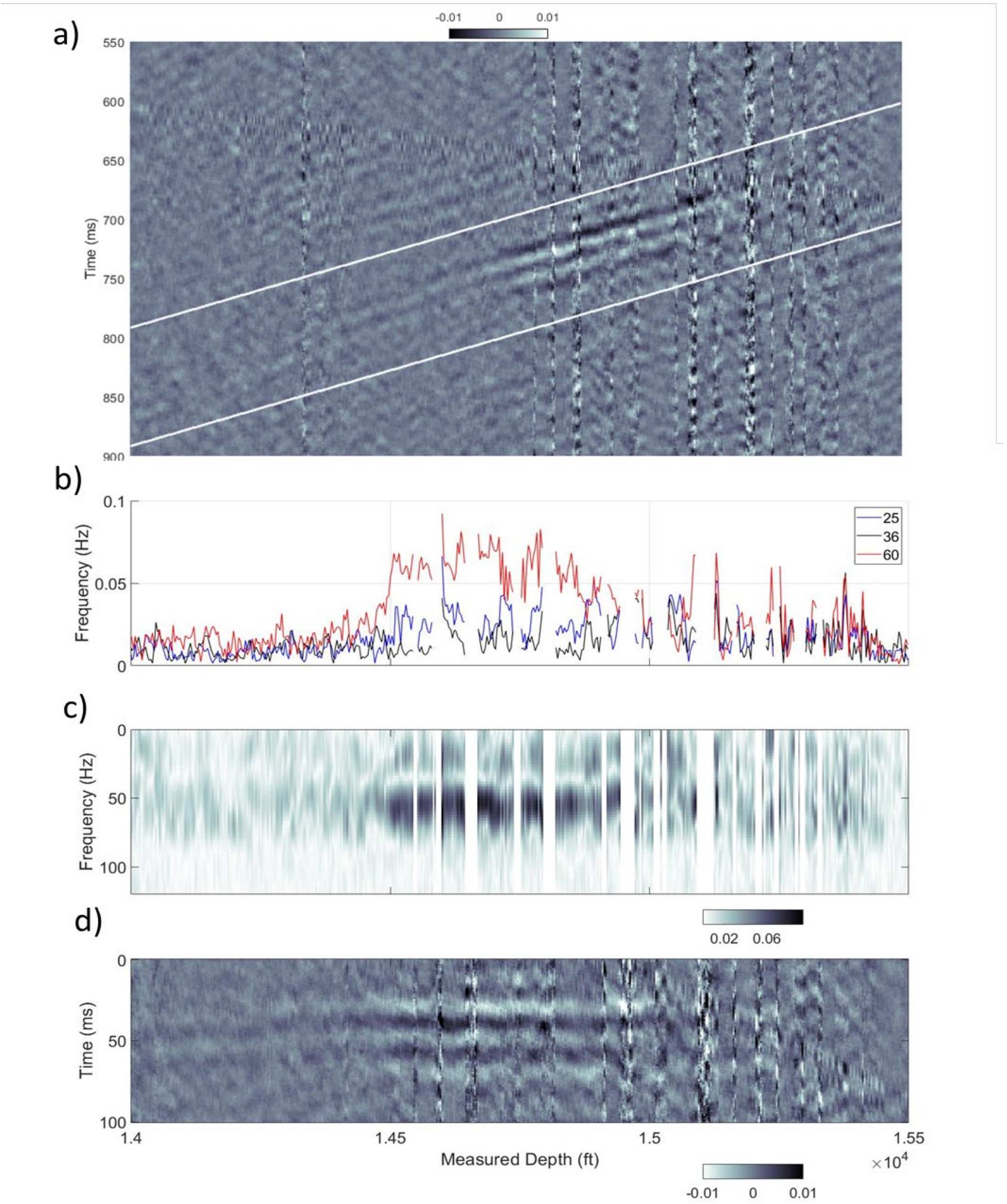

Figure 2.42 Time-lapse seismic response during Stage 7 in 1F, observed on the third day of the reservoir stimulation. The time-lapse seismic response flattened by assuming a P-to-S wave conversion (bottom) consists of three clearly visible negative phases, while the incident signal was nearly zero-phase wavelet. That is almost certainly a result of seismic interference of signals from two stimulated fractures. The distribution of the spectra vs distance to the fractures (middle) corroborate this assumption as we have a notch in the spectra at 40 Hz that corresponds to roughly 20 m spacing between the fractures. The amplitude vs distance curves for different frequencies provide an opportunity to quantify the fractures properties by matching the Born's simulations to the observed values.

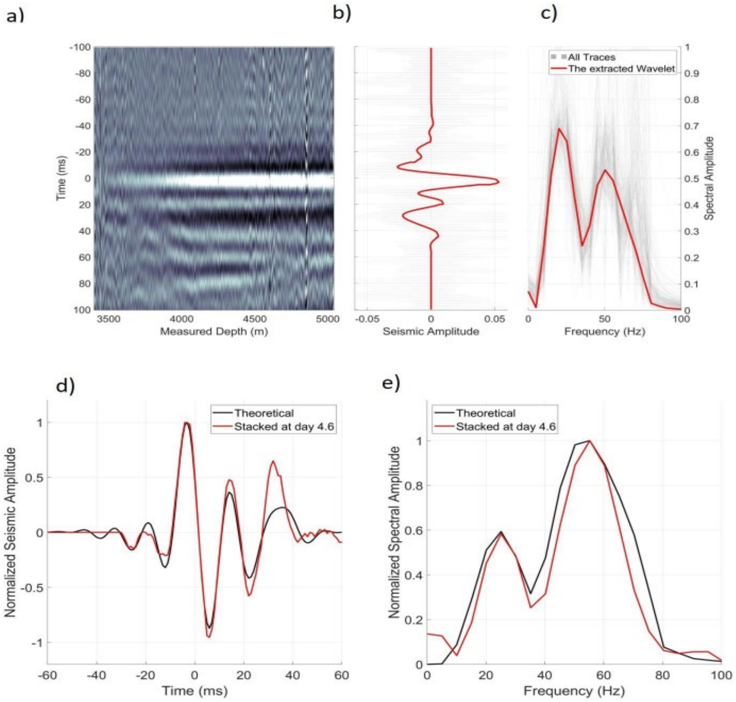

Figure 2.43 Incident and scattered seismic signals. From the monitor seismogram with applied normal move-out (a), we extracted an incident wavelet (b). The wavelet includes a surface-related multiple reflection at around 20 ms, which results in a notch is spectrum at 40 Hz (c). The scattered wavelet is very similar to the derivative of the incident wavelet, called 'theoretical', (d)-(e).

Rock physics modeling of fracture reflectivity

For realistic cases, where fractures have rough contacting surfaces and stimulation fluid contains high concentration of proppant grains, the compliance is hard to estimate without a directly observed seismic response. However, for activated fractures we may anticipate that an extremely large tangential fracture compliance, Z_T, will have a much larger impact on the fracture reflectivity compared with a large but finite Z_N. A fracture filled by ideal fluid with bulk modulus K_{fl} has compliance parameters $Z_N = h/K_{fl}$ and $Z_T = h/\mu_{fl} = \infty$, where μ_{fl} of the fracture fill is 0 for an ideal fluid, and h is fracture thickness that may reach 1 cm. For a more realistic case of granular pack inside the fractures, we use Hertz-Mindlin theory (Mavko et al., 2009). Such a model may capture the case of a proppant slur inside hydraulic fractures or analogously a friable pressurized fault gouge material. Figure 2.44 shows the predicted fracture filling material for varying pressure and porosity of the proppant slurry.

Reflection and transmission of a plane seismic wave at a stack of parallel plane fracture may be computed using matrix propagator method by (Born et al., 1999); Schoenberg and Protazio (2005). Figure 2.45a shows the angle-dependence of R_{PS} and R_{PP} for three types of fracture filling material (see Table 2.3). We see that the reflection gets stronger as the tangential component in the incident wave increases, due to a larger role of Z_T. Our field data corresponds to 60° incidence angle. Among the three modelled scenarios, the field data resembles the case of dense slur: R_{PS} is of the order of ~1%, which significantly exceeds both R_{PP} and T_{PS}. In the long-wavelength limit, the scattering coefficients are linearly proportional to angular frequency ω and tangential fracture compliance $R_{PS}(60^o)$, $R_{PP}(60^o)$, $T_{PS}(60^o) \sim i\omega Z_T$. For realistic subsurface parameters other terms in the power series are negligible. Figure 2.45b shows the frequency-dependence of these parameters for a fracture filled by the dense slur. All three of them change linearly with frequency as expected. This observation has two important implications for the future analysis. First, the fracture (thin layer) acts as a differentiator filter. Second, the scattering strength scales linearly with fracture compliance Z_T. Thus, for activated fractures, we always observe a combined effect of an increased fracture aperture and reduced contact area and/or softer pore filling material.

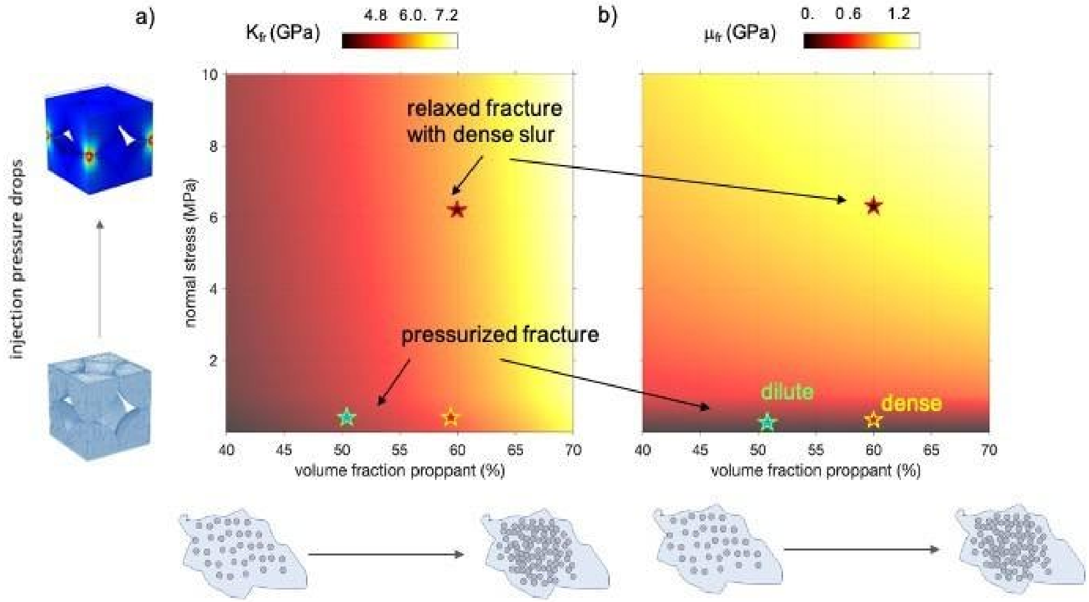

Figure 2.44 Bulk (a) and shear (b) moduli of fracture filling material, computed using parameters from Table 2.3.

Table 2.3 Summary of the seismic properties of the fracture fill and reservoir rocks.

Type	P-wave velocity (m/s)	S-wave velocity (m/s)	density (kg/m3)
brine	1,500	0	1,000
dilute suspension	1,456	75	1,700
dense slurry	1,570	236	1,800
intact reservoir	5,000	3,000	2,600
proppant grain	5,950	4,020	2,650

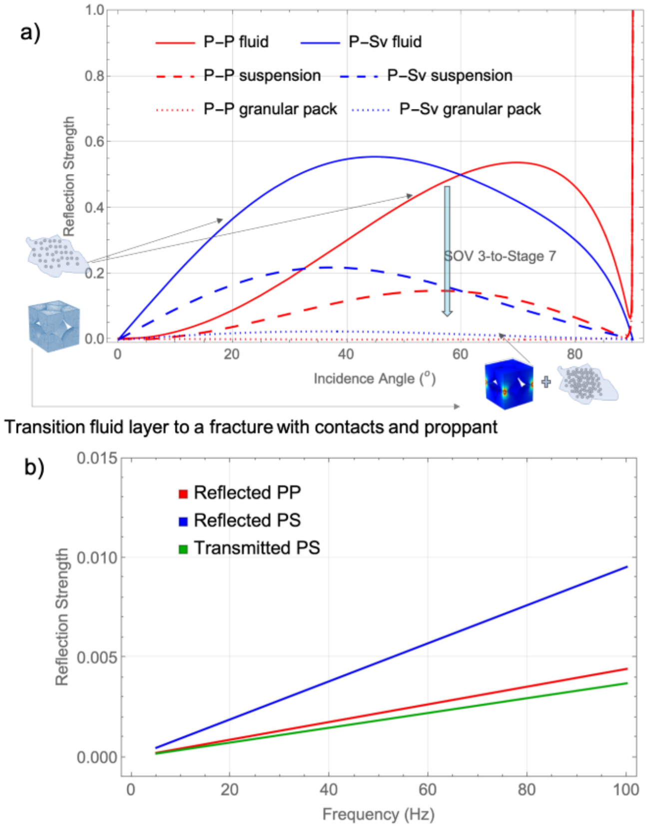

Figure 2.45 Reflection/transmission coefficients for infinite fractures. Type of the fracture fill, from an ideal fluid to a dense proppant slur, have a pronounced effect on the reflection coefficients at 60 Hz for PP- and PS-waves and a 5 mm fracture. For the slur (dashed line in the top plot), reflection and transmission coefficients show linear dependence on the frequency. The parameters of the fracture fill are listed in Table 2.3.

Numerical simulations of the seismic scattering on fracture planes

An infinite 1D reflector that approximated fractures in the previous section is just a first-order approximation of the seismic wave interaction with real natural fractures. When the fracture height is comparable with seismic wavelengths, around 100 m, diffraction effects play a major role (Born et al., 1999). Titov et al. (2021) used the amplitude distribution of transmitted PS-wave versus fiber length to estimate the height of SRV. To evaluate the effect of edges for finite fractures, we need to carry out numerical simulations.

Finite-difference time-domain simulations

Numerical modeling of seismic wave interaction with fractures is known to be a formidable task for grid-based methods. To represent the fracture geometry and heterogeneous high-contrast properties, one would have to refine the grid size and de- crease the time steps to intractable limits even for modern supercomputers. Especially, given that the model boundary effects require special treat- ment that require larger models and increase the computational costs further. As a result, the fractures are often approximated by 2D flat rectangles of exaggerated thickness, ~1 m, compared to realistic thickness ~1 mm (Wu et al., 2005). Such an approximation ignores potentially crucial effects associated with 3D wave propagation and fracture configuration, such as: proximity to lateral edges, irregular top and bottom edges, orientation relative to the fiber-optic cable, variable fracture compliance.

Nonetheless, we implemented a finite-difference time-domain (FDTD) approach to SOV/DAS modeling as a preliminary analysis. We used a seismic simulation software SOFI2D/SOFI3D (Bohlen et al., 2015). We split the simulation task into three steps. First, we simulated a full-scale seismic wave propagation from SOV-3 to the monitoring well in 2D Figure 2.46a to evaluate the configuration of the wavefield at the location of the activated fracture set: distribution of the amplitudes and incident angles. After that, we added a set of five fractures to evaluate the strength of various scattering types Figure 2.46b. These simulations helped identify the same scattering events in the field data.

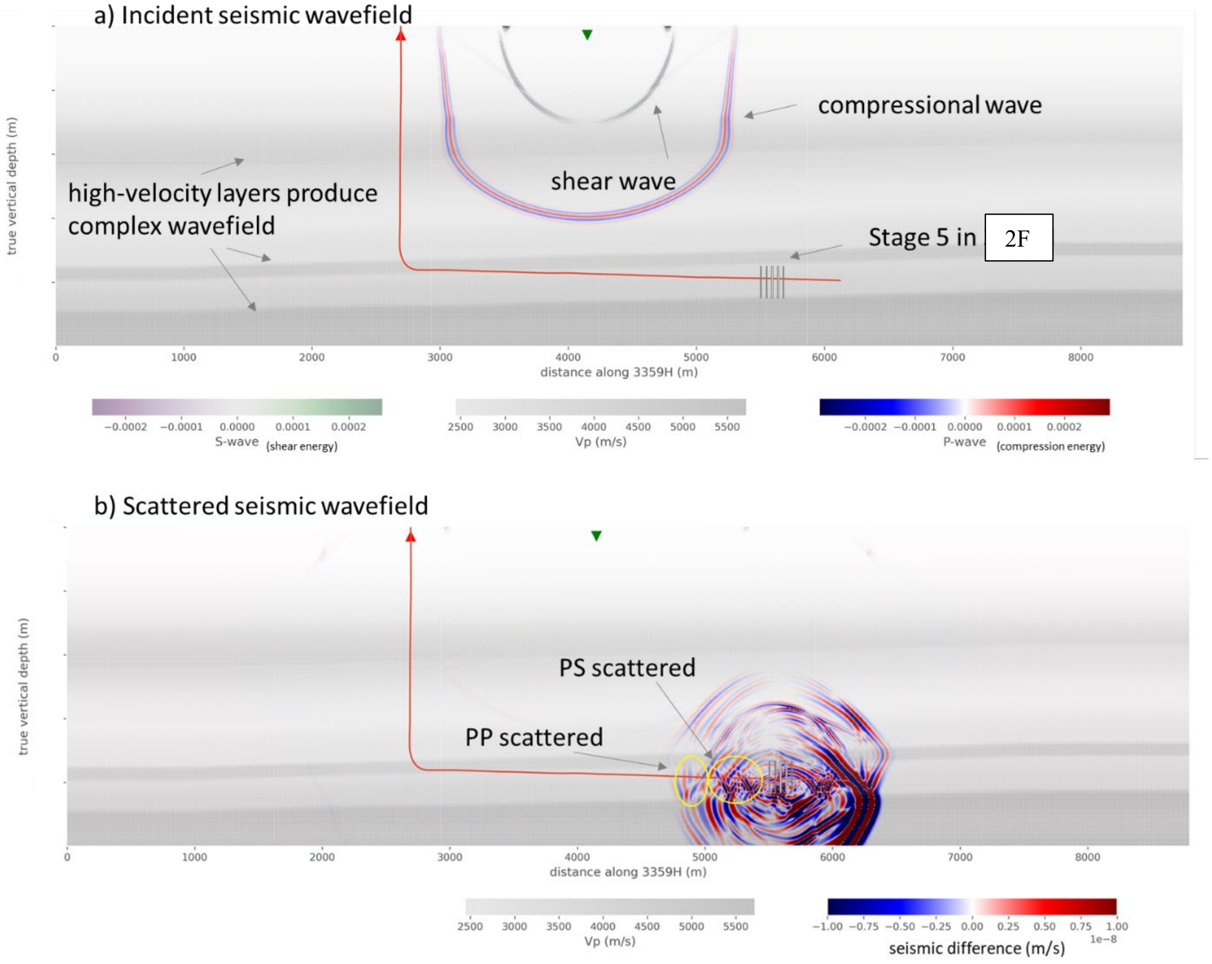
a) Incident seismic wavefield

b) Scattered seismic wavefield

Figure 2.46 Full-elastic 2D simulations of the VSP observations for SOV-3 to Well-3. The source is simulated as vertical force, which likely underestimates the generated shear energy. The incident shear and compressional wavefields (a) have complex shape due to a high-velocity layer at ~ 1 km depth. The incident compressional wave undergoes scattering into P- and S-waves (b), we show a horizontal velocity displacement.

Then, we simulated a plane P-wave interaction with various scenarios of fracture properties and fracture network configuration: half-length, half-height, fracture compliance ZN and ZT. Figure 2.47a shows a snapshot of the wavefield produced by the interaction with the facture of P-wave incident at 60o from below. We see the boundary reflections and also head waves in the boundary layer that is meant to damp these reflections. Figure 48b shows the corresponding seismogram for the described snapshot. We can clearly identify the direct wave and scattered events, although they are contaminated by the boundary reflections. If we subtract the baseline wavefield (without fracture), the majority of the artifacts disappear (Figure 2.48). The main issue with using FDTD data had to do with the high computational cost of each simulation, especially when we would like to consider realistic thin fractures. To reduce the thickness by a factor of 2, we have to increase the computational cost 16 times.

We propose a different simulation approach to alleviate the extreme cost in the next section.

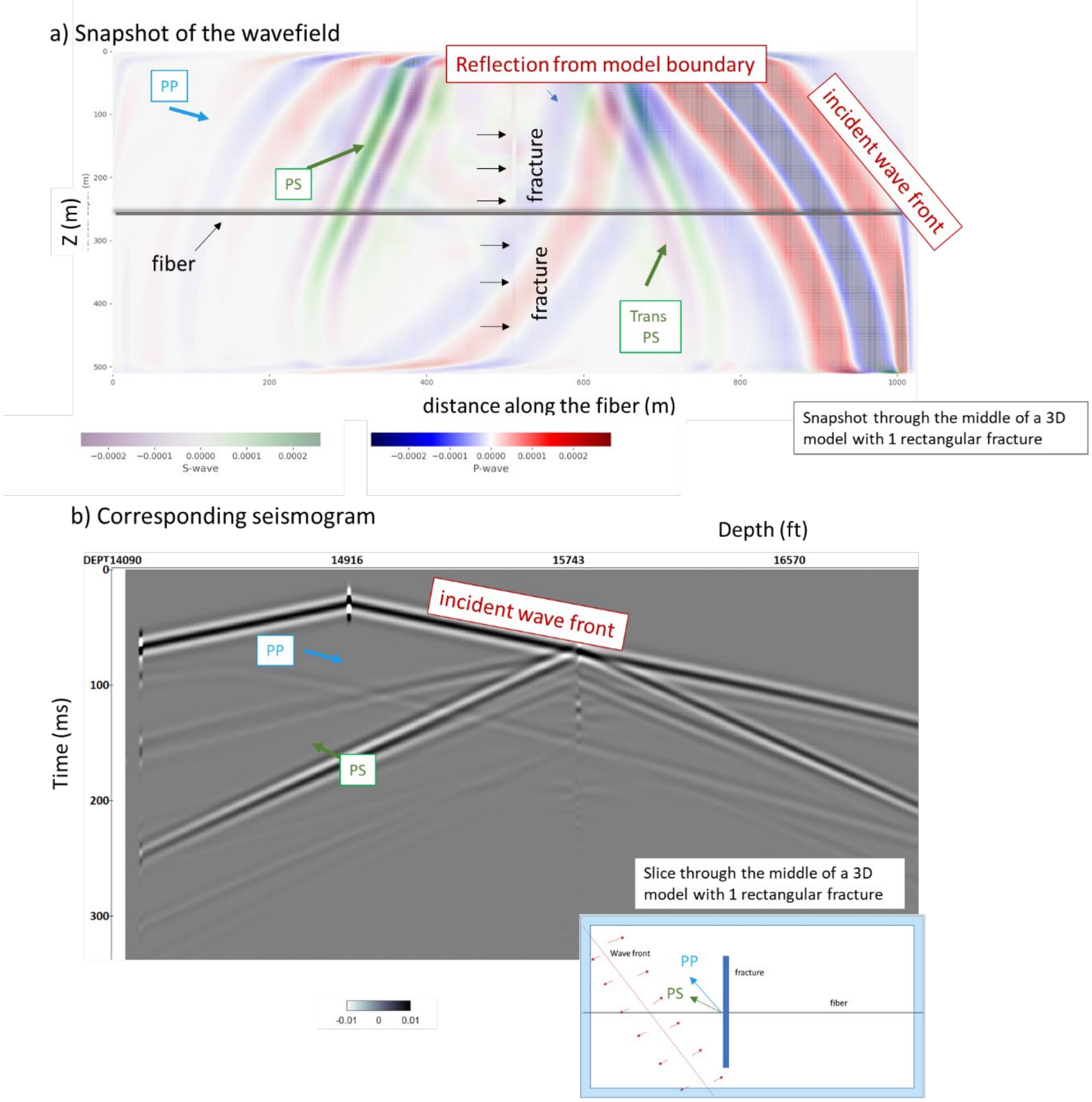

Figure 2.47 Full-elastic 3D simulations of a plane wave incident on a single 200 m high fracture. This geometry corresponds to the fracture scattering shown in Figure 5: VSP observations for SOV-3 to Well-3. The incident P-wave produces transmitted and reflected P-wave and converted transmitted and reflected shear wave (a). Furthermore, we see the effect of boundary conditions: very slow P- and S-waves in the perfectly-matched boundary layer and damped by visible boundary reflections. All of these wave types are clearly seen in the seismogram (b), where boundary reflections give rise to ghost waves mimicking the primary acts of scattering.

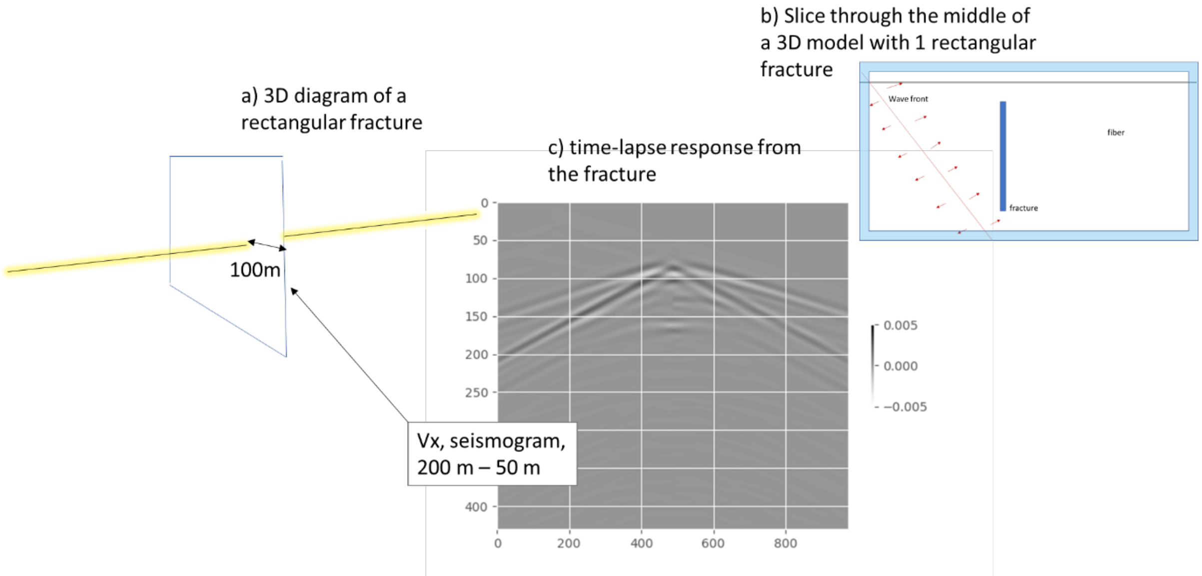

Figure 2.48 Full-elastic 3D simulations of the fracture scattering by a single 200 m high fracture (a) and (b). The time-lapse response is computed as difference between the baseline wavefield (no fracture, just a homogeneous box model) and the monitor vintage with fracture shown in Figure 2.47b.

Simulations using scattering integral

We implement a modeling approach that uses a single-scattering integral, Born approximation (Snieder, 2002). This approximation is often called a small-contrast approximation, which may sound incorrect for fractures. However, the essential requirement relates to the magnitude of phase shift accumulated inside each inhomogeneity compared with the baseline wavefield (Hudson, 1981). For thin low-reflectivity fractures this requirement is fulfilled.

The Born approximation approach considers each element of fractures as a source of scattered wavefield excited by an incident wave that would exist in a baseline medium, the medium without fractures. Thus, we may simply add the contributions of individual elements to estimate the scattering from the entire fracture. Further- more, we may switch on and off different types of scattering, so that we focus on P-to-S conversion and target frequency band by choosing an appropriate source function for the scattering elements.

For an incident plane wave, the scattering strength for each element is directly proportional to contrasts of density and stiffness inside the fracture. Thus, for a set of flat parallel fractures, we need to compute the scattered wavefield only once for an elementary fracture patch. The total wavefield is then a linear combination of such patches with appropriate complex amplitudes: the modulus depends on the contrast between the fracture and background, phase depends on the phase shift of the incident plane wave at the location of the patch.

Figure 2.49a illustrates the application of the Born modeling to scattering of the P-wave with 50 Hz frequency and incident at 60o on a 200 m high fracture, filled with a dense slurry (Table 2.3). The scattering is computed as interference of ten fractures with 20 m height and 400 m width and 2 mm thickness, stacked vertically. Figure 50b shows the strain amplitude distribution along the three vertical locations of the DAS receivers, shown in Figure 2.49a. For the same incident signal and fracture shape, the distance to the top of the fracture changes the observed trends drastically. Note how a bell-shaped curve for the DAS located at the top of the fracture transitions into a 2-peak curve for the DAS at the bottom of the fracture.

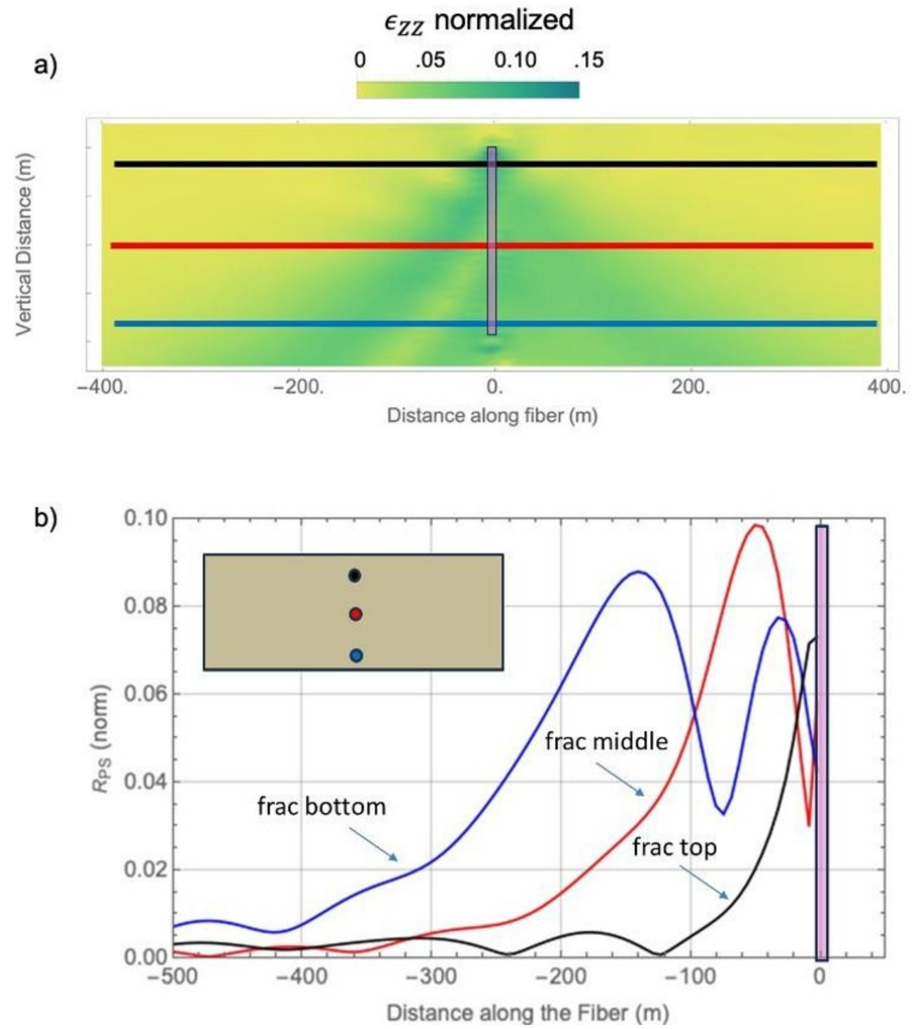

Figure 2.49 PS-wave amplitude for different positions of the monitoring fiber. The fracture dimensions are 200 m× 400 m × 2 cm, P-wave incidence angle is 60o and frequency is 50 Hz, properties of the fracture fill, dense slur, and the intact rock are in Table 1. A 2D distribution of absolute amplitude of axial strain field in the PS-wave (a). For the same fracture and incident signal, the reflected PS-wave amplitude versus distance varies significantly for different fracture heights above the fiber (b).

Estimation of the fracture shape/reflectivity

Now, we can invert the pre-stack seismic data quantitatively based on the Born modeling approach. Ideally, we would iterate through the locations, orientations, and reflection strength of individual fracture patches until we match the scattered wave- forms at different offsets from the fractures. Again, we need to restrict the inversion to a simpler estimation problem. First of all, we sampled the axial strain only along a single borehole. Second, the data is noisy with relatively extensive intervals of signal- to-noise ratio that precludes interpretation. We may only rely on a narrow frequency band around 60 Hz, where the stacked wavelet (Figure 2.43) has the strongest signal levels.

Thus, each monitoring vintage provides one curve of PS-wave amplitude along the fiber to estimate several parameters of multiple fractures. To constrain the search, we make five basic assumptions:

1. the fracture set consists of five fractures;
2. all fractures are rectangular;
3. fracture width is sufficient to neglect the diffraction from the lateral edges (>70 m from fiber);
4. the orientation is orthogonal to the borehole;
5. the fracture compliance is constant within each fracture, but may differ between the fractures.

These assumptions are necessary, if we would like to use the output of 1D de- convolution as an initial model for the search. Essentially, we refine this model and augment it by locations of the top and bottom of each fracture.

Figure 2.50 shows the results for three monitoring vintages. For each of them we performed a grid search over the fracture location along the fiber, vertical distance to the top and bottom, and fracture reflectivity in the range between 58 Hz-65 Hz. Interestingly, the best-fit fracture shapes also predict weak transmitted PS-wave: a puzzling field observation, as we mentioned in the preamble to this section. Figure 2.50d-f shows the predicted and observed amplitude curves for 25 Hz as a qualitative confirmation of the estimated fracture parameters. The noise level is however too high to make any quantitative estimates based on these curves.

The vertical extent changed: initially, the majority of the fractures were located above the monitoring fiber but intersected the borehole later (see diagrams in Figure 2.50d-f). We may not estimate the depth of the fracture bottom below the fiber: recorded PS-wave amplitudes are almost insensitive to the signals produced by the parts of the fracture, located under the fiber.

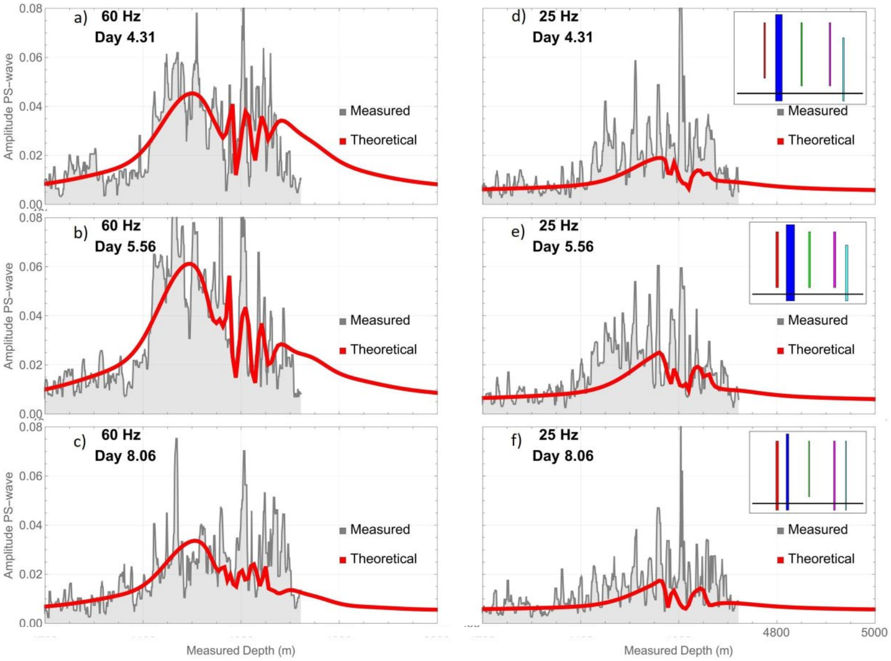

Figure 2.50 Observed (gray) and best-fit (red) amplitude of the scattered PS-wave versus distance for 60 Hz (a)-(c) and 25 Hz (d)-(f). The diagrams in the plots (d)-(f) illustrate the predicted change of the fracture shapes. Fracture aperture is a proxy for fracture reflectivity.

Reconstruction of the fracture activation

We believe that the scattering events for Stage 6-7 were largely caused by activation/relaxation of the same five natural fractures. We think that no new fractures propagated to the monitoring well during the nine days of monitoring, otherwise we would see clear fracture hits and induced seismicity. Instead, these natural fractures produced scattering events prior to the stimulation of the corresponding stages in the stimulation well, then the fractures got activated and remained visible five days after these stages. The changes of reflectivity were caused by their opening/closure and some moderate growth. Below we analyze some peculiar features in the evolution of the fracture reflectivity.

Strain anomalies first extended to the interval of interest on day 3.5 and 3.9. The anomalies do not appear as fracture hits. Nevertheless, the fracture reflectivity abruptly changed the decreasing trend (Figure 2.51). Most likely, the natural fracture set became hydraulically connected to a new cluster of hydraulic fractures created by fluid injection for Stage 5. Once the new fractures close at the end of injection, the natural fractures take a long time to release pressure. That is why the reflectivity trends are so smooth.

Then, Stages 6 and 7 injected much more fluid under higher overpressure, which boosted the reflectivity increase. At the same time, we detected a few events north-east of Well-3 where we expect to have fracture #2, which became the brightest fracture in the set at this point. Also, Stage 7 produced high overpressure at the depth 1970 m, far exceeding the fracture pressure. We believe that fracture #2 was strongly activated and grew laterally. However, we did not detect any fracture hits in the target interval, which suggests that the vertical extent did not change. Qualitatively, this conclusion agrees with the fact that the pressure gauge at 2010 m remained at ambient conditions. Also, no microseismic events were detected close to the stimulation well.

During the long wait period between Stage 7 and Stage 8, all of the fractures reached their maximum activation state and started closing down. Then, Stage 9 led to an extremely extensive strain anomaly, 1000 m, which had several fracture hits. Our Born-based interpretation suggests that fracture #1 intersected the monitoring fiber. This reflectivity of this fracture also changed the trend and stayed relatively high for the next three days. The next fluid injection, Stage 9, produced a strong strain anomaly, which included two interpreted fracture hits in the target interval. The Born modeling indicates that fracture #4 intersects the borehole and its reflectivity trend changes at the same time. In agreement with the seismic interpretation, the deeper pressure gauge, located at up to 40 m below the monitoring fiber, recorded noticeable overpressure.

We do not have reliable estimates of the extent of the natural fractures, except for the microseismic catalog. Events can be triggered outside of the activated fractures as well as some parts of the faults and fractures may slip aseismically (Eaton, 2018). But for our project, the vertical extent of microseismic clouds ∼100 m matches the results of the analysis of seismic scattering events. Also, orientation agrees with the borehole image logs (Figure 46) as well as the microseismic imaging by Ma et al. (2024).

Overall, our study clearly showed the value that continuous seismic monitoring using DAS may bring to the stimulation of unconventional reservoirs. The dimensions of the fracture set, height and spacing, were right at the edge of seismic resolution. Estimate fracture reflectivity, ∼ 1%, is below the noise level. However, the high repeatability and high frequency of the seismic snapshots along with a meticulous analysis of the seismic scattered amplitudes enabled a high-precision tracking of the fracture reactivation. Without it, a petroleum engineering team would be unable to decipher the atypical strain anomalies that extended far beyond the stimulated intervals as well as the patchy distribution of induced seismicity.

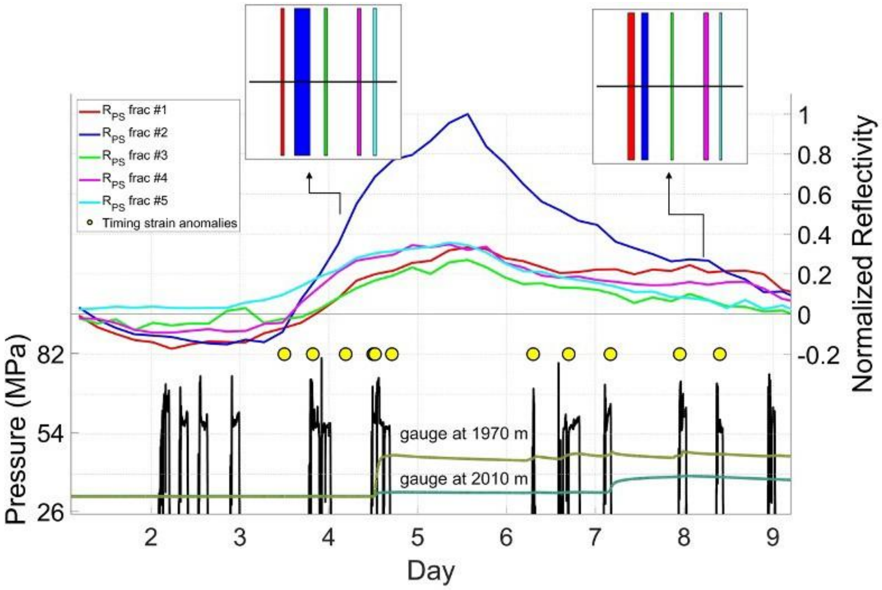

Figure 2.51 Estimated evolution of the fracture reflectivity similar to the three stages shown in Figure 9. The characterized fracture set consists of five fractures. The reflectivity in the first vintage is subtracted from the subsequent values, thus the curves start at (0,0). The bottom plot shows the bottom hole pressure (black) formation pressure gauge at depth 20-40 m shallower the fluid injections (green) and 20-40 m deeper (turquoise). The small inset diagrams depict the relative fracture locations along, the thickness of each rectangle corresponds to the strength of PS-reflection.

2.5.2 Low-frequency DAS

LF-DAS refers to the lower frequency range, typically below 0.5 Hz, of DAS data. LF-DAS data exhibits sensitivity to strain disturbances caused by mechanical and thermal factors, including events such as: hydraulic fracture approaching and intercepting the fiber, and in-well injection. It has found applications in many reservoirs for measuring dynamic strain, to monitor offset well fracturing (Jin and Roy, 2017), and to characterize near-wellbore fractures using in-well Rayleigh frequency shift based DSS (DSS-RFS) (Jin et al., 2021; Leggett et al., 2023). Cross-well LF-DAS signals contain information about connectivity between wells (Ning and Jin, 2023), fracture aperture can also be estimated using LF-DAS (Liu et al., 2020). In contrast to LF-DAS, which provides a dynamic measurement of strain, Brillouin-based DSS (Distributed Sensing Systems) offer absolute strain measurements. Previous studies have demonstrated the usefulness of LF-DAS and DSS modeling in interpreting the propagation of hydraulic fractures and their interaction with natural fractures (George et al., 2022; Gurjao et al., 2021).

In this section, our interest lies in comparing DAS and DSS in field settings, specifically examining their spatial resolution, timing of signals related to cross-well hydraulic fractures, as well as their amplitude and span. In this study, our initial focus is on analyzing frac-hits within the LF-DAS data obtained during hydraulic fracturing. Then we compared the integrated LF-DAS strain with the static strain measured by DSS at the locations where frac-hits occurred. Our findings demonstrate that during one fracturing stage, both integrated LF-DAS and DSS measurements exhibit similar levels of extension strain, during the opening and closing of fractures.

Data Description

DFOS data were recorded using a behind-casing multi-fiber bundle in Well 1F and Well 2F during hydraulic fracturing of the adjacent Wells. We used the Silixa Constellation fiber. DAS, DTS and DSS were recorded simultaneously using Silixa Carina IU, XT-DTS and a dynamic Brillouin optical time domain reflectometry (BOTDR)-based system (Luo et al., 2019).

DAS has a gauge length of 10 meters, < 1 με sensitivity and 1 kHz sampling rate. Brillouin-based DSS was conducted on a separate fiber installed in the same monitor wells. This method uses Brillouin backscattering to measure the static strain values along the fiber, with a strain magnitude resolution of 10-20 με (micro-strain) and temporal sampling every 20 minutes. DSS reading takes a much longer time compared with DAS, mainly due to computation needed to determine the Brillouin scattering frequency shift, since Brillouin scattering is 30 dB lower in power than Rayleigh scattering. We use a modified version of the BOTDR system described in Luo et al. (2019), which incorporates a short-time Fourier transform instead of frequency scanning. This modification enhances the measurement speed. The DSS measured strain is then temperature compensated using collocated DTS data (Saw et al., 2023), this DTS/DSS product is abbreviated as DSTS. The DTS has a resolution about 0.05 to 0.1 ◦C (2-4 με). The DSTS system also has a higher spatial resolution (2 m gauge length) than the DAS measurement. Table 2.5 summaries the data information.

Table 2.5 Comparison: LF-DAS has greater sensitivity and higher S/N; DSS provides a consistent view of absolute strain.

	LF-DAS	**DSTS**
Methodology	Rayleigh scattering	Brillouin optical time domain reflectometry (BOTDR)-based
Measurement	Strain rate	Strain
Gauge length	10 m	2 m
Strain Resolution	< 1 με	DSS: 10-20 με; DTS: 0.1 ◦C (2-4 με)
Sampling interval	1 s (low-pass filter at 0.5 Hz)	20 minutes
Applications	Seismic activity monitoring	Building/structure monitoring

LF-DAS data processing

LF-DAS is the lower frequency content (< 0.5 Hz) of DAS data. At 1 kHz sampling rate, one day of operation will acquire around 1 TB of DAS data for one well (5000 channels). The first step of extracting LF-DAS data is to apply a low-pass filter to DAS data patches. Then down-sample to 1 Hz and merge patches together. Figure 2.52 shows the workflow.

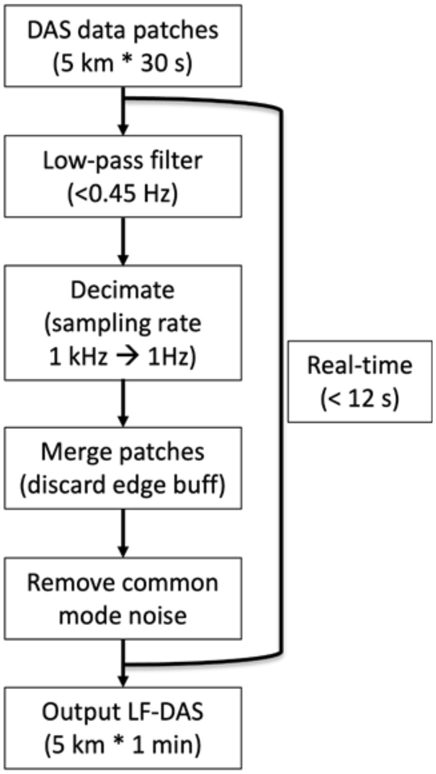

Figure 2.52 LF-DAS processing workflow.

To compare DSTS and DAS values, the DAS data (iDAS value) was converted to (nm/(m∗second)) by factoring out the gauge length and sampling rate. We also remove the mean value of channel 4000-4100 from the entire dataset at each timestamp, which will remove common mode noise. Without removing these background changes, strain calculated from LF-DAS is not comparable with DSTS in amplitude. Salt-and-pepper noise peaks are also reduced by removing spurious outliers. Finally, strain rate was integrated through time to calculate the cumulative aperture changes.

Table 2.6 illustrates the comparison of strain value from different methods.

Table 2.6 LF-DAS and DSTS (Saw, J. et al., 2023) processing workflow for strain value comparison

LF-DAS	DSTS
Linear conversion to nm/(m∗second) , strain rate	Select baseline Brillouin peak frequency shift before hydraulic fracturing
Subtract mean value of selected 100 channels at each timestamp (remove common mode noise)	Convert Brillouin frequency shift to strain
Remove noise spikes based on prominence	Convert DTS temperature to strain
Integrate over time for cumulative strain	Align Brillouin-based DSS and DTS, remove thermal-equivalent strain
Integrate over measured depth for aperture	

LF-DAS Frac-hit Picking

LF-DAS measures the strain changes (strain rate) along the fiber using Rayleigh scattering; hydraulic fracture propagation can be observed in LF-DAS in the vicinity of the fiber. Example of LF-DAS data is shown in Figure 54 top panel. Fractures reaching the fiber well are called "frac-hits" (Jin and Roy, 2017), they can be observed during stage 3, 4 and 5 in Figure 2.53. At the fracture location, we see extensional strain (in red), and stress shadows on the sides of the fracture are in blue color, which are the areas compressed by hydraulic fracture growth.

We also observed natural fracture interactions towards the heel area during several stages (Stage 4, 5 and 7), captured on LF-DAS. They are extensional strain signals propagating beyond the fracturing depth, usually accompanied with microseismic activities. For example in Figure 2.53, after the injection stopped, the extensional strain of Stage 4 kept propagating to Stage 5 measured depth.

Figure 2.53 also shows the DSTS in the bottom panel, DSTS data has a temporal resolution of 20 minutes, it is linearly interpolated to 0.5 Hz for visualization and comparison with LF-DAS. The star annotations are frac-hit locations picked in LF-DAS. We observed most extensional strain resulted from hydraulic fracturing both in cumulative LF-DAS and DSTS, and the locations correspond to each other.

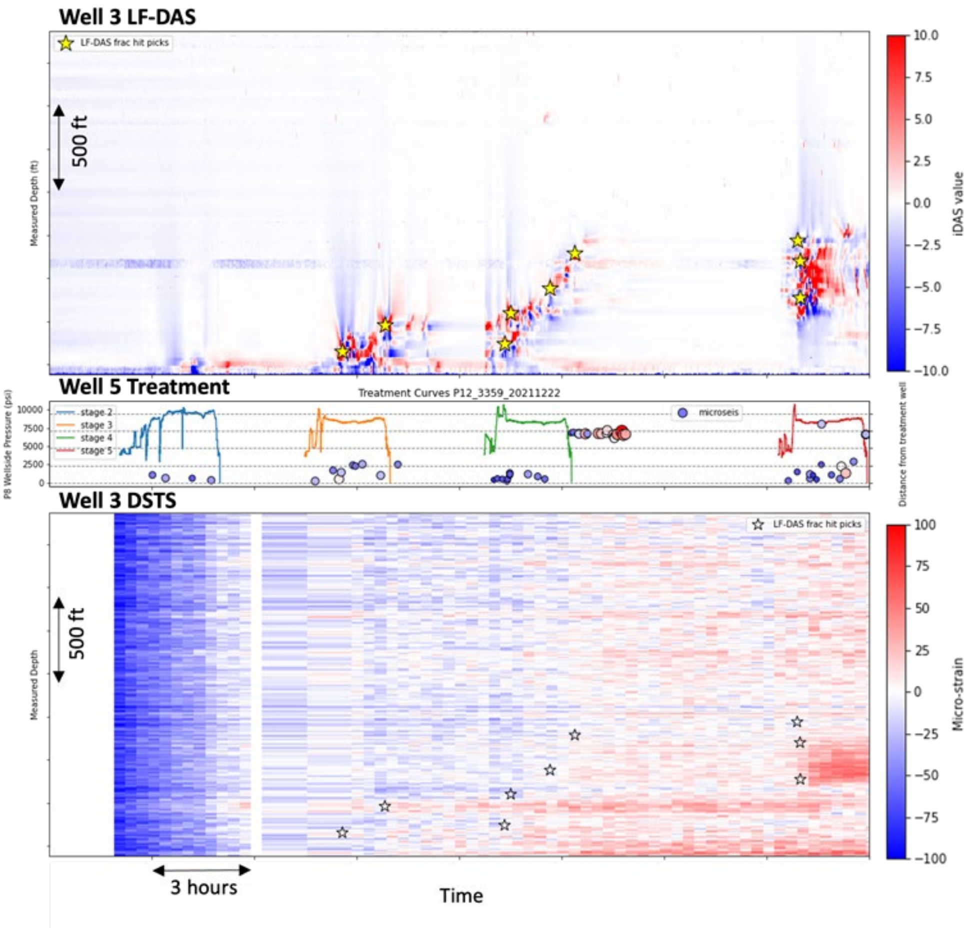

Figure 2.53 LF-DAS frac-hits can be observed during stage 3, 4 and 5, curves in the middle panel are Well 2F wellside pressure curves for each stage. The picked franc-hit locations are annotated with stars. LF-DAS frac-hit locations are also marked on DSTS data, temporal resolution of DSTS is coarser than LF-DAS, but we see extensional strain from stage 5 clearly. Well 3 is 1F, Well 5 is 2F.

Fracture Geometry Analysis

The locations of observed frac-hits and corresponding injection stages can indicate fracture length and azimuth, shown in Figure 2.54. Most of the hydraulic fracture reached the monitor well 1F, and are near perpendicular to the horizontal wells (Figure 2.55). Fractures propagating towards the heel direction and reactivation of previous stages are common, shown in Figure 2.55. After stage 12 of Well 2F, the first stage of zipper fracturing from Well 1F started, which caused more in-well noise for well 1F monitoring and less fracture hit identification.

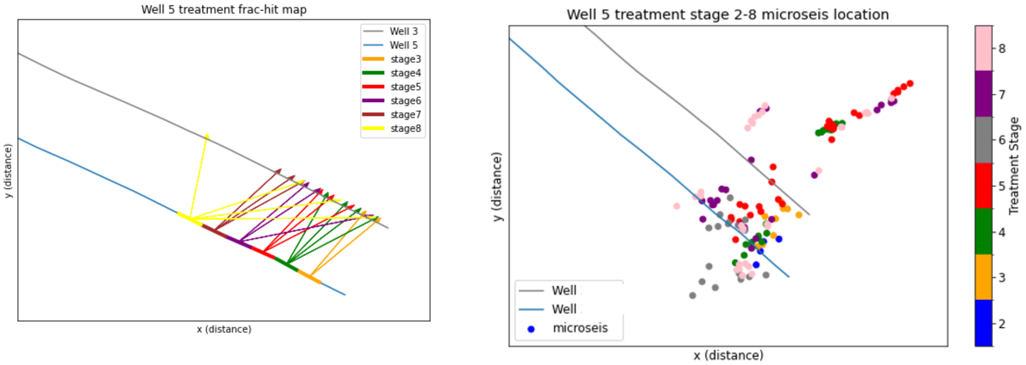

Figure 2.54 Left: Frac-hits picked from LFDAS, between Well 2F (treatment well) and Well 1F (fiber well), stage 3-8. Right: Microseismic locations of stage 2-8 from surface nodes catalog. In stage 8, a large area along the fiber well was reactivated. The microseismic locations of stage 8 also indicate re-activation. Well 3 is 1F, Well 5 is 2F.

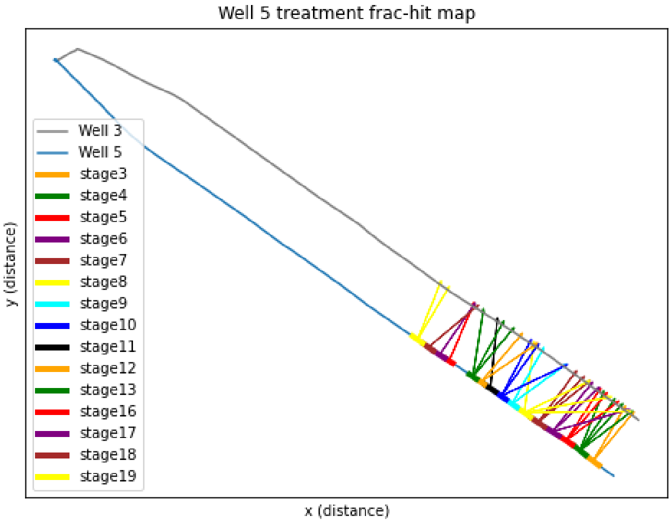

Figure 2.55 All frac-hits picked from LFDAS, between Well 2F (treatment well) and Well 1F (fiber well). Some of the treatment stages were not picked due to high noise level caused by in well treatments during zipper fracturing. Well 3 is 1F, Well 5 is 2F.

DAS vs DSTS

Following the LF-DAS data processing workflow, LF-DAS strain rate was integrated through time to calculate the cumulative aperture changes, resulting in cumulative LF-DAS in strain. DSTS is also in strain units, measuring from a baseline time before any operations in the wells. The measured depth along fiber of LF-DAS and DSTS is also matched by identifying the begin and end of the well, then interpolating evenly in between.

Figure 2.56 shows the cumulative LF-DAS plot compared with DSTS, DSTS data is linearly interpolated to 0.5 Hz when plotting, for comparison with LF-DAS. The star annotations are frac-hit locations picked in LF-DAS (Figure 54). The blue trace-like anomaly at stage 5 measured depth is probably a coupling difference at one section of the fiber, after closer observation from raw DAS data.

We observed most extensional strain resulted from hydraulic fracturing both in cumulative LF-DAS and DSTS, and the locations correspond to each other. Although DSTS has a smaller gauge length, LF-DAS was able to pick up narrower features, such as the activation signals at stage 4. This could be due to the smaller amplitude of this type of phenomenon below DSTS sensitivity.

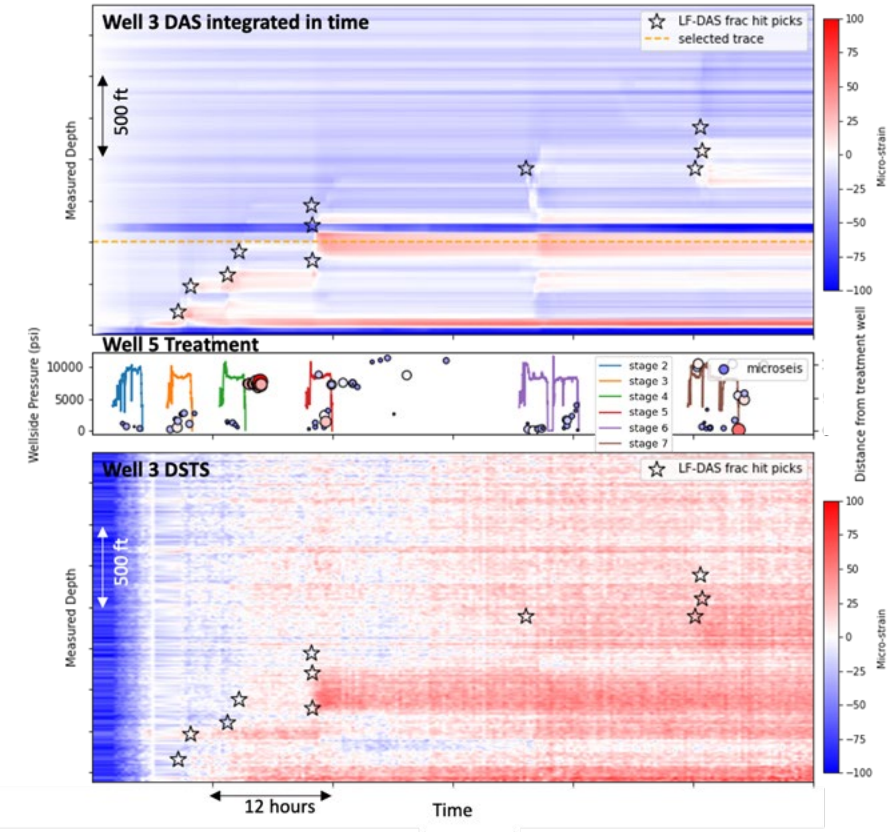

Figure 2.56 (a) Monitor well LF-DAS integrated in time, value is converted from iDAS to micro-strain. The star annotations were picked in LF-DAS. (b) Injection well treatment curve from stage 2 to 7, (c) Monitor well DSTS in micro-strain, stars marked frac-hit locations from LF-DAS. Well 3 is 1F, Well 5 is 2F.

Figure 2.57 is a zoomed-in view of the LF-DAS/DSTS comparison, note that the activation type of signals at 00:00 in LF-DAS were not visible in DSTS (marked with arrows). Timing of LF-DAS is also sharper than DSTS, since the temporal resolution is much higher.

The overall background strain changes are different in LF-DAS and DSTS, although DSTS is compensated using DTS to measure absolute strain, there could be some background strain changes unrelated to the fracturing. DSTS exhibits a slightly lower level of extensional strain than LF-DAS at fracturing locations. However, the extensional strain does not drop as much as LF-

DAS after the injection, which can be observed in Figure 8 and Figure 9 stage 4, 5 and 6. Therefore, the overall level of cumulative extensional strain is similar. DSTS is also insensitive to stress shadow, while LF-DAS calculated strain shows compression near an opening fracture in Figure 2.57 stage 4.

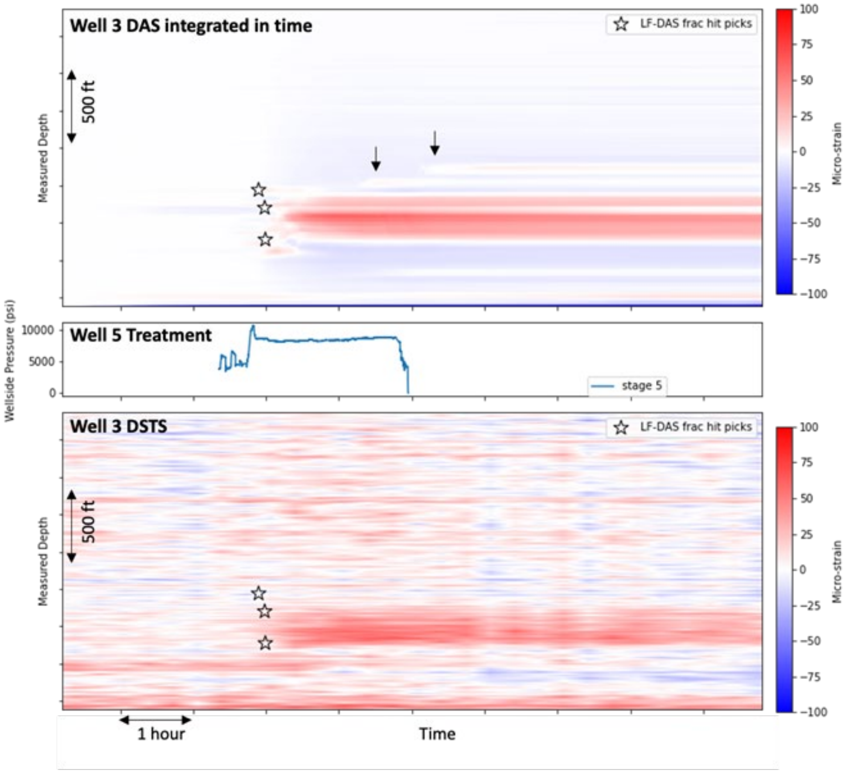

Figure 2.57 (a) Monitor well LF-DAS integrated in time, stage 5. Observed natural fracture interactions are annotated with an arrow. (b) Injection well treatment curve for stage 5, (c) Monitor well DSTS in micro-strain, stars marked frac-hit locations from LF-DAS. Well 3 is 1F, Well 5 is 2F.

Note that we compare and calibrate the LF-DAS strain rate values and the DSS strain values from a cross-well fracture monitoring perspective. The example showed a similar level of aperture changes in integrated LF-DAS and DSS after one stage of hydraulic fracturing; while the LF-DAS measurement showed greater sensitivity and higher S/N, the DSS measurement provided a consistent view of absolute strain. Because of the cross-well perspective, we're observing the fracturing some distance away from the treatment well; individual fracture hits can be differentiated in the LF-DAS, but much more challenging in DSS. Therefore, we decide to study the deformation caused by one stage of treatment as a whole, instead of individual fractures.

Fracture Aperture Estimation from DAS

We picked one location bracketing a stimulation stage to compare the strain amplitude from DAS and DSTS measurements. The average traces of the 10 nearby channels (10 m) of DAS and 30 nearby channels of DSTS are calculated and shown in Figure 2.58 and 60 bottom panel.

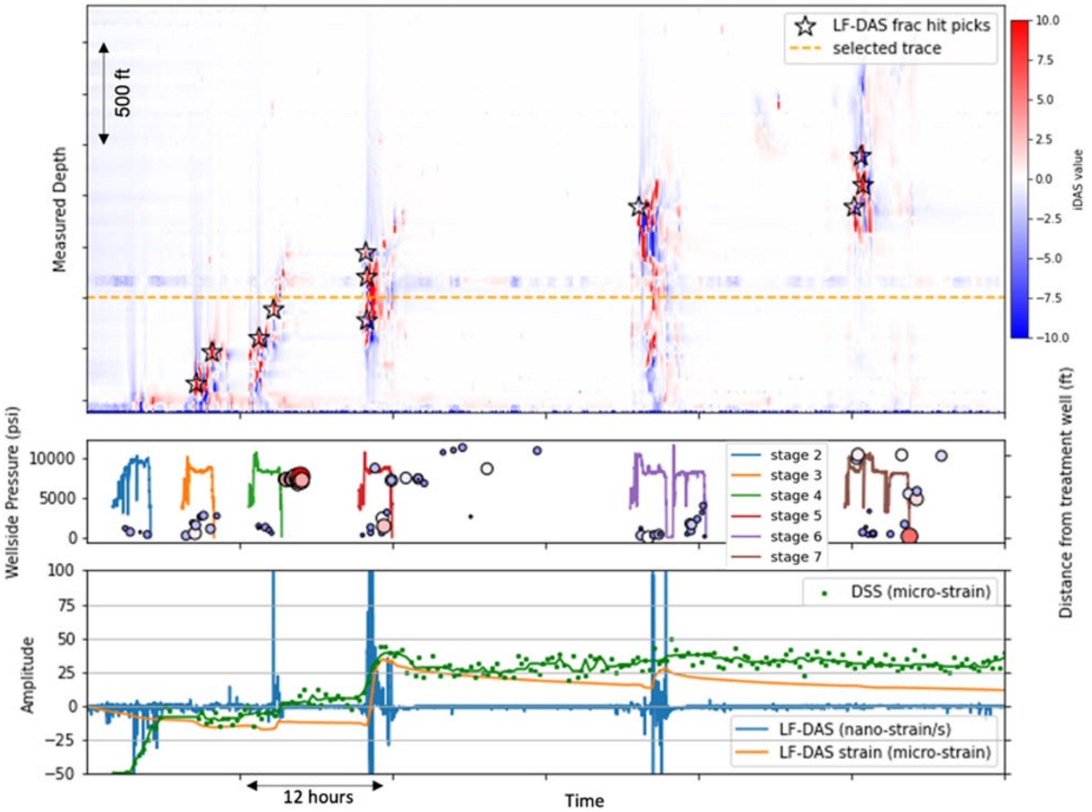

Figure 2.58 Monitor Well 1FLF-DAS data during Well 2F injection stage 2-7, shows frac hits corresponding to cross-well injection activities. The middle panel shows injection well treatment curves from stage 2-7 and microseismic catalog. The bottom panel shows LF-DAS, integrated LF-DAS strain compared with DSTS.

Across the selected measurement zone, both DSTS and LF-DAS show a cumulative aperture change around 25 με, before and after the stage 5 injection, 10 με before and after the stage 7 injection. In Figure 2.59 and 2.60, LF-DAS data is plotted in blue in nano-strain/s, and integrated LF-DAS shown in orange is in micro-strain.

From the integrated LF-DAS strain, we observed the area being compressed and recovered during previous stages' injection. We then see the expected positive cumulative strain (expansion) when stage 5 and 7 treatment occurred. When the injection stopped, the integrated LF-DAS strain value decreased, but did not recover, indicating that part of the fracture aperture remained open, or propped. This aperture is estimated to be 25 με over a 78-meter domain around the selected location (orange dash line in Figure 2.59), equivalent to a cumulative aperture of around 1957 micron. Temperature-compensated DSTS is plotted in green; limited by its 10-20 με resolution, the DSTS value oscillates.

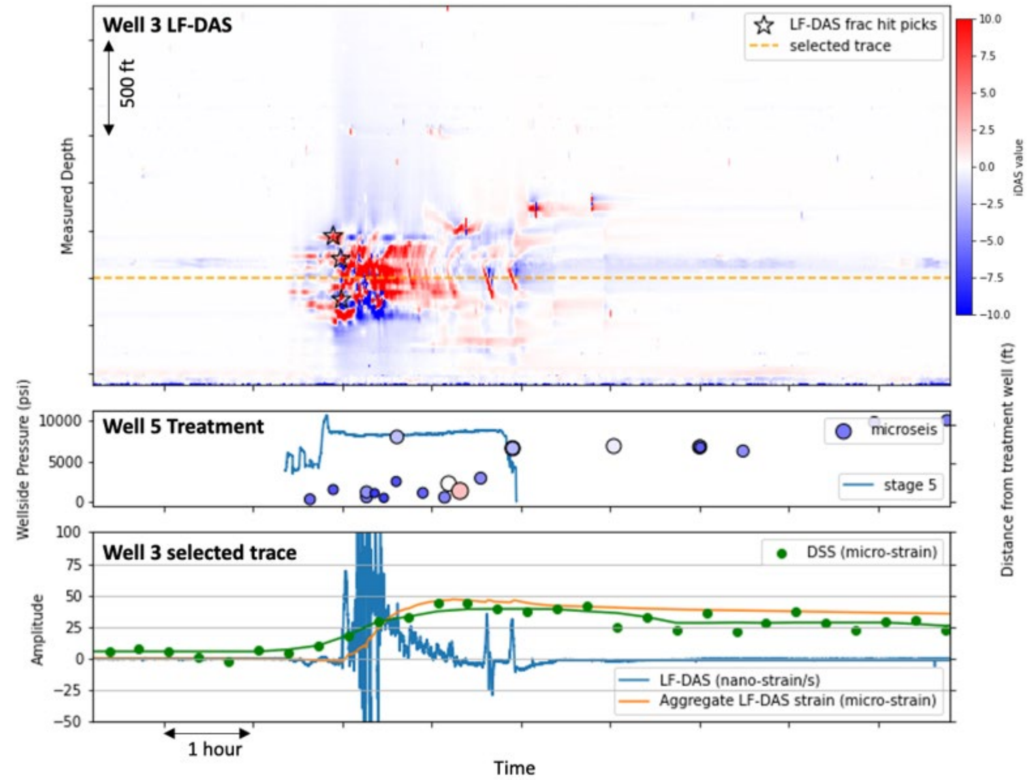

Figure 2.59 Monitor Well 1F LF-DAS data during Well 2F injection stage 5, shows frac-hits corresponding to cross-well injection activities. The middle panel shows injection well treatment curves from stage 5 and microseismic catalog. The bottom panel shows LF-DAS, integrated LF-DAS strain compared with DSTS (Well 1F is 3; Well 2F is 5).

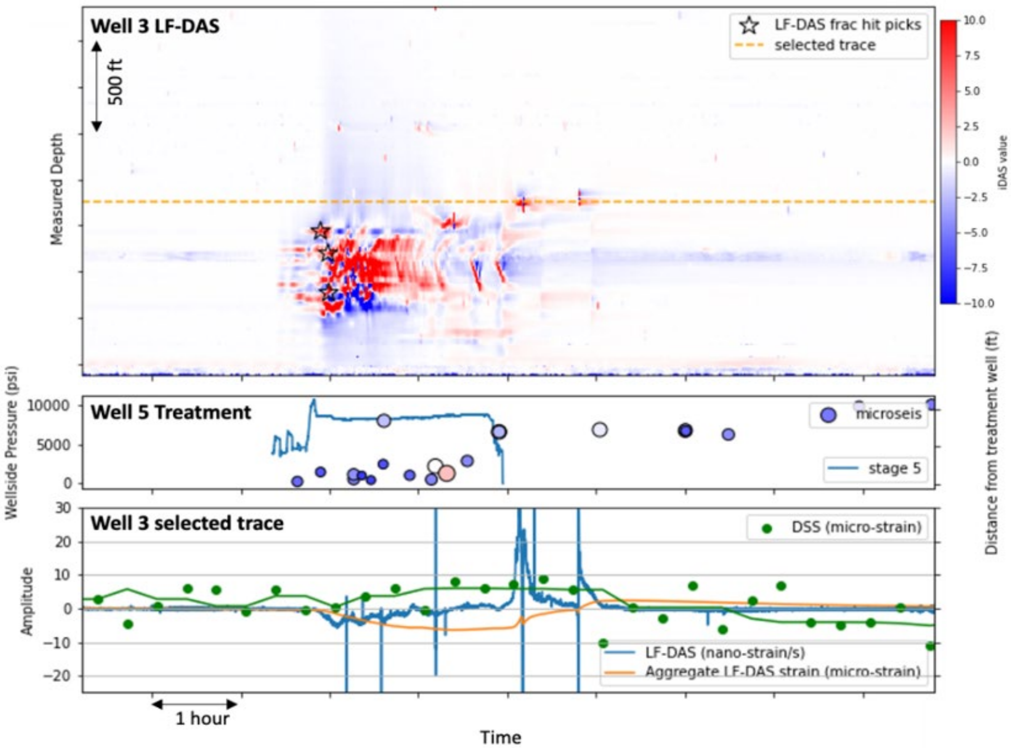

Figure 2.60 Monitor Well 1F LF-DAS data during Well 2F injection stage 5, with the bottom panel showing one selected trace of LF-DAS, integrated LF-DAS strain compared with DSTS. The trace location shows the stress shadow and frac-hit-like event propagating heel-ward, visible in LF-DAS and not DSTS. Well 3 is 1F, Well 5 is 2F.

Away from the primary frac-hit zone, we plot the LF-DAS data and integrated LF-DAS of the selected orange trace in Figure 2.61. The trace location passes the stress shadow of the primary frac-hit zone and another frac-hit like event. The stress shadow showed up as compression ~5 με in integrated LF-DAS, not shown in DSTS. The frac-hit-like event exhibits extension on LF-DAS around 7 με, while DSTS is insensitive to it. However, over 3.5 hours after the extension event, the strain value decreases to the background level. It seems the deformation recovered after the frac-hit like event, unlike the primary frac-hit, it did not cause enduring extension.

A similar width of extension strain and an amplitude of 10 με increase before and after stage 7 was observed. The aperture for stage 7 is estimated to be 10 με over a 86-meter domain around the selected location (orange dash line in Figure), equivalent to a cumulative aperture of around 1180 micron.

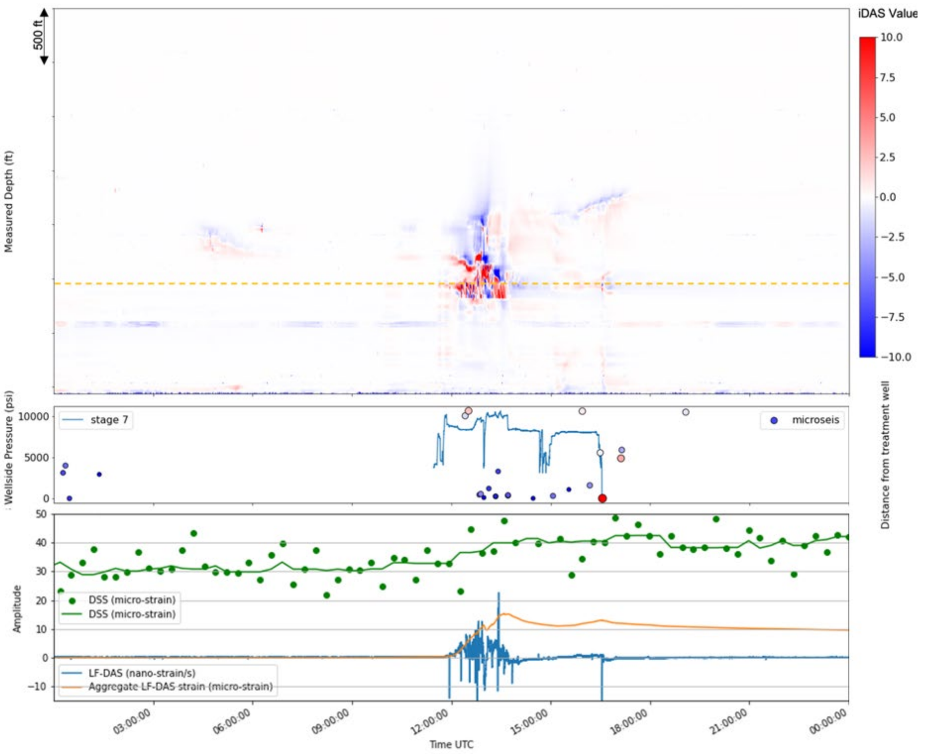

Figure 2.61 Monitor Well 1F LF-DAS data during Well 2F injection stage 7, shows frac hits corresponding to cross-well injection activities. The middle panel shows injection well treatment curves from stage 7 and microseismic catalog. The bottom panel shows LF-DAS, integrated LF-DAS strain compared with DSTS.

2.5.3 Microseismic detection with DAS

We first attempt to calibrate the velocity model using arrival times from some large well recorded microseismic events, while simultaneously relocating them. The initial model is the TTI anisotropic model established by MSI Inc. using the 3D interval velocity model from SM energy as Vp along the axis of symmetry, which is almost vertical and the P-wave anisotropy parameter $\varepsilon \sim 0.13$ (Helbig and Thomsen, 2005). We picked P-wave and S-wave arrival times on 8 well recorded events on the horizontal sections of the DAS arrays. We assume a homogenous model to calculate travel times to the horizontal sections of the wells as the wells follow the dip of the layering and the travel time curves appear to be simple. We perform a grid search for uniform Vp and uniform Vp/Vs ratio that provide the best fits to the observed arrival times, while simultaneously relocating the events. The best-fitting Vp and Vp/Vs ratio are 4.76 km/s and 1.81, respectively. We obtain a low value of misfit ~1.2 ms. For the example event shown in Figure 63, the original velocity model and the location fit the arrival times substantially worse at residual ~8 ms. The earlier than observed arrival times at greater distances indicate that the original MSI velocity model is too fast at greater depths (>2.1 km). We infer the actual velocities near the horizontal sections of the wells to be slightly greater (~2.5%) than the values in the original model (Figure 2.62).

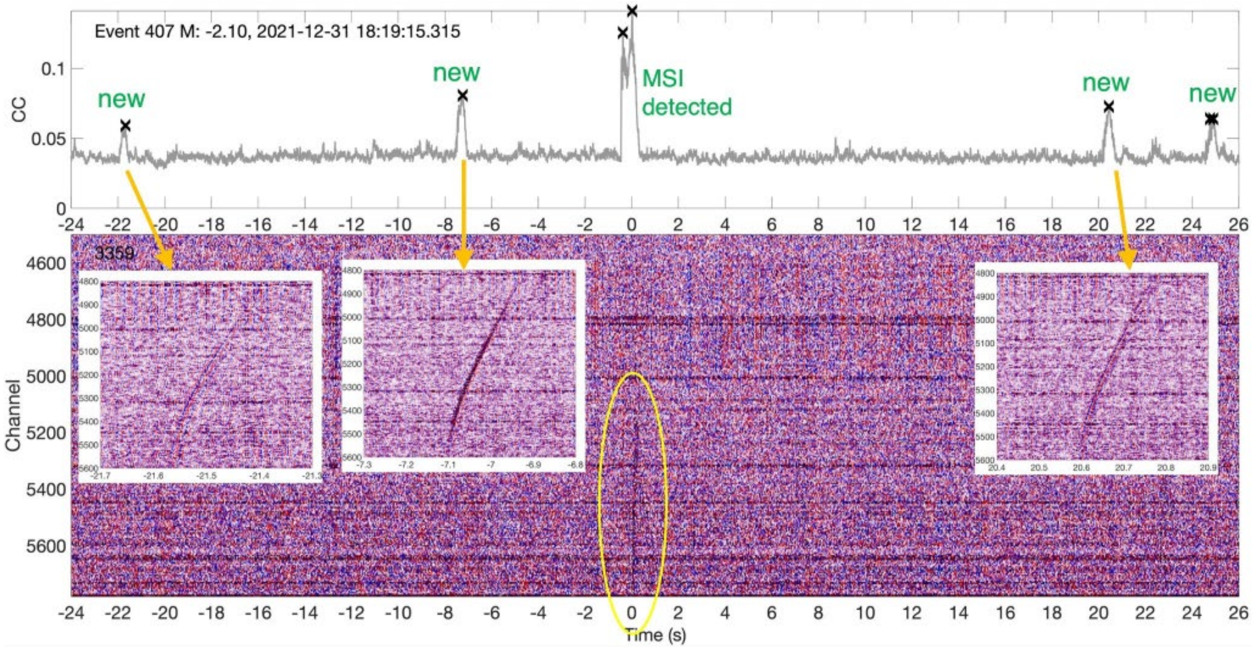

Figure 2.62 The top plot shows channel-to-channel coherence as a function of time. Peaks in the coherence are inferred to be detections. The bottom plot shows DAS record section at well 2F for the same time period. The signals from the large microseismic event at time t=0 s that was detected by the surface array ("MSI detected") are obvious (yellow ellipse). The inset plots show S waves for smaller microseismic events that were not detected by the surface array ("new"). The arrows show the waveforms corresponding to detections as inferred from the coherence peaks.

Whereas the signal-to-noise ratio of DAS microseismic signals on individual DAS channels are lower than that of individual geophones, direct body-wave records of microseismic events are highly coherent on the spatially dense DAS array and follow well-defined moveouts unlike noise that is either less coherent and/or follows different moveouts (Figure 2.62). We established a framework for simultaneous detection and location of microseismic events using channel-to-channel coherence (scale of 0-1; Rost and Thomas 2002) of the DAS data in the horizontal sections of the wells after correcting for travel-time moveouts for the uniform velocity model described previously (Figure 2.63). A source grid is established in the horizontal plane of the wells and the grid point for which the travel-time moveout correction leads to the highest channel-to-channel coherence for the signals on the DAS array is inferred to be the true location of the microseismic event (Figure 2.64). We analyzed around ~8.5 hrs of data till 6 Jan 2022, primarily centered around events previously detected by MSI. We detected ~217 new microseismic events (no corresponding event in the MSI catalog within 0.1 s), a ~17% increase over the number of events detected by MSI in the same time period. These events had detectable energy in both wells and therefore could be located. We also detected and located ~326 events that were also present in the MSI catalog. For these events, the horizontal distance between our locations and MSI locations was ~50-300 m, which is the grid spacing in our source grid (Figure 2.64).

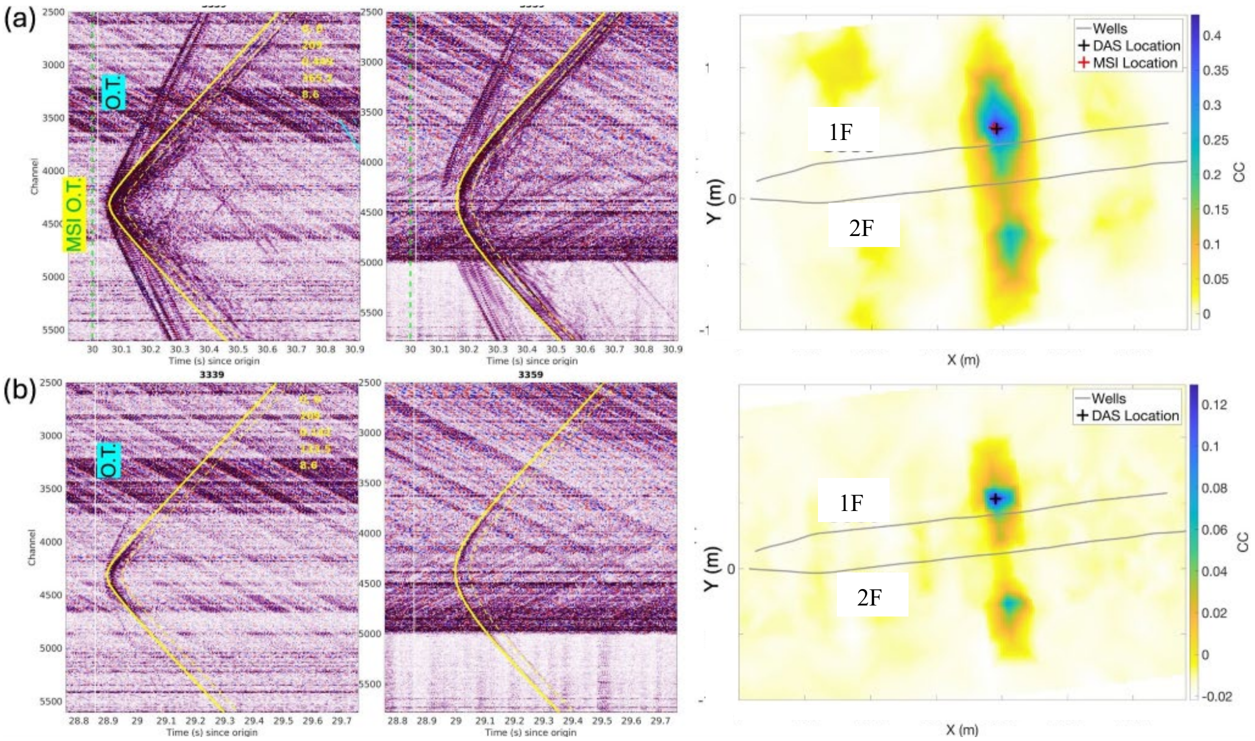

Figure 2.63 (a) DAS record sections for wells 1F (left) and 2F (center) for an example event that was detected by the surface geophone array. The yellow curves are the S-wave arrival times for the best-fitting location. Right subplot shows variation of coherence as a function of possible location in the XY plane. Black + sign marks the inferred best-fitting location that provides the highest coherence to the DAS data. Red + sign marks the MSI location. (b) Same as (a) but for a smaller event that was not detected by the surface geophone array but was detected by the DAS arrays.

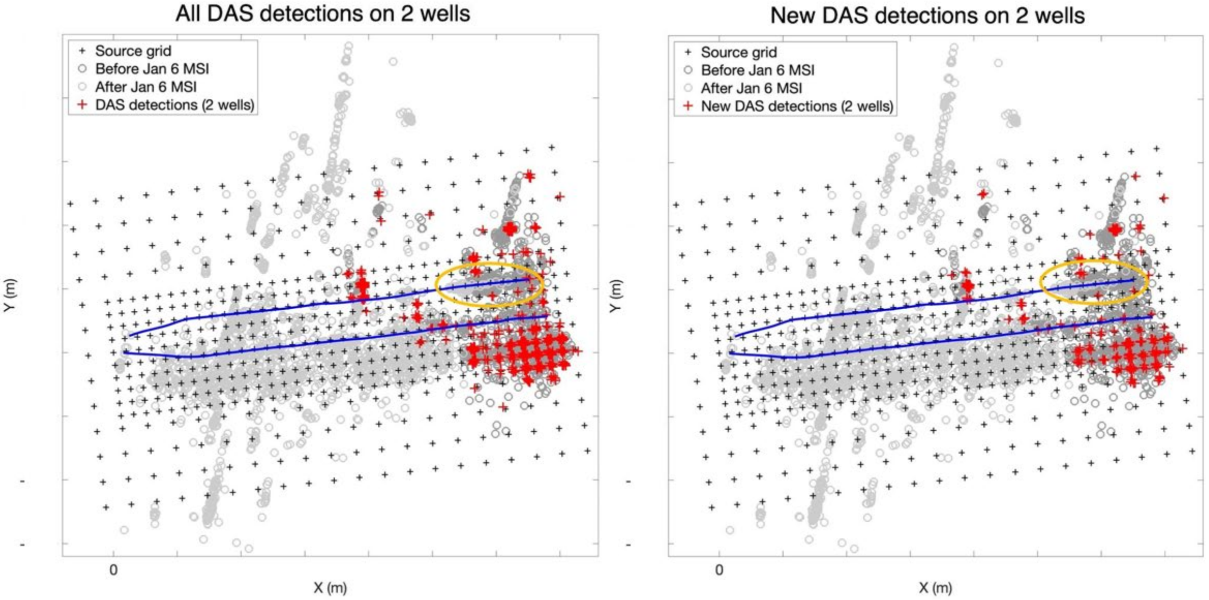

Figure 2.64 Figure shows locations of events (red + signs) detected and located by the DAS arrays on both wells - Left subplot: all events, right subplot: events that were not detected by the surface geophone array. Black + signs show the source grid. Wells: blue lines. Gray circles are other microseismic events in the MSI catalog.

Downhole DAS data is now routinely acquired on fiber-optic cables deployed in both vertical and horizontal wells for seismic imaging as well as monitoring of microseismicity, spatiotemporal changes in elastic properties, fracture growth, changes in fracture property, and low-frequency strain during geothermal and oil and gas operations such as hydraulic fracturing (Mateeva et al., 2014; Jin and Roy 2017; Karrenbach et al., 2018; Lellouch et al., 2020; Baird et al., 2020; Luo et al., 2021; Cheng et al., 2021; Titov et al., 2021; Norbeck et al., 2023). We develop a workflow for estimation of M_0 (seismic moment) and Mw (moment magnitude; Hanks and Kanamori, 1979) of microseismic events using strain data recorded by downhole DAS arrays. Magnitude estimates of induced microseismic events are crucial for calculating the extent of the stimulated reservoir volume and evaluating the efficiency of injection activities (Maxwell et al., 2009; Shapiro et al., 2011). Correct estimation of seismic magnitudes plays an important role in effective mitigation of induced seismicity (Bommer et al., 2006; Kwiatek et al., 2019; Utah FORGE 2020). We use the property of the seismic wavefield that at far-field distances, the time integral of axial strain is proportional to the displacement scaled by apparent slowness. Therefore, M_0 can be directly estimated from the amplitude of the low-frequency plateau of the spectrum of time-integral strain, similar to the methodology commonly employed for far-field displacement spectra (Shearer 2009; Kwiatek et al, 2019; Bethmann et al., 2011). We account for the effect of polarization on strain amplitudes for different types of body waves. Benefitting from the large spatial coverage provided by DAS arrays, moment estimates from multiple channels are averaged and an average radiation coefficient is assumed over the focal sphere. The workflow can be potentially extended to DAS arrays in vertical wells (Lellouch et al., 2020) and to S waves recorded on dark fiber DAS arrays at the surface. This methodology does not require any calibration beyond knowledge of local seismic properties and the use of the lowest possible frequencies reduces the influence of subsurface heterogeneities and the finite spatiotemporal extent of event ruptures. The capacity to estimate robust seismic magnitudes from downhole DAS arrays allows improved evaluation and management of fracture growth and more effective mitigation of induced seismicity. The results of the magnitude estimation section of this study are accepted for publication in the peer-reviewed journal *Bulletin of Seismological Society of America* as Nayak et al. (2024). The following is a brief summary of the main findings.

We propose the following expressions to calculate magnitudes from P and S waves

$$M_W \sim \langle \frac{2}{3}\log_{10}\left(\frac{4\pi\rho\alpha^4}{0.52}\frac{r}{(\cos\theta)^2}\langle\frac{\epsilon_{ii,P}(f)}{(2\pi f)}\rangle\right)\rangle - 10.73$$

$$M_W \sim \langle \frac{2}{3}\log_{10}\left(\frac{4\pi\rho\beta^4}{0.63}\frac{r}{(\cos\theta)(\sin\theta)}\langle\frac{\epsilon_{ii,S}(f)}{(2\pi f)}\rangle\right)\rangle - 10.73 \qquad (2.7)$$

α: Vp, β: Vs, ρ: density, ε: axial strain (from DAS), θ: angle between raypath and direction of the cable, f: frequency, r: distance. Division by 2πf is equivalent to integrating in time. The inner angle bracket implies averaging over low frequencies whereas the outer angle bracket implies averaging over channels in which θ, r and ε are specific to each channel. The standard deviation over measurements at multiple receiver locations and over measurements for P and S phases provides the uncertainty in the final magnitude estimate.($\cos^2\theta$) and ($\cos\theta\sin\theta$) are well understood polarization factors for P and SH waves, respectively. 0.52 and 0.63 are average P and S radiation patterns over the focal sphere (Shearer, 2009).

Figure 2.65 shows the data, workflow, and the results for one example event. We further compare the magnitudes estimated from the downhole DAS arrays with the magnitudes estimated from the surface geophone array for validation of the methods used in this study. We use three different approaches to calculate magnitudes from the surface geophone array – (1) moment tensor inversion for the largest microseismic events, (2) amplitude of the low-frequency plateau of the far-field P-wave displacement spectra for the intermediate-magnitude events, (3) for the smallest events, we first improve the SNR by stacking waveforms of closely spaced geophones and then use the low-frequency amplitudes of the far-field P-wave displacement spectra. Figure 2.66 shows the results for ~106 microseismic events with reasonable quality geophone and DAS data. The magnitudes derived from the DAS data and the geophones agree with each other and cluster in the vicinity of a 1:1 line in the magnitude range ~ –0.65 to +0.55. An ordinary least-squares straight line fit to the data yields a slope and intercept of 0.98+/-0.09 and –0.06+/-0.04, respectively, with the model parameter uncertainties represented by twice the standard deviation. The R^2 value of the fit is 0.81. The 95% confidence intervals of the prediction span ~0.23 magnitude units around the best-fitting line and the 95% quantile of the absolute difference between magnitude estimates from the two datasets is ~0.26 magnitude units. The DAS magnitude uncertainties generally vary between ~0.1 and ~0.23. These numbers are similar or slightly greater than typical magnitude uncertainties of >~ 0.1 units in regional catalogs (Clinton et al., 2006). DAS magnitudes estimated separately using P or S waves agree well with each other. The DAS magnitude estimates are also robust with respect to reduced Q (stronger attenuation). The events for which the body waves span a greater range of polarization factor values as quantified by standard deviation (> 0.1), we see a greater median decrease of ~0.04 units in the standard deviation for both P- and S-wave amplitudes upon correction for the polarization factors, which supports the polarization factors used in equation 1.

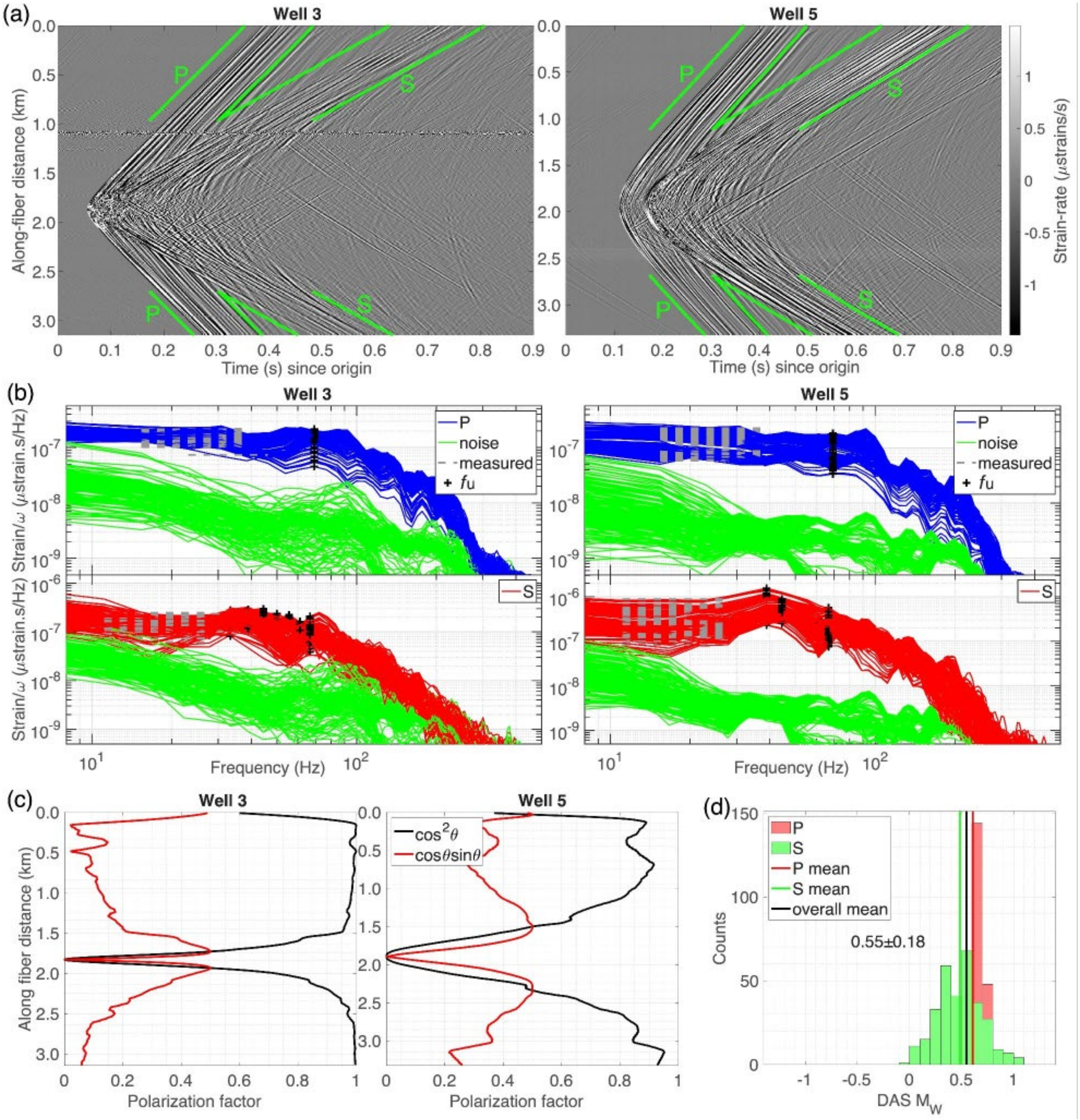

Figure 2.65 DAS data and magnitude estimate for an example event. (a) DAS record section on the horizontal section of the two wells (left panel: Well 1F or 3, right panel: Well 2F or 5). The beginning and the end of segments of far-field body waves used in spectral analysis are marked by green curves. (b) Strain spectra divided by frequency. Left and right panels correspond to wells 3 and 5, and the top and bottom panels correspond to P and S waves, respectively. Black + signs mark the upper limit of the frequency range (f_u) used to search for the low-frequency plateau in the spectra. The dashed gray lines mark the frequency range selected to measure the amplitude of the low-frequency plateau in the spectra. (c) Polarization factors for P and SH waves along the DAS arrays on the horizontal sections of the wells. (d) Histogram of magnitude estimates from different channels of the DAS arrays color-coded by phase type (P or S). The overall mean (vertical black line) and the standard deviation are mentioned in the plot. Well 3 is 1F, Well 5 is 2F. From Nayak et al. (2024).

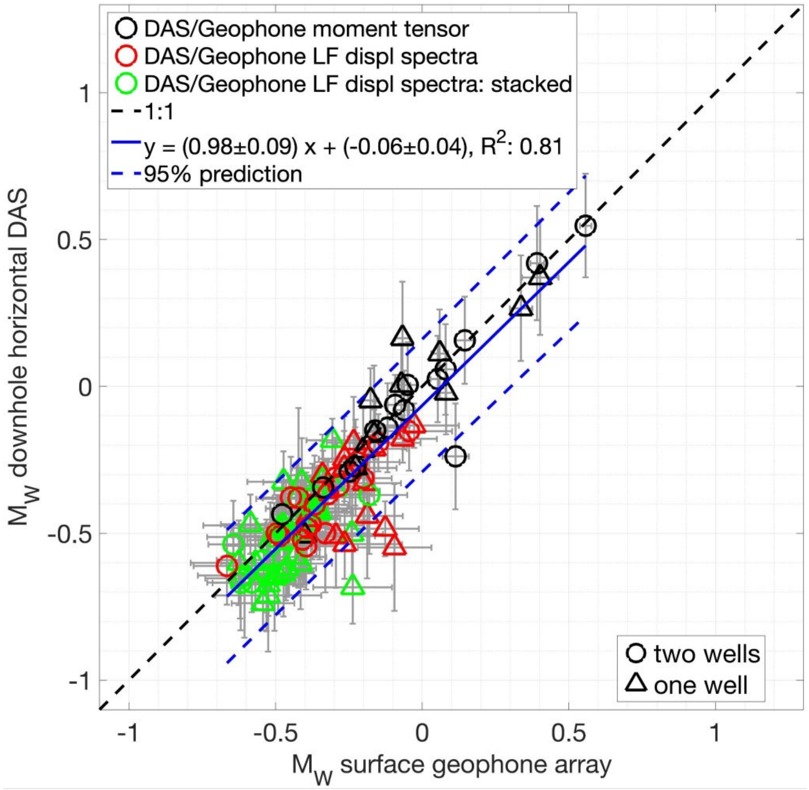

Figure 2.66 Comparison of magnitudes estimated from the downhole DAS arrays and the surface geophone array. Different colors indicate different methods employed to estimate magnitudes from the surface geophones – moment tensor inversion, low-frequency (LF) displacement (displ) spectral amplitudes, and low-frequency displacement spectral amplitudes derived from stacked waveforms; the method applied to the DAS data is the same for all events. Circles or triangles indicate if the DAS measurements come from both wells or predominantly from just one well. The error bars indicate uncertainties in magnitude estimates. Solid and dashed blue lines are the best-fitting straight line and the 95% confidence intervals for the prediction. From Nayak et al. (2024).

2.5.4 Fracture Imaging with DAS

The EFSL project focuses on the unconventional reservoirs in the Eagle Ford Shale and Austin Chalk in South Texas (Figure 2.67). This task targets the zipper-fracturing completion that was performed on two horizontal wells, notated in this study as well 1F and well 2F. Two engineered Constellation fibers (Silixa LLC), capable of supporting DAS and Distributed Strain Sensing (DSS), and a multi-mode fiber for Distributed Temperature Sensing (DTS) measurements, were permanently deployed in both wells for hydraulic fracture monitoring. The raw DAS microseismic data at the two wells were simultaneously recorded by two DAS interrogators (Carina, Silixa LLC) using a gauge length of 10 m, a channel spacing of 1.0 m, and a sampling rate of 1000 Hz. The microseismic wavefields and LF-DAS data presented in this paper were recorded in well 1F, as the stimulation of well 2F caused significant in-well noise and eventual fiber damage. Consequently, well 1F was chosen as the primary monitoring well for this study. For migration, we assumed a laterally isotropic 1D velocity model (Figure 68c), which is derived by averaging the 3D velocity model that was originally used to further calibrate microseimic depth using DAS data. The resulting Vp model, along with a uniform Vp/Vs ratio of 1.81, provided reasonable fits to the observed arrival times of the direct P and S waves in the DAS data recorded at the horizontal sections of the well.

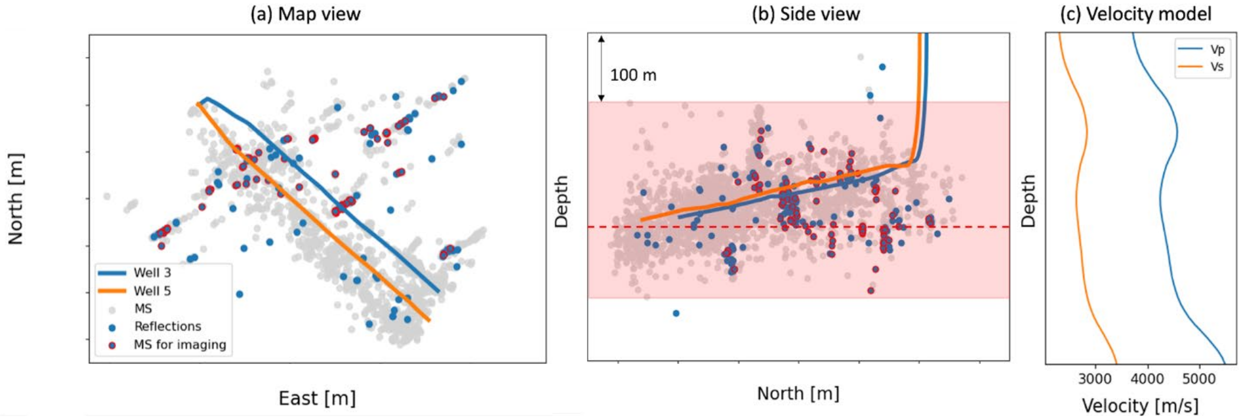

Figure 2.67 Fibers are permanently installed in two horizontal wells, Well 1F and Well 2F, to monitor hydraulic fracturing. A microseismic catalog derived by a surface geophone array is shown in (a) map view and (b) side view. (c) The layered isotropic velocity model for imaging (Well 1F is 3; Well 2F is 5).

DAS microseismic processing

To analyze DAS microseismic signals, we first remove DC bias, noise spikes, and apply a spatial median filter to attenuate common mode noise. We then apply a bandpass filter between 10 and 200 Hz to obtain a pre-processed wavefield. Figure 69 provides two representative examples of DAS-recorded microseismic reflections. The moment magnitude for event A and event B are -0.627 and -0.162 as determined by the surface array, respectively. In addition to direct P- and S-wave arrivals, the wavefields contains reflected S-waves with linear moveout, indicating the presence of nearby induced fractures or small faults. In event A (Figure 2.68a), the majority of the reflections propagate toward the heel of the well (right dip) and intersect with direct S-waves, potentially generated by seismic waves that are emitted from microseismic sources and then impinge on nearby hydraulic fractures of prior or current treatment stages. Since the reservoir was stimulated sequentially from the toe side towards the heel side of both wells, reflections propagating toward the toe side (left dip) likely originate from nearby pre-existing fault lineaments (Figure 2.68b), which is supported by the microseismic clouds (Figure 2.67a) as well. These reflections have been consistently recorded since the initial treatment stage, even when most of the wells were not stimulated. Although some events also exhibit reflected P-waves, this study focuses solely on reflected S-waves for imaging fractures, as reflected P-waves were less commonly observed and generally have lower amplitudes compared to reflected S-waves. Considering the relatively weak signal from the vertical section of the fiber, only the horizontal section of Well 1F (3130 traces for each source) was used for migration after removing bad traces caused by fiber breakage.

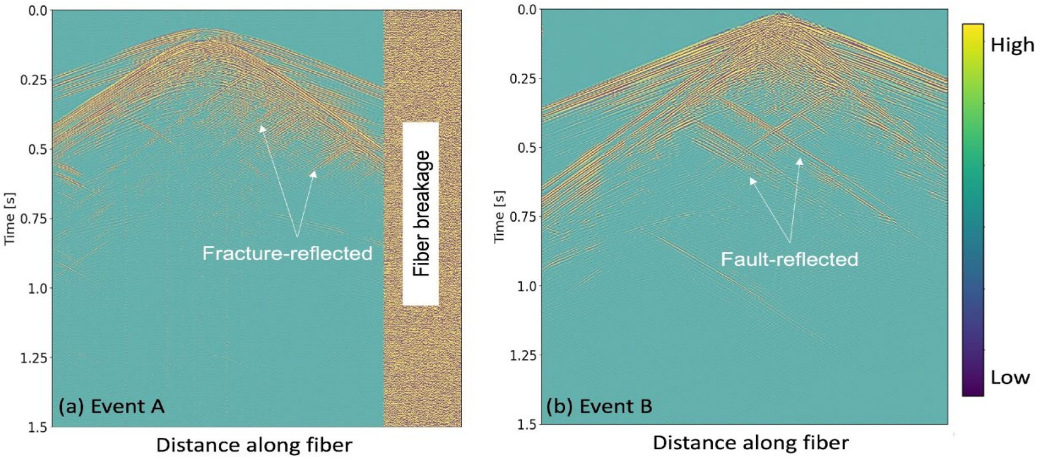

Figure 2.68 Two examples, (a) Event A (Mw=-0.627) and (b) Event B (Mw=-0.162), of observed microseismic wavefield with fault- and fracture-reflected waves recorded by fiber in Well 1F.

Event selection for fracture imaging

We completed event selection and analysis in FY2023 Q2. After analyzing the microseismic catalog identified by a dense, large aperture surface array of geophones (2653 events grey dots in Figure 68), we identified 232 events that exhibit imageable fracture- or fault-reflected S-waves on the DAS data (blue dots in Figure 2.69). To mitigate the potential impact of high noise levels in low signal-to-noise ratio (S/N) events on the final image quality, we reviewed and manually selected 100 events with the best-quality reflections for imaging (red circles in Figure 68). The event selection process only excludes sources with relatively weak reflections that are obscured by noise but maintains high illumination by retaining the best-quality sources in the vicinity. Microseismic sources that offer distinct illumination are also preserved for imaging. The magnitude and S/N distribution of the microseismic catalog are shown in Figure 70. Selected microseismic sources have relatively larger magnitudes (Mw ≥-1.50) and higher S/N, and cover a depth range of 300 m within the fracturing zone. The moment magnitude is estimated by the geophone data acquired by a dense surface array. The S/N is calculated by treating data prior to direct P waves as noise and the detected microseismic events that contain both P- and S-waves as signals.

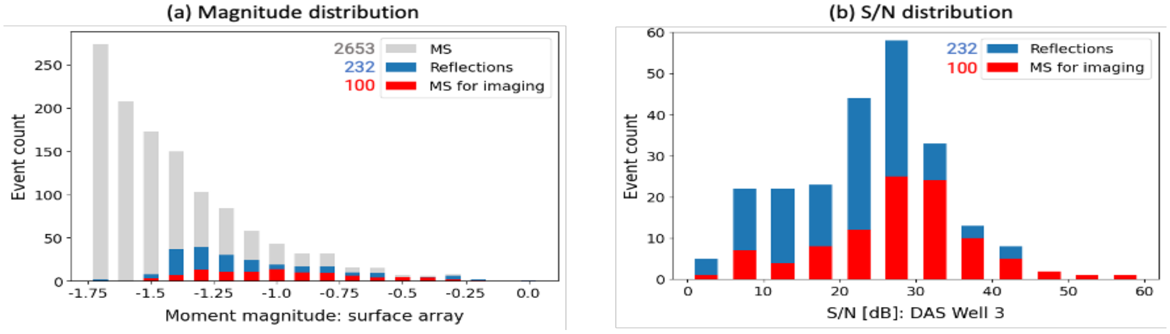

Figure 2.69 Event selection and data analysis. (a) Magnitude and (b) estimated S/N distribution of selected events for reflection imaging.

Fracture imaging methods

Our approach is similar to classical 3D crosswell or VSP reflection imaging (Harris et al., 1995; Zhou et al., 1995) except for (a) the use of microsesimic events as sources, (b) the use of DAS as the receiving modality, and (c) special-purpose stacking procedures required given the non-uniform source distribution. We treat each microseismic event as a high-frequency seismic source, consider each fiber channel as a receiver, and apply a pre-stack Kirchhoff migration method for reflection imaging. Figure 2.70 shows the overall processing workflow. The proposed method requires accurate microseismic event locations, the well geometry, a calibrated velocity model, and unclipped microseismic waveforms as input data. The imaging workflow includes several essential steps including preprocessing, event selection, wavefield separation, migration, stacking, and post-processing, as elaborated in following sections. The ultimate output of this workflow is a high-resolution 3D image volume of the subsurface.

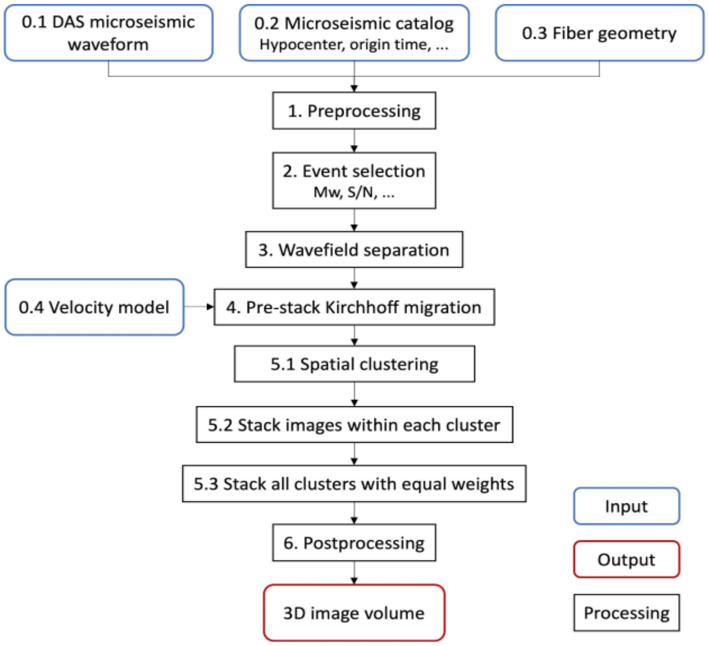

Figure 2.70 DAS microseismic reflection imaging workflow for fracture and fault mapping.

Wavefield separation

To extract reflected S-waves from the raw DAS data for imaging, we applied a preprocessing workflow (Ma et al., 2023b) similar to crosswell reflection imaging (Rector et al., 1995). An *f-k* filter is first applied to separate the raw data into heel- and toe-ward wavefields (Figure 2.71b). Then, we manually mute signals above the red lines to exclude the influence of the direct waves on the final fracture images (Figure 2.71c). This red line can be determined by the S-wave velocity but needs to be slightly adjusted to remove as much residual interference as possible.

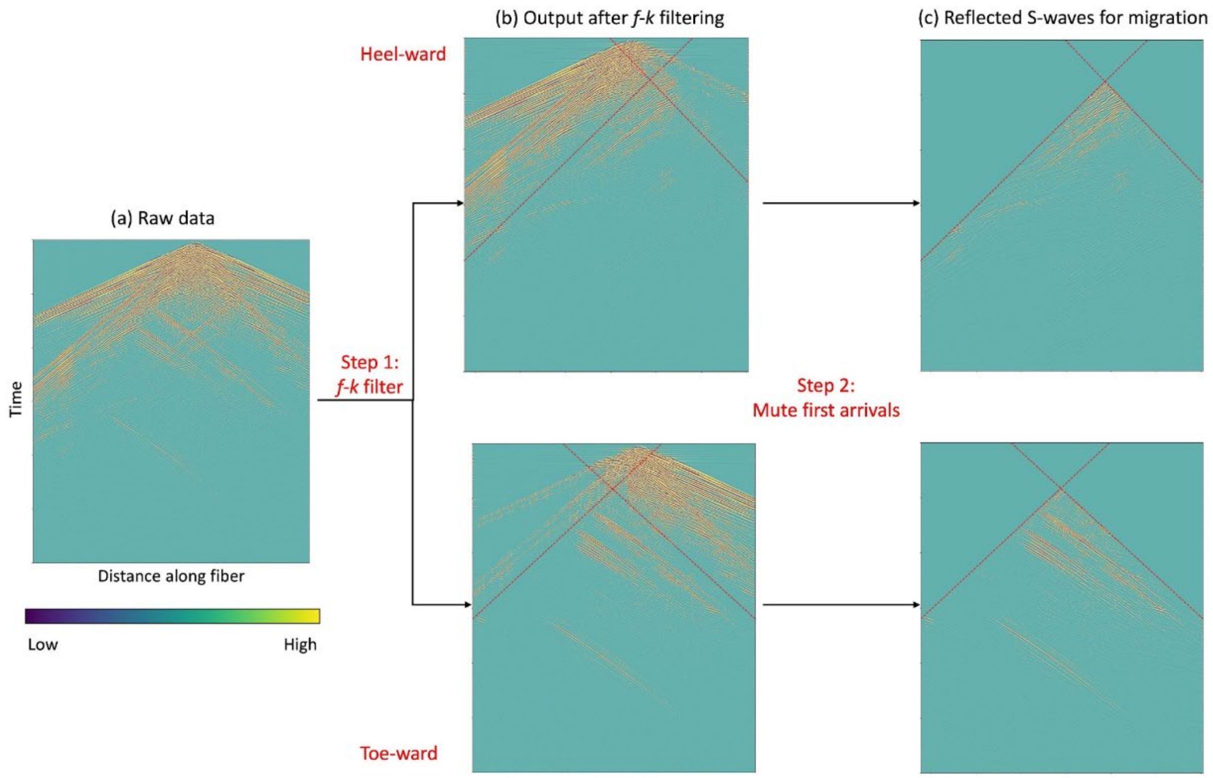

Figure 2.71 Wavefield separation, including applying an f-k filter and removal of direct waves, to extract pure reflections for imaging. (a) Raw data of event B. (b) Output after applying f-k filter. (c) Heel-ward and toe-ward reflected S-waves of event B for Kirchhoff migration.

Kirchhoff migration

Following the wavefield separation process, we separately apply conventional 3D pre-stack Kirchhoff migration (Yilmaz, 2001) to the reflected wavefields propagating towards the toe and towards the heel of the lateral. An Eikonal equation solver (Luu, 2022) is employed to calculate the travel time volume of each source-receiver pair. Then two half images are merged to form the complete fracture image illuminated by an individual source. This approach minimizes image errors caused by incomplete removal of direct waves and ensures thorough quality control to achieve accurate and reliable migrated volumes. Within the migration procedures, we utilize a calibrated S-wave velocity model (Figure 2.67C) to compute traveltime tables, then migrate the microseismic traces and output an S-wave image volume on a 10 × 10 × 10 m grid. Due to the limited depth constraints provided by microseismic reflections, only a depth range of 300 m within the fracturing zone was processed (as shown by the red mask in Figure 2.67b).

The Kirchhoff migration output for two individual events (Figure 2.68) is presented in Figure 2.72, with a horizontal slice at the depth within the fracturing zone (marked by the red dashed line in Figure 69b). The solid dots represent the epicentral location of the corresponding microseismic sources. The colorbar displays the unweighted, normalized raw data amplitude within the range of [-1, 1]. Due to the geometry of unevenly distributed microseismic sources, radiation pattern, and the specific orientation of the DAS array, different sources may illuminate different parts of the reservoir. In Figure 2.72a, the image of event A characterizes most of the cross-well fractures from stimulation stages prior to the origin time of event A. The absence of reflectors near the toe side from early stages is caused by the lack of available data resulting from fiber breakage, as shown in the raw data (Figure 2.72a). In contrast, event B in Figure 2.72b reveals the structure of far-field faults (the red arrow in Figure 73b) that likely take stimulation fluid, as well as a portion of the cross-well fracture growth. Given the proximity of event B to the monitoring fiber and the intrinsic single-component limitation of fiber-optic sensing, the image of event B exhibits a symmetrical feature on both sides of Well 1F. Although both examples exhibit migration artifacts arising from the narrow aperture (Yilmaz, 1987) of individual sources, these distortions can be mitigated by stacking results for multiple sources with a broader combined aperture. Nevertheless, the images still reveal geologically interpretable features, including the identification of hydraulic fractures extending from well 2F to well 1F, as well as natural structures aligning with the maximum horizontal stress orientation (S_{Hmax}) (Heidbach et al., 2016; Snee and Zoback, 2022).

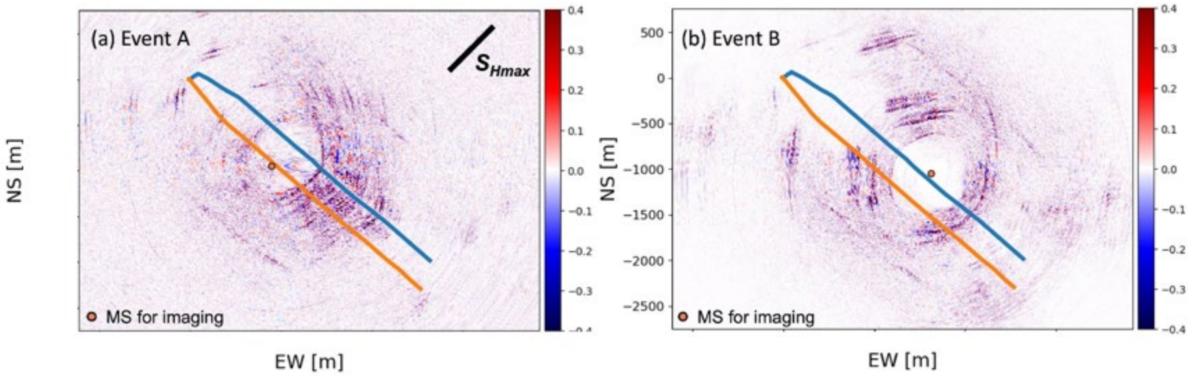

Figure 2.72 Imaging results of two single source in (a) Event A and (b) Event B, showing horizontal slices of the seismic image volume within the fracturing zone (the dashed line in Figure 1b).

Spatial clustering and stacking

Following the imaging of individual sources, all detected reflectors are stacked into a 3D reflectivity volume, enabling the delineation of multiple discrete reflectors. In contrast to the uniformity of active seismic sources, microseismic reflection imaging faces the technical challenge of dealing with a non-uniform source geometry, determined by a combination of completion activities and the geometry of existing natural features. To address this challenge, we have developed a stacking strategy for microseismic reflection imaging grounded in spatial clustering techniques.

The first challenge is the variability of both focal mechanisms and magnitudes of microseismic sources. Due to variable focal mechanisms, subsurface imaging points may be illuminated by seismic waves with opposing polarities generated by different microseismic sources. The substantial differences in magnitudes can result in reflected energy from smaller sources being overshadowed by the energy emitted from stronger sources. To mitigate the influence of varying sources on stacking, we adopt a normalization step for all images of every single shot, which are then combined by taking their absolute values to build the final 3D fracture image volume. While this straightforward workflow may accumulate image noise and slightly decrease the resolution, it effectively prevents the cancellation of useful contributions from sources with opposite polarities at the same image point. A 3 × 3 median filter is also applied at the last step of the imaging workflow to remove background noise.

The second challenge of microseismic imaging is the irregular distribution of microseismic sources and subsurface reflection fold, unlike active source imaging with a specifically designed geometry to provide multi-azimuth coverage of a particular subsurface objective. In cases where a microseismic cluster is significantly denser than others and illuminates a very similar volume multiple times, stacking individual sources with equal weights can generate strong artifacts and obscure weaker reflectors. To attenuate imaging artifacts caused by the irregularity of microseismic sources, we spatially classify selected sources into different clusters based on their hypocenter locations and assign equal weights to each cluster instead of each source. It should be noted that a trade-off exists between the aperture and image S/N ratio due to the irregular spatial fold of the reflection geometry, particularly in subsurface regions with fewer large microseismic events.

Figure 2.73 demonstrates the imaging results within eight representative clusters. Small oranges dots represent the entire microseismic catalog and black stars indicate the epicentral location of selected sources within each cluster for imaging. Microseismic sources within each cluster share a similar aperture and therefore can image similar subsurface reflectors. Different spatial clusters illuminate varying portions of subsurface structures. Figure 2.73a-d reveal the fracture growth as the stimulation was conducted from toe side to the heel side. Direct wave residues are evident as highlighted by the white arrows. However, these residues should not pose a significant issue when stacking multiple clusters, which will be demonstrated in the results section. The imaged reflectors in Figure 2.73a possibly reveal pre-existing structures since this cluster of microseismic sources is recorded during the very early injection stages. Figure 2.73e-h highlight four clusters that make the most substantial contribution to fault lineaments imaging, which not only exhibit a remarkable level of consistency with microseismic clouds but also offer additional details beyond the geometry of these clouds. In Figure 2.73e and f, fault lineaments exhibit a scattering pattern on the east side of well 1F. These fault zones do not appear to directly connect with the injection well from both microseismic and fracture imaging but still possibly serve as pathways for fluid movement. On the west side of the well pad, a significant concentration of fault lineaments is evident near the heel of well 2F as shown in Figures 2.73g and 2.73h. The prominent linear energy captured in the image exhibits a perpendicular alignment with the injection well, extending seamlessly from well 2F to the far field at least a distance of 1 km. This intriguing observation potentially indicates the connectivity of hydraulic fractures with pre-existing fault zones or other structures.

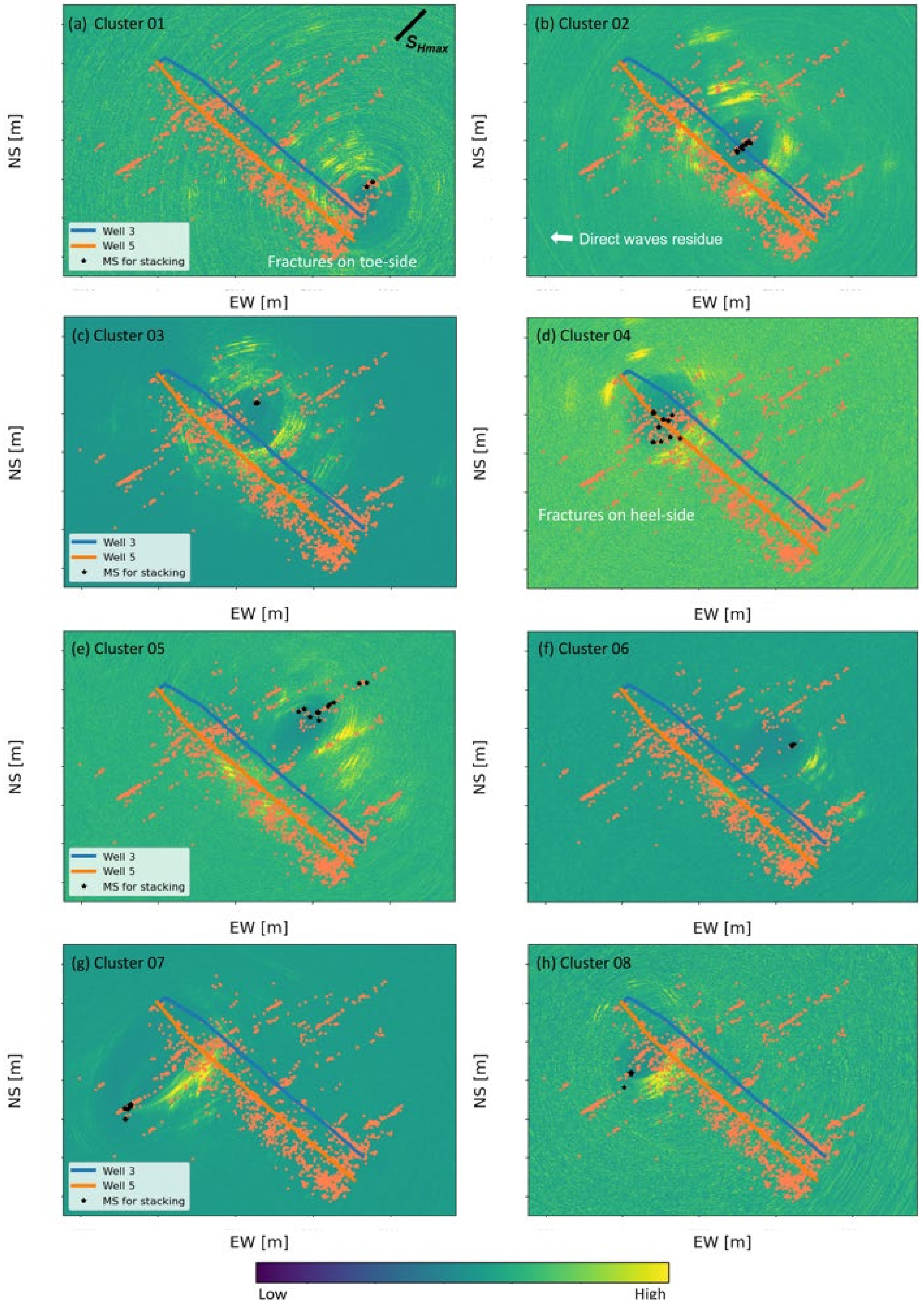

Figure 2.73 Stacked images within each cluster. (a)-(h) show the images of cluster 01-08. Well 3 is 1F, Well 5 is 2F.

Fracture imaging results

Figure 2.74 demonstrates the final imaging results obtained by stacking reflectivity results for the 100 microseismic sources (orange dots with white outline) with a horizontal slice within the fracturing zone at the same depth of Figure 2.72 (the red dashed line in Figure 2.67b). Microseismic clouds (orange solid dots) and frac-hits interpreted by LF-DAS (white solid dots along well 3) are overlain on the slice for further validation. Despite some residual direct waves as indicated by white arrows on far field of both heel and toe sides, reflection imaging provides a high-resolution map of subsurface reflectivity with numerous interpretable features. The fracture imaging results show high consistency with microseismic clouds including similar fracture network, azimuth, and fluid propagation range (Figure 2.74a). Slight variations in intricate details are showcased within the fracture images, which can be perceived as extensions of the microseismic clouds, as indicated by the red arrow, encoding complementary information. The image may not capture the utmost far-field structures, primarily due to the absence of valid sources in that region and the proposed workflow is designed to depict structures within the range between the sources and the monitoring fiber. Since only data from Well 1Fwas used to build the image in Figure 75, the imaged fractures present symmetrical features on both sides of the monitoring fiber. Combining reflection data from multiple monitoring fibers has the potential to enhance the image quality, primarily because it offers more comprehensive coverage across the imaging area.

Figure 2.74b provides a closer view of the cross-well region, demarcated by the white rectangle in Figure 2.74a, offering enhanced insight into details of the hydraulic fractures. Due to strong noise produced by in-well injection, only frac hits from early stages are accurately picked (white dots), where unfortunately most reflected waves are lost due to fiber breakage in a later treatment stage of Well 3. Despite this, two frac hits from the last interpretable stage, as marked by red lines in Figure 2.74b, are well-matched with the imaged two fractures. Across more than eleven treatment stages (blacks circles along Well 2F) where frac hits are not visible on LF-DAS and fracture azimuth cannot be accurately estimated by microseismic clouds, microseismic reflection imaging can provide reliable monitoring of fracture propagation with high-resolution. The measured fracture length is at least 400 m in half length. It is important to note that the actual fractures may be longer than the imaged reflectors since the visibility of reflections requires a sufficient impedance contrast. The fracture azimuth estimated by reflection imaging results is 42.5°, which is consistent with the maximum local stress orientation. The slight change in fracture azimuth across Well 1Fmay be the result of imaging artifacts due to the relatively narrow aperture even after stacking. Since only slow shear waves are used in this study, the imaging results are expected to be sensitive to fluid-filled fractures or faults. Strong far-field reflectivity zones are inferred to be related to fluid-filled faults and the reflection visibility may reveal the fluid propagation range from the injection well to reservoir.

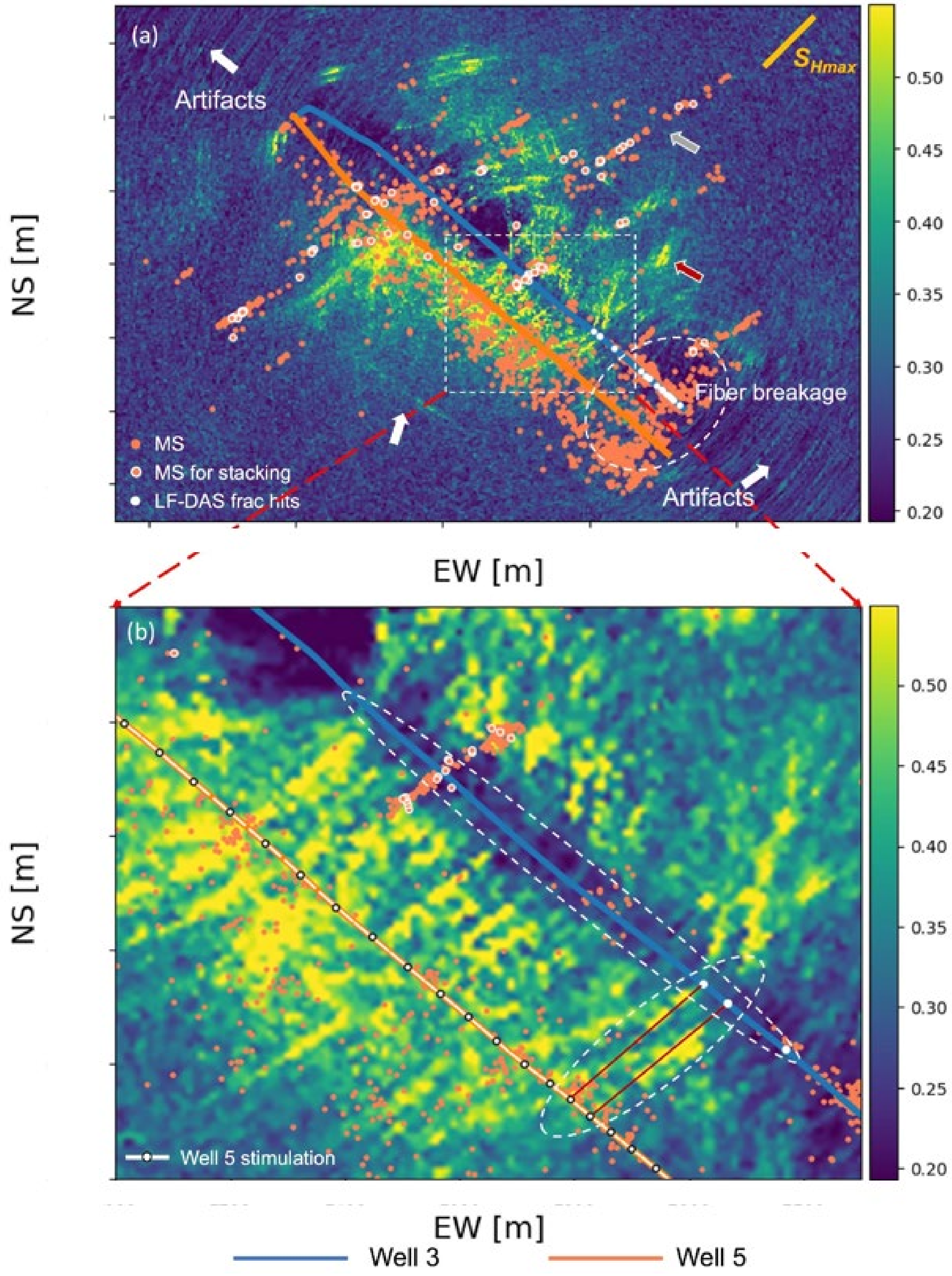

Figure 2.74 3D image volume constructed by stacking reflectivity results from 100 microseismic sources. (a) Horizontal slice of seismic image volume at the depth marked by the red dashed line in Figure 2.67b. (b) Enlarged horizontal slice showing high-resolution cross-well fractures (Well 1F is 3; Well 2F is 5).

Figure 2.75 displays vertical slices through the image volume along Well 1Fand Well 2F. At least 300 m height of vertical fracture growth is imaged with the best reliability, aligning with the frac hits or the position of stimulation stages. Fractures beyond the fracturing zone are still imageable, however, they are selectively clipped to optimize interpretation as the imaged depth range benefits from the most reliable constraints on migration furnished by microseismic reflections. Reflection imaging can help to constrain fracture height even when vertical fibers are not available. Strong energy with a larger width in Figure 9b may reveal fracture connecting with nearby faults, which is consistent with the side view of microseismic clouds in Figure 2.67b. The relatively weak reflectors around Well 1F in Figure 2.74b and Figure 76a are due to the muting of near-fiber reflections. In this case study, the majority of microseismic sources are located within the stimulation volume and close to the monitoring fiber, resulting in a very small time delay between the direct and reflected waves. As a result, it becomes difficult to separate the direct and reflected wavefield, posing a challenge in imaging reflectors within 40 m of the fiber. Advanced wavefield separation methods, especially for near-apex DAS microseismic data separation, are required to address this issue. Fortunately, LF-DAS can provide reliable near-wellbore observation of fracture propagation.

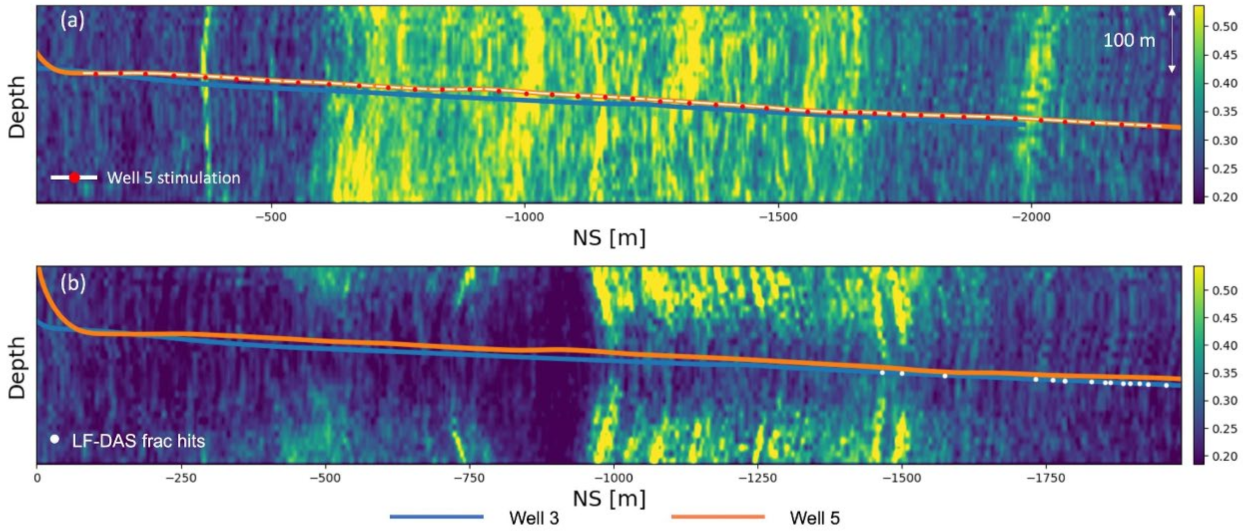

Figure 2.75 3D image volume by stacking 100 microseismic sources. Vertical slice through seismic image volume along the fiber in (a) the injection Well 2F and (b) the monitoring well 3.

Integration with LF-DAS

To further validate the fracture imaging results and mapped fractures, we extract the plane containing both the injection well (Well 2F) and the monitoring well (well 3) from the 3D imaging volume as shown in Figure 2.76a. This 2D plane is then compared with a fracture connection map derived from LF-DAS data (Zhu et al., 2023). Frac interactions across eight stages between Well 2F and Well 1Fare picked and colored by stage in Figure 2.76b. As elaborated above, reflections originating from early stages are obscured due to fiber breakage on the toe side and LF-DAS data only observe the best quality data primarily during early stages because of strong interference arising from later in-well operations. However, both reflection imaging and LF-DAS depict stage 13 as shared points of interest. This alignment underscores a high degree of consistency in the fracture geometry observed through both DAS-derived methodologies. The observed minor shift in fracture azimuth during stage 13 may signify a reactivation of this fracture, influenced by subsequent stages. While LF-DAS reveals stress field changes mostly induced by the current stage, reflection imaging captures potential reflectors throughout the entire injection process. Stage 8 presents a scenario wherein reactivation of prior fractures and fluid propagation appears to connect with pre-existing structures as indicated by the corresponding frac hit (purple dot). This hit is situated proximal to a microseismic cloud (black arrow in Figure 2.74b), agreeing with maximum local stress. Fracture imaging results exhibit relatively subdued energy along the fracture azimuth of stage 8 compared to the majority of fractures, suggesting potential fluid pathways but requiring additional evidence to establish this interpretation definitively. The left-top strong reflector in Figure 10a point the concentrated energy of fault lineaments as shown in Figure 2.73g and Figure 2.74a. Reflection imaging results encompass later stages; LF-DAS primarily monitors the early stages for this project. The consistent fracture azimuth demonstrated in both datasets offers an opportunity to cross-validate and compile a comprehensive depiction of the complete fracture geometry.

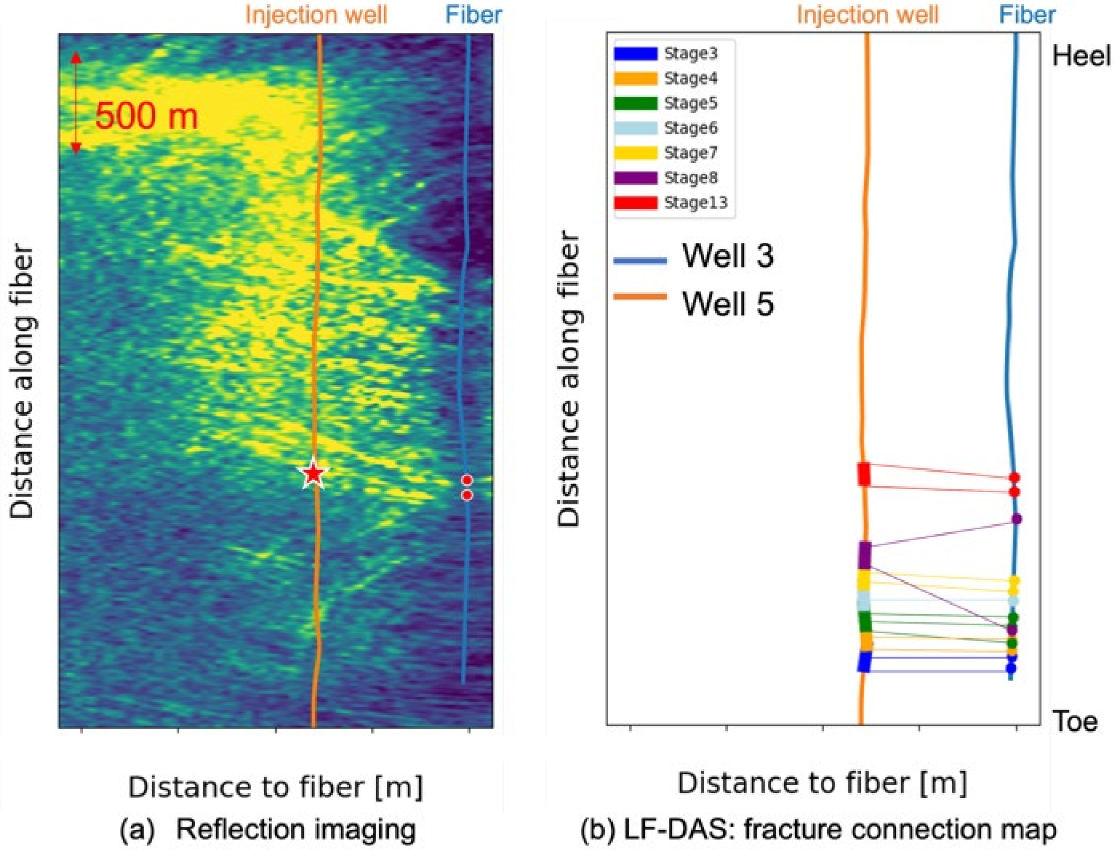

(a) Reflection imaging

(b) LF-DAS: fracture connection map

Figure 2.76 Fracture characterization by integrating reflection image volume with LF-DAS data. Well 3 is 1F, Well 5 is 2F.

2.5.5 Distributed Strain Sensing (DSS) Data Analysis

Our in-depth examination involves the utilization of our home-made interrogator designed for distributed strain sensing (DSS). This interrogator provides Brillouin frequency shift (BFS) measurements, which encapsulate both strain and temperature influences. These measurements are translated into strain with temperature effects.

We initially process the DSS readings by selecting the reference Brillouin Frequency Shift (BFS) at a time of no fracturing activity, established as the baseline from which the strain values are later computed. We then subtract this reference value from all BFS values and apply a moving average filter with a window size of 10 elements. Given that BFS is influenced by both temperature T and strain ε, and hence we convert BFS to strain using Equation 1, incorporating approximations of $C_T \sim 1.025\ MHz/°C$ and $C_\varepsilon \sim 20\ \mu\varepsilon/MHz$. This conversion yields strain measurements with temperature effects.

The microstrain readings depicted in Figure 2.77 showcase the spatio-temporal distribution of strain along the DSS cable. Depth (i.e., distance along the sensing cable) is represented on the y-axis and time on the x-axis. Compressive strain is denoted by the color blue, while tensile strain is represented by red. Upon initiation of Stage A, the initial compression, induced by fracking fluid injection, is followed by subsequent well relaxation. This distinct pattern persists through Stages B, C, and D.

Figure 2.78 presents the spatio-temporal distribution of temperature change measured by DTS. Decrease in temperature is denoted by the color blue, while increase in temperature is represented by red. Initiation of Stage A manifests as initial temperature decrease (transition from red to blue) and thermally induced well compression due to the injection of the relatively cold fracking fluid, succeeded by well relaxation and borehole temperature recovery (transition from blue to red). This pattern is consistent for Stages B, C, and D. As illustrated in both Figures 2.77 and 2.78, the compression and relaxation features distinctly align with the progression of fracturing stages. Stage A, the initial stage, manifests at the deepest well location, while Stages B, C, and D successively occur at progressively shallower locations. This observation underscores the correlation between strain dynamics and the vertical advancement of treatment stages of the multi-stage hydraulic fracturing process.

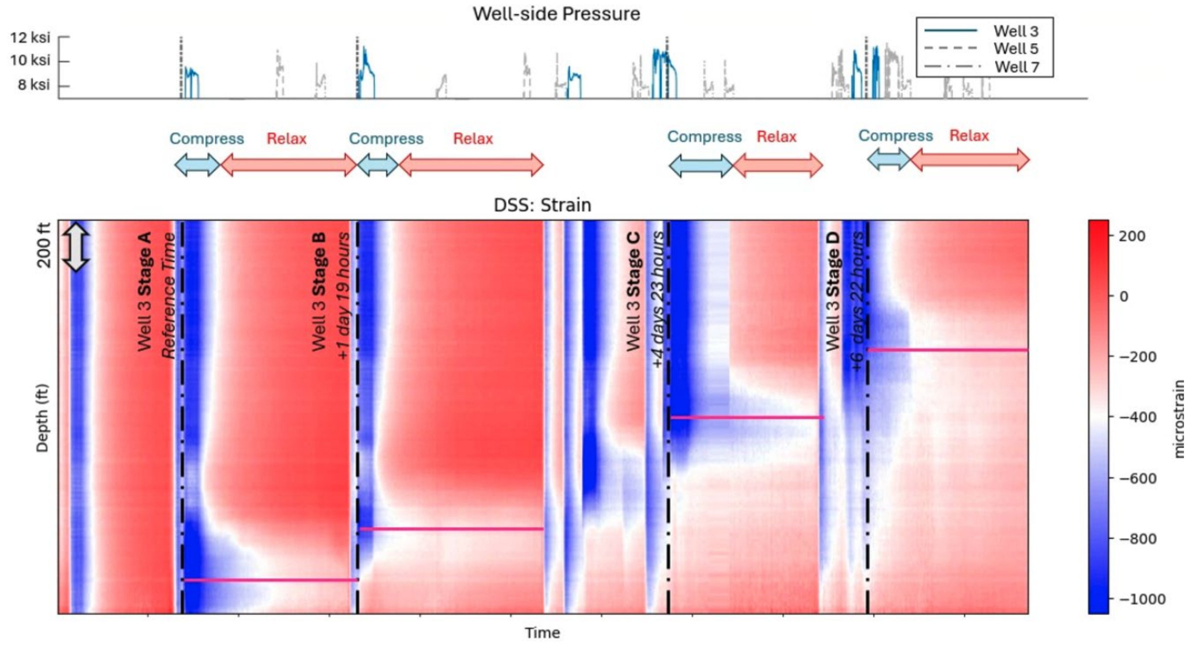

Figure 2.77 (Top) Well-side pressure distribution. (Bottom) Spatio-temporal distribution of DSS measurements in well 1F. Horizontal lines are plotted to indicate the upward trend of the stages, where later stages occur at progressively shallower locations in the well. Well 3 is 1F, Well 5 is 2F, Well 7 is 1H.

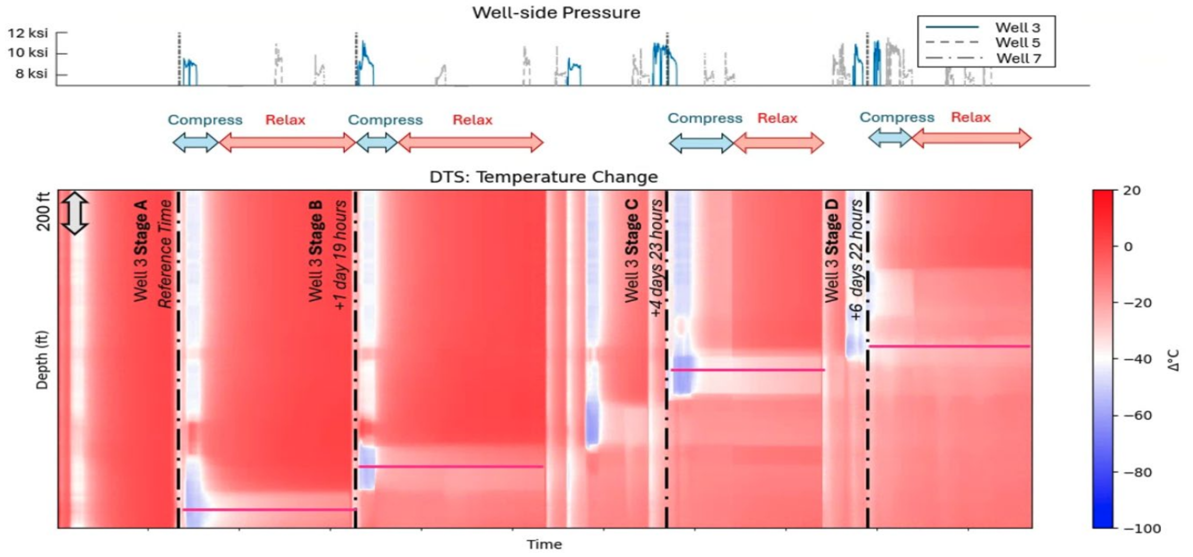

Figure 2.78 (Top) Well-side pressure distribution. (Bottom) Spatio-temporal distribution of DTS measurements in well 1F. Horizontal lines are plotted to indicate the upward trend of the stages, where later stages occur at progressively shallower locations in the well. Well 3 is 1F, Well 5 is 2F, Well 7 is 1H.

Temperature Compensation

A separate cable dedicated to distributed temperature sensing (DTS) was deployed in well 1F. Relative changes in temperature from the baseline were translated into strain using the coefficient of $20.5\ \mu\varepsilon/\Delta°C$. The resultant spatio-temporal distribution of temperature-induced strain is plotted on Figure 2.79 where we observe similar patterns of compression and relaxation of the well that are initiated at the start of each stage. Given that the DSS and DTS measurements occur at different spatial and temporal intervals, we align the readings through resampling and linear interpolation.

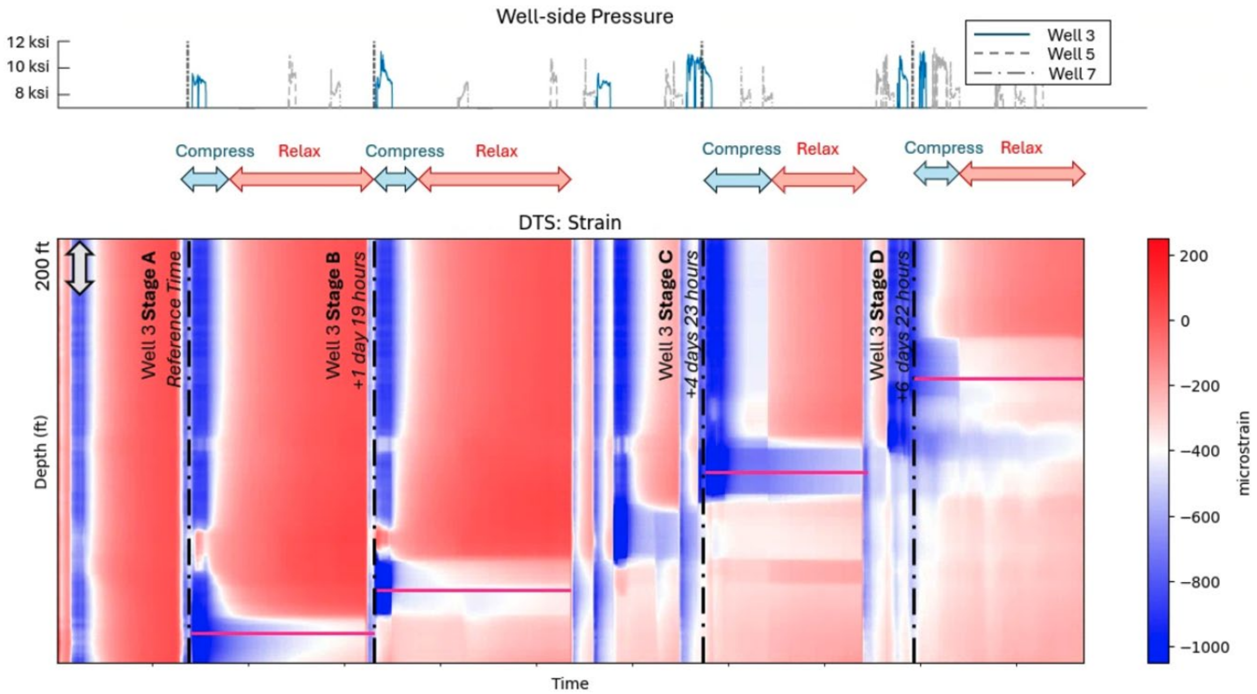

Figure 2.79 (Top) Well-side pressure distribution. (Bottom) Spatio-temporal distribution of DTS strain measurements in well 1F. Horizontal lines are plotted to indicate the upward trend of the stages, where later stages occur at progressively shallower locations in the well. Well 3 is 1F, Well 5 is 2F, Well 7 is 1H.

Once the readings are aligned with consistent spatial and temporal sampling, we assume that the temperature at the DTS fiber reflects the temperature at the DSS fiber, given their proximity. We are then able to subtract the temperature-induced strain (from DTS measurements) from strain with temperature effects (from DSS measurements) to obtain temperature-compensated strain, shown in the bottom panel of Figure 2.80. We observe the presence of strong strain signals, characterized by alternating bands of blue, compressive strains and red, tensile strains spanning approximately 150-250 ft in width. Notably, we see a clear correlation with the borehole pressure, shown in the top panel of Figure 2.80: (1) The onset of these strain signals aligns with a rapid surge in pressure; (2) the highest strain magnitudes, represented by the dark red and blue colors in the plot, persist for a duration comparable to the peak pressure; and (3) the strain magnitudes diminish as the pressure rapidly declines. By cross-referencing the operation documentation, we confirm that the time stamps indicating the initiation of operations for each stage align with the pressure increase and the appearance of the strain signals, thus confirming the identification of stages in the multi-stage hydraulic fracturing process.

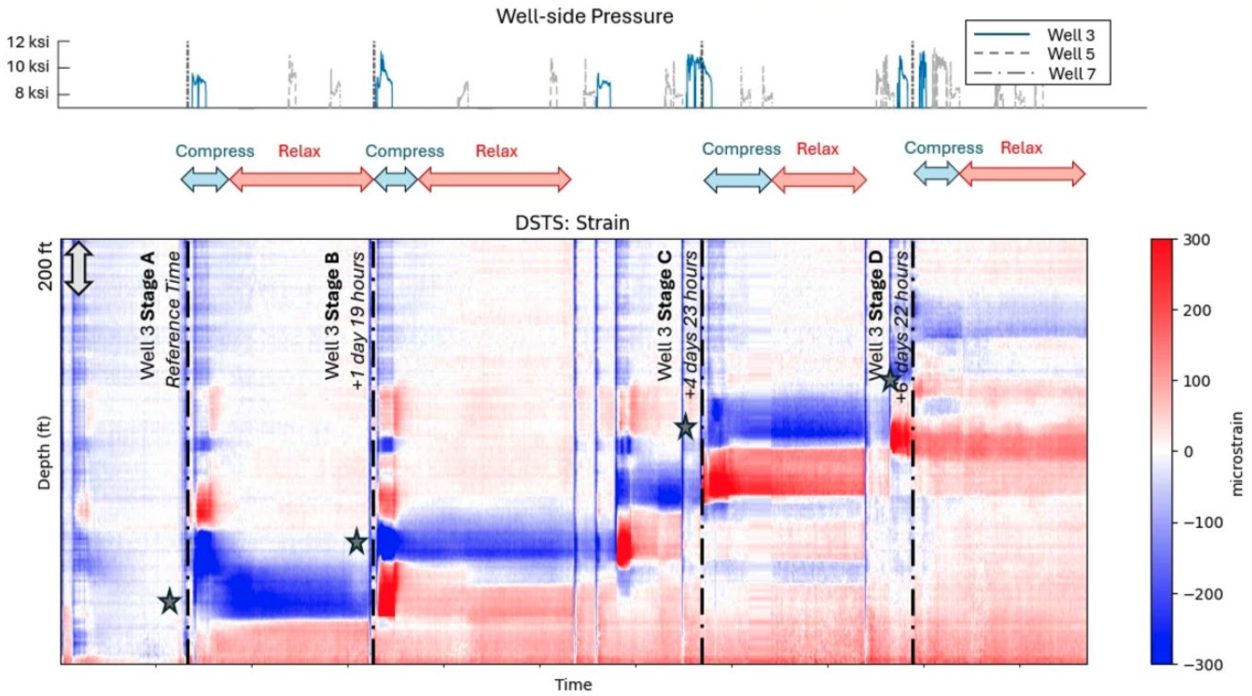

Figure 2.80 (Top) Well-side pressure distribution. (Bottom) Temperature-compensated strain after removing temperature-induced strain (DTS) from strain with temperature effects (DSS). Stars are plotted to indicate the center depth of plug and shot locations that were performed at each stage. Well 3 is 1F, Well 5 is 2F, Well 7 is 1H.

Examination of Individual Stages

We examine the spatio-temporal distribution of temperature-compensated strain for each individual stage. We identify positive, tensile strains in the fracture zones, where the opening of fractures leads to the stretching of the fiber that spans the fracture width. Negative strains are observed in the compressive reaction zones, where the fiber experiences compression due to increased pressure resulting from the injection of fracking fluid.

Stage B is illustrated as an example in Figure 2.81A, which shows distinct strain patterns within the fracture and compressive reaction zones. Figure 2.81B shows strain variations at depths corresponding to the fracture and compressive reaction zones during Stage B. Within the fracture zone, an increase of approximately 500 microstrain is observed as the fracture opens, followed by a gradual decline to approximately 56 microstrain as the fracture closes and dissipates. The compressive reaction zone exhibits an inverse trend: a rapid increase in compressive strain, peaking at approximately -790 microstrain, before gradually diminishing to around -194 microstrain. The surge and the subsequent weakening of tensile strain indicates the opening and closing of the fracture; the corresponding pattern in compressive strain indicates the injection of the fracturing fluid and dissipation of pressure.

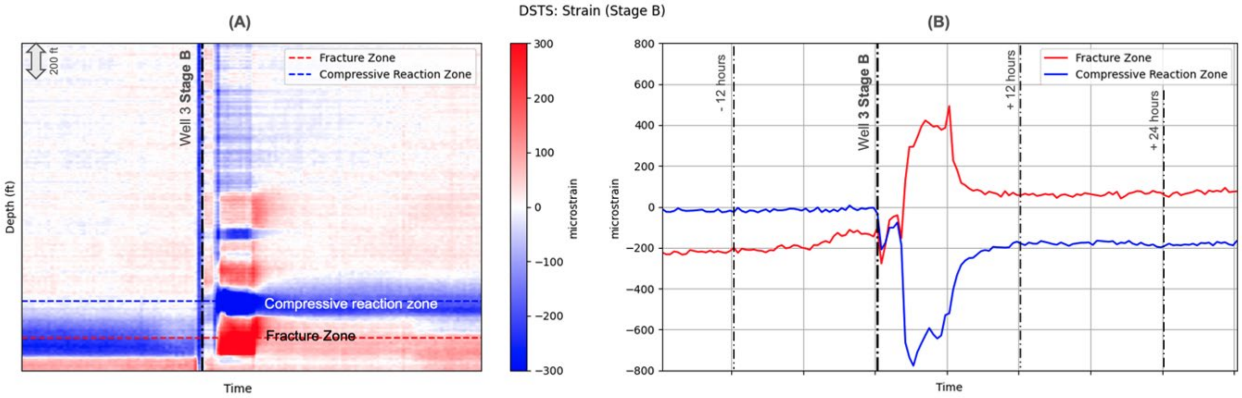

Figure 2.81 Examination of Stage B: spatio-temporal distribution of temperature-compensated strain (A) and time series of strains corresponding to fracture zone and compressive reaction zone (B). The striated strain features above the compression zone are identified as residual strains, discussed later in the report.

With these observations, we also identify residual strain features, shown in Figure 2.82. Initially, at the onset of each stage, we observe the highest levels of both tensile and compressive strains. Over time, the strength of the strain signals gradually diminishes, yet localized extrema persist. At a subsequent stage, there is sometimes a recurrence of strain signals, at a lower amplitude, spatially confined to the vicinity of the treated stage.

To investigate their origin, temperature-compensated strain data during a prior period – when the stimulation of Well 2F took place – is examined in Figure 2.82A. The stimulation of Well 2F, which is situated at a distance from Well 3, was prior to the stimulation of Well 3. During this period, a fracture generated at Well 2F can reach Well 1Fand form cross-well influence. The depths of these cross-well strain features in Figure 2.82A correspond to locations where strong strain signals were detected during Well 2F fracturing, indicated by horizontal arrows. Examining Figures 2.82A and 2.82B, arrow 1.1 points to the occurrence of a tensile strain observed in Well 1Fduring the treatment of Well 2F, which reoccurs as indicated by arrows 1.2, 1.3, and 1.4 when Well 1Ftreatment takes place. Similarly, arrows 3.1 through 3.4 point to the initial generation of the tensile strain signature during the treatment of Well 2F, followed by its reoccurrence during the treatment of Well 3. The tensile strains indicated by arrows 4.1 and 4.2 reoccur as compressive strains, indicated by arrows 4.3 and 4.4. The tensile strain indicated by arrow 5.1 switches to compressive strain (arrow 5.2) and reverts back to tensile strain (arrow 5.3). The alignment of cross-well strain in Figure 2.82A and in-well strain in Figure 2.74B – where the features occur at the same locations at multiple times throughout the study period – demonstrate that cross-well results can aid the interpretation of in-well dynamics.

These observations align with the findings of Karrenbach et al. (2019), who reported similar phenomena in a treatment well instrumented with DAS: with the rise in borehole pressure, the strain signal was localized at the stage location and then diminished further away from the stage. In contrast to the strong, localized strain signatures generated when the treatment of each stage is implemented, smaller magnitude strain signals occurred at multiple instances over time. They were interpreted as residual strain signals and used to interpret the generation of microseismic events.

Given that these residual strains can extend into future stages, the potential for fracture reconnection and the creation of multiple pathways for subsequent fractures may be considered. Similar interpretations were made by Leggett et al. (2023) who conducted an analysis of LF-DAS measurements collected from the same field laboratory and interpreted such strain features as indicators of fracture fluid communication with prior stages, with can lead to re-stimulation and reopening of previously stimulated fractures.

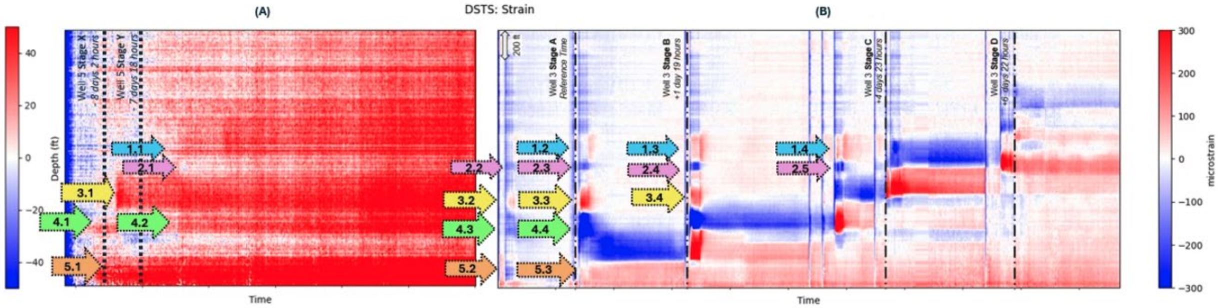

Figure 2.82 Examination of cross-well DSTS strains observed in a prior period, where Well 2F operations occurred (A) help the interpretation of horizontal striations observed in the in-well DSTS strains during the ten-day period when Well 1Fwas fractured (B). Arrows indicate the locations of residual strains. The blue arrows are labeled 1.1 – 1.4, pink arrows 2.1 – 2.5, yellow arrows 3.1-3.4, green arrows 4.1-4.4, and orange arrows 5.1-5.3 to aid the interpretation of the residual strain features.

Fracture Width Estimation

The temperature-compensated strain may also be further analyzed to analyze the fractures created at each stage. By computing the average strain within the fracture zone and its corresponding width for each stage, we can multiply these values to obtain an estimate of the fracture width. The resulting fracture width time series (Figure 2.83) reveals nonlinear patterns, with dotted circles indicating the nonlinear increase and decrease in fracture width during the stage operations. This suggests that the injection of fracturing fluid induces strain and propagates fractures at the target depth. The fluid entering the fractures generates stress on the surrounding rock, causing an increase in strain and fracture width. As the fractures grow and expand, stress and strain are released, resulting in a decrease in strain and ultimately a decrease in fracture width. This consistent nonlinear pattern is observed for Stages A, B, C, and D.

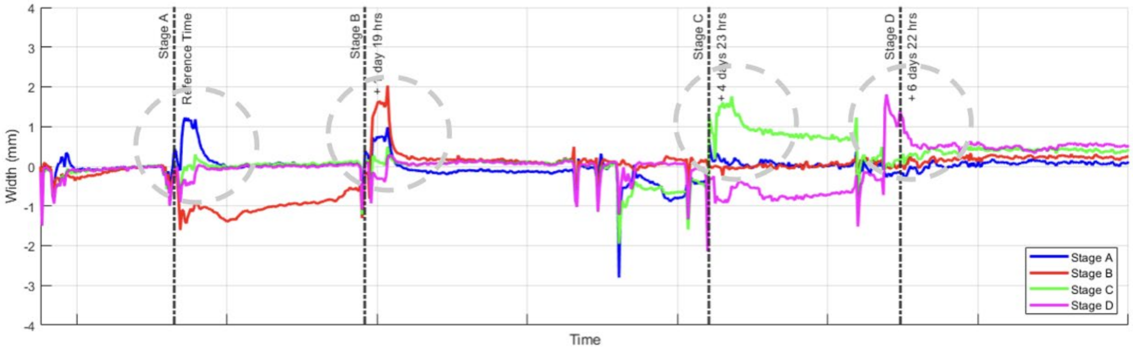

Figure 2.83 Fracture width time series, obtained by multiplying the average strain within the fracture zone and its corresponding width for each stage. Dotted circles indicate the nonlinear increase and decrease in fracture width during the stage operations.

These fracture width estimates, such as the maximum fracture width at each stage (Figure 2.84), can be used as performance metrics that can be used by the operator to track and evaluate their fracking performance. Future research may involve the optimization of operational parameters such as well-spacing, stage height, volume of injection fluids and proppants, for which estimates from distributed strain and temperature sensing such as maximum fracture widths may be used as an evaluation metric (Figure 2.85).

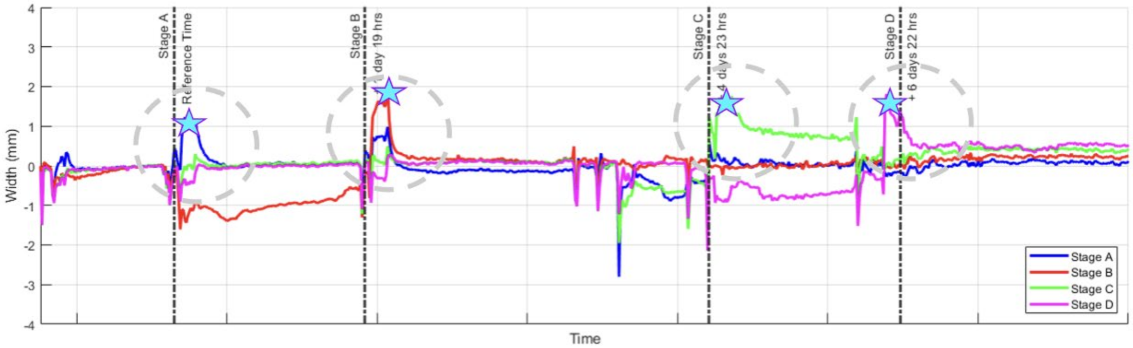

Figure 2.84 Maximum fracture width obtained at each stage, indicated with a star

Table 2.7 Maximum fracture width estimated for each stage

Stage	**A**	**B**	**C**	**D**
Maximum Fracture Width (mm)	1.23	2.03	1.76	1.81

3. Distributed Temperature Sensing (DTS) and Distributed Acoustic Sensing (DAS) for Fracture Diagnosis

Summary

We have been working on the examination of downhole monitoring using DTS/DAS fiber optic cables for Wells 1F and 2F. Interpretation was conducted with the models developed for fluid distribution. The injection rate for each cluster is estimated by each of the DTS and DAS interpretation methods and compared. The injected fluid volume distribution can be efficiently obtained by a novel approach of DTS interpretation based on the Péclet number theory. The coefficient of the linear acoustic equation is estimated from the single cluster stage and used for the DAS interpretation method for estimating fluid volume distribution. The uniformity of injected fluid volume distribution is compared with several completion parameters such as injection rate, injected fluid loading, and proppant loading. The statistical analysis illustrates that high injection rate would be one of the primary design parameters to maximize the fracture stimulation performance.

3.1 Approach

Methodology of DTS Interpretation

The fluid allocation can be estimated by performing a temperature history match with DTS data using a thermal simulator as a forward model. In this study, the two-phase thermal model presented by Yoshida et al. (2018) is used for the DTS interpretation. It consists of a 3D reservoir thermal model and a 1D wellbore thermal model. Each domain has distinct governing equations for fluid flow and energy transport. To efficiently perform a temperature history match, a type curve approach based on Péclet number theory presented by App (2022) is implemented. The Péclet number method does not require any numerical minimization algorithms but finds the solution from generated type curves which represent a relationship between the Péclet number and sandface temperature.

Using a single fracture case shown in Figure 3.1(a), we investigate how the sandface temperature during warm back is related to the injection rate during fracture stimulation. A series of forward simulations are run for generating the type curve with changing injection rate from 0.1 to 10 bbl/min. In each run, temperature is simulated from injection to warm-back continuously, and the sandface temperature at the fracture location at three hours after shut-in is calculated. Figure 3.1(b) shows the procedure of the type curve generation based on the Péclet number theory. We can observe that the sandface temperature is proportional to the injection rate which determines the Péclet number. When the injection rate is high, the temperature warms back more slowly since the convective heat transfer is more significant. When we have observed data, the polynomial curve fitting with the unique type curve determines the injection rate.

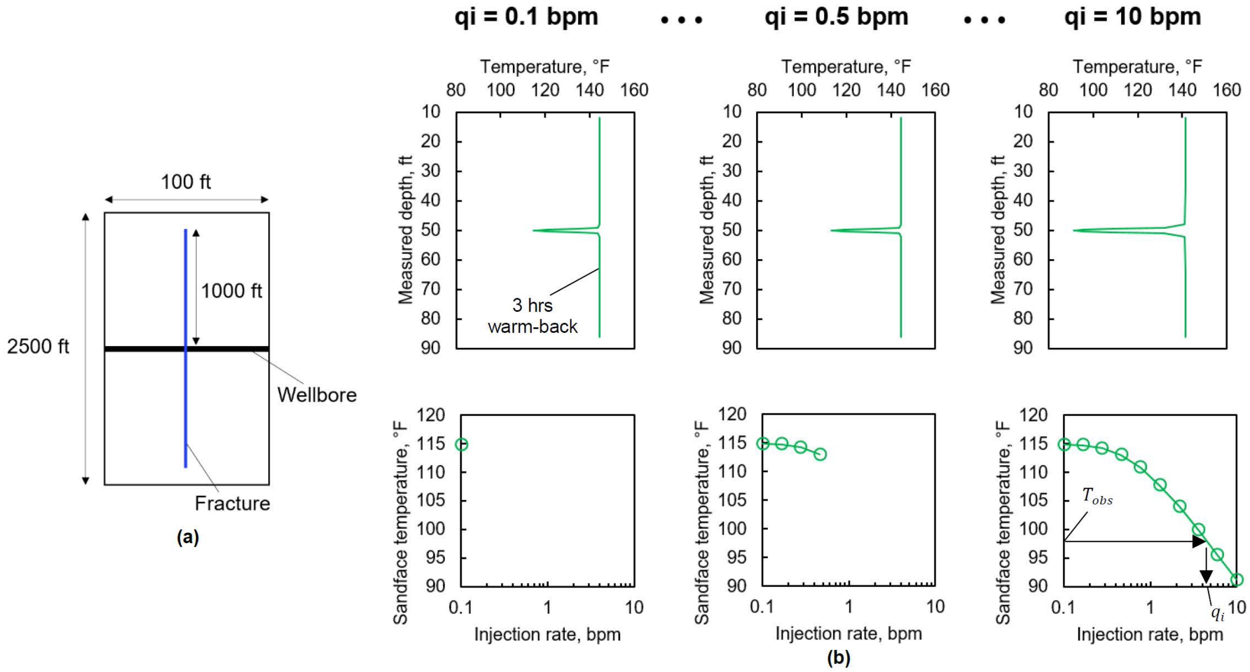

Figure 3.1 Single fracture case demonstrating the Péclet number method: (a) Geometry of single fracture; (b) Procedure of type curve generation based on the Péclet number theory.

Methodology of DAS Interpretation

Pakhotina et al. (2020) showed the workflow of DAS interpretation method based on the linear acoustic equation. This interpretation method estimates the fluid-flow rate for the clusters over time based on the DAS signal and can calculate the subsequent cumulative fluid distribution. The relationship between the fluid-flow rate through a perforation and the sound it generates is estimated based on laboratory experiments and numerical simulations (Chen et al. 2015, Pakhotina et al. 2020). Both clearly show linear correlations between the log of the flow rate and the measured or calculated sound pressure level (Figure 3.2). We calibrate the coefficient of the linear equation with the single cluster stage and calculate the fluid distribution for multi-cluster stages.

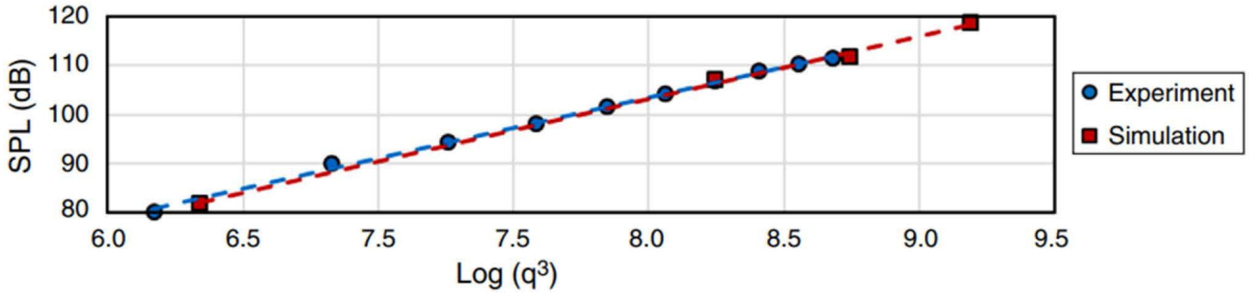

Figure 3.2 Correlation between flow rate and sound pressure level (SPL) (Pakhotina et al. 2020)

3.2 Results and Discussion

DTS Interpretation Result

Stage 17 of Well 1F fracture treatment is selected as an example to show the interpretation workflows and demonstrate the integration of them to diagnose the fracture treatments. In general, a cool-down event is observed in temperature profile along a lateral during fracturing treatment due to fluid injection with high flow rate. A good agreement between the measured and simulated temperature profiles after the stage interval was shut in provides the injected fluid volume for each fracture as shown in Figure 3.3.

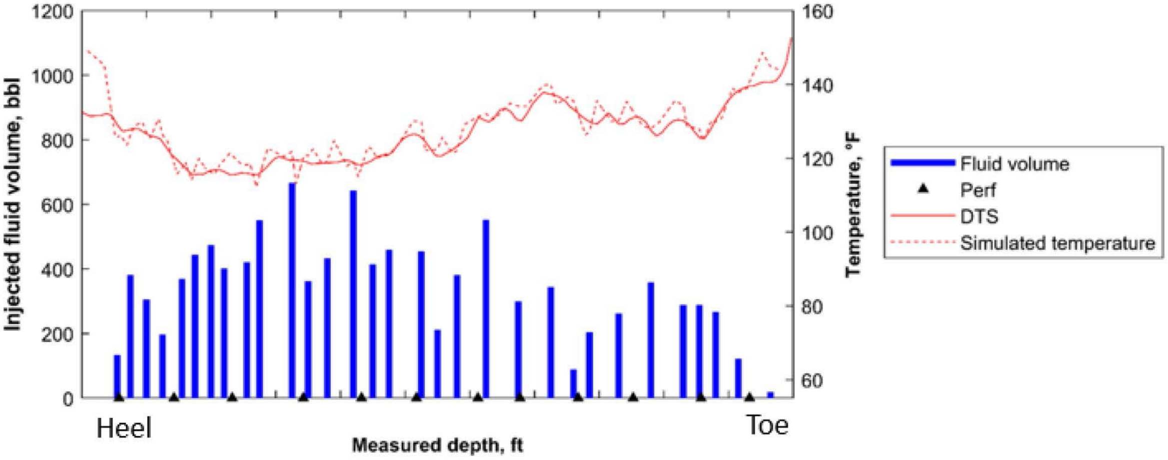

Figure 3.3 Estimated injected fluid volume distribution for Stage 17 with matched temperature at 6 hours after shut-in.

Using the matched temperature profile during the warm-back after the Stage 17 treatment as an initial condition, the temperature is matched with the DTS data along the Stage 17 interval during the Stage 18 and Stage 21 treatments by performing the Péclet number method. The matched temperature profiles at 3 hours warm-back after the Stage 18 and Stage 21 treatments are shown in Figure 3.4(a) and (b), respectively.

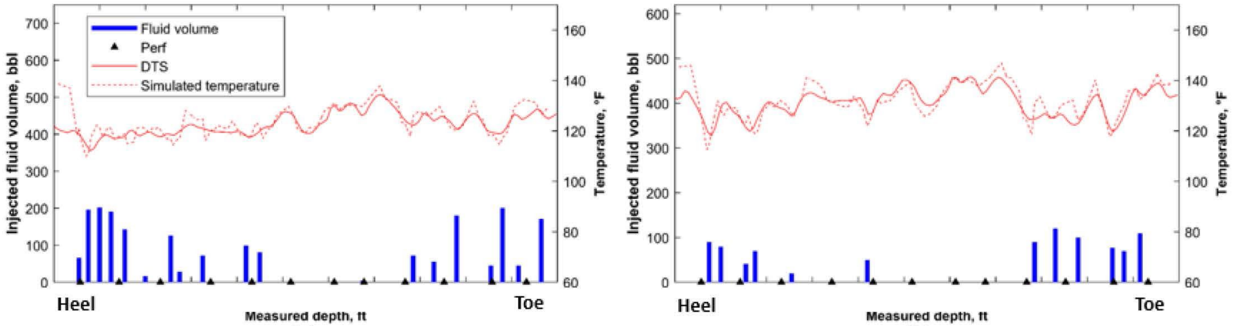

(a)

(b)

Figure 3.4 Estimated injected fluid volume distribution along Stage 17 interval: (a) During Stage 18 treatment; (b) During Stage 21 treatment.

DTS/DAS waterfall plots were used to evaluate if a stage is properly isolated from prior stages during treatment. Based on the qualitative interpretation of DTS and DAS, leakage is confirmed at Stage 17 during the Stage 18 and Stage 21 treatments. As Figure 4 shows, the lower injected fluid volume during the Stage 18 and 21 treatments is due to the leakage.

DAS Interpretation Result

DAS signals during Stage 17, 18 and 21 fracturing treatments are interpreted following the methodology based on the linear acoustic equation. The calculated fluid allocations for Stage 17 clusters during each stimulation are shown in Figure 3.5.

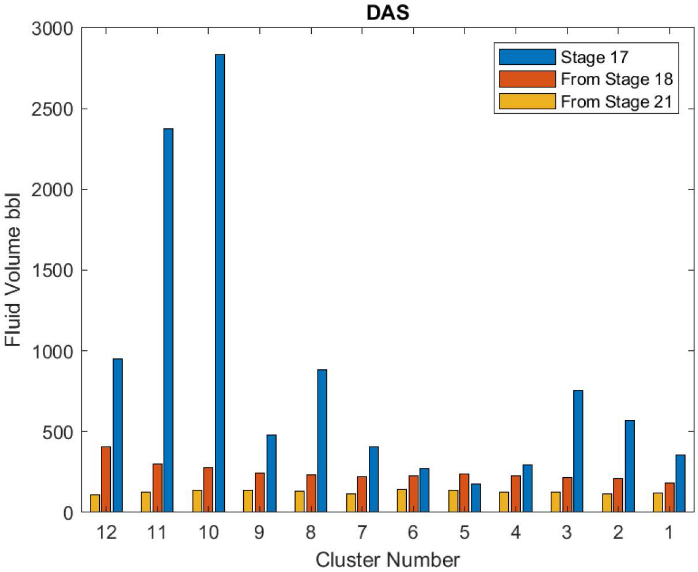

Figure 3.5 Estimated fluid injection volume for Stage 17 clusters during Stage 17, 18 and 21 treatments

The fluid allocations from Stage 18 and 21 fracturing treatments show that all clusters had almost equal amount of fluid volumes. The clusters have less flow rate because of the leakage and the DAS signal is weak. Therefore, the importance of fluid containment and distribution needs to be incorporated into the DAS and DTS interpretation to evaluate the performance and design impact of each stage interval.

Evaluation of Completion Design

The fluid allocation was calculated by using the DTS interpretation method for all the 25 stages which have fiber data in Well 1F. The DTS based injected fluid volume distribution is estimated by the Péclet number method. This calculation considers plug leakage. The stimulation design is evaluated by using the concept of uniformity index of fluid distribution, defined as 1 minus the ratio of the standard deviation of a cluster volume to the mean cluster volume (Sakaida et al., 2023). The uniformity of the fluid distribution is calculated for all the stages and compared with the completion parameters, including rate per cluster, fluid loading, and proppant loading (Figure 3.6).

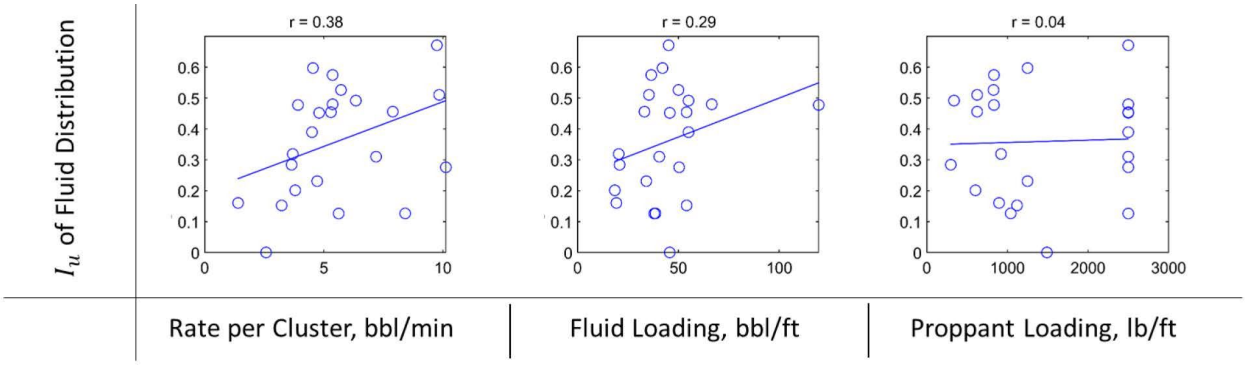

Figure 3.6 Correlation between completion designs and uniformity of fluid distribution and total eroded area of perforations

The results show that the rate per cluster and fluid loading have positive correlations with the uniformity of the fluid distribution. Therefore, higher flow rate and larger amount of fluid injection could be the primary contributing factors to create uniform fluid distribution. A larger sample base is needed to make a stronger conclusion about the optimal fracturing design.

4. Experimental Investigation of Monitoring Fracturing Geometry with Low-Frequency DAS

Summary

Low-frequency distributed acoustic sensing (LF-DAS) exploits the optical phase shift of Rayleigh backscatter in fiber-optic cables to obtain distributed measurements of changes in strain. LF-DAS in an untreated well provides far-field strain measurements while treatment wells are hydraulically fractured. Such a configuration is called cross-well LF-DAS sensing. Cross-well LF-DAS measurements have proved useful in diagnosing fracture hits, fracture azimuth, planarity, cluster efficiency, fracture propagation rates, and the dynamic distance to the fracture front. In the Austin Chalk Eagle Ford Field Laboratory project, we used fiber-optic cables for cross-well LF-DAS to measure changes in strain-rate along the monitor well during fracturing treatment. Two new approaches were proposed to estimate the evolving locations of the fronts of propagating fractures from cross-well LF-DAS data. First, we developed a rapid model, the “Zero Strain Location Method”, to efficiently interpret the data generated by LF-DAS. It provides an analytical means of estimating the dynamic location of the fracture front nearest the fiber-instrumented monitor well. The second method involves solving the inverse problem using a semi-analytical model for an elliptical fracture as a forward model. Lab-scale hydraulic fracture experiments with embedded optical strain sensors were also conducted to understand the response of LF-DAS to fracture propagation.

In contrast, in-well LF-DAS is conducted on the actively fractured well. Due to cool fracture fluid being injected at high injection rates, the strain component of the LF-DAS response may be obscured by temperature changes. In permanent fiber-optic cable installations, distributed temperature sensing (DTS) is often conducted simultaneously with LF-DAS. In the Austin Chalk Eagle Ford Field Laboratory project, we developed a method to estimate the in-well strain profile during multistage hydraulic fracture completions. We applied this method to decouple the temperature and strain components of LF-DAS sensors to observe strain changes on in-well LF-

DAS and locate the fracture initiation points within the actively treated region along the fractured well.

4.1 Approach

Lab-Scale Hydraulic Fracture Experiments

Transparent epoxy blocks were used to visualize fractures induced by dyed water injection. The strain response was recorded using fiber Bragg grating sensors and compared with Sneddon's solution for a penny-shaped crack. A method to estimate fracture geometry from fiber-optic strain data was developed and validated against experimental results. Figure 4.1 shows a schematic of the laboratory-scale hydraulic fracture experiment. This setup mimics a field condition with a treatment well (injection tubing in the experiment) and an observation well with fiber-optic sensors installed along with it (the fiber cable in the experiment).

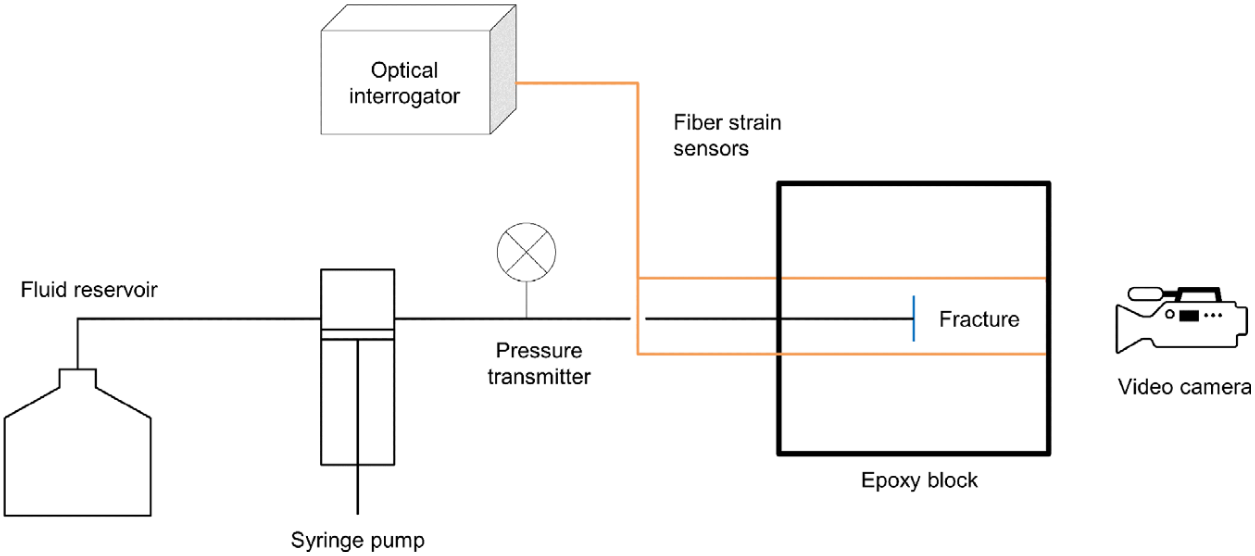

Figure 4.1 Schematic representation of the laboratory-scale hydraulic fracture experiment

Cross-Well LF-DAS

The first new method, “The Zero Strain Rate Location Method”, approximates the shape of the fracture front as an arc. Curve fits reduce Sneddon’s classic solution for a radial fracture to a simple quadratic equation. This equation predicts the location of the fracture front nearest the fiber from the transition from extending to compressing regions observed in LF-DAS data. The model domain adapted to consider a fiber instrumented monitor well is illustrated in Figure 4.2. The wells are parallel, and the modeled fracture is transverse. The nearest distance from the monitor well to the fracture front, d_f, lies on the hypotenuse of the triangle with legs consisting of the vertical and lateral offsets. The location of zero strain, z_0, has a one-to-one correspondence to fracture radius for a radial fracture (Leggett et al. 2022). The location of zero strain is extracted from the outline of the converging pattern on LF-DAS waterfall plots.

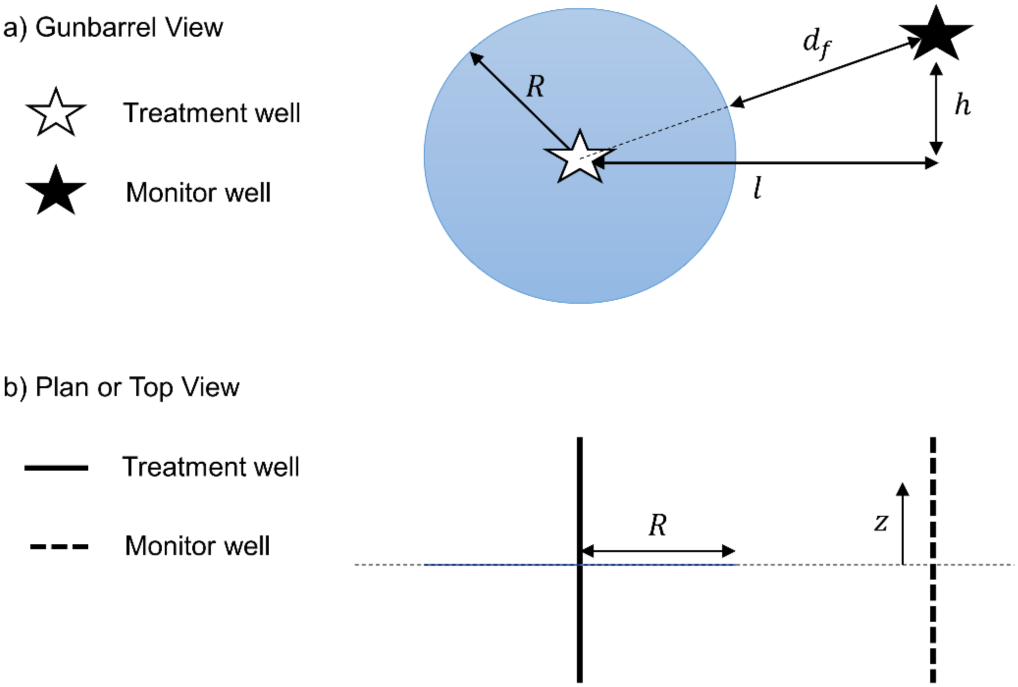

Figure 4.2 Domain of the radial fracture model for strain on the fiber.

In the second method, we used numerical inversion for fracture properties with an elliptical crack forward model. LF-DAS data is matched by solving the inverse problem. The forward model computes far-field strains due to an elliptical hydraulic fracture. Fracture and geomechanical parameters are optimized to best fit the observed LF-DAS signal via the modified Levenberg-Marquardt algorithm. The fracture is not constrained to be centered at the treatment well. Figure 4.3 illustrates the domain of the elliptical crack model adapted to consider a monitor well. The gunbarrel view in Figure 4.3a shows an elliptical fracture that is not necessarily centered at the treatment well. The closest distance from an elliptical fracture to the monitor well, d_f, is more complex to compute compared to a radial fracture. d_f lies on a line perpendicular to the tangent of the nearest point of the ellipse to the monitor well.

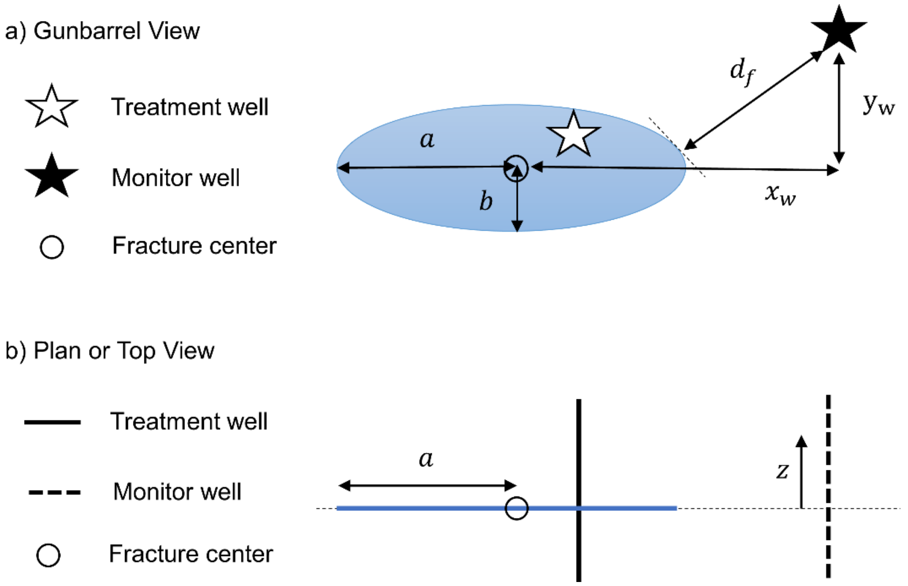

Figure 4.3 Domain of the elliptical crack model for estimating strain along the monitor fiber.

Solving the inverse problem consists of finding the optimal values for input parameters that minimize residual error between the model output and measurements. LF-DAS provides measurements proportional to the far field strain rate during offset hydraulic fracturing operations. The data can be integrated over time to obtain data proportional to strain along the fiber. Inversion is conducted via the modified Levenberg-Marquardt method. This method interpolates between Gauss-Newton and gradient descent methods to minimize the residual function by changing model inputs. A penalty function serves to constrain matched parameters within justifiable intervals.

In-Well LF-DAS

The LF-DAS response is modeled as linearly dependent on strain and temperature changes. Theoretical LF-DAS temperature and strain sensitivity coefficients are derived based on the changes to the index of refraction and length of the fiber. Using the DTS measurements, temperature changes are computed, smoothed, filtered, and compared to the LF-DAS response. Crossplots of the in-well LF-DAS measurements and temperature changes from DTS measurements far from the actively fractured region are used to validate the theoretical sensitivity coefficients. Uncertainty in the temperature component of the LF-DAS response is quantified.

Along the wellbore, there is a clear correspondence between the LF-DAS and DTS derivative measurements. Far from the interval being hydraulically fractured, the induced strain on the fiber is negligible compared to temperature changes induced by injecting cool fracture fluid at high rates. Figure 4.4(a) consists of a crossplot of the corresponding LF-DAS and DTS derivative measurements in an interval far from the fracture stage. Figure 4.4(b) displays a histogram of error between measured values and the best-fit line. We used the measured slope to convert changes in temperature to changes in the LF-DAS measurement.

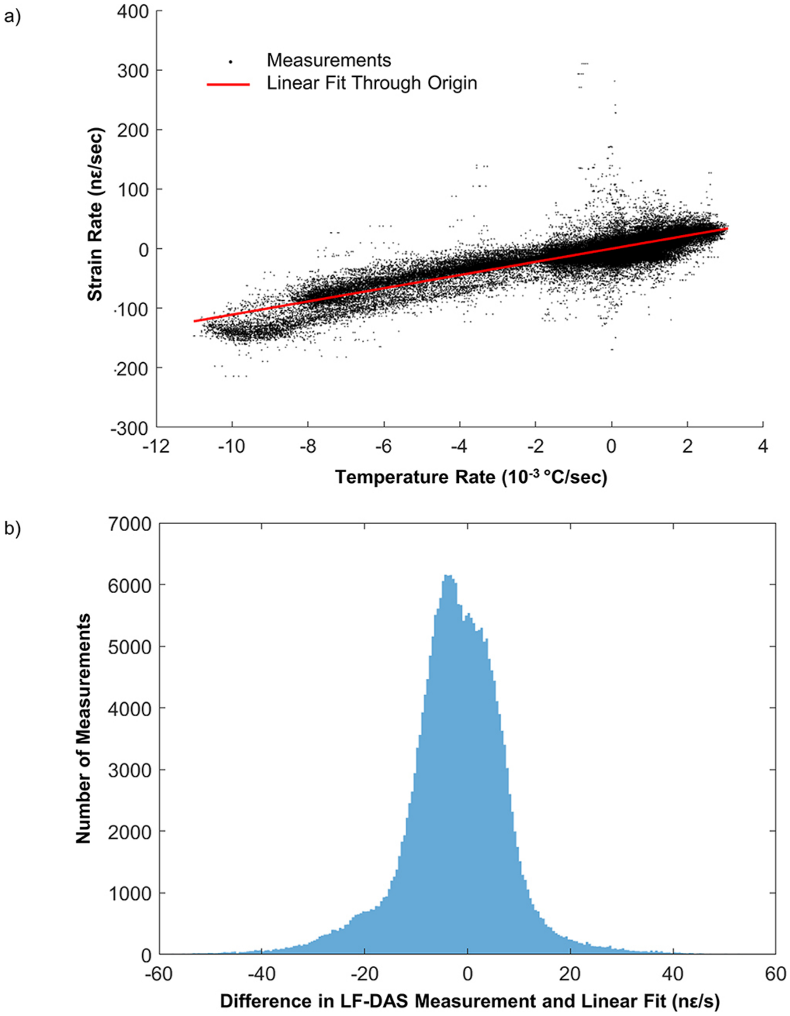

Figure 4.4 Determination of uncertainty in DTS derivative on LF-DAS measurements by (a) crossplotting the LF-DAS measurement and DTS derivative with a best-fit line through the origin and (b) plotting a histogram of the difference between the best-fit and measured values.

4.2 Results and Discussion

Results of Fracture Experiments

Multiple fracture experiments under different conditions were performed in a laboratory setting with an 8-inch cube of epoxy and embedded high-definition fiber optic cables. In the first experiment, dyed water was injected to create a radial hydraulic fracture, confirming the characteristic strain-rate pattern observed in LF-DAS data when the fracture intersects fiber cables. The study highlighted the need for adequate spatial resolution to accurately determine the timing of fracture hits.

In the second experiment, LF-DAS response to fractures under shear and normal stresses was explored. It revealed an asymmetrical strain response over the fracture plane, emphasizing the influence of shear stress. Additionally, the zero-strain location method effectively predicted fracture radius and distance to the front.

The third experiment focused on LF-DAS response to two parallel propagating fractures. It showed strain responses to both fractures, with the lower fracture receiving more fluid. Interestingly, while the upper fracture initiated first, the lower one grew significantly larger. Both fractures intersected the fibers, confirming strain signatures as multiple fractures approach. The zero-strain-rate method effectively estimated fracture propagation dynamics, aligning well with recorded fracture dimensions.

Results of Cross-Well LF-DAS

The results indicate that the strain can be rapidly matched by varying a minimal number of parameters: Poisson’s ratio, fracture extent (radius or major and minor elliptical axes), and the coordinates of the fracture center. Normalizing the LF-DAS data ensures the match is independent of net fracture pressure or Young’s Modulus. Representative fracture growth rates are computed from multiple field cases, including during a unique single-point entry fracture stage conducted recently. These rapid, analytical models have the potential to dynamically estimate the location of the fracture front in real time from LF-DAS measurements.

In the Austin Chalk Eagle Ford Field Laboratory project, The Zero Strain Rate Location Method was applied to LF-DAS data acquired during hydraulic fracture completions. The first 10 stages were analyzed to interpret the number of frac hits, their timing, and instantaneous fracture propagation rates. Figure 4.5 shows a waterfall plot from a stage with 5 interpreted fracture hits. Frac hits were determined based on the presence of the characteristic converging region of positive strain rate (tension positive). The interpreted frac hits are outlined in black. The first arrival is toe-ward and the final arrival is heel-ward relative to both the monitor and treatment well. The zero strain rate locations were determined by digital image analysis, selecting the location of the white boundary between the red and the blue.

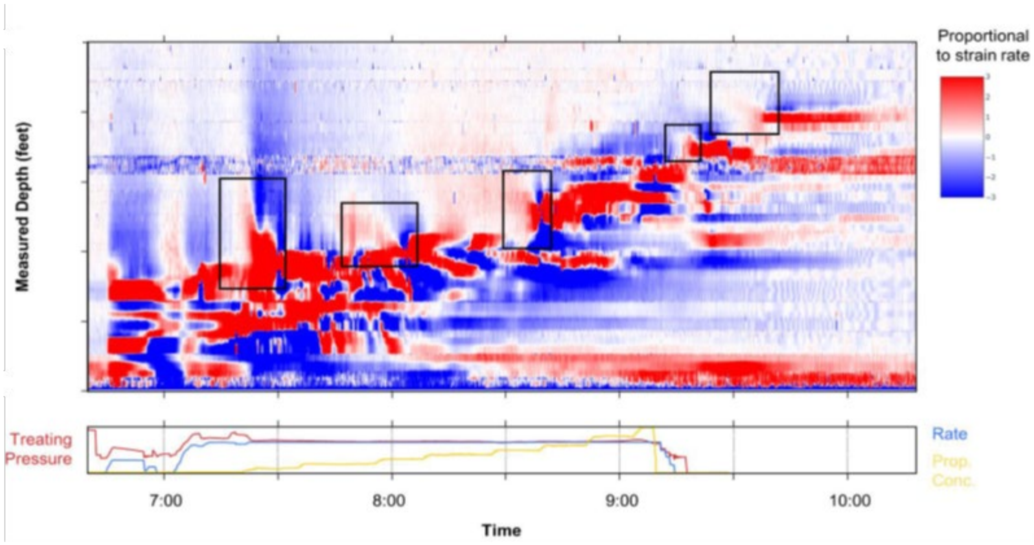

Figure 4.5 Waterfall plot with 5 frac hits exhibiting the characteristic cone-shaped convergence of the strain rate pattern

13 frac hits were clearly identified in the first 10 stages and analyzed. The z locations of zero strain were used to estimate the distance to the fracture front and fracture propagation rates. The fracture propagation rates associated with the waterfall plot in Figure 4.6 are presented in dimensionless form in Figure 4.6. The normalized fracture propagations rates are cross plotted against various completion parameters in Figure 4.7.

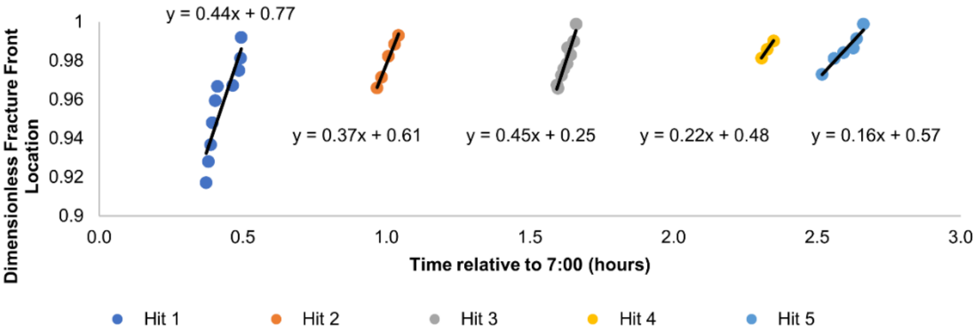

Figure 4.6 Interpreted dynamics dimensionless locations of the fracture front.

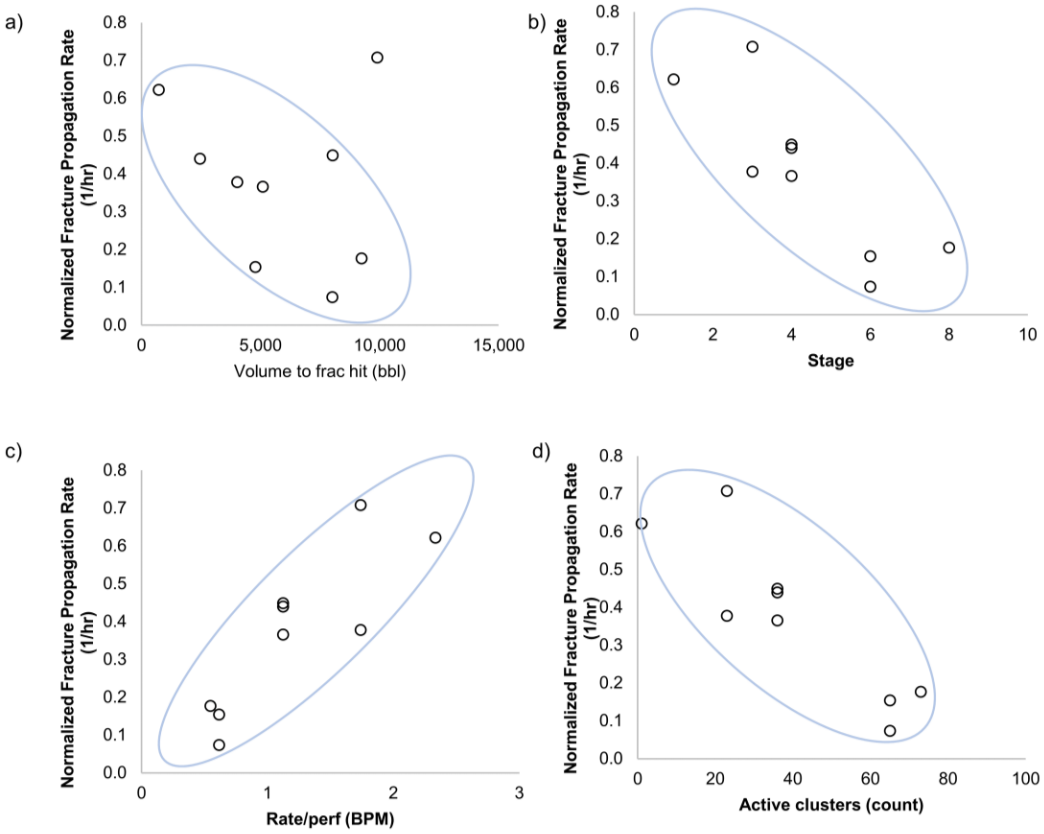

Figure 4.7 Cross plots comparing fracture propagation rates to a) the volume injected when the frac hit occurred, b) the Stage number, c) the normalized rate based on the average injection rate per perf and d) the number of clusters observed taking fluid from DTS measurements on the treatment well.

Figure 4.7(a) shows an inverse relationship between fracture propagation rate and the volume injected at the time of the frac hit. As would be expected, faster instantaneous fracture propagation rates result in a quicker arrival of the fracture at the monitor well. Figure 4.7(b) plots the fracture propagation rate against the stage number. Due to the cross-stage communication, the higher the stage number, the more clusters were available to receive flow. There were therefore lower injection rates per cluster and per perforation as the stage number increased. Figure 4.7(c) and Figure 4.7(d) highlight the correlation of instantaneous fracture propagation rate with the average flow rate per cluster. Low instantaneous fracture propagation rates can be used as a proxy for prior stage communication. Conversely, a rapid fracture propagation rate may indicate a runaway fracture and low uniformity of cluster efficiency.

Results of In-Well LF-DAS

Collocated DTS and in-well LF-DAS measurements can be used to obtain a temperature-compensated strain profile during and at the end of hydraulic fracture stages. We expected to see peaks in the measured strain along the in-well fiber at the end of each fracture stage corresponding to locations of fracture initiation. The opening of fractures should stretch the fiber that spans the gap of the fracture width. Figure 4.8 shows the strain profile along the fiber at the end of a single stage in relation to the cluster locations. The strain peaks correspond to locations along the wellbore where one or more fractures are initiated. The DTS-measured temperature 3 hours after the end of the stage is also plotted. In general, peaks in the strain response correspond to cool regions of the wellbore. Areas where fractures receive significant fluid should warm more slowly than other areas.

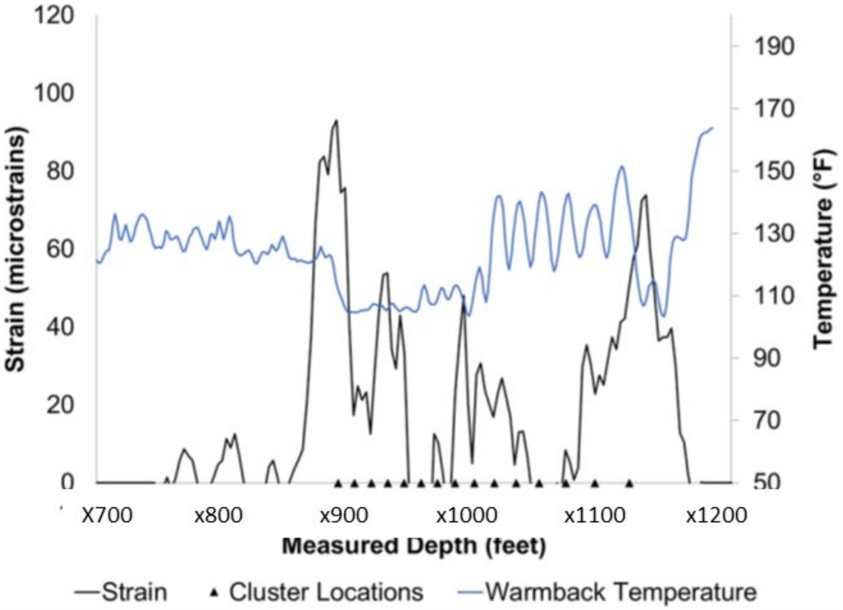

Figure 4.8 Filtered, in-well LF-DAS strain at the end of a single fracture stage compared to cluster locations and warmback temperature.

One of the largest strain peaks in this stage occurs at x1,126 ft, near the lowest recorded temperature at x1,146 ft. However, there are tensile strains estimated between x770 and x840 ft, which is 120 ft heel-ward from the nearest perforation. These relatively minor peaks in strain do not correspond to a relatively cool region of the wellbore. Similar behavior was observed in eight of the ten stages analyzed. In some cases, tensile strains were observed hundreds of feet heel-ward of the perforated stage interval. These results suggest that fracture initiation may regularly occur heel-ward of the actively treated stages. In each stage with these types of fractures, warmback occurred relatively quickly heel-ward of the stage interval. This implies that these fractures do not receive a significant amount of injected fluid.

Additionally, we used the strain estimates to evaluate the effectiveness of different completion designs used along the treatment wellbore. In the Austin Chalk Eagle Ford Field Laboratory project, completion designs varied along the lateral. For the stage shown in Figure 14, 75% of the stage interval registered tensile strains. The percentage of a stage interval with tensile strain can serve as a stimulation efficiency metric to evaluate stimulation designs. Figure 4.9 highlights a section of one well where three different stimulation designs were used. Proppant and fluid loading, perforation design, stage length, and cluster spacing varied between the different designs. The summation of the strain profiles at the end of each of these 10 stages indicates some intervals not under tensile strain. We interpret intervals without tensile strain to lack transverse fractures and therefore as unstimulated. Figure 4.10 summarizes how, on average, the stimulated portion of the stage interval differed depending on which design was used. The sample size is too small to make any definite conclusions about the effectiveness of each completion design. However, this approach may prove useful to judge the effectiveness of different completion designs along a single lateral.

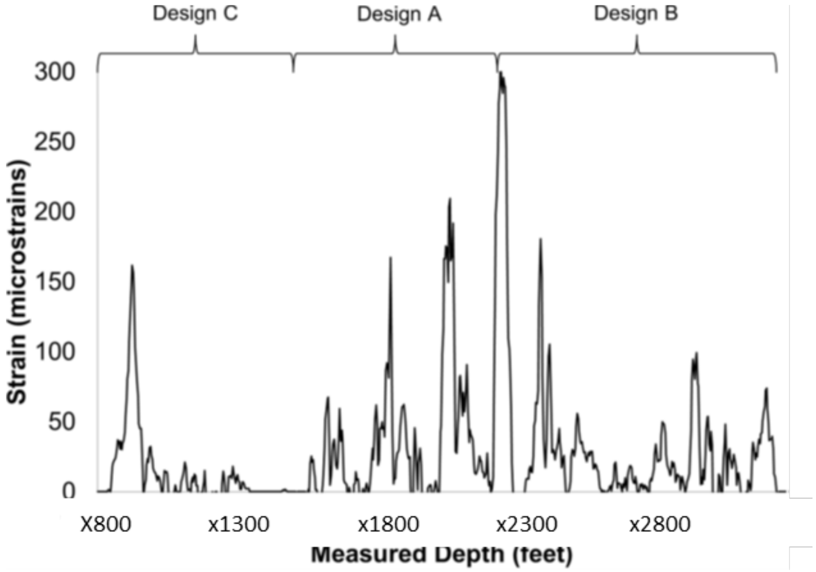

Figure 4.9 The percentage of the stage interval that registers a positive strain can serve as a standard to judge the effectiveness of different completion designs

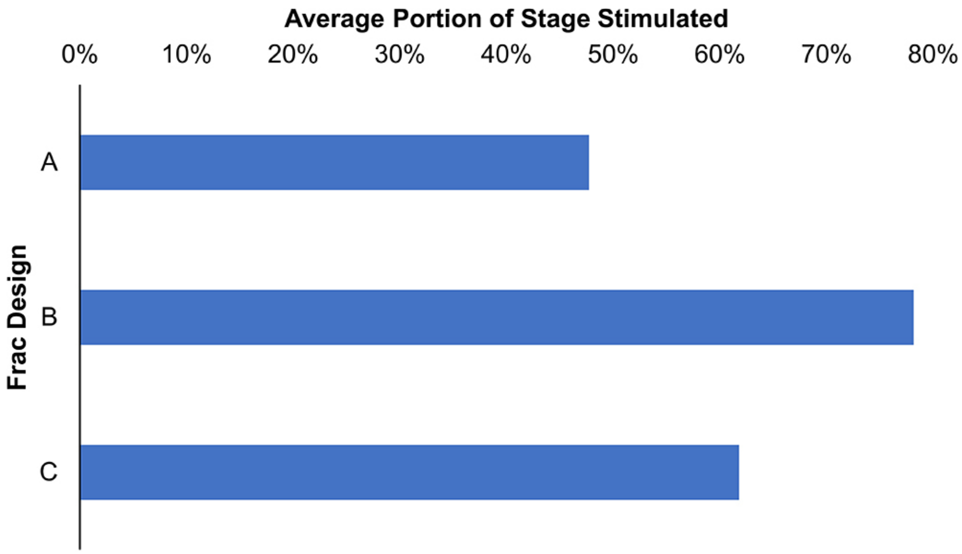

Figure 4.10 Comparison of stimulated stage interval percentages to evaluate the effectiveness of different completion designs

5. Post-Stimulation and Production Monitoring

Summary

Following the stimulation, all six wells are drilled out to commence the production phase. Production logging was conducted in one of the wells in the southern pad. The log data is available along only six stage intervals due to a measurement issue. Temperature log shows clear cooling events at some perforation cluster locations. They represent gas entry since the Joule-Thomson cooling effect occurs due to gas expansion around a wellbore. The degree of temperature drop indicates the amount of gas produced at the cluster location. Therefore, we can qualitatively evaluate the performance of stimulated stages. The team developed two methods to interpret the inflow profile in a multi-phase flow well based on production log and temperature log data.

5.1 Approach

Interpretation Method of Multiple-Sensor Array Tool

To assess the downhole flow conditions more accurately, multiple probe tools and arrayed spinner flowmeters are used to measure the phase holdup and local fluid velocity along the well. As shown in Figure 5.1, the cross-sectional area of the wellbore is divided into five segments.

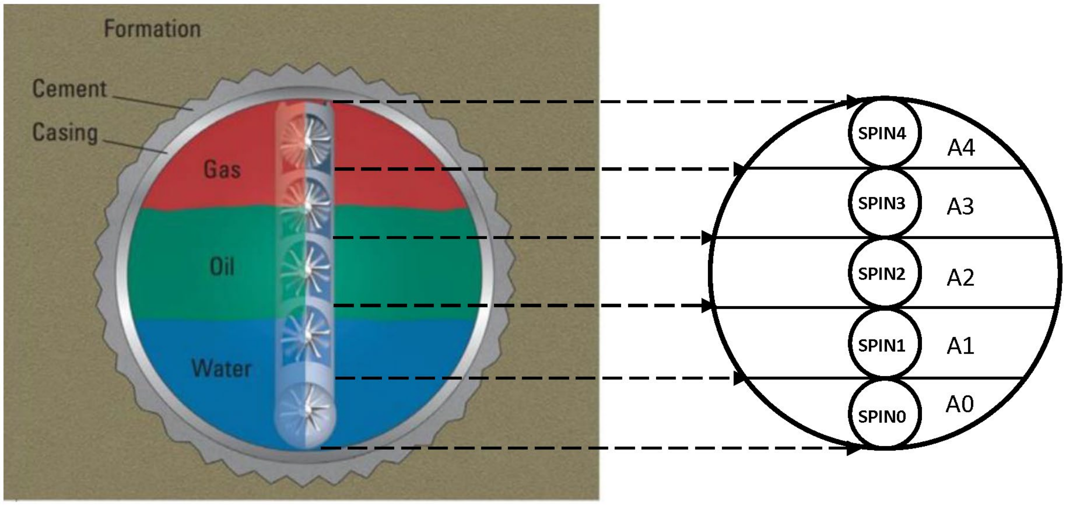

Figure 5.1 Arrayed mini spinner configuration

In each segment, we interpreted the local velocity from the array spinner flowmeter response for each phase. The phase distribution of gas, oil, and water within each wellbore segment along the well is assigned based on the phase holdup values obtained from the optical and electrical probes in the multiple-sensor array tool. Starting from the heel-most station that is the closest to the surface, we calculated the total flow rate for each phase. Then, a number of interpretation stations along the well were chosen to repeat the calculation and compute the complete inflow profile for three phases.

Interpretation Method of Temperature Log

Temperature log interpretation also provides the inflow profile along the well based on the cooling anomalies. Figure 5.2 shows the geothermal temperature and temperature profile during production acquired by the logging tool. The amount of temperature drop caused by Joule-Thomson cooling at the cool locations is related to the amount of gas produced at each location.

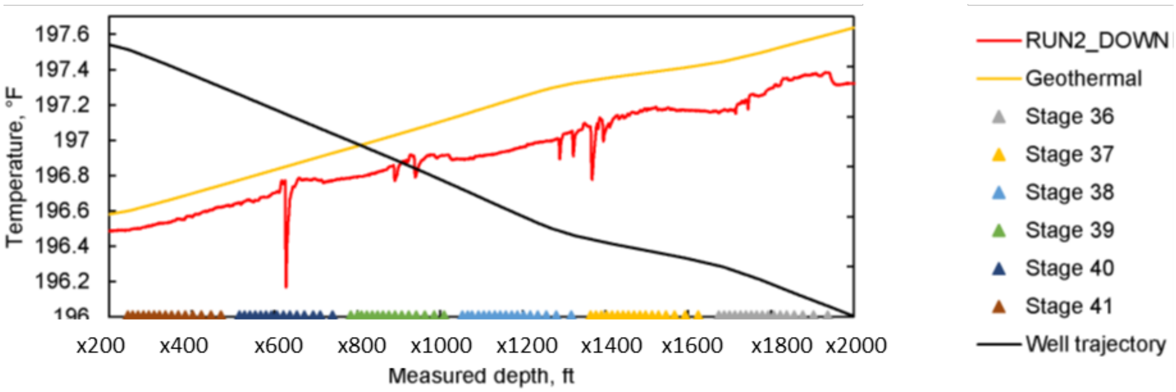

Figure 5.2 Temperature log during production showing Joule-Thomson cooling events due to gas expansion at active cluster locations

We quantitatively estimated the inflow profile based on the Péclet number approach presented by App (2022), which generates a type curve describing the relationship between the inflow rate and the temperature drop for each cluster. The inflow profile can be numerically simulated by performing a temperature history match with the temperature log using a thermal simulator as a forward model. Figure 5.3(a) shows the matched temperature profile, and Figure 5.3(b) shows the estimated inflow profile. Contribution from the cluster at 7630 ft of measured depth in Stage 40 is the most significant, which is also confirmed qualitatively. The estimated total production rate is 978 STB/day of oil, 2321 MSCF/day of gas, and 665 STB/day of water, which is reasonably matched with the measured total a rate.

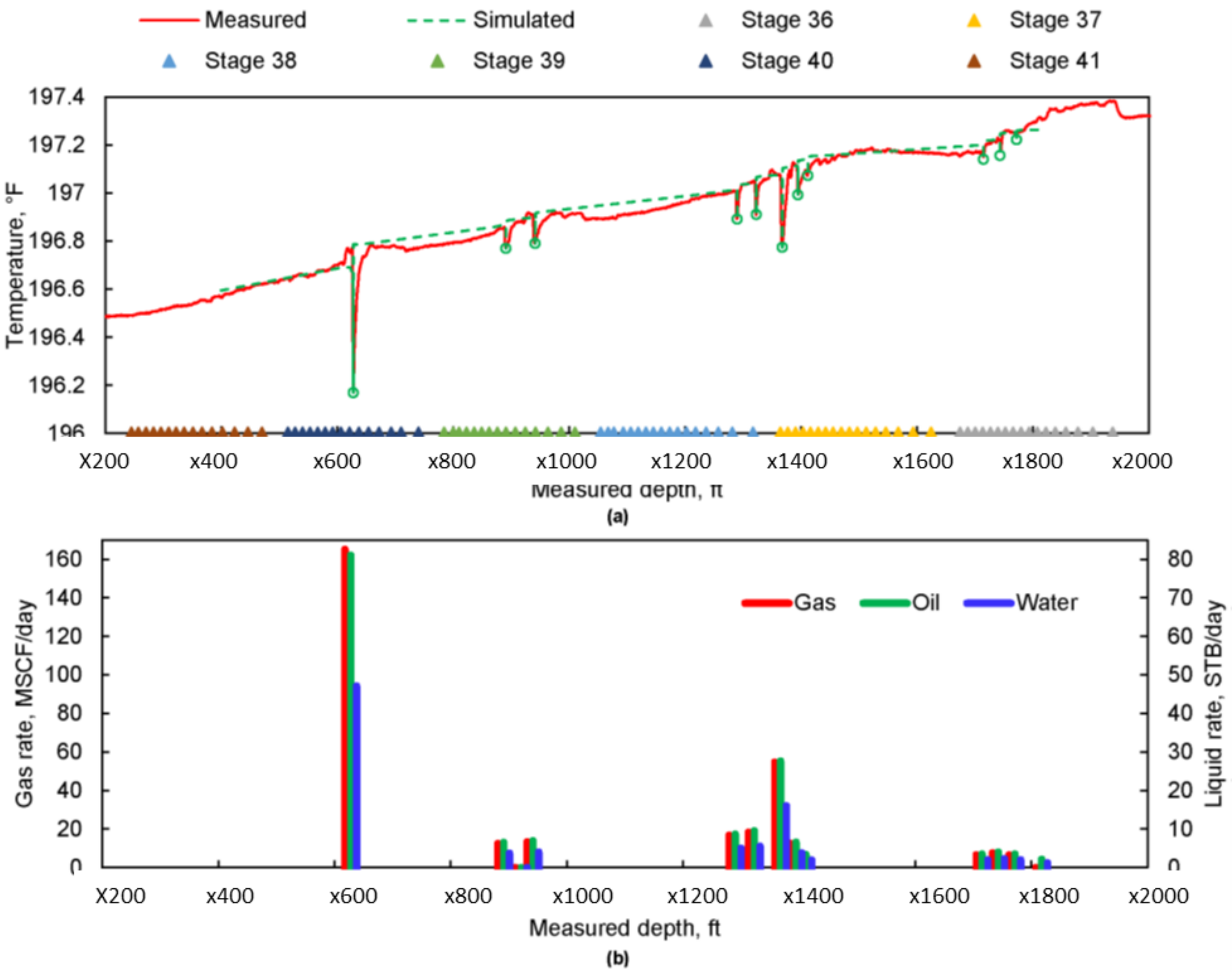

Figure 5.3 Results of inflow profile estimated by Péclet number approach. (a) Matched temperature profile. (b) Estimated inflow profile.

5.2 Results and Discussion

The obtained flow profiles of gas, oil and water show a similar trend to the inflow distribution interpreted by a commercial production log interpretation software, as shown in Figure 5.4.

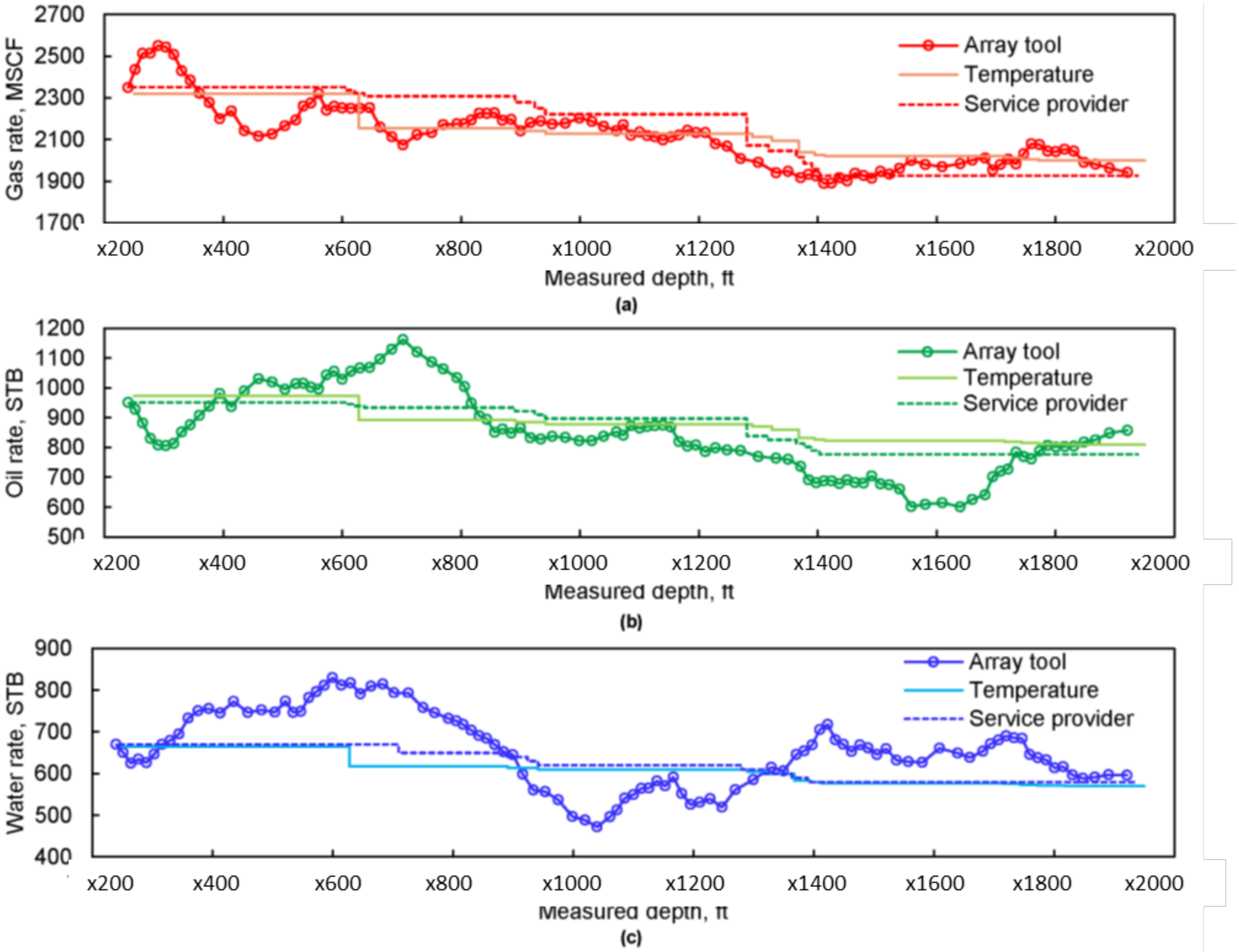

Figure 5.4 Comparison of our array tool interpretation, temperature log interpretation (Péclet number method), and the logging service provider result. (a) Gas rate. (b) Oil rate. (c) Water rate.

The production performance for each stage and corresponding completion design is evaluated. We compared the inflow profiles estimated by the temperature log interpretation based on the Péclet number method against three fracture stimulation design variables, as shown in Figure 5.5. All three varying stimulation parameters have little correlation with the produced gas and oil rates. However, due to the limited sample size in this case study, these correlation coefficients should not be considered as indicative of a statistical relationship between stimulation design variables and production outcomes. To obtain more reliable correlation results, a larger and more diverse dataset is needed.

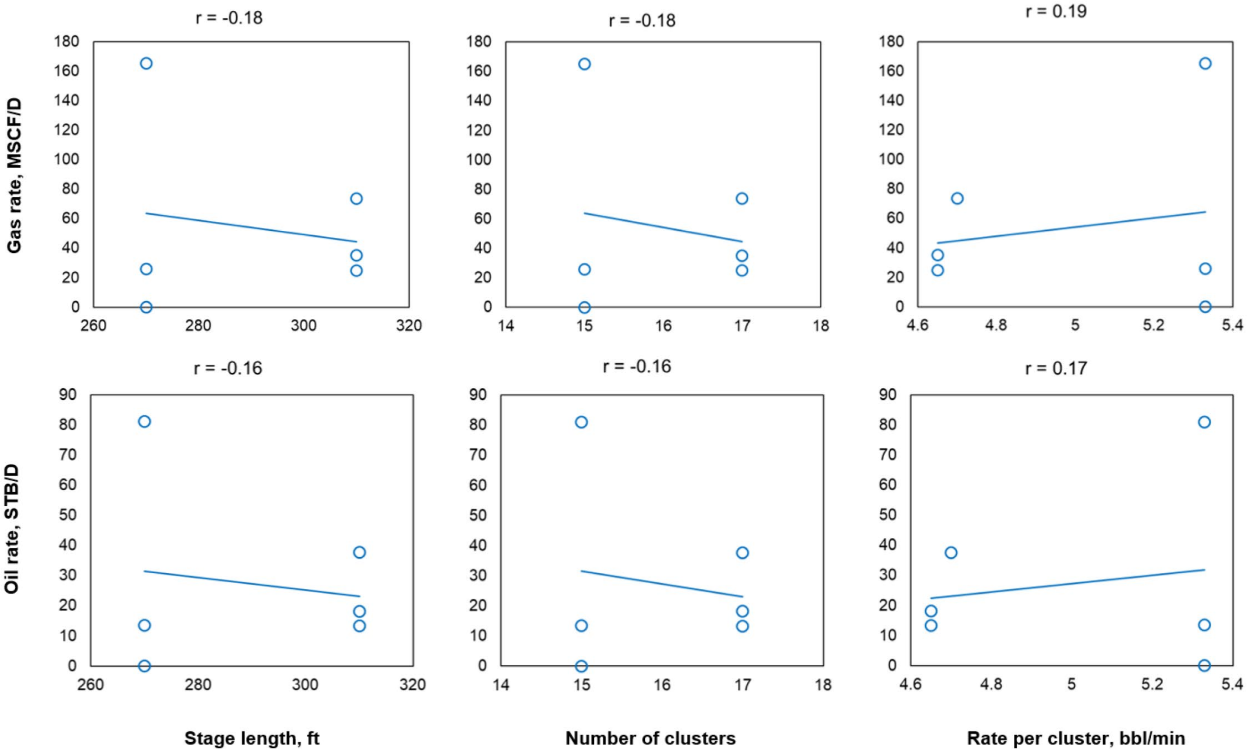

Figure 5.5 Comparison of production rates by temperature log interpretation and stimulation design.

6. Sealed Wellbore Pressure Monitoring (SWPM) Analysis

Summary

Sealed wellbore pressure monitoring (SWPM) has emerged as a low-cost diagnostic tool for fracture hit detection in unconventional development. In the Austin Chalk Eagle Ford Field Laboratory project, we used one of the offset monitor wells as a sealed wellbore to monitor pressure changes as hydraulic fractures propagate towards and intersect the monitor well. The sealed wellbore has no perforations connected to the formation, thereby preventing fluid flow into or out of the wellbore. A pressure increase in the sealed wellbore is a clear indication of fracture intersection. The team developed an integrated numerical model consisting of a fracture propagation model, a 3D geomechanics model, and a 3D transient fluid flow model to analyze the sealed wellbore pressure responses. When multiple fractures intersect the casing, a higher surface pressure increase is observed compared to a single fracture hit.

6.1 Approach

The integrated numerical model comprises three interconnected subdomains: a fully 3D fracture propagation model STIMPLAN (NSI, 2024) to simulate fracture geometry and net pressure during stimulation, a 3D finite element based transient fluid flow model to simulate reservoir pressure in deformable porous media, and a 3D finite element based geomechanics model to simulate stress and strain changes within the fractured formation. The geomechanics model also includes an analysis of sealed casing response. We first simulated fracture propagation and generate fracture geometry and net pressure distribution at each time step using the fracture simulator STIMPLAN. Figure 6.1 shows an example snapshot of the fracture width distribution after 68 minutes of pumping.

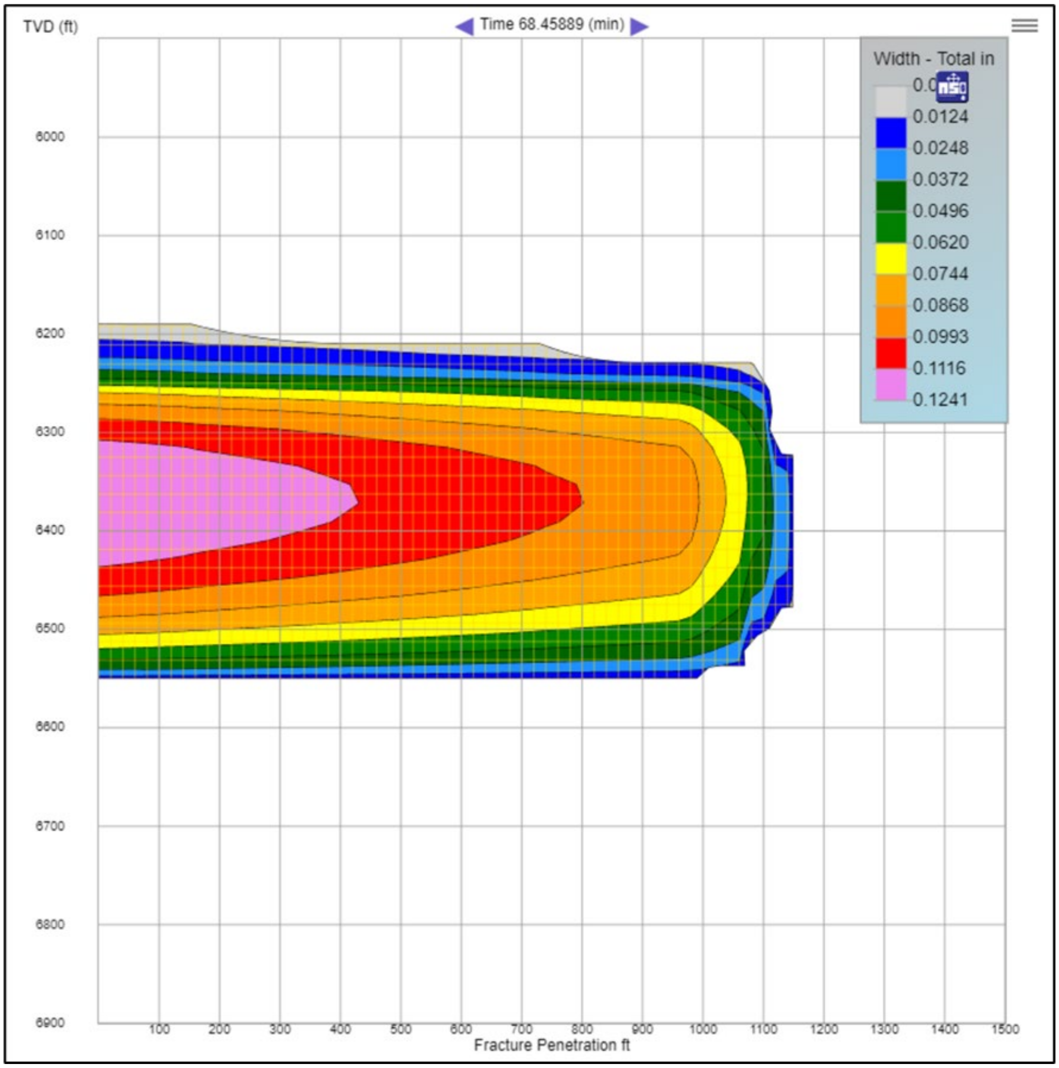

Figure 6.1 Fracture geometry output for the treatment well from fracture model.

The sealed wellbore displacement or compression can be estimated from the pressure, stress and strain modeling. This integrated numerical model is designed to investigate the interaction between fracture opening, propagation, and closure with the sealed wellbore at an offset location. Adopting this integrated approach, the internal volume change of the wellbore, and the corresponding surface pressure change can be evaluated. Figure 6.2 shows the 3D simulation domain in the finite element models including the treatment well, propagating fracture and sealed wellbore.

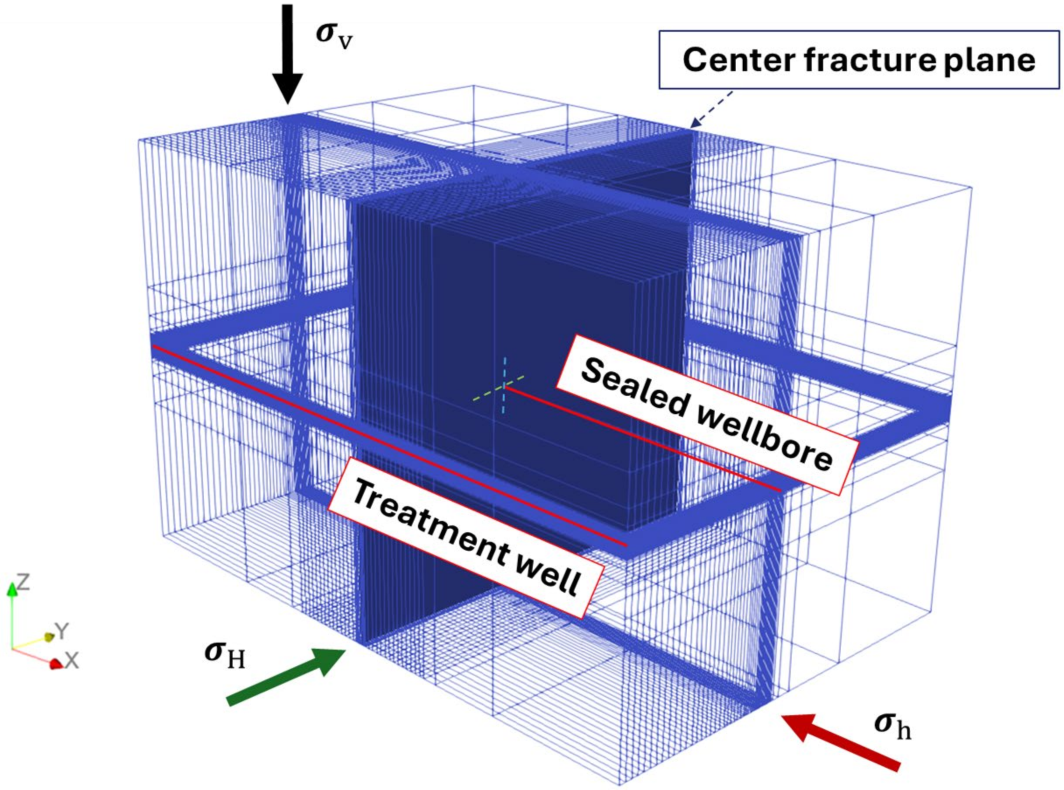

Figure 6.2 Simulation domain of the 3D finite element model.

6.2 Results and Discussion

We first analyzed the sealed wellbore pressure response due to the fracture intersection from a single cluster stage in Well 1F. Figure 6.3 shows the history matching result with field sealed wellbore pressure data. The result indicates a distinct pattern in casing pressure behavior during fracture stimulation in the offset well. Initially, sealed casing pressure experiences a sharp increase upon the first interaction with the propagating fracture (fracture arrival). Subsequently, as the fracture traverses the offset wellbore, the rate of pressure increase becomes more stable. Upon the end of injection at the treatment well, the increase in offset wellbore pressure begins to slow down gradually. Notably, even after pumping stops, the fracture front continues to propagate away from the monitor well during the tip extension stage. Finally, casing pressure exhibits a more rapid decline as the fracture starts to close. This sensitivity analysis shows that a lower permeability and a lower leak-off coefficient correspond to a more significant increase in sealed wellbore pressure after fracture intersection. To achieve a good match with the field data, a repeated process of adjusting fluid leak-off is required in the pressure matching process.

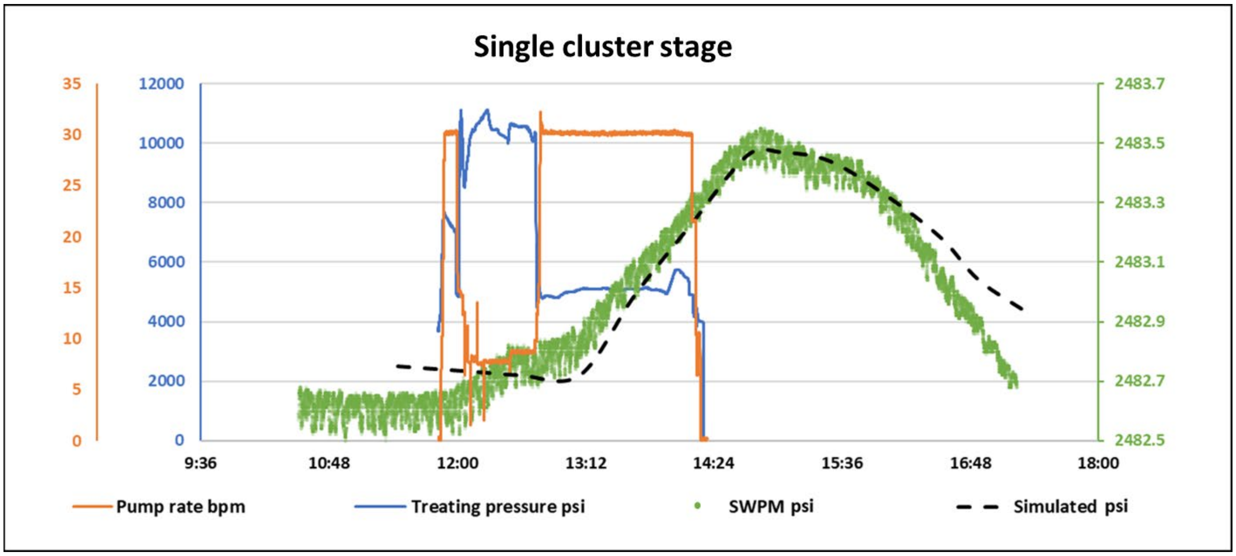

Figure 6.3 History matching with field sealed wellbore pressure data

The offset sealed wellbore pressure response varies with the number of intersecting fractures. To analyze the impact of multiple fracture hits on sealed wellbore pressure, we simulated a stage with two clusters and compare it with a single cluster stage. Figure 6.4 illustrates the simulated offset wellbore pressure for both single-cluster and two-clusters scenarios.

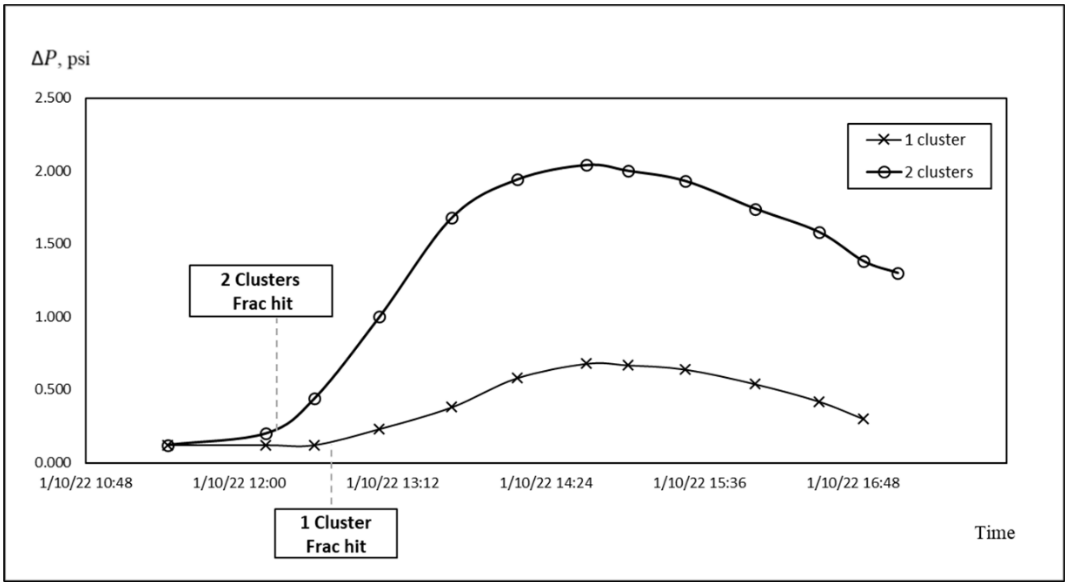

Figure 6.4 Comparison of pressure response between two scenarios

Notably, the first inflection point on the two clusters pressure curve occurs faster than in the single cluster case. This indicates a more significant pressure change and casing displacement early on in the two clusters stage due to the increased number of fracture intersections and longer displacement interval along the casing compared to the single cluster stage. The pressure increase magnitude for the two-clusters case is 2.04 psi, which is three times higher than that of the single cluster stage (0.68 psi). This observation highlights the significance of the number of fractures intersecting the offset monitor well as a critical completion parameter affecting the magnitude of sealed wellbore pressure.

Sealed wellbore pressure analysis provides information such as the magnitude of pressure increase, Volume to First Response (VFR), fracture arrival time and fracture propagation rate. The magnitude of pressure increase in the sealed wellbore correlates with the intensity of hydraulic fracturing and the extent of reservoir stimulation. Analyzing this pressure increase from SWPM data helps to assess the performance of completion designs, optimize fracturing strategies, and enhance reservoir development plans. We conducted a comparison between completion designs and sealed wellbore pressure increases for multiple stages in a subset of designs tested. Figure 6.5 and Figure 6.6 show the magnitude of pressure response compared with the number of clusters, cluster spacing, maximum injection rate and fluid loading. The results indicate that the number of clusters, injection rate and fluid loading positively related to the magnitude of pressure response, while cluster spacing shows a negative correlation with pressure response.

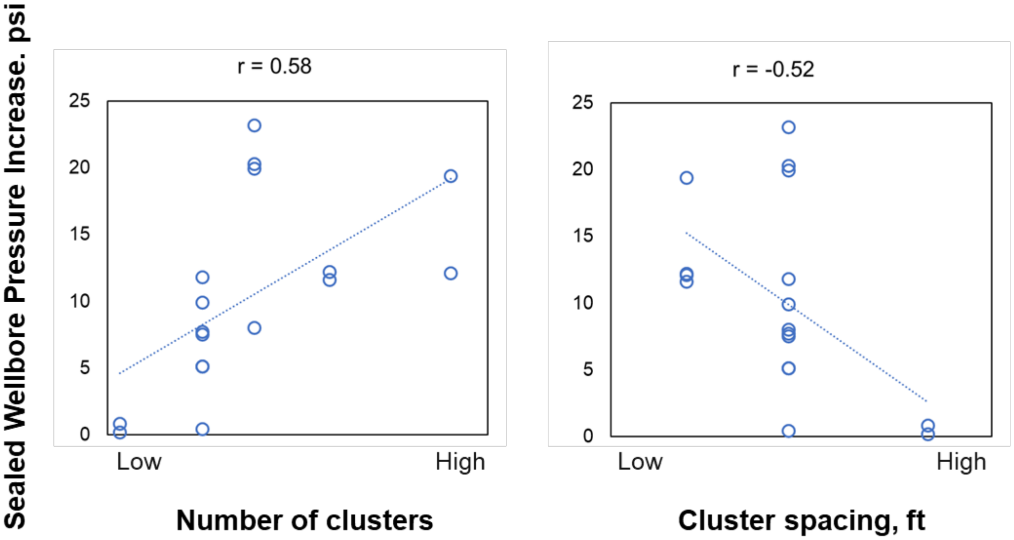

Figure 6.5 Sealed wellbore pressure increases versus the number of clusters and cluster spacing in a subset of designs tested

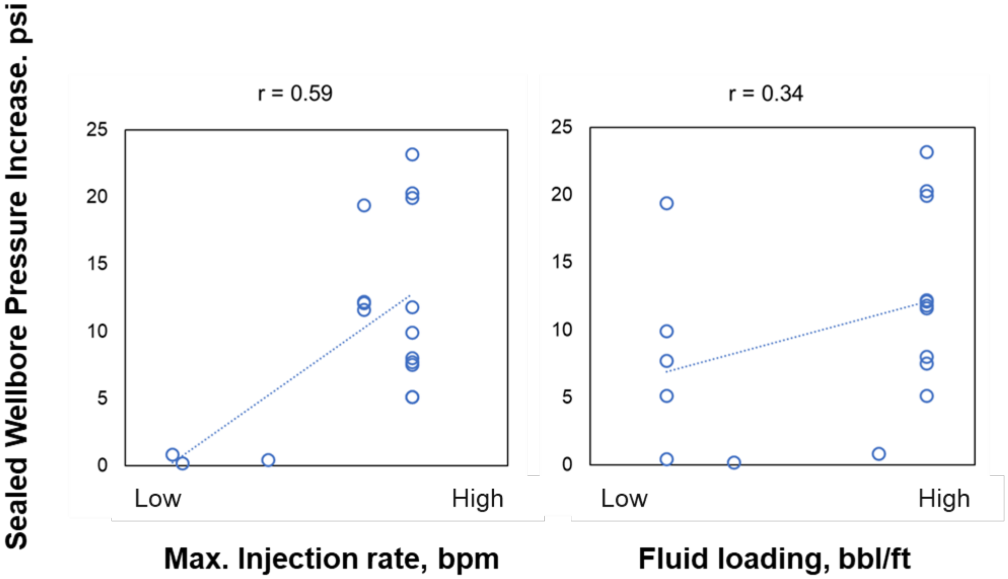

Figure 6.6 Sealed wellbore pressure increases versus the maximum injection rate and fluid loading in a subset of designs tested

VFR quantifies the amount of injected fluid after propagating fracture first intersects the offset monitor well. A higher VFR indicates a more uniform distribution of injected fluid among the different fracture clusters (Cipolla et al. 2022). To standardize the comparison, VFR is normalized by dividing the number of clusters per stage. Figure 6.7 plots the normalized VFR versus the number of clusters. The result suggests that completion efficiency decreases as the number of cluster increases.

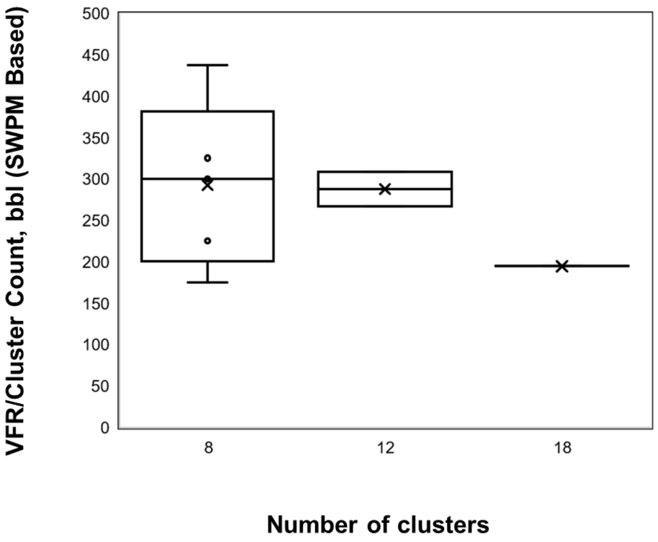

Figure 6.7 VFR/cluster versus number of clusters

7. Stress Profiling and Fracture Height Modeling

Summary

The comprehensive field data at ACEFFL provides an excellent opportunity to study how the state of stress at depth impacts hydraulic fracture growth and the characteristics of microseismicity caused by fluid injection. We used a combination of regional data and well logs to characterize the state of stress at the site and the variations of stress with depth. Sonic log data was used to constrain the range of elastic stiffness and determine the variations in viscous stress relaxation with depth using two independent methods. Both stress models were compared to DFIT measurements of the least principal stress and the instantaneous shut-in pressures from hydraulic fracturing stages in different stratigraphic units. We used the stress models and operational data to simulate hydraulic fracture propagation in different stages to understand the relationship between the state of stress and fracture growth. We also compared the simulated fracture areas to the distribution of microseismic events associated with those stages and timing of the events with respect to frac hits recorded by DAS.

7.1 Approach

The ACEFFL is located in the southwest corner of the Eagle Ford field in an area of normal/strike-slip faulting (Figure 7.1). There are several borehole stress measurements near the site indicating that the direction of the maximum principal stress is approximately N45E. The area is in more compressional state of stress compared to Hydraulic Fracturing Test Sites-1 and -2 (HFTS-1, -2), in the Midland and Delaware basins.

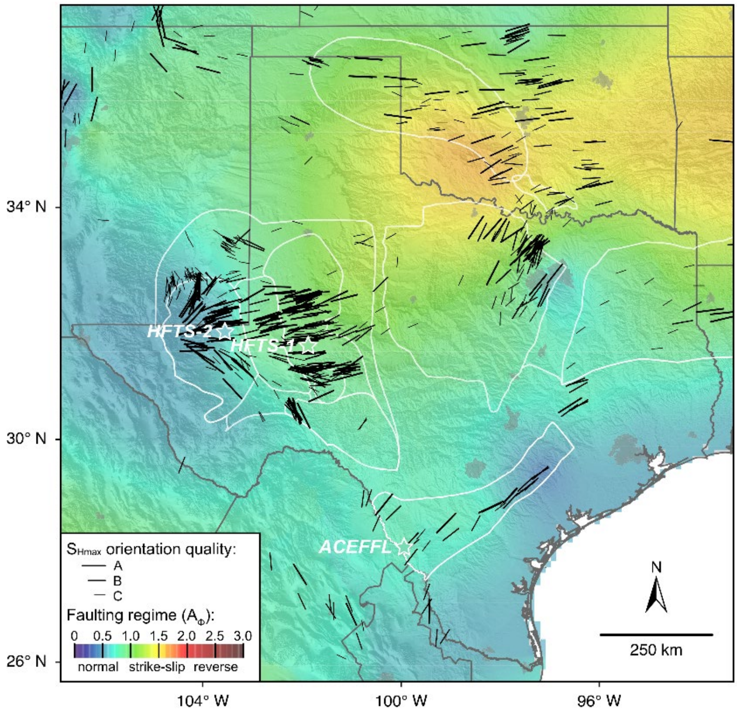

Figure 7.1. Map of the state of state in Texas highlighting several hydraulic fracturing test site, Hydraulic Fracturing Test Sites -1 and -2 (HFTS-1, -2) and the Austin Chalk Eagle Forld Field Laboratory (ACEFFL). The background color is the value of the stress ratio parameter A_Φ that represents the relative magnitudes of the principal stresses. Black lines on the map indicate measurements the orientation of the maximum compressive stress. Line length correspond to the quality of the measurement. Adapted from Lund Snee & Zoback (2020).

Our approach to characterizing the state of stress at the ACEFFL site was focused on constraining the variations of stress with depth. Specifically, we were concerned with the value of the minimum principal stress S_{hmin}, which determines the pressure need to propagate hydraulic fractures greater after the first several meters of growth. In other hydraulic fracture test sites (HFTS-1, -2), we have observed that the value of S_{hmin} varies with depth due to variations in pore pressure and the degree of viscous stress relaxation (Kohli & Zoback, 2021). Horizontal wells that are drilled toe-up or toe-down may encounter different stratigraphic units with different S_{hmin} values, resulting in variations in how the reservoir is stimulated in different stages (Fig. 7.2).

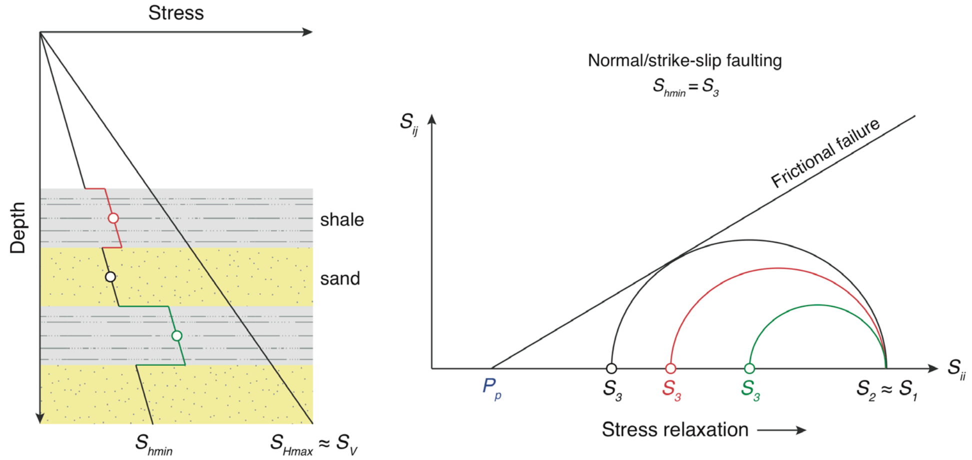

Figure 7.2. Illustration of how viscous stress relaxation over geologic time can result in variations of the least principal stress (S_{hmin}*) with depth. (left) Hypothetical layered sequence of shale and sand in a normal/strike-slip faulting regime (*$S_{hmin} < S_{Hmax} \approx S_V$*). (right) Viscous stress relaxation in shale layers results in lower differential stress i.e., greater* S_{hmin} *and decreases the likelihood of frictional failure.*

We estimated variations in S_{hmin} due to viscous relaxation by two methods. First, we used published laboratory data to relate variations in elastic properties from sonic logs to variation in viscous creep behavior (Sone & Zoback, 2014). Then, assuming the strain rate and depositional age of the Eagle Ford unit, we calculated the differential stress as a function of depth. Second, we used an effective medium model that assumes each layer is composed of varying degrees of stiff and compliant endmembers based on elastic properties (Sone & Zoback, 2013).

We compared the two stress models to measurements of S_{hmin} from DFIT tests and ISIP values from stages in different stratigraphic units in the same well. We then examined the distribution of microseismic events in those stages to study the impact of stress variations with depth on stimulation in different strata. The stress models were used to simulate hydraulic fracture propagate and footprint using ResFrac software. We also studied the timing of microseismic events and frac hits interpreted by DAS in select stages and used the stress model to understand a case where fluid was routed through a fault by a hydraulic fracture causing a microseismic swarm and off axis frac hit in an adjacent well.

7.2 Results and Discussion

For this report, we will focus on the analysis of well 1 (Fig. 7.3). From lithologic and sonic logs, we found that the well is drilled into mostly calcareous lithologies in the Austin Chalk, but within these units there are significant variations in elastic properties. Laboratory data from the literature indicates that calcareous rocks from the underlying Eagle Ford formation show a negative correlation between Young's modulus and viscous creep. This signifies that more stiff rocks are expected to support more differential stress over geologic time. We used the correlation between elasticity and creep from the laboratory data to determine a profile of S_{hmin} over the Austin Chalk units (S_{hmin}_lab). We also used an effective medium model to calculate expected creep behavior based on elastic modulus (S_{hmin}_eff). Both models are in good agreement with a DFIT test at the toe of well 1 and the ISIP values from hydraulic fracturing stages 5 and 30, but S_{hmin}_lab shows higher frequency and higher amplitude variations in stress due to greater uncertainty in the lab data. Both models predicts an increase in S_{hmin} over well 1 from heel to toe, as well as an increase in S_{hmin} values above the well.

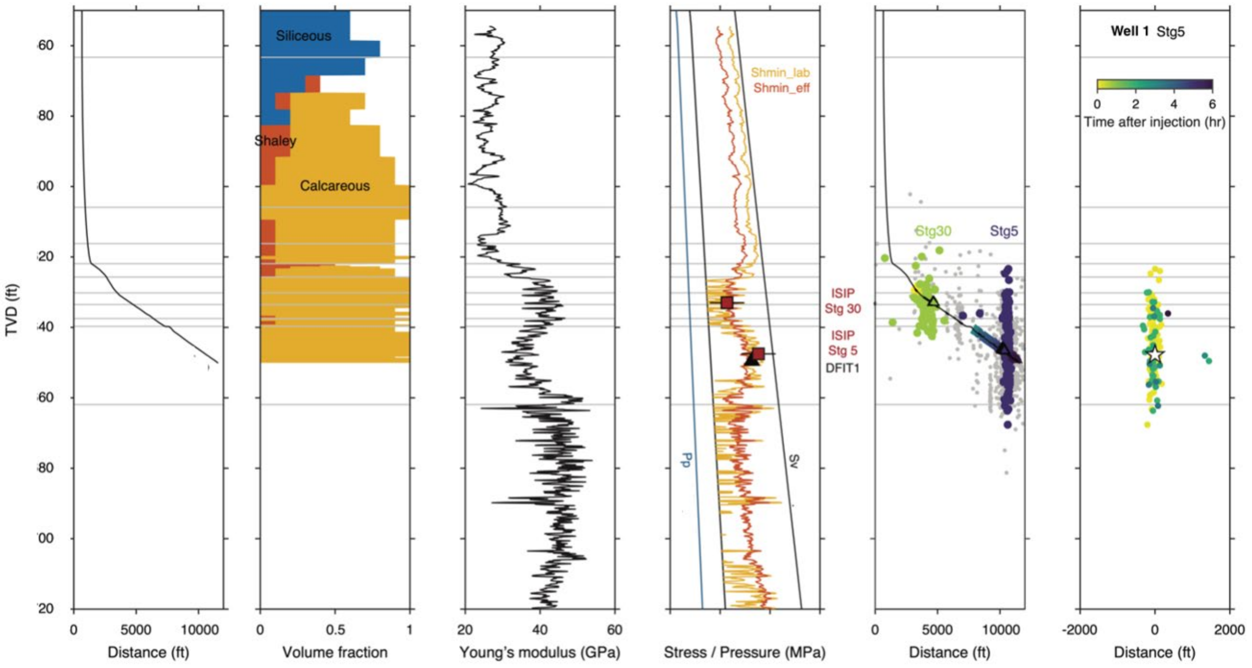

Figure 7.3. Rock properties, stress, and microseismicity in ACEFFL well 1. (a) Well trajectory. (b) Lithologic profile. (c) Young's modulus from sonic log in a vertical pilot well. (d) Stress and pore pressure profiles. Red lines represent estimates of the minimum horizontal stress, S_{hmin}, using the concepts of frictional equilibrium and viscous stress relaxation. The black triangle represents the estimate of S_{hmin} from the DFIT test at the toe of well 1. The red squares represent estimates of S_{hmin} from the instantaneous shut in pressures of stages 5 and 30. (e) Microseismicity recorded in well 1 (grey) with stages 5 (blue) and 30 (green) highlighted. (f) Gun barrel view of microseismicity in stage 5 colored by the time after injection.

We used the stress model to understand the variations in the microseismic response of stages in different stratigraphic units across the same well (Fig. 7.3). In stage 30, microseismicity is vertically bounded by the two higher stress layers above and below at ~200 and ~400 ft. The hydraulic fractures are unlikely to grow up or down into the higher stress layers, so there is no change in fluid pressure to drive microseismicity. In contrast, the microseismicity in stage 5 has a greater vertical extend, passing through the high stress unit below the well that was a barrier in stage 30 and into the underlying Eagle Ford formation. The higher value of S_{hmin} at the stratigraphic level of stage 5 signifies that pressure had to be raised more for hydraulic fracturing, which explains why microseismicity could be triggered far above and below the injection zone. Above the Austin Chalk, the stress is predicted to increase in more shaley units, forming an apparent hydraulic fracture barrier for all stages in well 1.

We investigated the effects of each of the stress models on hydraulic fracture growth using the commercial modeling software ResFrac. Figures 7.4b and 7.4c show gun barrel views of the simulated fracture areas (grey) and the microseismic events for well 1 stage 5 for S_{hmin}_eff and S_{hmin}_lab respectively. Both stress models result in similar overall fracture heights and match the vertical distribution of microseismic events; however, the model using S_{hmin}_lab shows much longer fractures by over a factor of 2. Although the simulated fractures appear to grow most laterally in the same layers (corresponding to regions with relatively low S_{hmin}), the fine-scale variations in S_{hmin}_lab result in much longer fractures overall. This is likely because S_{hmin}_lab has lower S_{hmin} values approaching frictional equilibrium (black line in Fig. 1a). We observed similar differences between the two stress models in the fracture simulations for well 1 stage 30 (Figure 7.5). Because this stage lands in a stratigraphic unit with a lower S_{hmin} value, the fracture is bounded above and below and grows more laterally in zone compared to stage 30. In the S_{hmin}_lab case, there are several microseismic events that occur above the predicted fracture footprint.

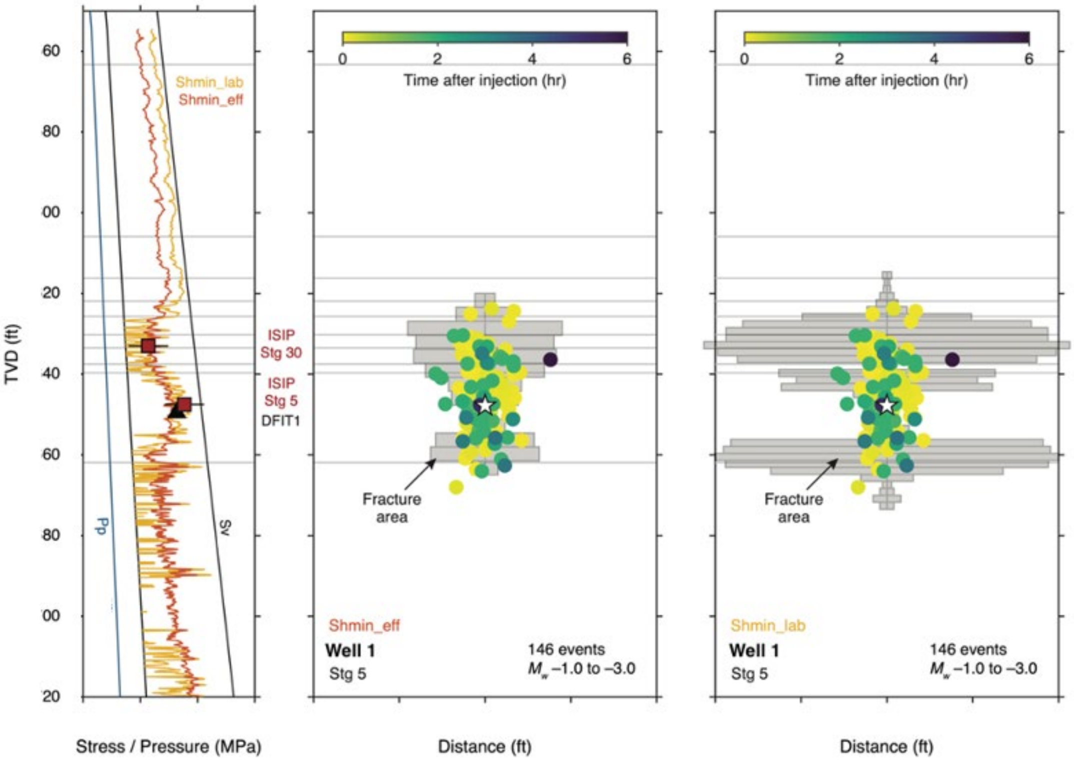

Figure 7.4. Modeling hydraulic fracture propagation in ACEFFL well 1 stage 5 using two different stress models. (a) Stress and pore pressure profiles. Red and orange lines represent estimates of the minimum horizontal stress, S_{hmin}, using two different methodologies. The black triangle represents the estimate of Shmin from the DFIT test at the toe of well 1. The red squares represent estimates of S_{hmin} from the instantaneous shut-in pressures of stages 5 and 30. (b) Gun barrel view of simulated fracture area using S_{hmin}_eff compared with microseismicity in stage 5 colored by the time after injection. (c) Gun barrel view of simulated fracture area using S_{hmin}_lab compared with microseismicity in stage 5 colored by the time after injection.

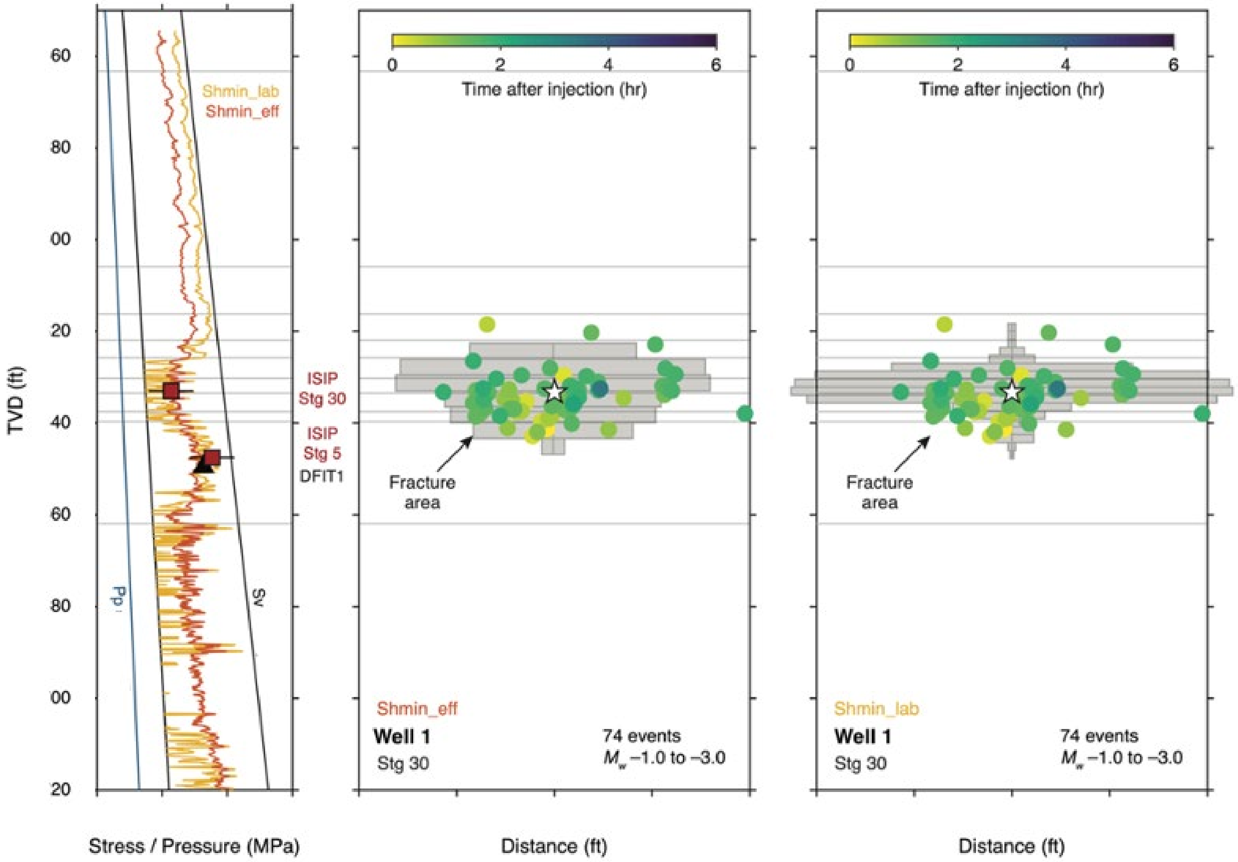

Figure 7.5. Modeling hydraulic fracture propagation in ACEFFL well 1 stage 30 using two different stress models. (a) Stress and pore pressure profiles. Red and orange lines represent estimates of the minimum horizontal stress, S_{hmin}, *using two different methodologies. The black triangle represents the estimate of* S_{hmin} *from the DFIT test at the toe of well 1. The red squares represent estimates of Shmin from the instantaneous shut-in pressures of stages 5 and 30. (b) Gun barrel view of simulated fracture area using* S_{hmin}*_eff compared with microseismicity in stage 30 colored by the time after injection. (c) Gun barrel view of simulated fracture area using* S_{hmin}*_lab compared with microseismicity in stage 30 colored by the time after injection.*

We also examined the relationships between the spatiotemporal distribution of events and frac hits recorded by low frequency DAS in a neighboring well. We focused our analysis on individual stages of well 2 during which a fiber was deployed in neighboring well 1. In Figure 7.6, we plot the events resulting from stimulation of well 2 stage 35 (circles) and frac hits recorded in well 1 (stars) colored by time after injection. Interestingly, in this stage the first frac occurs further towards the toe on well 1 than the equivalent position of the perforations in well 2. The frac hits then appear to migrate both toe-wards and heel-wards in time, traveling further towards the stage 35 than away. The spatiotemporal distribution of events is typical of a frac stage in this well, but we do see a swarm of events near the first frac hit. These events outline a steeply dipping plane oblique to the maximum horizontal stress. This population of events may represent slip on a pad scale fault. If this fault is a permeable pathway for fluids, it may explain why the first frac hit occurs further towards the toe than expected, off axis of stage 35. The migration of the frac hits with time may indicate that a single set of perforations may generate multiple permeable pathways for stimulation. In the future, we plan to investigate these relationships for a large number of stages to study the effect of different completion designs (Kohli et al. In Preparation). The distance-time plot of the microseismic events show the events propagate out from the well at rate of ~1000 ft/hr until the distance of the interpreted vertical fault plane. After this point in time, the events occur on this vertical plane at similar distances from the well and only a few events occur further away. This suggests again that fluid pressure from the growing hydraulic fracture may have been routed along this fault, subsequently resulting in a frac hit further towards the toe of well 1.

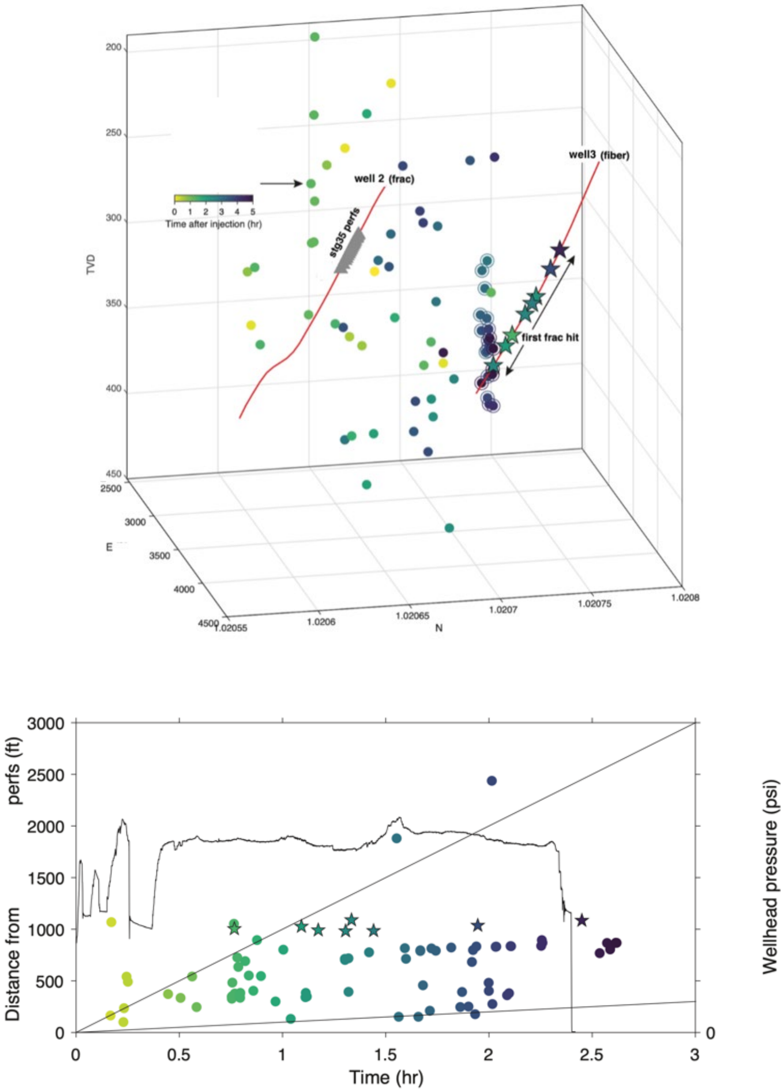

Figure 7.6. (top) 3D view of hydraulic fracturing of well 2 stage 35. During fracturing, a fiber was installed in neighboring well 3. Events recorded during stage 35 (circles) and frac hits recorded on the fiber in well 1 (stars) are colored by the time after injection. A swarm of microseismic events that may represent slip on a vertical fault are circled. (bottom) Pumping record and distance-time plot of microseismic events from well 2 stage 35. Events are colored by time after the start of injection. Star events represent those on the interpreted vertical fault plane.

8. Micro-scale Laboratory Assessment of Drill Cuttings and Rock Fragments Geomechanical Properties

The following report forms part of our proposed novel methodology for obtaining laboratory rock geomechanical properties using drill cuttings. As part of our ongoing drill cuttings study, our team conducts geomechanical characterization of rock properties using rock fragments cut from extracted core samples. This is done to simulate actual drill cuttings due to our current lack of access to authentic drill cuttings.

In our study, we employ a micro-scale surface mechanical testing apparatus to assess shale mechanical properties. The evaluation of elastic mechanical properties, including Young's modulus, Poisson's ratio, and the Transversely Isotropic (TI) stiffness matrix, is conducted using the Hysitron® micro-indenter, as detailed in our previous annual report. Testing is carried out on randomly oriented rock cuttings with a maximum dimension of less than 5 mm, obtained from core samples. The measured indentation modulus serves as input for an inverse constrained algorithm developed to determine the transversely isotropic stiffness matrix and unknown cuttings' bedding orientations. This algorithm is based on contact mechanics theory derived for indentation testing and incorporates mathematical constraints to ensure parameter accuracy, along with Monte Carlo simulation to address experimental uncertainties. Furthermore, we validated our findings through an Ultrasonic Pulse Velocity (UPV) test on a 1-inch cube sample, observing good agreement in the measured TI stiffness matrix between the micro-scale and macro-scale methods.

For fracture properties assessment, we utilize the Revetest® scratch tester with a load capacity ranging from 0.5 N to 200 N. The sample size for the scratch study is approximately 5 mm x 10 mm x 15 mm, and all scratches are performed with a 3-mm scratch length and loading up to 80 N. The experimental procedure involves scratching the rock surface with a diamond indenter under progressively increasing normal load. During the test, we record parameters such as indentation depth (Pd), tangential force (Ft), Acoustic Emission (AE), Coefficient of Friction (COF), and measured normal force, with AE activities indicating energy release phenomena related to crack/fracture development. Upon completion of the test, panoramic pictures of the sample surface along the scratch length are captured to characterize fracture formations and determine critical lengths. These critical lengths, derived from recorded peak values in tangential force and indentation depth, are used to calculate energy release rate and strain energy density, validated against reference materials like fused quartz. Our experiments include testing Austin chalk samples in different orientations (arrester, divider, and short transverse direction) to comprehensively assess fracture behavior.

Supplemental Figures

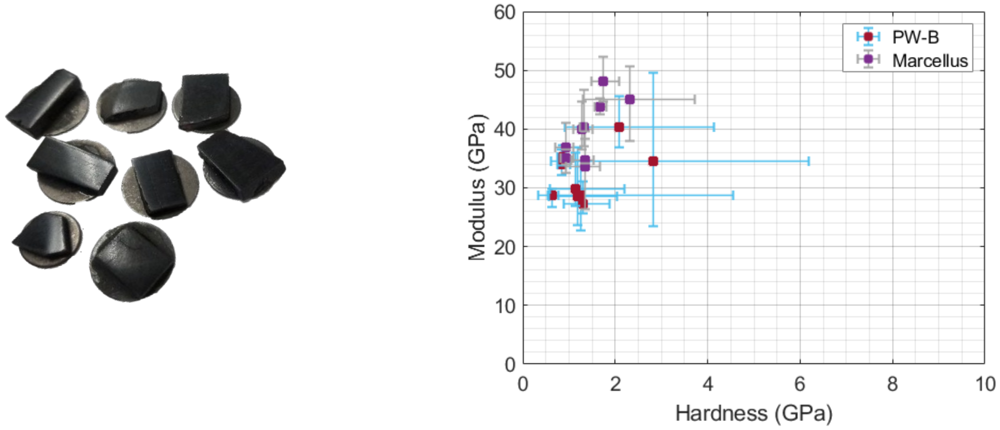

Figure 8.1 (left) Rock cutting samples attached onto a 25-mm diameter AFM discs. (right) Experimental indentation modulus vs hardness for Marcellus and Permian Wolfcamp B (PW-B) samples

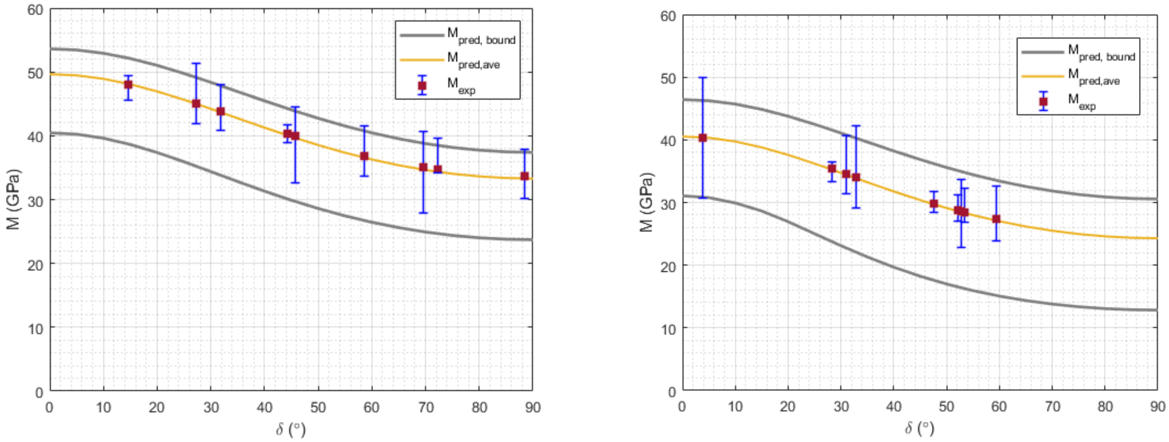

Figure 8.2 Predicted indentation modulus and cuttings' bedding orientations on: (left) Marcellus and (right) (PW-B) samples

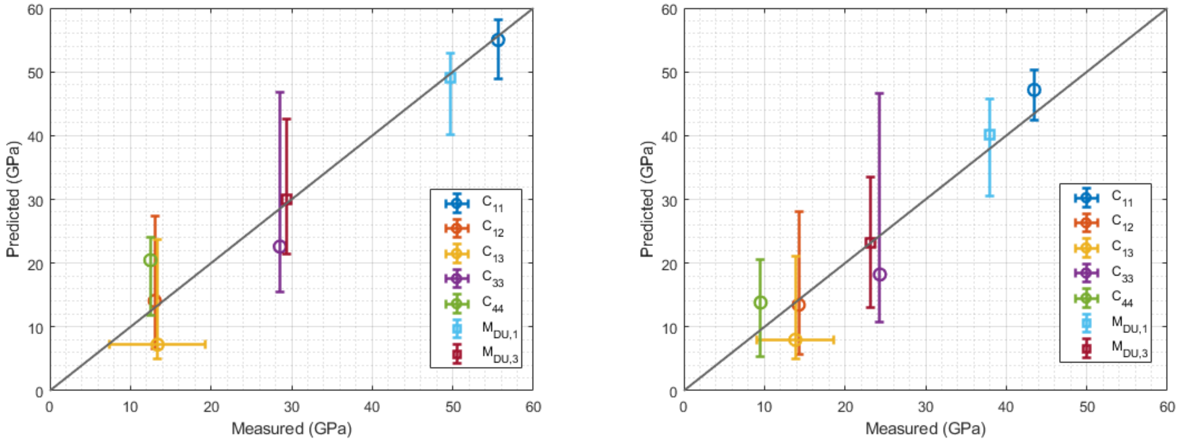

Figure 8.3 Predicted transversely isotropic stiffness constants based on micro-indentation test (labelled "Predicted") and UPV test (labeled "Measured"): (left) Marcellus and (right) (PW-B) samples

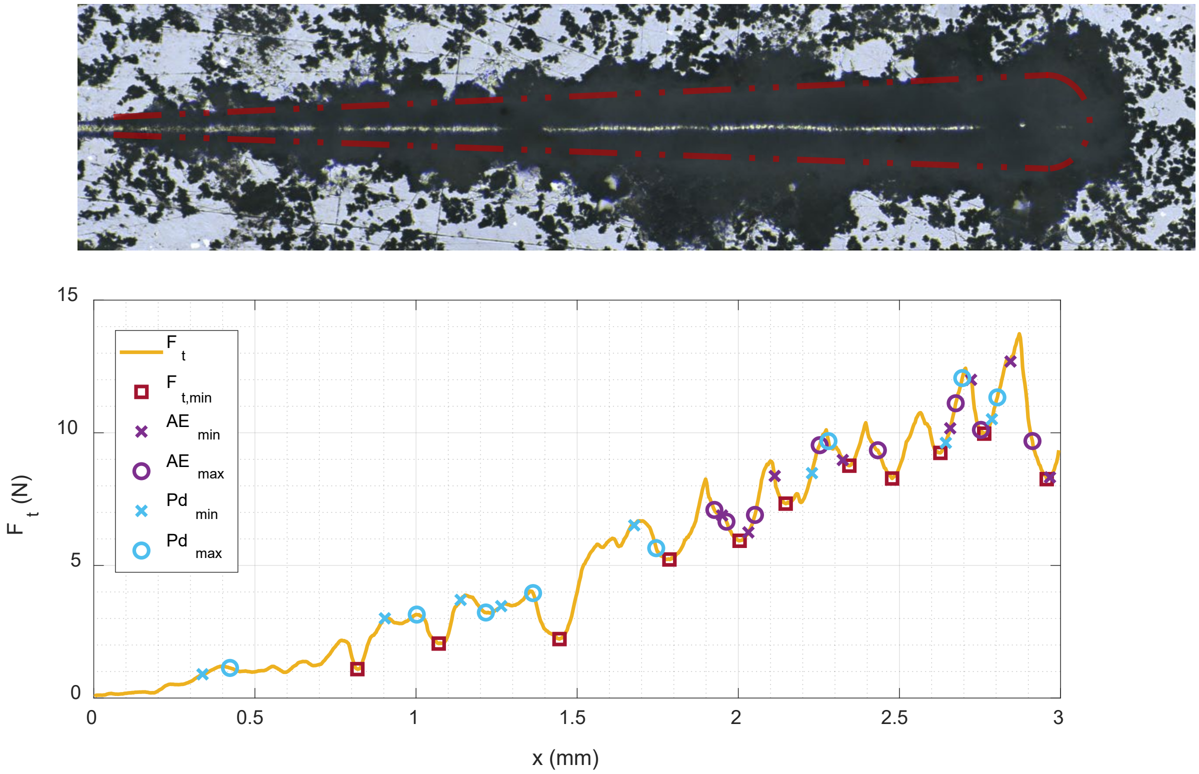

Figure 8.4 Scratch test results: (above) Panoramic picture of sample surface after the scratch test. (below) Recorded tangential force (F_t) - scratch distance (x) with peaks locations observed in acoustic emission (AE) and indentation depth (P_d).

Table 8.1 Shear fracture energy approximation

Material	$\mathcal{G}_{II}$ J/m^2	$\mathcal{G}_{II,reference}$ J/m^2
FQ	3.3 ± 1.2	3
AC-85-A	118.1 ± 22.4	-
AC-85-D	111.3 ± 63.9	-
AC-85-ST	91.9 ± 13.3	-
AC-86-A	30.3 ± 9.4	-
AC-86-D	38.8 ± 23.1	-
AC-86-ST	60.1 ± 24.8	-
AC-87-A	48.0 ± 18.1	-
AC-87-D	46.4 ± 16.0	-
AC-87-ST	87.7± 26.6	-

9. Fast History Matching Using EDFM and FMM Simulation for Multi-Fractured Horizontal Wells

Summary

This work focuses on developing an efficient workflow by integrating a multi-resolution simulation model and a multi-objective evolutionary algorithm (MOEA) for application to multi-well unconventional reservoirs. In this approach, hydraulic fractures are represented using a dual porosity dual permeability (DPDP) system facilitated by an embedded discrete fracture model (EDFM). A novel fast marching simulation method is employed to cut down on computational expenses by an order of magnitude, greatly accelerating the history matching process. A variety of integrated monitoring technologies were implemented to map out the hydraulic fracture network. Insights into hydraulic fracture locations were gleaned from warm-back analysis of distributed temperature sensing (DTS) data, and these locations were then assimilated into the simulation model as embedded discrete fractures. For the simulation, a fast-marching-based multi-resolution model was used to partition the reservoir into local and shared domains guided by the “Diffusive-Time-of-Flight” (DTOF) principle. The local domain maintained the original 3D grids near the wells while transforming the remaining area into 1D grids to accelerate the simulation process. Prior to history matching, a thorough sensitivity analysis was conducted to pinpoint the most impactful parameters. Subsequently, the model was fine-tuned using production data through a multi-objective evolutionary algorithm. The most sensitive parameters in history matching were identified as fracture geometry and conductivity, fluid saturations, and rock compressibility in the Stimulated Reservoir Volume (SRV) areas. After history matching, there was a noteworthy reduction in the uncertainty of these tuning parameters. The calibrated parameters are valuable to evaluate the effectiveness of the well completion design. Overall, this work emphasizes the innovative combination of techniques applied, the efficiency gains in the history-matching process, and the scalability of the approach to other oilfield applications.

9.1 Approach

This work demonstrates a rapid workflow that combines a multi-resolution simulation model and multi-objective evolutionary algorithm and applies it to a multi-well unconventional reservoir with hydraulic fractures. Hydraulic fractures are modeled using a dual porosity dual permeability system generated by an embedded discrete fracture model (Li and Lee 2008). In the EDFM, fractures are explicitly described in a separate computational domain as two-dimensional planes in addition to the matrix domain (Xue et al. 2019). The fracture grid blocks are then connected with corresponding matrix grid blocks via non-neighbor connections (NNCs). The fracture locations integrated in the EDFM model are interpreted from the distributed temperature sensing data and the interpretation method is introduced by Sakaida et al. (2022). A novel multi-resolution simulation method was used to create reduced models, improving the computational efficiency and substantially speeding up the history-matching process. A genetic Algorithm was used to calibrate reservoir properties and fracture parameters using field production history. The following steps summarize the overall workflow and are illustrated in Figure 9.1.

- Interpret hydraulic fracture locations from the warm-back analysis of the distributed temperature sensing (DTS) data
- Incorporate hydraulic fractures into the simulation model using EDFM
- Calculate DTOF using FMM, discretize DTOF levels, and determine local and shared domains
- Construct the multi-resolution simulation model
- Rank and identify the most influential parameters using sensitivity analysis
- Calibrate reservoir properties and fracture parameters using a Pareto-based multi-objective evolutionary algorithm (MOEA)

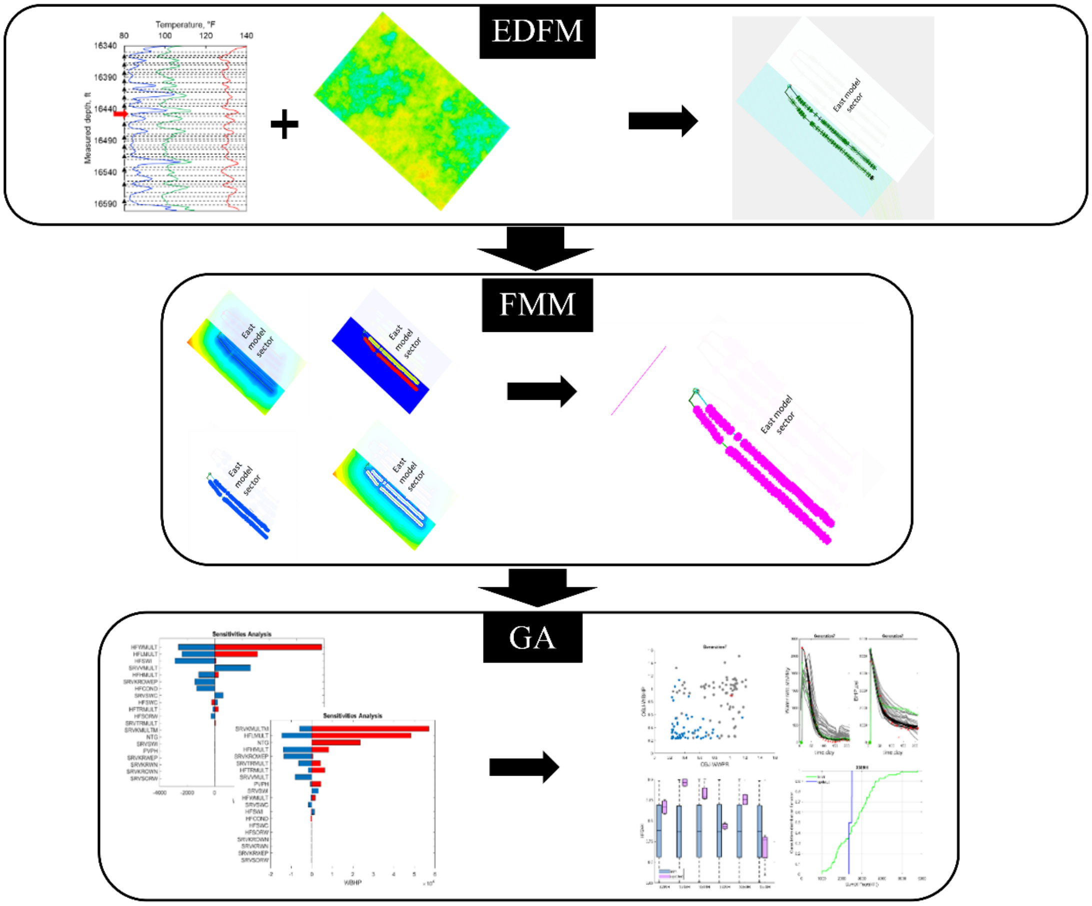

Figure 9.1 The overall workflow of a rapid history matching method.

9.2 Multi-Resolution Simulation.

The DTOF represents the travel time of the pressure front propagating from a well. Vasco et al. (2000) derived the Eikonal equation governing the pressure front propagation:

$$\nabla^T \tau \boldsymbol{k} \nabla \tau = \phi \mu c_t \tag{9.1}$$

where τ is the DTOF, $\mathbf{k}$ represents the permeability tensor, ϕ is the porosity, μ is the fluid viscosity, and c_t is the total compressibility.

In previous studies, the Eikonal equation is discretized using finite difference form, which imposes limitations on grid geometry to its application. Chen et al. (2021) formulated the Eikonal equation in a finite volume form with complex gridding systems:

$$\sum_{i}^{\substack{upstream\\connections}}\left((\tau-\tau_i)^2T_i\right)=V_p\mu c_t \tag{9.2}$$

where i denotes the upstream connection index, T_i represents the transmissibility of the connection, V_p is the pore volume, μ is the fluid viscosity, and c_t is total compressibility.

The boundary value problems in the Eikonal equation can be solved by an efficient numerical method called the Fast Marching Method proposed by Sethian (1999). Chen et al. (2021) discussed the details of the application of FMM in solving the Eikonal Equation and provided a workflow for building multi-resolution grid systems (Chen et al. 2023). Using the computed DTOF, we can build a multi-resolution simulation model following the workflow illustrated in Figure 9.2. According to Eq. 2, reservoir properties are required to compute DTOF, including transmissibility, pore volume, fluid viscosity, and total compressibility. Therefore, the first step is to run the forward model for a small timestep and read the simulation output as the input of Eq. 2. We can discretize levels, which are the coarse-scale cells in the multi-resolution grid system made from a group of 3D cells that fall within a certain range of DTOF. Then, the levels are used to determine the boundaries of the local and shared domains. A local domain containing a set of levels is in the vicinity of each well, which dominates the flow in the near-well region. The shared domain is the set of levels whose flow is affected by multiple wells. In addition, we need to introduce the concept of the preserved region. The preserved region is part of the reservoir, which is preserved as original fine cells for the purpose of keeping high accuracy in the vicinity of wells. The size of the preserved region, therefore, gives us the flexibility to balance the efficiency and accuracy of the multi-resolution simulation. A case study in the next section will demonstrate the influence of the preserved region on the simulation efficiency and accuracy. The next step is constructing the multi-resolution grid system and computing grid properties and transmissibilities. A multi-resolution grid system includes (1) fine grids in the preserved domain; (2) 1D level cells transferred from the levels in local domains; (3) 1D level cells transferred from the levels in the shared domain; (4) and non-neighboring connections that connect preserved grids and 1D level cells. The multi-resolution simulation model requires upscale properties and transmissibility for the reconstructed grid system. More details of the upscaling can be found in Chen et al. (2023).

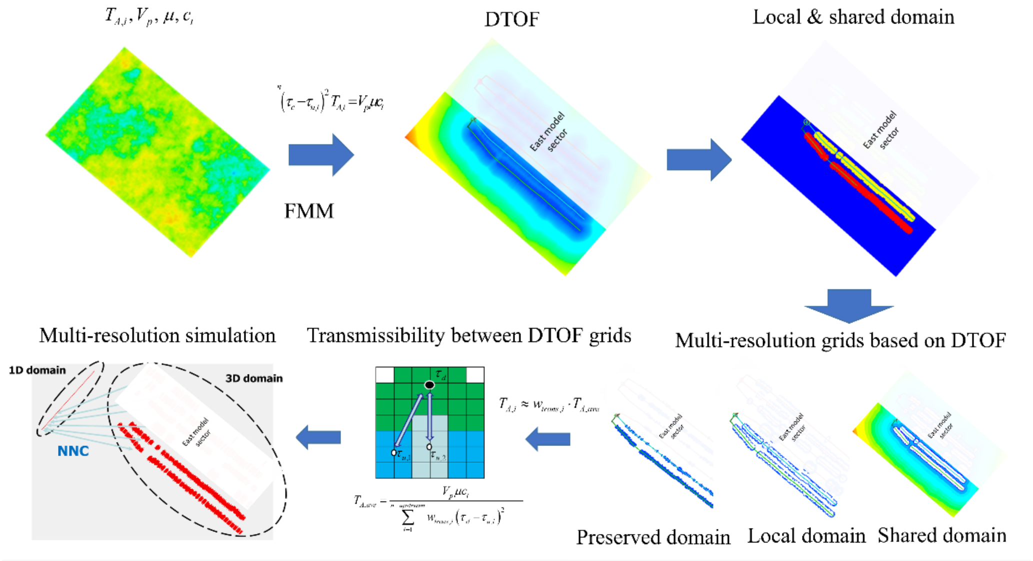

Figure 9.2 Multi-resolution simulation model workflow.

9.3 Pareto-based Multi-objective Evolutionary Algorithm

In this section, we briefly discuss the methodology and workflow of the history matching method. The non-dominated sorting genetic algorithm (NSGA-II) is applied to handle the optimization problem in the history matching process (Park et al. 2013; Sanghyun and Stephen, 2018). The concept of domination needs to be introduced first.

As shown in Figure 9.3, we project all the solution points in the objective space. Then, one model is randomly selected as solution O, and the whole objective space is divided into four parts centered on solution O. For area A, the two objectives of these three points are lower than those of Solution O. They are better solutions and dominate the solution O. For area C, the two objectives of these two models are higher than those of solution O. They are worse solutions, and they are dominated by solution O. While the solutions in areas B and D have no absolute superior rank compared to solution O. There is no domination relationship between the area B&D solutions and solution O. The domination relationship based on solution O is illustrated in Figure 9.3. As an illustration, we determine the Pareto rank using the concept of domination as shown in Figure 9.4. Each solution is selected as solution O and the domination relation between the selected solution and the others can be decided. The solutions having no domination relationship belong to the same rank. The solutions dominating other models belong to a higher (better) rank. The priority of solutions in one specific Pareto rank is determined using the estimation of crowding distance, as shown in Figure 9.5. This concept will be used to select optimal populations in the selection operation as one of the evolution procedures in addition to Pareto ranks.

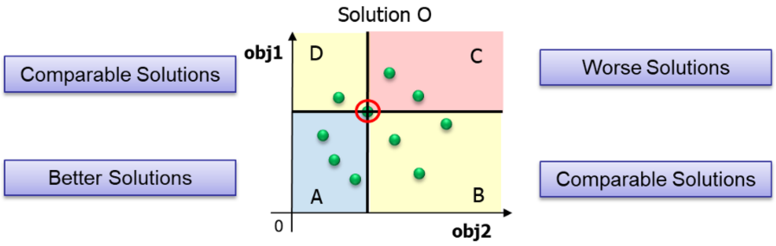

Figure 9.3 Concept of domination.

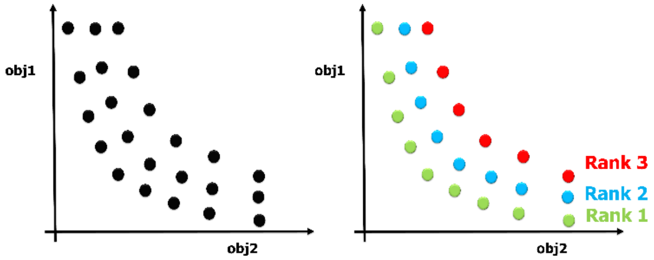

Figure 9.4 Pareto ranking.

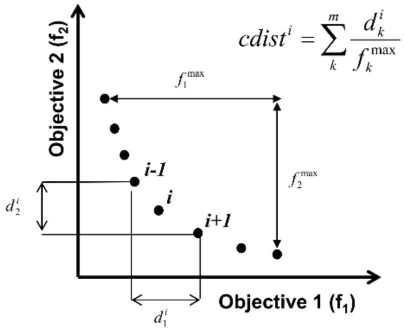

Figure 9.5 Estimation of crowding distance (Park et al. 2013).

Figure 9.6 summarizes the multi-objective history matching workflow. The first step is to generate initial models set as the first generation using Latin Hypercube Sampling with the heavy hitters selected by sensitivity analysis. Second, we decide on the objectives: bottom-hole pressure misfit and water rate misfit are chosen in this study. Next, forward simulations accelerated by multi-resolution simulation models compute well responses to evaluate the objective functions, which measure the misfits between the simulated well responses and the observed data. Then, all models are projected to the objective space, and Pareto ranks are determined based on the domination relationship among the models in the space. The genetic operators (selection, crossover, mutation) are applied to the parent population at the current generation to generate an offspring population. Before approaching the next generation, a portion of the current generation is selected as the parents of the next generation based on the Pareto ranking and crowding distance, based on a preserve ratio which is chosen to be 50% in this study. Because we set the size of the population at the beginning, we select the parent population for the next generation using non-dominated sorting. The basic idea is to preserve the population with a higher rank. So highly ranked models have more opportunities to be preserved. However, sometimes a whole rank cannot fit into the parent population. Then models with higher crowding distance have the privilege of being selected. The following step is to continue the genetic operations (crossover and mutation). This process will iterate until we reach the prespecified number of generations. We can select optimal models as the final model set depending on the Pareto ranking and crowding distance.

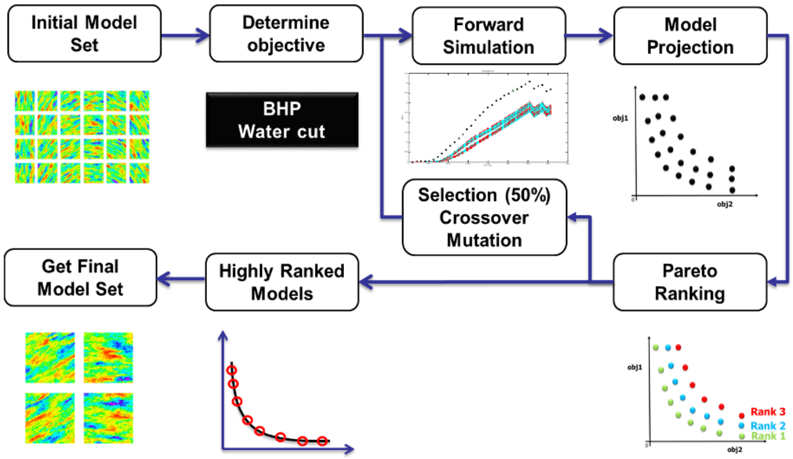

Figure 9.6 Multi-objective history matching workflow.

9.4 Results and Discussion

The field under consideration is an unconventional oil reservoir. The initial reservoir pressure is overpressured. The permeability of the oil reservoir falls within the range of 10^{-2} to 10^{-4}. The average initial water saturation is considered. Six horizontal wells are hydraulically fractured and have a production history of 200 days.

9.4.1 Model Description.

The matrix layer has 2.87 million cells (160×640×28) with six hydraulically fractured horizontal wells. More than 700 fractures are embedded into a 3D EDFM, and the EDFM has about 10 million cells, where 2.12 million cells are active. The fracture configuration is illustrated in Figure 9.7**.**

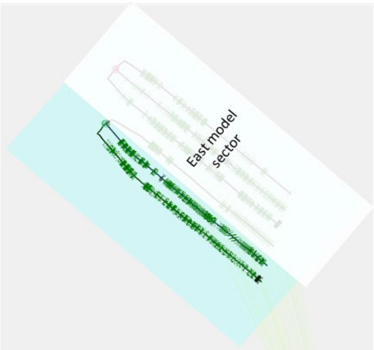

Figure 9.7 Top view of the matrix model and fracture configuration.

9.4.2 Multi-resolution Grid Setting.

DTOF is computed by the finite-volume-based FMM, as shown in Figure 9.8(a). Figures 9.8(b) and (c) illustrate the local domains and shared domains. Eq. 9.3 is used to detect well interaction. Figure 9.8(b) demonstrates the drainage volume at 50 days which corresponds to a DTOF threshold of $14.14\sqrt{day}$. The pressure propagation fronts of neighboring wells collided at the threshold, which means that well interactions are detected.

$$\frac{DTOF^2}{4\times Production\ days} = 1 \tag{3}$$

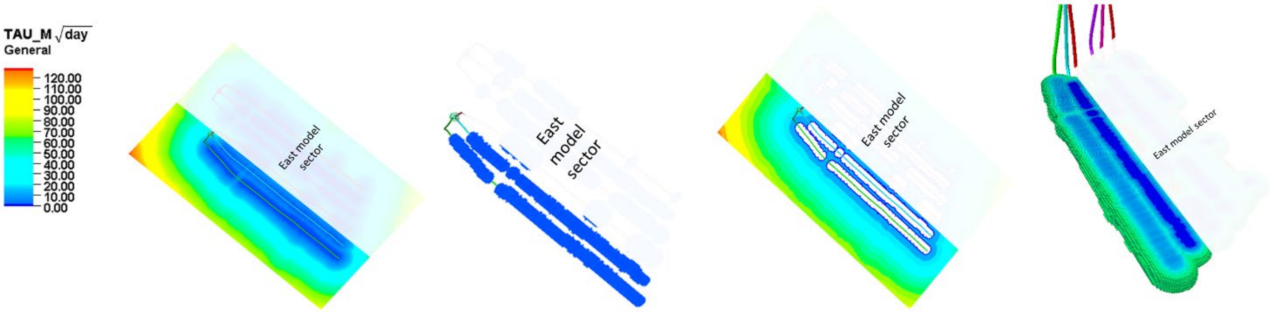

Figure 9.8 (a) DTOF; (b) Local domains; (c) Shared domain; (d) Drainage volume at 50 days.

9.4.3 Selection of Preserve Ratio.

In this section, we find the balance between the efficiency and accuracy of the multi-resolution simulation with an optimal ratio of the preserved domain. The preserve ratio represents the ratio of the maximum DTOF value in the preserved domain to the maximum DTOF value in the corresponding local domain. Two cases are presented to demonstrate the influence of preserved ratio on multi-resolution simulation efficiency and accuracy.

In the first case, the preserve ratio of each of the six wells is equal to 40% of cells in the local domain, and no cells in the shared domain are preserved. The configuration of the multi-resolution grid system is shown in Figure 9.9(a). There are 0.15 million active cells in total. The run time comparison shown in Figure 9. 9(b) suggests that the multi-resolution simulation is about 12 times faster than the original fine-scale model. Figure 9.10 compares the well responses (BHP and water cut) of the original fine-scale simulation and multi-resolution simulation for a 3-year production. A large mismatch exists in the BHP curves of wells A, B, and C. Therefore, the preserve ratio needs to be increased to improve accuracy in the BHP response.

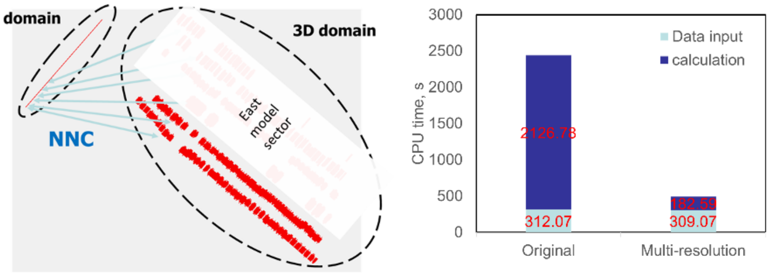

Figure 9.8 (a) Multi-resolution grid system; (b) Run time comparison.

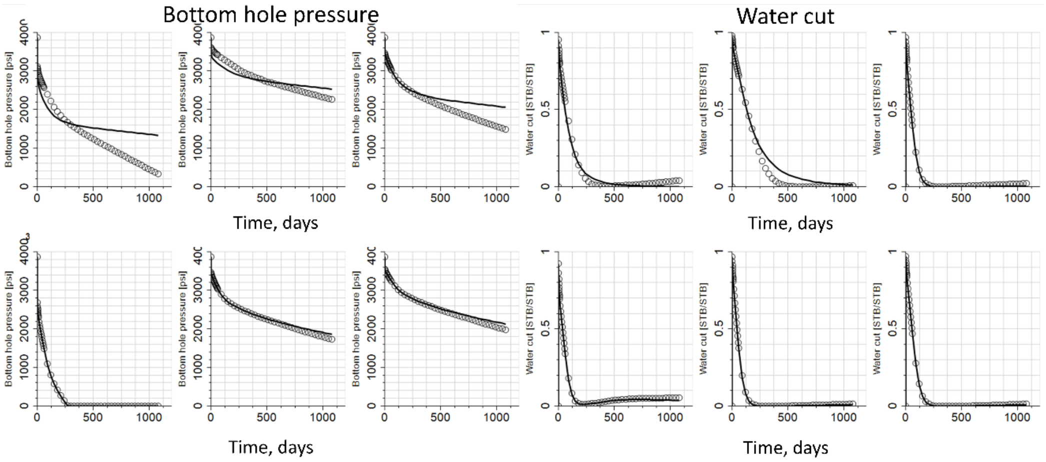

Figure 9.10 Well response comparison (fine model vs. multi-resolution model).

In case 2, we increase the preserve ratio (Figure 9. 11) for each well based on the performance in case 1 in order to improve the accuracy of BHP curves. The selected preserve ratio is determined by examining the accuracy of the well response. The active cell number increases to 0.23 million because of the increasing preserve ratio. The configuration of the multi-resolution grid system is shown in Figure 9.12(a). The run time comparison shown in Figure 9. 12(b) suggests that multi-resolution simulation is about eight times faster than the original fine-scale model. The well responses in Figure 9.13 indicate a high level of accuracy in the performance of the multi-resolution model. Therefore, this combination of preserve ratio is applied to the history matching process for the purpose of simulation acceleration.

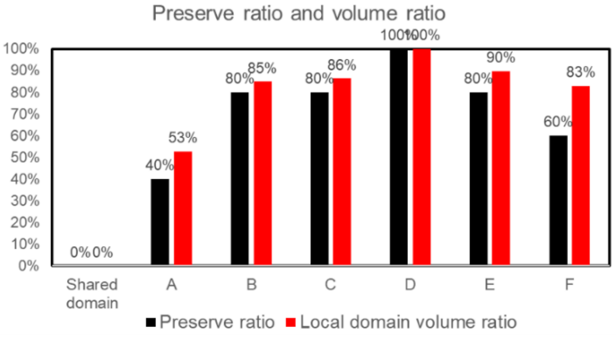

Figure 9.11 Preserve ratio and corresponding local domain volume ratio.

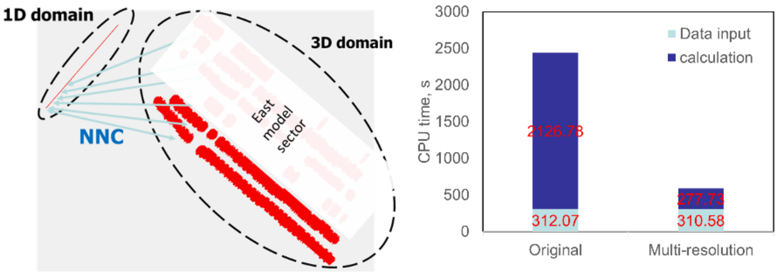

Figure 9.12 (a) Multi-resolution grid system; (b) Run time comparison.

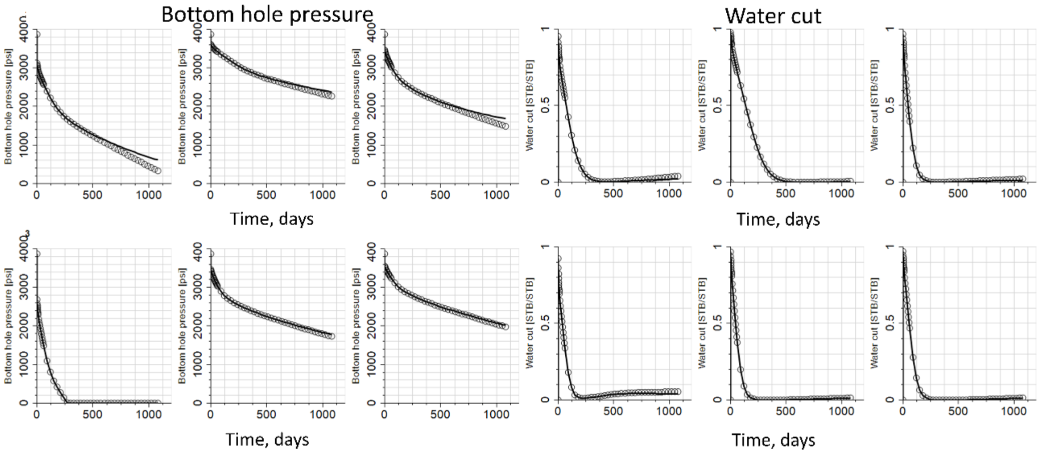

Figure 9.13 Well response comparison (fine model vs. multi-resolution model).

9.4.4 History Matching

This section presents the results of the multi-objective history matching using the non-dominated sorting genetic algorithm. First, sensitivity analysis is conducted to identify heavy hitters among reservoir and hydraulic fracture properties. Starting from a case with base values, only one parameter at a time is switched to its maximum or minimum values, and the rest of the parameters are fixed at their base values. Table 9.1 shows the potential parameters that could be tuned in history matching and had an influence on objective functions of BHP and water rate. The pressure and rate are obtained from simulations to evaluate the effects of each parameter on the selected objective function. The sensitivity tornado plots in Figure 9.14 rank the influence of the listed parameters on BHP and water rate. The parameters with the strongest effect on the objective functions will be chosen, and other low-sensitive parameters will be removed and assigned base values in history matching. According to the magnitude of influence, we select 12 high-influence parameters that are tuned in history matching, including fracture half-length multiplier, fracture width multiplier, fracture height multiplier, fracture conductivity, initial water saturation in fracture, residual oil saturation in fracture, SRV compaction exponent, initial water saturation in SRV, connate water saturation in SRV, SRV NTG, initial solution gas-oil ratio in SRV, and pore volume compressibility coefficient.

Table 9.1 Reservoir and fracture property list.

Variable Name	Min	Max	Base
Fracture half-length multiplier	0.21	1	0.8
Fracture width multiplier	1	10	8
Fracture height multiplier	1	5	2
Fracture conductivity	1	100	15
Fracture compaction exponential	-4	-3	-3.5
Initial Sw in fracture	0.6	0.99	0.8
Connate Sw in fracture	-	-	-
Residual So in fracture	-	-	-
Initial solution gas-oil ratio in fracture	0	0.1	0
PV compressibility coefficient in fracture	6	30	6
SRV compaction exponent	-4	-3	-3.5
Initial Sw in SRV	-	-	-
Connate Sw in SRV	-	-	-
Krw end-point in SRV	0.1	1	0.76
Krw exponential in SRV	1.1	3	2
Residual So in SRV	0.1	0.4	0.3
Kro end-point in SRV	0.1	1	0.85
Kro exponential in SRV	1.1	3	2
SRV volume size	0.2	1	1
SRV transmissibility multiplier	10^{-2}	10^{2}	$10^{-0.65}$
NTG	0.5	1	0.6
Kv/Kh	0.01	1	0.1
Initial solution gas-oil ratio in SRV	0	2.938	0.075
PV compressibility coefficient in SRV	6	30	10

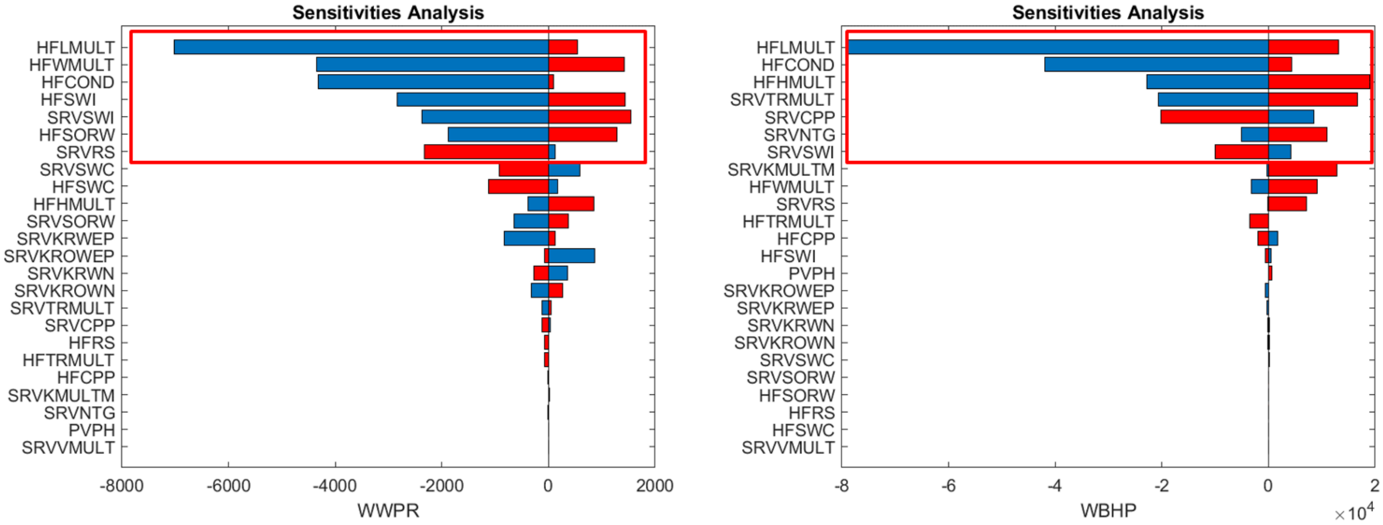

Figure 9.14 Sensitivity tornado plot.

We calibrated the reservoir model using the stochastic-search method, NSGA-II, to find the solution space of the reservoir and fracture parameters. The GA is carried out for seven generations, and the first generation is initialized using a population of 70 realizations. The objective functions are calculated well by well. Figure 9.15 shows the objective function (well responses misfit) of BHP and the water rate of the six wells in the 7th generation, compared to the initial generation. After seven generations, the misfit of two objectives concentrates on lower values, indicating an improvement in history matching quality. Also, the populations move toward the lower left of the figure with a reduction in misfit for both objectives with some indications of a trade-off between the two objective functions. We select ten highly ranked models using the non-dominant sorting and plot the BHP and water rate curves in Figure 9.16. The selected models plotted in black lines are compared with the initial models in grey lines, and the observed data in red stars. The well response comparison confirms the improvement in history matching observed in the objective space.

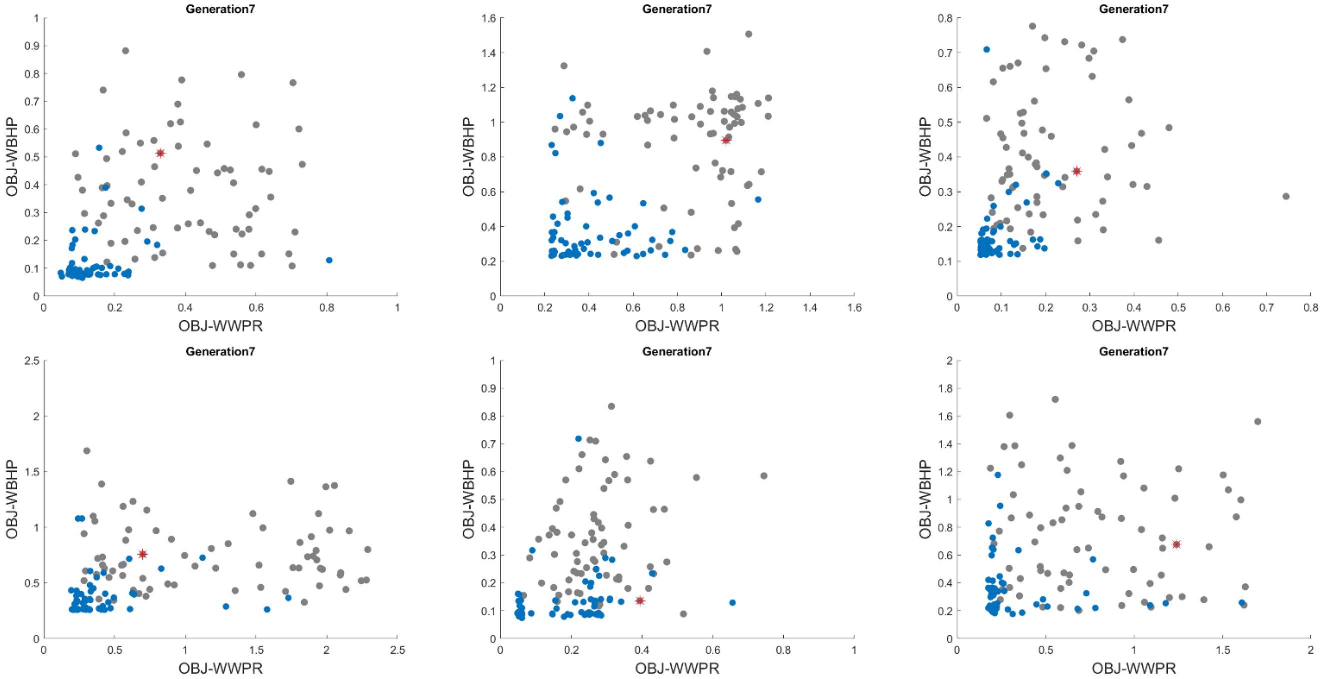

Figure 9.15 The objective function of BHP and water rate at the final generation (blue), compared to the first generation (grey) and the base model (red star) of 6 wells.

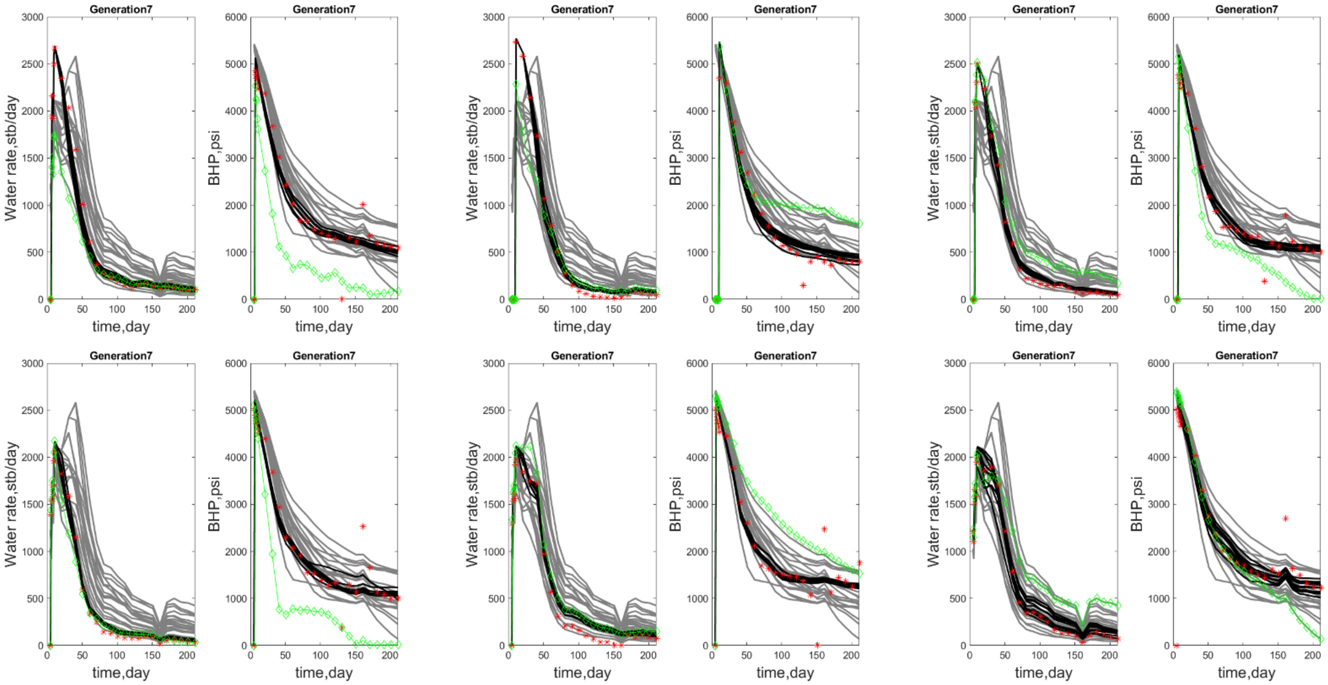

Figure 9.16 The simulation results of the initial models (grey lines) compared with the updated models (black lines), the base model (green diamonds), and the true model (red stars) of 6 wells.

In Figure 9.17, each plot represents the trend of one parameter for each of the six wells, and the boxes represent the range of 25 to 75 percentile of the parameter distributions. The updated reservoir and fracture properties are summarized in Figure 9.17 in comparison to the initial parameter trends, and the shrinkage in the box indicates the decreasing span of parameter ranges and, therefore, a reduction in parameter uncertainty. Most parameter ranges get narrow after seven generations, and few parameters still maintain a high level of uncertainty with shifted median values.

Figure 9.18 illustrates the cumulative distribution of linear flow response. Each plot shows the distribution of one well. The distributions get narrow after seven generations, and the median value shifts to the left-hand side, indicating the overestimation in the linear flow response in the initial models. In Figure 9.19, we evaluate the flow response within fractures using the cumulative distribution functions of total fracture conductivity. The range of distributions is significantly reduced except for the sixth well, which falls into a bimodal distribution. The significant reduction in cumulative distribution functions of the two composite parameters indicates that the history matching is able to detect the fracture and linear flow response with an improved level of confidence. This is valuable to the field operator in terms of the effectiveness of the well completion design.

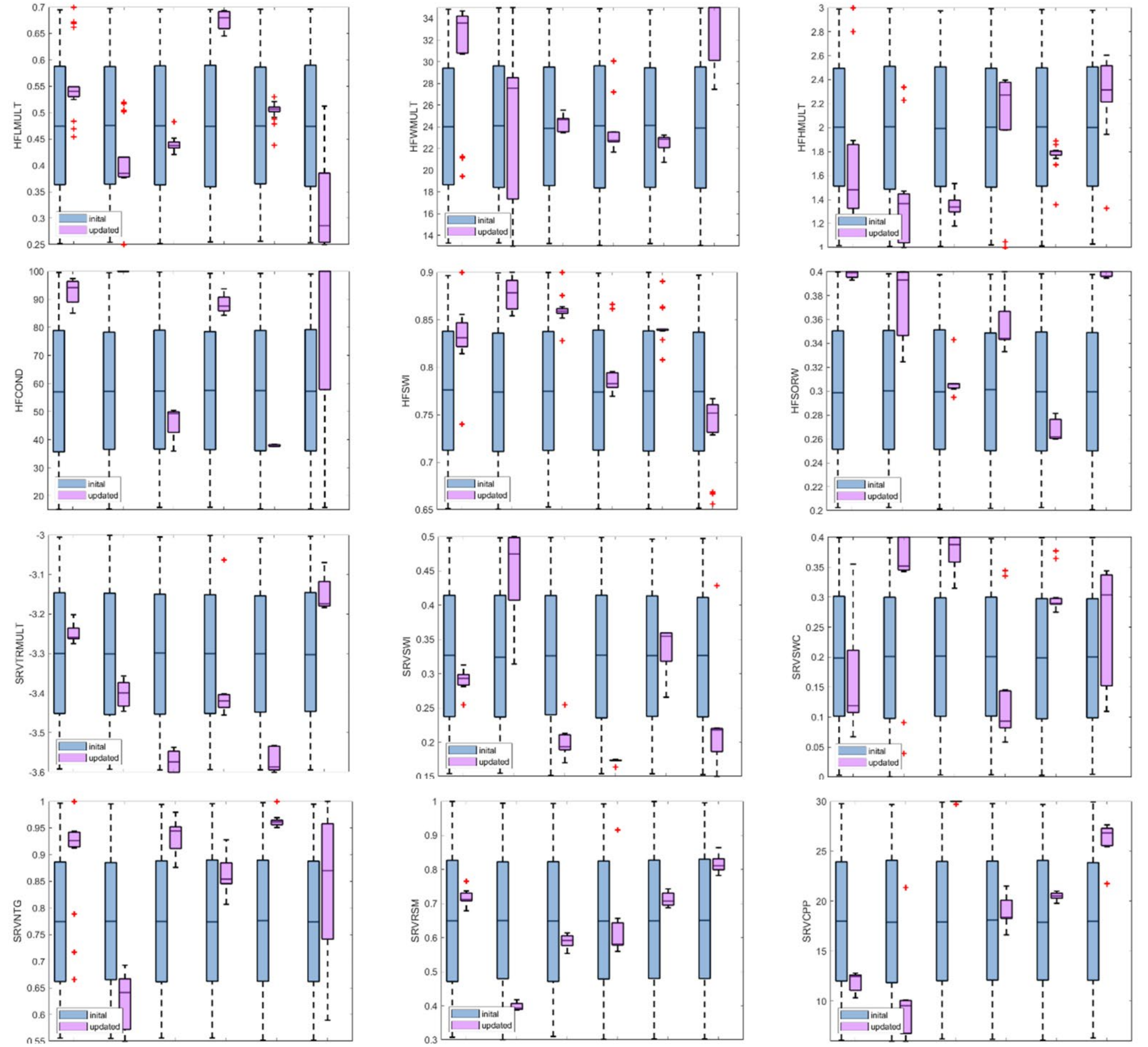

Figure 9.17 Tuned parameter trend comparison (blue box: 25 to 75 percentile range of initial models; pink box: the range updated models).

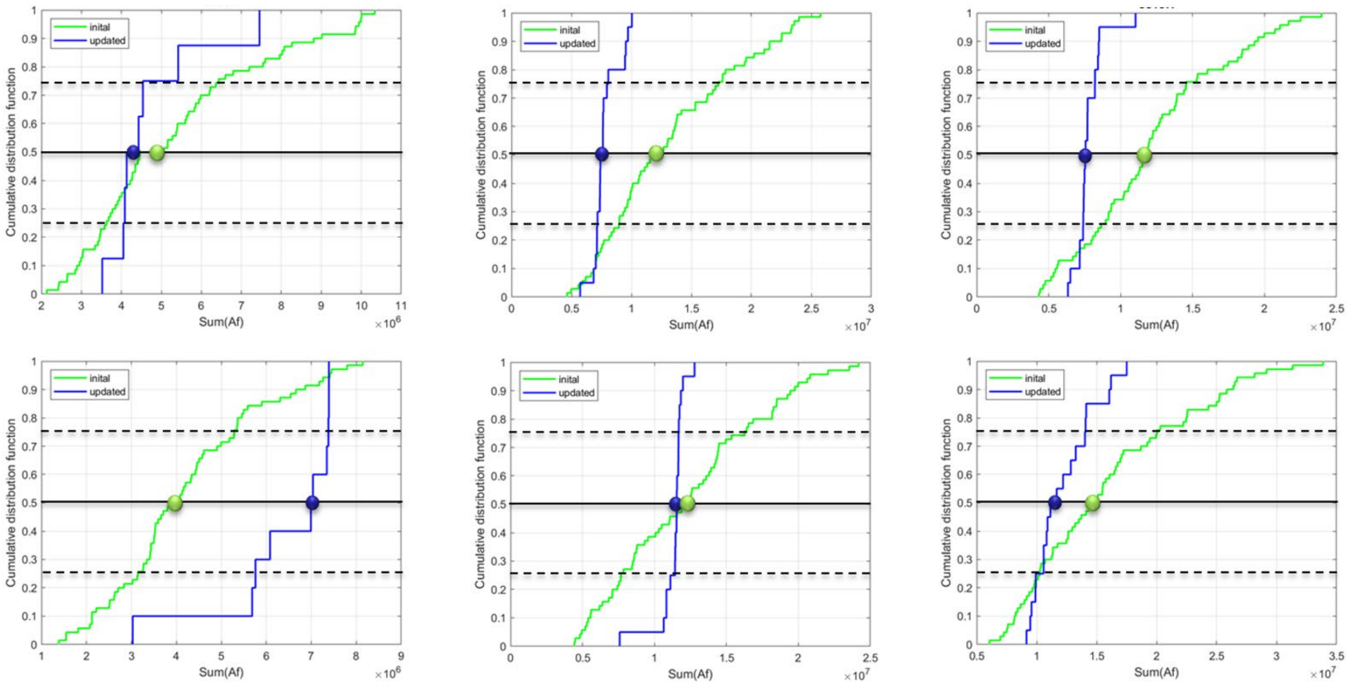

Figure 9.1—CDF plot of $\mathbf{sum}\left(\boldsymbol{x_f h_f \sqrt{k_{SRV}}}\right)$ *of six wells (green: initial; blue: updated).*

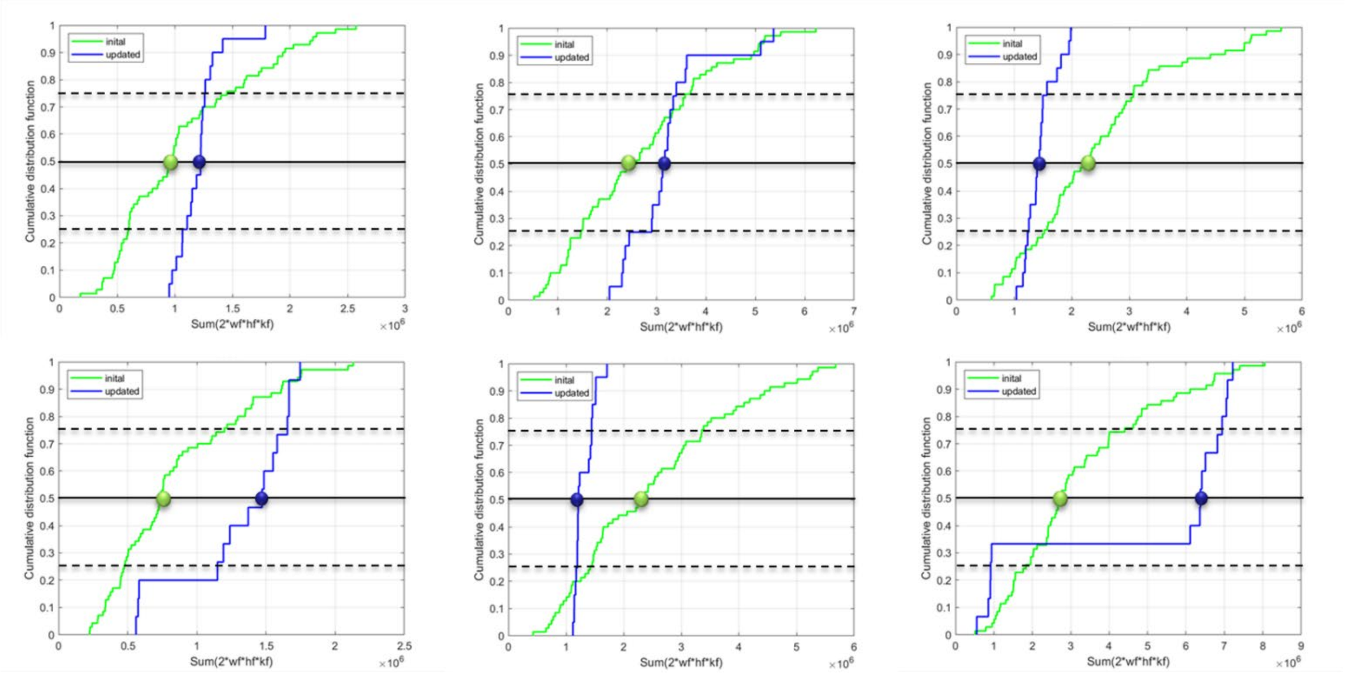

Figure 9.19 CDF plot of cumulative fracture conductivity of six wells (green: initial; blue: updated).

9.5 Conclusions

We have presented a rapid history matching workflow enhanced by a multi-resolution reduced physics model and multi-objective evolutionary (MOEA) algorithm. This workflow has been applied to a field-scale multi-well unconventional reservoir. EDFM is used to set up the fracture model and enable MOEA to tune fracture geometry and conductivity during the history-matching process. This application demonstrates the high efficiency of the multi-resolution simulation model and the effectiveness of the MOEA. The multi-resolution simulation model accelerates the high-resolution reservoir simulation by about an order of magnitude. The MOEA automates the gradient-free history matching and uncertainty analysis with great flexibility and efficiency. It can significantly decrease the misfit of the two objectives (BHP and water rate) for the six wells simultaneously and reduce the uncertainty of the 12 influential parameters.

The novel fast marching-based multi-resolution simulation model applied in this work, combined with the MOEA, enables the scalability of the approach to other oilfield applications. The efficiency and flexibility of the proposed workflow ensure its capability to estimate the reservoir and fracture parameters by inverse modeling of well performance data. The history-matched model is used for performance forecasting with updated reservoir and fracture parameters. The fast-marching-based method allows us to visualize the evolution of the individual well drainage volume and well interactions, making it a powerful tool for optimizing well spacing.

10 Near Wellbore Fracture Geometry Modeling

The aims of this research are realized by investigating fracture initiation in a particular site within the Austin-Chalk formation, which is acknowledged to be a highly complex geologic formation that extends from southern Texas and central Louisiana and overlies the Eagle Ford Shale formation. The Eagle Ford Shale is a sedimentary formation that dates to the Late Cretaceous to Early Paleogene periods and is composed primarily of shale, with interbedded layers of sandstone and siltstone.

The Austin Chalk is a Cretaceous-age formation that is primarily composed of chalk, but also contains shale, clay, and organic-rich marl. The particular site, the properties and conditions of which were used in this study, was located at Webb County, Texas and was part of the Austin Chalk Eagle Ford Field Laboratory project. The input data used in the simulation studies is summarized in Table 10.1. We conducted several sensitivity analyses in an effort to identify and evaluate the factors and conditions that control the initiation, morphology and propagation of near-wellbore propagation of fractures associated with a single fracture cluster under variable completion settings.

Table 10.1 indicates that the Austin Chalk formation is defined by a strike-slip stress regime, in which $\sigma_H > \sigma_v$. The base simulation scenario involves a perforation density of two shots per foot with perforation phasing $\phi = 0°$, and the perforations are placed at the top of the horizontal well. The perforation diameter d_p = 0.01 m (0.4 in) and the perforation tunnel length L_p = 0.1 m (4 in). The constant injection rate of the fracturing fluid is Q_{inj} = 0.008 m/s (3 bbl/min), and the injection duration of t_{inj} = 7.5 ms. The simulated domain has dimensions of 2 m (6.56 ft) in height, 2 m (6.56 ft) in length, and 3 m (9.84 ft) in width.

Table 10.1 Input data used for fracture initiation simulation in Austin Chalk formation.

Properties and parameters	**Value, units**	**Properties and parameters**	**Value, units**
Minimum horizontal stress, σ_h	-	Injection fluid viscosity, μ	0.001 Pa·s (1 cp)
Maximum horizontal stress, σ_H	51-63 MPa	Perforation diameter, d_p	~0.01 m (0.4 in)
Vertical stress, σ_v	43-53 MPa	Perforation density, n_p	-
Pore pressure, P_p	Overpressured	Perforation tunnel length, L_p	0.1 m (4 in)
Poisson's ratio, v	0.22-0.28	Perforation phasing, ϕ	-
Young's modulus, E	50 GPa (7.25×10^6 psi)	Outer wellbore diameter, D_{OD}	-
Total injection rate, Q_{inj}	0.008 m/s (3 bbl/min)	Inner wellbore diameter, D_{ID}	-
Injection time, t_{inj}	7.5 ms	Hole diameter, D_h	-

The fracture morphology predicted by the base-case simulation is illustrated in Figure 10.1. Instead of the two transverse fractures initiating from two perforation tunnels coalesce and form a complex fracture network system in the near-wellbore region instead of proceeding independently as separate fractures.

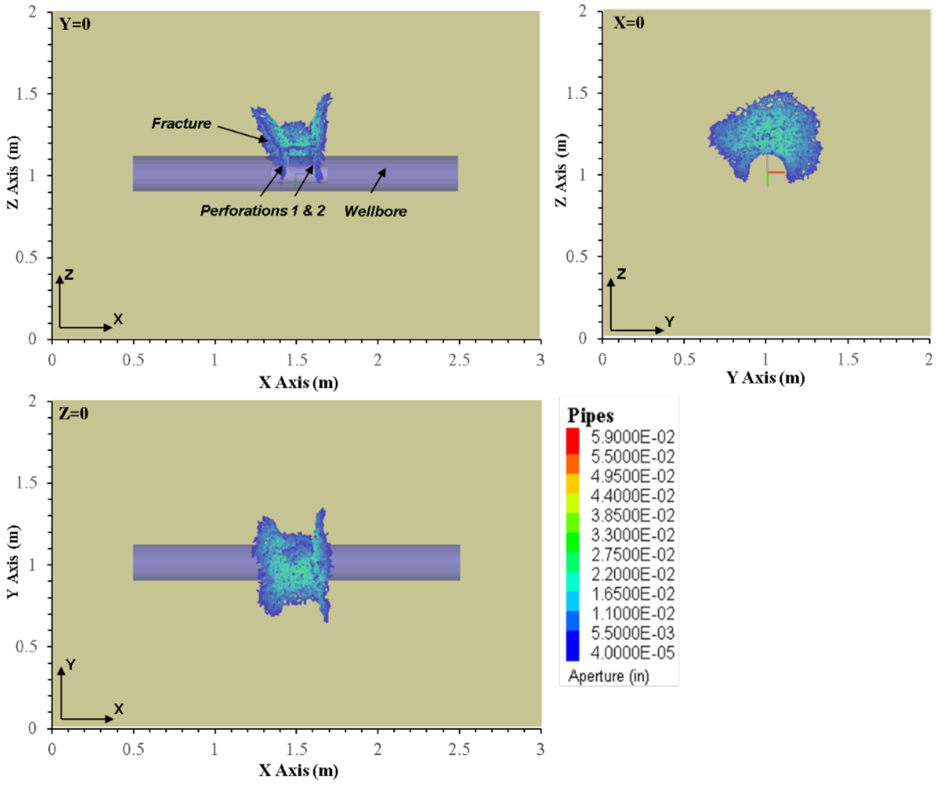

Figure 10.1 Base case scenario: the fracture morphology for single cluster in Austin Chalk formation. The three panels depict projections of the fracture morphology on a plane (involving two dimensions) at a specific location in the 3^{rd} dimension (indicated in the upper left corner of each panel).

Effects of Perforation Tunnel Length

To investigate the impact of the perforation tunnel length on the fracture initiation, we conducted simulations using the properties and conditions of the Austin Chalk formation described in Table 10.1 for two different scenarios. The first scenario considered a short L_p = 0.05 m (2 in), n_p = 2 spf with $\phi = 0°$. The second scenario differed from the first only in the longer L_p = 0.2 m (8 in).

The results of the simulation in the short L_p scenario are depicted in Figure 10.2 and indicate that the transverse and longitudinal fractures (each initiating from separate perforations) tend to coalesce with each other. In contrast to the base case scenario, where the axial fracture formed only between perforations, in this case, the fracture extends in an axial direction beyond the location of one of the two perforations. Conversely, the longer L_p in scenario #2 leads to two fractures that develop and advance independently along a slightly curbing path (Figure 10.3), not merging with each other and not coalescing at any time. Instead, the fractures had a slightly curved path. These findings suggest that increasing the length of the perforation tunnel can have a significant impact on the stability and predictability of the fracture propagation morphology and path, causing the desirable evolution of distinct individual fractures. The obvious conclusion is that L_p is an important (if not a key) parameter affecting the performance of hydraulic fracturing as it can limit/ mitigate (and eliminate) the influence of the near-wellbore conditions on the fracture morphology.

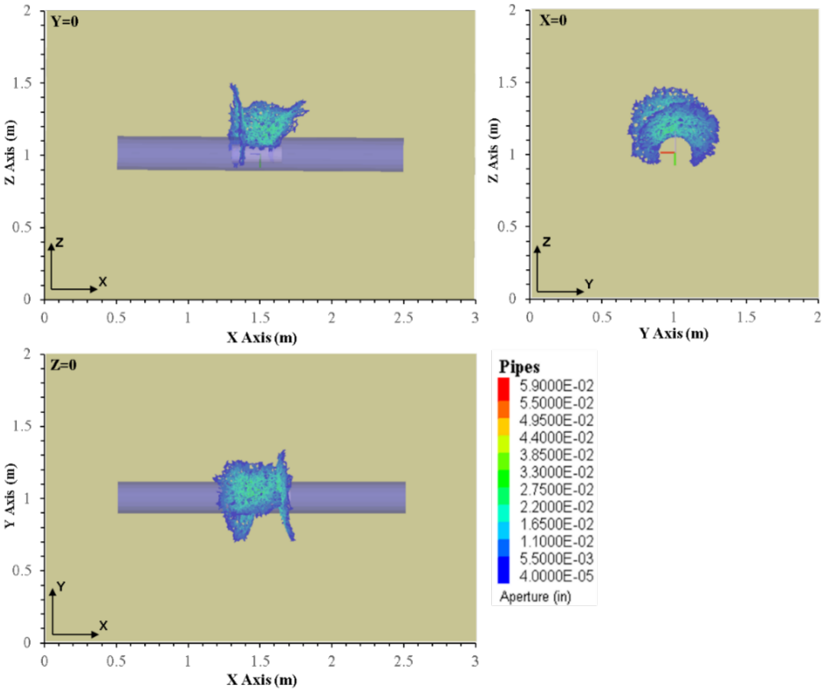

Figure 10.2 The fracture morphology for single cluster in Austin Chalk formation. L_p = 0.05 m (2 in).

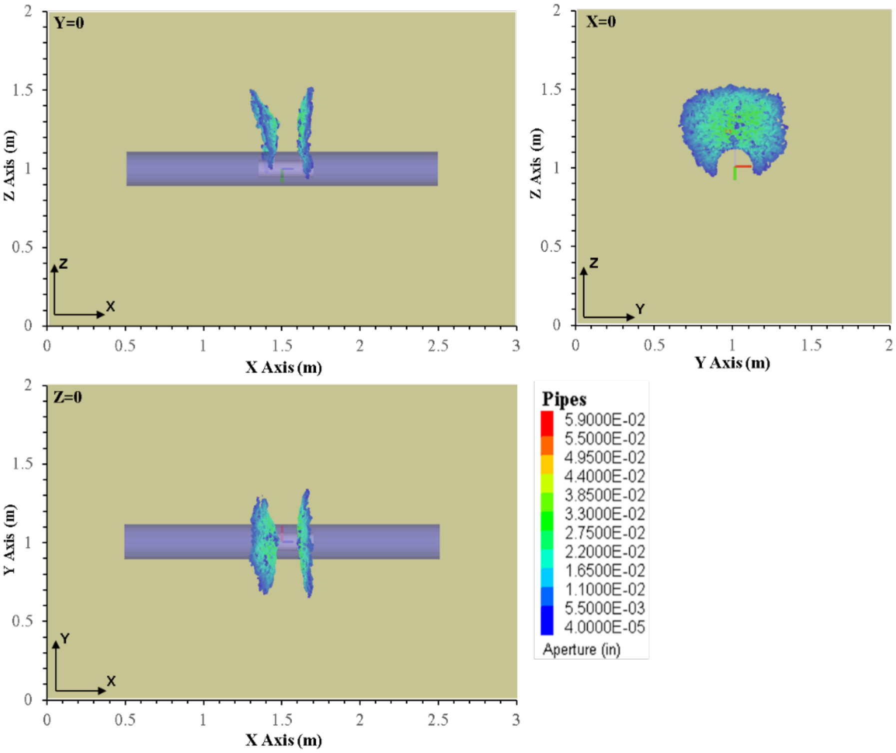

Figure 10.3 The fracture morphology for single cluster in Austin Chalk formation. L_p = 0.2 m (8 in).

Effects of Perforation Diameter and Injection Rates

Downhole video-based imaging (Cramer *et al,* 2020) and acoustic imaging (Robinson *et al,* 2020) in unconventional reservoirs revealed a significant variation in the perforation diameter d_p along the wellbore. Some of the variations were attributed to improper centralizing of the perforating gun (Pongratz *et al,* 2007) and to proppant erosion. Reducing d_p is a common practice of the perforation limited entry technique to promote even (more uniform) fluid distribution and to enhance the cluster efficiency. However, there is a limited understanding of how d_p can affect the fracture initiation in the near-wellbore region.

We simulated the evolution of fractures originating from perforations with a d_p ranging between 0.0038 m (0.15 in) and 0.02 m (0.8 in). The rest of the input parameters were as in the base case (see Table 10.1). The results of these simulations in Figure 10.4 indicated that the size of d_p can significantly affect the fracture morphology. For $d_p = 0.0038$ m (0.15 in), a single fracture evolved from the tip of the perforation, while the fracture initiation from the second perforation appeared to be suppressed.

When $d_\mathrm{p} = 0.02$ m (0.8 in), two fractures initiate from the two perforations, but they are narrower and slightly curved compared to those for the case of $d_p = 0.0038$ m (0.15 in), as shown in Figure 10.5. We note that when $d_p = 0.0038$ m (0.15 in) and the injection rate Q_{inj} increases from 0.008 m/s (3 bbl/min) to 0.026 m/s (10 bbl/min), fractures evolve from both perforations and form a complex fracture network in the near-wellbore region (Figure 10.6). This behavior is consistent with the findings from laboratory studies by Fallahzadeh *et al* (2017) and Weijers *et al* (1994), and from the numerical studies of Li *et al* (2022).

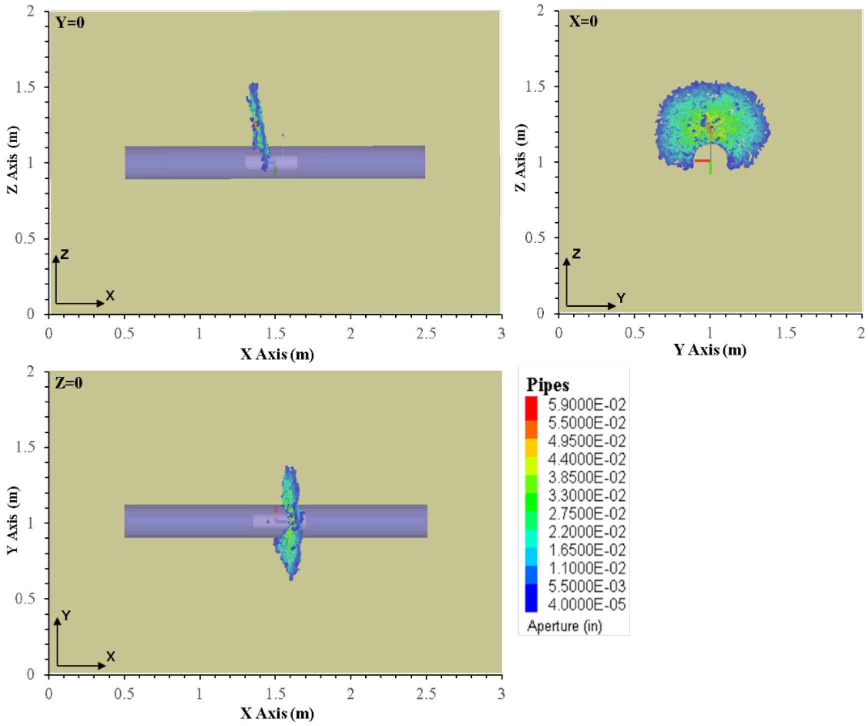

Figure 10.4 Fracture morphology for single cluster in Austin Chalk formation. $d_p = 0.0038$ *m (0.15 in).*

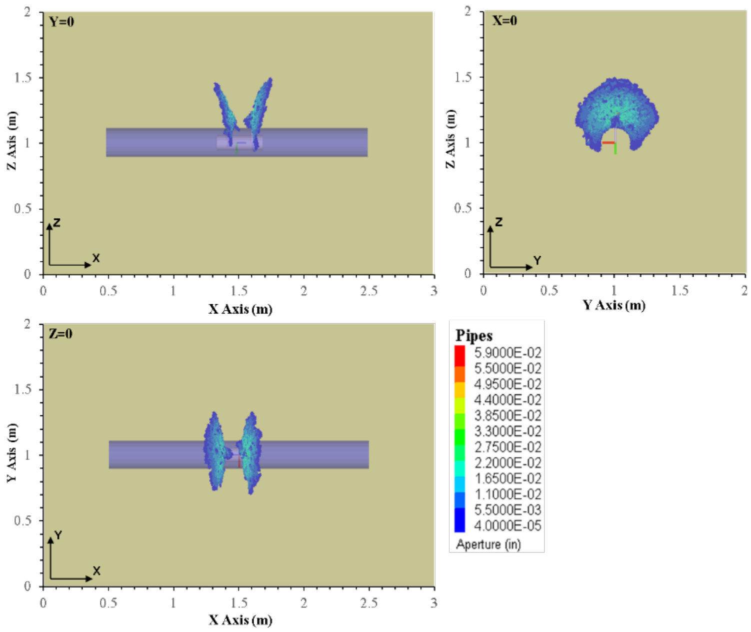

Figure 10.5 Fracture morphology size for single cluster in Austin Chalk formation. d_p *= 0.02 m (0.8 in).*

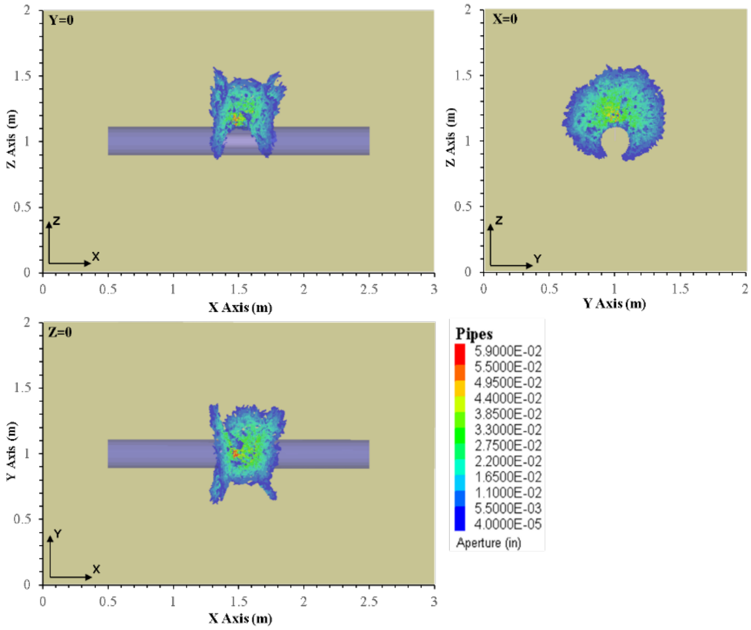

Figure 10.6 Fracture morphology for single cluster in Austin Chalk formation. d_p *= 0.0038 m (0.15 in).* Q_{inj} *= 0.026 m/s (10 bbl/min).*

11 Lessons Learned (Operator & Industry Applications Perspective)

This outstanding research project has significantly advanced the industry's understanding of hydraulic fracturing mechanics, reservoir engineering, completions / operations engineering, and geological sciences. This is leading to enhanced subsurface development and operational efficiencies. By integrating cutting-edge technologies in new ways to assess intricate geologic and subsurface dynamics, the project has unveiled critical insights into in-situ conditions, corresponding stress behaviors, fracture / natural fault propagation characteristics, and valuable wellbore interactions. These findings have not only optimized current operator development efficiencies but have also paved the way for innovative approaches in reservoir management and development strategy standardization. Several of the latest learnings are discussed below and are shared in numerous recent publications and will continue to be shared for many years to come.

The data collected spans multiple disciplines and is filled with rich insights. Many areas involved in subsurface development all across the United States and many international regions as well will benefit from these lessons learned, observations, and real-world applications. The operator and research teams have worked closely together to summarize important factors, which are listed below.

Summary Learnings

- Utilized DFIT and fiber optics to accurately measure the characteristics needed for a comprehensive stress tensor model.
- Detailed the subsurface interaction factors including plugs, cement, chemicals, isolation, and multi-cluster propagation behavior.
- Enhanced wellbore injection initiations and wellbore solids management procedures.
- Leveraged new diagnostic methods to advance natural fracture detection and activation analysis.
- Refined subsurface design standards and elucidated the mechanisms affecting wellbore integrity.

Each of these factors are being discussed in publications, reports, and industry discussions with in extensive details. For instance, in 2024, a 30 page paper (SPE 217780) has documented the critical value of pumping the first ever Diagnostic Fracture Injection Test across fiber optics on two adjacent wells. This study has significantly enhanced our understanding of some complexities in hydraulic stimulations, going beyond traditional DFIT theory. Combined use of advanced datasets like fiber optics and systematic testing approaches help identify key factors affecting fracture mechanics and pressure analysis. This would not have been possible for an operator to achieve alone due to the required instrumentation, expertise, intervention, and monitoring requirements. With that said, several major conclusions can be drawn from the study:

- LF-DAS fiber response has now been shown that it can be used to understand fracture growth in both the treatment well and offset monitor wells. Comparison of the fiber signals in both wells improves understanding of fracture geometry evolution.

- Hydraulically driven fractures in a horizontal well environment are not planar. Near-well tangential stress concentration causes initiation and propagation of longitudinal (wellbore co-axial) fractures that are identifiable on fiber.
- Injected fluid is partitioned between longitudinal and transverse fractures. Partitioning of the injected fluid volume affects the rate of fracture growth and time of first arrival at offset monitor wells.
- After the end of injection, fluid flow between the longitudinal and transverse fractures is driven by anisotropy in the earth stress tensor. Fluid expelled from the longitudinal fractures into the transverse fractures supports the observed well pressure and delays fracture closure.
- Fiber strain interpretations suggest that fracture closure is effectively uniform and simultaneous at the injection site perforations and at the fracture tip or monitor well location.
- Longitudinal fractures may extend for hundreds of feet along the treatment well and can affect fracture initiation and growth from subsequent stages when perforated intervals overlap the induced fracture plane.

These factors are critically important for all operators as accurate estimation of fracture growth rate and extent is essential for determining the stimulated reservoir volume, which contributes to the effective drainage area and ultimate recovery, as well as for assessing the stimulated system's flow capacity that controls the post-frac production rate.

In addition to these extremely important factors affecting subsurface dynamics, several other confounding factors have been identified throughout the project and will continue to be discussed and published upon. For instance, tests were proactively implemented to capture clear examples of factors contributing to isolation. These include plug integrity and the implications to prior current and prior stimulation locations. They also include tests that assess how chemicals can adversely and positively effect multi-cluster, non-planar, multi-stage development at the beginning of injection periods and throughout the duration of injection. Finally, the data captured allows for a full picture of how the cementing, natural fracturing conditions, and injection architecture play a role in reservoir extraction and management.

Moreover, the advanced downhole monitoring equipment, offset monitoring equipment downhole, and multiple types of surface data acquisition equipment (microseismic, active seimic, and sealed wellbore pressure monitoring) allowed for extensive testing of different chemicals, volumes, and architectures to ensure safe, efficient operations. Having this comprehensive look at what was happening before, during, and after an injection period as well as near-field and far-field measurements allow unprecedented capabilities for triangulation of issues commonly encountered in challenging downhole subsurface environments. One of these issues for instance is the positive and negative relationships between particle transport, rheological properties, and fluid mechanics. Adjusting each of these factors allowed the operator to test / showcase how the wellbore and reservoir responds to more significant variability during the injection period, relaxation period, and flowback period.

Within these systematic tests, many critical natural geologic features were able to be studied. This was due to advanced core lab tests, in-situ downhole measurements, and all of the multi-pronged diagnostics. These factors illuminated how more efficient stimulations have a relationship to complex geologic interactions. By understanding the interactions with these factors, the industry and researchers can integrate these learnings into their diagnostic interpretations and lab testing configurations.

This field test side provides unique insights that influence our understanding of well development by directly tying common field tests to subsurface fundamentals with more advanced diagnostics to improve our predictive workflows. Many of the factors explored include near well failure mechanics, fracture growth & volume characteristics, and dynamic responses related to poroelasticity and stress. These learnings continue to deliver actionable knowledge that can be used to drive resource development efficiency and optimization for many operators to continue advancing the petroleum industry.

12 Summary of Project Publications

1. Carrascal-Delgado, Fabián, Abedi, Sara, Hill, A. D., and Ding Zhu. (2022) "Feasibility of Using Drill Cuttings as Proppants in Unconventional Reservoirs." Paper presented at the SPE Hydraulic Fracturing Technology Conference and Exhibition, The Woodlands, Texas, USA, February 2022. doi: https://doi-org.srv-proxy1.library.tamu.edu/10.2118/209173-MS

Summary: This study investigates the feasibility of incorporating drill cuttings into the proppant slurry during hydraulic fracturing as a solution to disposal challenges. Conductivity experiments with varying cuttings fractions show minimal impact on fracture conductivity, suggesting that adding up to 25% drill cuttings to the proppant has insignificant effects. Results indicate a potential environmentally friendly disposal method while reducing fracturing costs.

2. Chen, Hongquan, Onishi, Tsubasa, Park, Jaeyoung, and Akhil Datta-Gupta. "Computing Pressure Front Propagation Using the Diffusive-Time-of-Flight in Structured and Unstructured Grid Systems via the Fast-Marching Method." SPE J. 26 (2021): 1366–1386. doi: https://doi.org/10.2118/201771-PA

Summary: This paper introduces a new method for computing diffusive-time-of-flight (DTOF) in unconventional reservoir analysis. Unlike traditional finite difference approaches, it utilizes finite volume discretization and the fast-marching method (FMM). The method is validated with analytical solutions and applied to various complex grid systems, demonstrating its broad applicability and ease of implementation in commercial reservoir simulators.

3. Chen, Mengyuan, Tang, Jin , Zhu, Ding , and Alfred Daniel Hill. (2021) "Classification and Localization of Low-Frequency DAS Strain Rate Patterns with Convolutional Neural Networks." Paper presented at the SPE Europec featured at 82nd EAGE Conference and Exhibition, Amsterdam, The Netherlands, October 2021. doi: https://doi-org.srv-proxy1.library.tamu.edu/10.2118/205136-MS

Summary: This study develops a machine learning-based workflow to identify and locate fracture-hit events in simulated strain rate responses correlated with low-frequency distributed acoustic sensing (DAS) data. By training a custom convolutional neural network (CNN) model, near-perfect predictions are achieved for both event classification and localization. The study also explores edge detection techniques for event pattern recognition, highlighting the effectiveness of CNN models over traditional methods for real-time event detection from fiber-optic sensing data.

4. F. Cheng, J. Correa, B. M. Freifeld, T. Wood, K. Nihei, D. Guerra, D. Hill, J. Birkholzer, and J. B. Ajo-Franklin. (2019). "Using Surface Orbital Vibrators (SOV) and Distributed Acoustic Sensing (DAS) for monitoring of unconventional reservoirs: preliminary results from the Eagle Ford Shale", 2019, AGUFM, 2019, H11D-05

Summary: This study explores the potential of combining Surface Orbital Vibrators (SOVs) with fiber-optic Distributed Acoustic Sensing (DAS) for seismic monitoring in unconventional reservoirs. A field test demonstrates the high repeatability achievable with semi-permanent SOV sources, crucial for time-lapse analysis. Results suggest that DAS is more sensitive with inline excitation, revealing clear P and S reflections as well as mode conversions, indicating potential for high-temporal-resolution seismic monitoring of unconventional reservoirs at a low cost.

5. Cheng, Feng & Correa, Julia & Dou, Shan & Freifeld, Barry & Wood, Todd & Nihei, Kurt & Guerra, Dante & Birkholzer, Jens & Chi, Benxin & Ajo-Franklin, Jonathan. (2020). "Testing of a Permanent Orbital Surface Source and Distributed Acoustic Sensing for monitoring of unconventional reservoirs: preliminary results from the Eagle Ford Shale." Geophysics. 86. P. 10.1190/geo2020-0403.1.

Summary: Distributed Acoustic Sensing (DAS) and Surface Orbital Vibrators (SOVs) offer high repeatability and resolution for in-well monitoring. A field VSP test in the Eagle Ford play pairs SOV sources with DAS to evaluate their potential for monitoring unconventional reservoirs. Results show promise for low-cost, high-resolution seismic monitoring.

6. Fu, Jia, Chen, Hongquan, Yao, Changqing, Sakaida, Shohei, Kerr, Erich, Johnson, Andrew, Datta-Gupta, Akhil, Zhu, Ding, and A. Daniel Hill. "Field Application of a Novel Multi-Resolution Multi-Well Unconventional Reservoir Simulation: History Matching and Parameter Identification." Paper presented at the SPE/AAPG/SEG Unconventional Resources Technology Conference, Denver, Colorado, USA, June 2023. doi: https://doi.org/10.15530/urtec-2023-3857125

Summary: This study develops an efficient workflow for multiwell unconventional reservoirs, integrating a multiresolution simulation model and a multiobjective evolutionary algorithm (MOEA). It utilizes a novel fast-marching simulation method to accelerate history matching, aided by distributed temperature sensing data insights. Sensitivity analysis identifies key parameters for calibration, reducing uncertainty and facilitating evaluation of well completion design effectiveness.

7. Guerra, Dante, Arceneaux, Deron, Zhu, Ding, and A. D. Hill. (2022). "Relative Permeability Behavior of Oil- Water Systems in Wolfcamp and Eagle Ford Fractures." Paper presented at the SPE International Hydraulic Fracturing Technology Conference & Exhibition, Muscat, Oman, January 2022. doi: https://doi-org.srv-proxy1.library.tamu.edu/10.2118/205295-MS

Summary: This study experimentally investigates oil-water relative permeability in fractures using downhole cores from the Wolfcamp and Eagle Ford Shale formations. Results reveal a clear relationship between relative permeability and saturation, following the generalized Brooks-Corey correlation. The study also underscores the impact of surfactants on oil-water relative permeability, providing insights for fracture fluid design optimization.

8. Hill, A. D., Laprea-Bigott, M., Zhu, D., Moridis, G., Schechter, D. S., Datta-Gupta, A., Selvan, K. (2020, July 20). "The Eagle Ford Shale Laboratory: A Field Study of the Stimulated Reservoir Volume, Detailed Fracture Characteristics, and EOR Potential." Unconventional Resources Technology Conference. doi:10.15530/urtec-2020-2973

Summary: The Eagle Ford Shale Laboratory project, sponsored by the DOE and industry partners, aims to enhance understanding and monitoring of key processes in unconventional oil production. It involves advanced diagnostic methods to map hydraulic fractures, proppant distribution, and stimulated reservoir volume. Through a multidisciplinary approach, including field monitoring, laboratory testing, and coupled modeling, the project seeks to improve initial stimulation, re-fracturing, and enhanced oil recovery (EOR) processes.

9. Hill, A. D., Zhu, D., Kerr, E., Scofield, R., Jordan, D., Estrada, E., Brashear, A. T., and T. Tajima. Fracture Conductivity Created by Acids and Proppants in the Austin Chalk Formation. Paper presented at the SPE Annual Technical Conference and Exhibition, Houston, Texas, USA, October 2022. doi: https://doi-org.srv-proxy2.library.tamu.edu/10.2118/210213-MS

Summary: This study assesses proppant and acid fracturing stimulation efficiency in the Austin Chalk formation through conductivity tests using downhole core and outcrop samples. Results suggest differences in conductivity behavior between the two methods, with propped fractures exhibiting sustained conductivity at high closure stress, while acid fractures depend on injection conditions and rock integrity. Both methods show potential for creating sufficient conductivities in the low permeability Austin Chalk formation.

10. Iino, Atsushi, Jung, Hye Young, Onishi, Tsubasa, and Akhil Datta-Gupta. "Rapid Simulation Accounting For Well Interference in Unconventional Reservoirs Using Fast Marching Method." Paper presented at the SPE/AAPG/SEG Unconventional Resources Technology Conference, Virtual, July 2020. doi: https://doi.org/10.15530/urtec-2020-2468

Summary: This study introduces a novel extension of the Fast Marching Method (FMM) for rapid simulation of multi-well problems in unconventional reservoirs. By incorporating dynamic changes in drainage boundaries and allowing communication between subdomains using inter-partition transmissibility, the proposed approach improves accuracy and computational efficiency. Benchmarked against a commercial finite difference simulator, results demonstrate benefits for optimizing well spacing and minimizing frac-hits in unconventional plays.

11. Julia Correa, Avinash Nayak, Feng Cheng, Linqing Luo, Jaewon Saw, Todd Wood, Kenichi Soga, Barry Freifeld, Jonathan Ajo-Franklin, 2022, Continuous and Automated Seismic Monitoring using Fiber-Optics Sensing and Surface Orbital Vibrators during Hydraulic Stimulation of an Unconventional Reservoir, AGU Fall Meeting Abstracts, S16A-05.

Summary: This study proposes using distributed acoustic sensing (DAS) and surface orbital vibrators (SOV) for high-temporal time-lapse seismic monitoring of hydraulic fracturing in unconventional reservoirs. Preliminary results show continuous monitoring every hour before, during, and after stimulation, with data processed through edge computing. Additionally, distributed temperature sensing (DTS) and distributed strain sensing (DSS) are utilized for comprehensive fiber-optic monitoring.

12. Kerr, Erich, Barree, Robert, and Erick Estrada. "What Can You Learn from a DFIT on Fiber Optics?." Paper presented at the SPE Hydraulic Fracturing Technology Conference and Exhibition, The Woodlands, Texas, USA, February 2024. doi: https://doi-org.srv-proxy2.library.tamu.edu/10.2118/217780-MS.

Summary: This paper presents the analysis of a large-scale DFIT treatment conducted as part of the Austin Chalk/Eagle Ford Field Laboratory (ACEFFL). The DFIT pressure analysis was compared with fracture geometry information obtained from the low-frequency DAS response of an optical fiber in an offset well.

13. Kryvenko, S., Moridis J. G., Blasingame A. T. (2021). "Modified Higher-Order 3D Displacement Discontinuity Method for Prediction of Fracture Propagation." Paper presented at SPE/AAPG/SEG Asia Pacific Unconventional Resources Technology Conference on Nov. 16-18, 2021.

Summary: This study examines hydraulic fracturing in infill multi-fracture horizontal wells using numerical methods. Higher-order numerical schemes are introduced to improve accuracy and computational efficiency. The application of higher-order 3D HDDM accurately predicts fracture width and fluid flow distribution, validated against analytical models. The simulator developed in this study is effective for designing fracturing in unconventional reservoirs.

14. Leggett, S., Zhu, D., Hill, A.D., Kerr, E. (2022) "Rapid Estimations of Dynamic Hydraulic Fracture Fronts From Cross-well Low-Frequency Distributed Acoustic Sensing Strain-Rate Measurements." Paper presented at the Unconventional Resources Technology Conference, Houston, TX, June 20-22, 2022. URTeC 3722728.

Summary: This study introduces two novel approaches to estimate fracture front locations from low-frequency distributed acoustic sensing (LF-DAS) data. The first method approximates the fracture front shape as an arc using curve fitting, while the second method solves the inverse problem by optimizing fracture and geomechanical parameters to match observed LF-DAS signals. Both methods rapidly estimate evolving fracture front locations with minimal parameters, showing potential for real-time fracture front estimation from LF-DAS measurements.

15. Leggett, Smith Edward, Zhu, Ding, and Hill, A. D.: Thermal Effects on Far-Field Distributed Acoustic Strain-Rate Sensors, *SPE Journal* 27 (02): 1036–1048. DOI: 10.2118/205178-PA

Summary: This study examines temperature effects on LF-DAS-measured strain responses, proposing a model to relate strain, temperature, and optical phase shift. A workflow simulates LF-DAS responses, integrating strain and temperature effects. Initial strain dominance shifts to temperature over time. Comparison with field cases enhances LF-DAS interpretation, and a proposed sensing configuration identifies "wet fractures" intersecting wells.

16. Leggett, Smith, Reid, Teresa, Zhu, Ding, and A. D. Hill (2022). "Experimental Investigation of Low-Frequency Distributed Acoustic Strain-Rate Responses to Propagating Fractures."

Paper presented at the SPE Hydraulic Fracturing Technology Conference and Exhibition, The Woodlands, Texas, USA, February 2022. doi: https://doi-org.srv-proxy1.library.tamu.edu/10.2118/209135-MS

Summary: Lab-scale hydraulic fracture experiments with embedded optical strain sensors were conducted to understand the response of low-frequency distributed acoustic sensing (LF-DAS) to fracture propagation. Transparent epoxy blocks were used to visualize fractures induced by dyed water injection. The strain response was recorded using fiber Bragg grating sensors and compared with Sneddon's solution for a penny-shaped crack. A method to estimate fracture geometry from fiber-optic strain data was developed and validated against experimental results.

17. Leggett, Smith, Sakaida, Shohei, Zhu, Ding, Hill, A. D., Kerr, Erich: Interpretation of Fracture Initiation Points by In-Well Low-Frequency Distributed Acoustic Sensing in Horizontal Wells, *SPE Journal* (2023), DOI: 10.2118/212328-PA

Summary: This study proposes separating temperature and strain components in LF-DAS sensing for in-well strain monitoring. Theoretical coefficients are derived and validated using distributed temperature sensing (DTS) data. Extracting the temperature component reveals nonzero LF-DAS measurements are primarily within the treated region, suggesting fracture initiation points.

18. Li, Gongsheng, Morita, Nobuo, Zhu, Ding, Kerr, Erich, Johnson, Andrew, Ross, Katie, Estrada, Erick, and Reid Scofield. "Integrated 3D Numerical Modelling of Pressure Behavior and Casing Response at Offset Monitor Well During Fracturing." Paper presented at the SPE Hydraulic Fracturing Technology Conference and Exhibition, The Woodlands, Texas, USA, January 2023. doi: https://doi-org.srv-proxy1.library.tamu.edu/10.2118/212316-MS.

Summary: This study introduces an integrated model to simulate casing response and pressure changes during hydraulic fracturing in offset wells. An analytical model based on stress in a thick wall cylinder was developed. This integrated numerical model includes fracture propagation, 3D geomechanics, and transient fluid flow modeling. The model calculates displacement and stress-strain behavior, estimating changes in casing volume and surface pressure. Simulation results align with existing analytical solutions, showing pressure increases as fractures intersect the casing, followed by a pressure decline during fracture closure.

19. Li, Gongsheng, Sakaida, Shohei, Zhu, Ding, Hill, A. D., and Erich Kerr. "Evaluation of Fracture Stimulation Performance Based on Production Log Interpretation." Paper presented at the SPE Hydraulic Fracturing Technology Conference and Exhibition, The Woodlands, Texas, USA, February 2024. doi: https://doi.org/10.2118/217801-MS

Summary: This paper discusses the use of production logging to assess and optimize fracture stimulation designs in hydraulically fractured horizontal wells. Using multiple sensors array tool and temperature log, the study interprets volumetric flow rates and identifies fluid entry locations along the wellbore. By comparing these interpretations, the paper evaluates fracture design effectiveness based on stage production performance using temperature log interpretation.

20. Ma, Yuanyuan & Ajo-Franklin, Jonathan & Nayak, Avinash & Correa, Julia & Kerr, Erich. (2024). DAS microseismic reflection imaging for hydraulic fracture and fault lineament characterization. GEOPHYSICS. 1-49. https://doi.org/10.1190/geo2023-0582.1

Summary: This study introduces a novel workflow using downhole DAS to characterize hydraulic fractures in 3D without assuming fracture orientation. By treating microseismic events as high-frequency sources and applying prestack Kirchhoff migration, it generates high-resolution 3D reflectivity volumes, revealing detailed subsurface fracture networks. Validation with data from the Eagle Ford Shale and Austin Chalk improves understanding of fracture geometry and enables direct estimation of fracture height and length.

21. Ma, Yuanyuan, Ajo-Franklin, Jonathan, Nayak, Avinash, Zhu, Xiaoyu, and Julia Correa. "DAS microseismic reflection imaging for hydraulic fracture and fault zone mapping." Paper presented at the SEG/AAPG International Meeting for Applied Geoscience & Energy, Houston, Texas, August 2023. doi: https://doi.org/10.1190/image2023-3907834.1

Summary: This study presents a new method for 3D fracture imaging using microseismic reflections recorded by DAS. It applies prestack Kirchhoff migration to individual microseismic events, stacking results to generate a 3D reflectivity volume revealing subsurface fracture and fault networks. Application to a dataset from the Eagle Ford Shale and Austin Chalk improves understanding of fracture geometry and fault lineaments compared to conventional methods.

22. Martogi, D., Abedi, S. (2020) "Microscale approximation of the elastic mechanical properties of randomly oriented rock cuttings." Acta Geotech. https://doi.org/10.1007/s11440-020-01020-9

Summary: This study proposes a method to estimate the elastic properties and bedding orientations of rock cuttings using microindentation tests. An inverse algorithm predicts these properties by minimizing errors between experimental and predicted moduli, with results matching well with ultrasonic pulse velocity measurements.

23. Martogi, D., Abedi, S. (2021). "Fracture formation of brittle and ductile materials from scratch test." Paper presented at the 55th U.S. Rock Mech./Geomech. Symp., Houston, Texas, 2021/6/20-23/.

Summary: This study explores scratch-induced fractures in brittle materials using a micro-scratch device. Experimental data, including tangential force, scratch depth, and Acoustic Emission activity, are collected during the tests on fused quartz and borosilicate glass. Fracture initiation occurs under tensile loading, progressing to mixed tensile-shearing loading and eventually shearing loading. Fracture toughness is approximated, with only Mode-II fractures identified in the rock samples.

24. Martogi, D., Abedi, S., Crystal, S., & Mitchell, I. (2019). "Mechanical properties of drill cuttings based on indentation testing and contact mechanics solutions." Paper presented at the 2019 SPE Annual Technical Conference and Exhibition. https://doi.org/10.2118/196214-ms

Summary: This study presents a method to assess shale rock mechanical properties using indentation tests on randomly oriented cuttings. By employing microindentation and a constrained inverse algorithm, elastic constants are deduced from contact mechanics solutions, addressing challenges posed by indistinguishable bedding orientation. Validation through Ultrasonic Pulse Velocity tests confirms the accuracy of the approach, offering a cost-effective alternative to traditional core sample retrieval for shale characterization.

25. Martogi, D., Prakash, R., Varanasi, V.R.S.B., and Abedi, S. (2022). "Impact of Oil Based Mud on Chemo-Mechanical Properties of Cuttings and its Treatment." Paper presented at the 56th US Rock Mechanics/Geomechanics Symposium held in Santa Fe, New Mexico, USA, 26-29 June 2022. ARMA 22-440.

Summary: This study examines the effects of oil-based mud (OBM) contamination on the chemo-mechanical properties of rock cuttings from Eagle Ford and Marcellus formations. Various cleaning methods, including wiping, solvent soaking, and diesel soaking, were tested. Results show that solvent soaking caused the most significant degradation, while wiping preserved properties the best. Higher cuttings to OBM contamination ratio worsened the effects on cuttings integrity.

26. Martogi, D., Vaibhav, A., Noshadravan, A., & Abedi, S. (2020, October 21). "Approximation of Rock Fracture Toughness using Scratch Test and Phase-Field Modeling Approach." Paper presented at the 2021 SPE Annual Technical Conference and Exhibition. doi:10.2118/201451-MS

Summary: This study investigates rock failure mechanisms using micro-scratch testing and phase field modeling on rock fragments. The phase field approach models crack growth and initiation based on energy minimization principles, with a regularization scalar order parameter indicating material state during fracture formation. Scratch testing provides load-displacement data for stress-strain history. Preliminary results from Eagle Ford formation samples suggest lower fracture toughness for samples tested parallel to bedding orientation.

27. Pakhotina, I., Sakaida, S., Zhu, D., & Hill, A. D. (2020, January 28). "Diagnosing Multistage Fracture Treatments with Distributed Fiber-Optic Sensors." Society of Petroleum Engineers. doi:10.2118/199723-MS

Summary: This study introduces a method to interpret flow-rate distribution from DAS measurements by correlating acoustic signals with flow rates based on experimental and computational investigations. By comparing interpretations with distributed temperature sensing (DTS) results, the study validates the accuracy of the DAS interpretation method, providing insights into cluster efficiency in multistage fracture treatments.

28. Pakhotina, J., Zhu, D., & Hill, A. D. (2020, October 21). "Evaluating Perforation Erosion and its Effect on Limited Entry by Distributed Acoustic Sensor DAS Monitoring." Society of Petroleum Engineers. doi:10.2118/201538-MS

Summary: Limited entry in multistage fracturing aims to evenly distribute fracture fluid among perforation clusters, but erosion of perforation holes can hinder this process. Distributed Acoustic Sensing (DAS) monitors fluid flow by analyzing changing responses at perforation clusters during fracturing. By correlating DAS signals with fluid flow rates, erosion can be assessed. A method was developed that incorporates fluid velocity, perforation area, and erosion rate to improve the accuracy of fluid distribution calculations during fracturing treatments.

29. Rassouli, F. S., and M. D. Zoback. "Preliminary Results on Multistage Creep Experiments of the Wolfcamp Shale at Elevated Temperature." Paper presented at the 54th U.S. Rock Mechanics/Geomechanics Symposium, physical event cancelled, June 2020.

Summary: This study conducted multi-stage creep experiments on shales from the Wolfcamp formation at three different temperatures. Results showed that temperature had a greater impact on viscoplastic deformation in horizontally drilled samples with bedding planes compared to vertically drilled samples, despite the latter containing more clay and organic matter.

30. Reid, T., Li, G., Zhu, D., and A. D. Hill. "Experimental Investigation Using Low-Frequency Distributed Acoustic Sensing for Two Parallel Propagating Fractures." Paper presented at the SPE Hydraulic Fracturing Technology Conference and Exhibition, The Woodlands, Texas, USA, February 2024. doi: https://doi.org/10.2118/217761-MS

Summary: This study investigates the response of low-frequency distributed acoustic sensing (LF-DAS) to multiple fractures propagation using laboratory-scale experiments. Results show strain responses to two parallel fractures, validating LF-DAS signatures of approaching fractures. Using the zero-strain-rate method, the study dynamically estimates fracture propagation, providing insights into stress shadowing effects and enhancing LF-DAS diagnostic capabilities in field applications.

31. Reid, T., Zhu, D., and A. D. Hill. "Experimental Investigation Using Low-Frequency Distributed Acoustic Sensing for Propagating Fractures with Shear and Normal Stresses." Paper presented at the SPE Annual Technical Conference and Exhibition, San Antonio, Texas, USA, October 2023. doi: https://doi-org.srv-proxy1.library.tamu.edu/10.2118/214809-MS

Summary: This study investigates the response of low-frequency distributed acoustic sensing (LF-DAS) to hydraulic fracture propagation under shear and normal stresses using laboratory-scale experiments. By simulating fracture propagation with embedded optical fiber sensors in epoxy blocks subjected to uniaxial compression, the experiment aims to enhance LF-DAS data interpretation at observation wells. Results show strain responses with asymmetrical signatures due to shear stress, providing insights into stress status during fracture propagation and improving fracture front evaluation in field applications.

32. Sakaida, S., Zhu, D., & Hill, A. D. (2020). "Completion Effects on Diagnosing Multistage Fracture Treatments with Distributed Temperature Sensing." Paper presented at the Society of Petroleum Engineers Annual Technical Conference and Exhibition, October 26 – 29, 2020. doi:10.2118/201604-MS

Summary: This paper explores the influence of completion designs on distributed temperature sensing (DTS) interpretation for diagnosing multistage hydraulic fracture treatments. Field data often show irregular temperature variations caused by completion hardware and cement quality. To address this, a method considering completion effects was developed, calibrating the overall heat transfer coefficient along the wellbore using upstream stage intervals. By incorporating these effects, the new method enhances the accuracy of fracture treatment diagnosis based on DTS data.

33. Sakaida, Shohei, Hamanaka, Yasuyuki, Zhu, Ding, Hill, A. D., Kerr, Erich, Estrada, Erick, Scofield, Reid, and Andrew Johnson. "Evaluation of Fluid Containment and Perforation

Erosion in Multistage Fracture Treatment." Paper presented at the SPE Annual Technical Conference and Exhibition, San Antonio, Texas, USA, October 2023. doi: https://doi-org.srv-proxy1.library.tamu.edu/10.2118/215165-MS

Summary: This paper examines fiber optic sensing for fracture monitoring during hydraulic fracturing. It analyzes DTS and DAS measurements to assess fluid distribution, stage isolation, and perforation erosion. Field examples demonstrate the relationship between injection rate, fluid distribution, and perforation erosion, informing completion and fracture treatment design optimization.

34. Sakaida, Shohei, Pakhotina, Iuliia, Zhu, Ding, and A. D. Hill. (2022). "Evaluating Effects of Completion Design on Fracturing Stimulation Efficiency Based on DAS and DTS Interpretation." Paper presented at the SPE Hydraulic Fracturing Technology Conference and Exhibition, The Woodlands, Texas, USA, February 2022. doi: https://doi-org.srv-proxy1.library.tamu.edu/10.2118/209167-MS

Summary: This study explores how completion parameters correlate with hydraulic fracturing performance using DAS and DTS interpretation. The integrated interpretation method estimates fracture half-length distribution for each stage, assuming fractures are initiated in a swarm pattern from each perforation cluster. Results indicate that high injection rates are associated with more uniform fracture distribution and higher productivity, suggesting its importance in optimizing fracturing performance.

35. Sakaida, Shohei, Pakhotina, Iuliia, Zhu, Ding, and A. D. Hill. (2022) "Estimation of Fracture Properties by Combining DAS and DTS Measurements." Paper presented at the SPE International Hydraulic Fracturing Technology Conference & Exhibition, Muscat, Oman, January 2022. doi: https://doi-org.srv-proxy2.library.tamu.edu/10.2118/205233-MS

Summary: In this work, the injected fluid volume distribution obtained by the DAS interpretation is used as an input parameter for a forward model which computes the temperature profile in the reservoir. By conducting temperature inversion to reproduce the temperature profile that matches the measured temperature with the fixed injection rate for each cluster, the distribution of injected fluid along a wellbore can be estimated. This approach can be a valuable means to evaluate the fracturing treatment design and further understand the field observation of hydraulic fractures.

36. Sakaida, Shohei, Zhu, Ding, and Hill, A. D.: Development of Comprehensive and Efficient DTS Interpretation Method for Fracture Diagnosis, Proceedings of the 63rd SPWLA Annual Logging Symposium, Stavanger, Norway, June 10-15, 2022. D031S005R003.DOI: 10.30632/SPWLA-2022-0025

Summary: This study expands existing DTS interpretation to match temperature profiles at multiple time slices, enhancing accuracy despite increased data and model complexity. Understanding the link between fracturing efficiency and productivity, it emphasizes the importance of accurately estimating injected fluid volume distribution for effective performance diagnosis.

37. Saw, Jaewon, Luo, Linqing, Correa, Julia, Soga, Kenichi, Zhu, Xiaoyu, Ajo-Franklin, Jonathan, Kerr, Erich, and Robert Bohn. "Hydraulic fracture stage identification and size

estimation using distributed strain and temperature sensing." Paper presented at the SEG/AAPG International Meeting for Applied Geoscience & Energy, Houston, Texas, August 2023. doi: https://doi.org/10.1190/image2023-3915606.1

Summary: This case study examines distributed strain sensing (DSS) and distributed temperature sensing (DTS) measurements from a hydraulically fractured well. It identifies distinct strain signatures for different fracturing stages, allowing estimation of fracture widths within the zone. The study highlights the effectiveness of distributed fiber optic sensing in monitoring hydraulic fracturing and assessing resulting fracture systems.

38. Tang, Jin, and Ding Zhu. (2022) "Characterize Fracture Development Through Strain Rate Measurements by Distributed Acoustic Sensor DAS." Paper presented at the SPE International Hydraulic Fracturing Technology Conference & Exhibition, Muscat, Oman, January 2022. doi: https://doi-org.srv-proxy1.library.tamu.edu/10.2118/205267-MS

Summary: This study introduces a methodology to simulate strain-rate responses to assumed fracture systems. It employs a 2D fracture propagation model and Displacement Discontinuity Method (DDM) to estimate rock deformation and strain rate on fiber-optic sensors. By analyzing strain rate patterns, fracture development can be recognized. Examples demonstrate the relationship between injection rate distribution and strain rate responses, highlighting DAS's potential for diagnosing fracturing treatments.

39. Zhu, Xiaoyu, Ajo-Franklin, Jonathan, Correa, Julia, Ma, Yuanyuan, Saw, Jaewon, Luo, Linqing, and Kenichi Soga. "Hydraulic fracture aperture estimation using low frequency DAS and DSS in Austin Chalk and Eagle Ford Shale." Paper presented at the SEG/AAPG International Meeting for Applied Geoscience & Energy, Houston, Texas, August 2023. doi: https://doi.org/10.1190/image2023-3906411.1.

Summary: This study uses distributed fiber optic sensing to characterize cross-well fracture growth and aseismic closure during hydraulic fracturing. Low-frequency distributed acoustic sensing (LF-DAS) and Brillouin-based distributed strain sensing (DSS) detect similar aperture changes post one stage of hydraulic fracturing, with LF-DAS showing higher sensitivity to strain changes and better signal-to-noise ratio, while DSS provides a consistent view of absolute strain.

40. Kryvenko, Serhii, Moridis, George Julius, and Thomas Alvin Blasingame. "Numerical Investigation of the Primary Mechanisms Leading to Complex Fracture Morphology in the Near-Wellbore Region." Paper presented at the SPE EuropEC - Europe Energy Conference featured at the 84th EAGE Annual Conference & Exhibition, Vienna, Austria, June 2023. doi: https://doi.org/10.2118/214403-MS

41. Ma, Y., Ajo-Franklin, J., Nayak, A., Zhu, X., Correa, J., & Kerr, E. (2024). DAS microseismic reflection imaging for hydraulic fracture and fault lineament characterization. Geophysics, 0(ja), 1-49. https://doi.org/10.1190/geo2023-0582.1

Summary: This paper presents the results of using microseismic events acquired with distributed acoustic sensing to image fractures due to hydraulic stimulation. The paper describes the procedure to isolate reflections from fractures and using their signal as input to seismic migration.

41. Correa, J., Glubokovskikh, S., Nayak, A., Wood, T., Luo, L., Zhu, X., & Ajo-Franklin, J. (YYYY). Continuous Seismic Monitoring of Hydraulic Fractures Reveals Complex Subsurface Dynamics: Observations Using Distributed Acoustic Sensing and Surface Orbital Vibrator at the Austin Chalk Eagle Ford Field Laboratory. Accepted with Minor Revision in Geophysics Journal.

Summary: This manuscript presents the timelapse data recorded using the distributed acoustic sensing system and surface orbital vibrators. We describe the seismic data and the changes observed during to hydraulic fracturing. We infer that such changes on the seismic data can provide insights into fracture compliance and fracture connectivity.

42. Glubokovskikh, S., Correa, J., Ajo-Franklin, J., Zhu, X., & Freifeld, B. (2024). Continuous Surface-to-DAS Snapshots Explain Activation of Individual Natural Fractures During an Unconventional Reservoir Stimulation. Under review in Geophysics Journal.

Summary: This manuscript describes the timelapse seismic data acquired with distributed acoustic sensing and surface orbital vibrators and proposes an interpretation of the signal from a geomechanical standpoint. It also inverts the seismic signal into discrete fractures, explaining the changes in reflectivity of the seismic signal over time.

43. Nayak, A., J. Correa, and J. Ajo-Franklin (2024). Seismic magnitude estimation using low-frequency strain amplitudes recorded by DAS arrays at far-field distances, accepted, Bull. Seism. Soc. Am.

Summary: This paper proposes a novel method for magnitude estimation of seismic events and microseismic events using distributed acoustic sensing. Event magnitude estimation with DAS is a novel topic, and we used the rich ACEFFL data from DAS and geophones to propose a new method for magnitude estimation of strain rate data.

References

App, J. F. "Flow Profile Estimation in Horizontal, Hydraulically Fractured Wells Using a Péclet Number Approach. "Paper presented at the SPE/AAPG/SEG Unconventional Resources Technology Conference, Houston, Texas, USA, June 2022. doi: https://doi.org/10.15530/urtec-2022-3723405

Baird, A. F., A. L. Stork, S. A. Horne, G. Naldrett, J.-M. Kendall, J. Wookey, J. P. Verdon, and A. Clarke (2020). Characteristics of microseismic data recorded by distributed acoustic sensing (DAS) systems in anisotropic media, Geophysics 85, no. 4, KS139– KS147, doi: 10.1190/geo2019-0776.1.

Bethmann, F., N. Deichmann, and P. M. Mai (2011). Scaling relations of local magnitude versus moment magnitude for sequences of similar earthquakes in Switzerland, Bull. Seismol. Soc. Am. 101, no. 2, 515–534, doi: 10.1785/0120100179.

Binder, G., Titov, A., Liu, Y., Simmons, J., Tura, A., Byerley, G., & Monk, D. (2020). Modeling the seismic response of individual hydraulic fracturing stages observed in a time-lapse distributed acoustic sensing vertical seismic profiling survey. Geophysics, 85(4), T225-T235. https://doi.org/10.1190/geo2019-0819.1

Bohlen, T., Nil, D. D., & Kohn, D. (2015). SOFI 3D: seismic modelling with finite differences 3D - acoustic and viscoelastic version. User Guide.

Bommer, J. J., S. Oates, J. M. Cepeda, C. Lindholm, J. Bird, R. Torres, G. Marroquín, and J. Rivas (2006). Control of hazard due to seismicity induced by a hot fractured rock geothermal project, Eng. Geol. 83, no. 4, 287–306, doi: 10.1016/j.enggeo.2005.11.002.

Born, M., Wolf, E., & Bhatia, A. B. (1999). Principles of Optics: Electromagnetic Theory of Propagation, Interference and Diffraction of Light. Cambridge University Press. https://books.google.com/books?id=nUHGpfNsGyUC

Chen, H., Onishi, T., Park, J. et al. 2021. Computing Pressure Front Propagation Using the Diffusive-Time-of-Flight in Structured and Unstructured Grid Systems via the Fast-Marching Method. SPE J. **26** (3): 1366–1386. SPE-201771-PA. https://doi.org/10.2118/201771-PA.

Chen, H., Li, A., Terada, K. et al. 2023. Rapid Simulation of Unconventional Reservoirs by Multidomain Multiresolution Modeling Based on the Diffusive Time of Flight. SPE J. **28**: 1083–1096. https://doi.org/10.2118/214308-PA.

Cheng, F., J. Correa, S. Dou, B. Freifeld, T. Wood, K. Nihei, et al. (2021). Testing of a permanent orbital surface source and distributed acoustic sensing for monitoring of unconventional reservoirs: Preliminary results from the Eagle Ford Shale, Geophysics 86, no 2, P1–P12, doi: 10.1190/geo2020-0403.1

Chen, K., D. Zhu, and A. D. Hill. 2015. "Acoustic Signature of Flow from a Fractured Wellbore." In Day 2 Tue, September29, 2015, D021S020R002. SPE. https://doi.org/10.2118/174877-ms.

Cipolla, Craig, McKimmy, Michael, Hari-Roy, Stephanie, Wolters, Jennifer, Haffener, Jackson, Haustveit, Kyle, and Mouin Almasoodi. 2022. “Evaluating Stimulation Effectiveness with Permanent Optical Fiber and Sealed Wellbore Pressure Monitoring: Bakken Case Study.” SPE Hydraulic Fracturing Technology Conference and Exhibition. https://doi.org/10.2118/209129-MS

Clinton, J. F., E. Hauksson, and K. Solanki (2006). An evaluation of the SCSN moment tensor solutions: Robustness of the Mw magnitude scale, style of faulting, and automation of the method, Bull. Seismol. Soc. Am. 96, 1689–1705, doi: 10.1785/0120050241.

Correa, J., Isaenkov, R., Yavuz, S., Yurikov, A., Tertyshnikov, K., Wood, T., Freifeld, B. and Pevzner, R., (2021). DAS/SOV: Rotary seismic sources with fiber-optic sensing facilitates autonomous permanent reservoir monitoring. Geophysics, 86(6), pp.1-42.

Cramer, D., Friehauf, K., Roberts, G., and J. Whittaker. (2020). Integrating Distributed Acoustic Sensing, Treatment-Pressure Analysis, and Video-Based Perforation Imaging To Evaluate Limited-Entry-Treatment Effectiveness. SPE Production and Operations 35 0730–0755.

doi: https://doi.org/10.2118/194334-PA.

Daley, T., & Cox, D.A. (2001). Orbital vibrator seismic source for simultaneous P- and S-wave crosswell acquisition. Geophysics, 66, 1471-1480.

Durak, L. & Arikan, O., 2003. Short-time Fourier transform: Two fundamental properties and an optimal implementation. IEEE Transactions on Signal Processing, 51(5), p. 1231– 1242.

Eaton, D. W. (2018). Passive Seismic Monitoring of Induced Seismicity: Fundamental Principles and Application to Energy Technologies. Cambridge University Press. https://books.google.com/books?id=fElVDwAAQBAJ

Egorov, A., Glubokovskikh, S., Bóna, A., Pevzner, R., Gurevich, B., & Tokarev, M. (2017). How rough sea affects marine seismic data and deghosting procedures. Geophysical Prospecting, n/a-n/a. https://doi.org/10.1111/1365-2478.12535

Fallahzadeh, S., Hossain, M., James Cornwell, A., and V. Rasouli. (2017). Near Wellbore Hydraulic Fracture Propagation from Perforations in Tight Rocks: The Roles of Fracturing Fluid Viscosity and Injection Rate. Energies, 10(3), 359. doi: https://doi.org/10.3390/en10030359.

Fehler, M. (1982). Interaction of seismic waves with a viscous liquid layer. Bulletin of the Seismological Society of America, 72(1), 55-72. https://doi.org/10.1785/bssa0720010055

Glubokovskikh, S., Correa, J., Ajo-Franklin, J., Zhu, X., & Freifeld, B. (2024). Continuous Surface-to-DAS Snapshots Explain Activation of Individual Natural Fractures During an Unconventional Reservoir Stimulation. Under review in Geophysics.

Glubokovskikh, S., Gurevich, B., Lebedev, M., Mikhaltsevitch, V., & Tan, S. (2016). Effect of asperities on stress dependency of elastic properties of cracked rocks. International Journal of Engineering Science, 98, 116-125. https://doi.org/http://dx.doi.org/10.1016/j.ijengsci.2015.09.001

Hanks, T. C., and H. Kanamori (1979). A moment magnitude scale, J. Geophys. Res. 84, no. B5, doi: 10.1029/JB084iB05p02348.

Harris, J. M., Nolen-Hoeksema, R. C., Langan, R. T., Schaack, M. V., Lazaratos, S. K., and Rector, J. W., 1995. High-resolution crosswell imaging of a west Texas carbonate reservoir: Part 1—Project summary and interpretation. GEOPHYSICS 60: 667-681. https://doi.org/10.1190/1.1443806

Heidbach, O., M. Rajabi, K. Reiter, M. Ziegler, and the WSM Team (2016). World Stress Map Database Release 2016, *GFZ Data Services*, http://doi.org/10.5880/WSM.2016.001

Helbig, K., and L. Thomsen (2005). 75-plus years of anisotropy in exploration and reservoir seismics: A historical review of concepts and methods, Geophysics 70, no. 6, 9N–23N, doi: 10.1190/1.2122407.

Hudson, J. A., and J. R. Heritage, 1981, The use of the Born approximation in seismic scattering problems: Geophysical Journal International, **66**, 221–240.

Hudson, J. A. (1981). Wave speeds and attenuation of elastic waves in material containing cracks. Geophysical Journal of the Royal Astronomical Society, 64(1), 133-150. https://doi.org/10.1111/j.1365-246X.1981.tb02662.x

James, J., 2011. A Student's Guide to Fourier Transforms 3rd ed. New York: Cambridge University Press.

Jin, G., and B. Roy (2017). Hydraulic-fracture geometry characterization using low-frequency DAS signal, The Leading Edge 36, 975–980, doi: 10.1190/tle36120975.1.

Karrenbach, M., S. Cole, A. Ridge, K. Boone, D. Kahn, J. Rich, K. Silver, and D. Langton (2018). Fiber-optic distributed acoustic sensing of microseismicity, strain and temperature during hydraulic fracturing, Geophysics 84, no 1, D11–D23, doi: 10.1190/geo2017-0396.1.

Kohli, A., & Zoback, M. (2021). Stratigraphically controlled stress variations at the hydraulic fracture test site-1 in the Midland Basin, TX. *Energies*, *14*(24), 8328.

Kwiatek, G., T. Saamo, T. Ader, F. Bluemle, M. Bohnhoff, M., Chendorain, G. Dresen, P. Heikkinen, I. Kukkonen, P. Leary, et al. (2019). Controlling fluid-induced seismicity during a 6.1-km-deep geothermal stimulation in Finland, Sci. Adv. 5, eaav7224.

Leggett, Smith, Reid, Teresa, Zhu, Ding, and Hill, A. D. 2022. Experimental Investigation of Low-Frequency Distributed Acoustic Strain-Rate Responses to Propagating Fractures. Proc., SPE Hydraulic Fracturing Technology Conference and Exhibition. https://doi.org/10.2118/209135-MS.

Leggett, Smith, et al. "Interpretation of Fracture Initiation Points by In-Well Low-Frequency Distributed Acoustic Sensing in Horizontal Wells." SPE Journal (2023): 1-10

Lellouch, A., N. J. Lindsey, W. L. Ellsworth, and B. L. Biondi (2020). Comparison between distributed acoustic sensing and geophones: Downhole microseismic monitoring of the FORGE geothermal experiment, Seismol. Res. Lett. 91, no 6, 3256-3268, doi: 10.1785/0220200149.

Li, L. and Lee, S.H., 2008. Efficient Field-Scale Simulation of Black Oil in a Naturally Fractured Reservoir Through Discrete Fracture Networks and Homogenized Media. SPE Res Eval & Eng **11**: 750–758. https://doi.org/10.2118/103901-PA.

Li M., Zhou F., Dong E., Zhang G., Zhuang X., and Wang B. (2022). Experimental study on the multiple fracture simultaneous propagation during extremely limited-entry fracturing. *Journal of Petroleum Science and Engineering, 218*. doi: https://doi.org/10.1016/j.petrol.2022.110906

Luo, B., G. Jin, and F. Stanek (2021). Near-field strain in distributed acoustic sensing-based microseismic observation, Geophysics 86, no 5, P49–P60, doi: 10.1190/geo2021-0031.1

Luu, K. 2022, fteikpy: Accurate Eikonal solver for Python [Computer software]. https://doi.org/10.5281/zenodo.4269352

Ma, Y., Ajo-Franklin, J., Nayak, A., Zhu, X., Correa, J., 2023a. DAS microseismic reflection imaging for hydraulic fracture and fault zones mapping. 2023 IMAGE.

Ma, Y., Eaton, D., Wang, C., and Aklilu, A., 2023b. Characterizing hydraulic fracture growth using distributed acoustic sensing-recorded microseismic reflections. GEOPHYSICS 88: WC47-WC57. https://doi.org/10.1190/geo2022-0607.1

Mateeva, A., J. Lopez, H. Potters, J. Mestayer, B. Cox, D. Kiyashchenko, P. Wills, S. Grandi, K. Hornman, B. Kuvshinov, et al. (2014). Distributed acoustic sensing for reservoir monitoring with vertical seismic profiling, Geophys. Prospect. 62, no. 4, 679–692, doi: 10.1111/1365-2478.12116.

Mavko, G., Mukerji, T., & Dvorkin, J. (2009). The Rock Physics Handbook: Tools for Seismic Analysis in Porous Media. Cambridge University Press.

Maxwell, S. C., C. K. Waltmann, N. R. Warpinski, M. J. Mayerhofer, and N. Boroumand (2009). Imaging seismic deformation induced by hydraulic fracture complexity, SPE Reservoir Evaluation & Engineering 12, 48–52, doi: 10.2118/102801-PA.

Meek, R., Hull, R., Woller, K., Wright, B., Martin, M., Bello, H., & Bailey, J. (2019). Estimation of Hydraulic Fracture Height and Pressure Deflation Using a Pulsed Vertical Seismic Profile and a DAS Fiber in the Midland Basin. SPE/AAPG/SEG Unconventional Resources Technology Conference.

Nayak, A., J. Correa, and J. Ajo-Franklin (2024). Seismic magnitude estimation using low-frequency strain amplitudes recorded by DAS arrays at far-field distances, accepted, Bull. Seism. Soc. Am.

Norbeck, J., T. Latimer, C. Gradl, S. Agarwal, S. Dadi, E. Eddy, et al. (2023). A review of drilling, completion, and stimulation of a horizontal geothermal well system in north-central Nevada, Proceedings, 48th Workshop on Geothermal Reservoir Engineering Stanford University, Stanford, California, February 6-8, 2023.

Oelke, A., Alexandrov, D., Abakumov, I., Glubokovskikh, S., Shigapov, R., Krüger, O. S., Kashtan, B., Troyan, V., & Shapiro, S. A. (2013). Seismic reflectivity of hydraulic fractures approximated by thin fluid layers. Geophysics, 78(4), T79-T87. https://doi.org/10.1190/geo2012-0269.1

Pakhotina, Iuliia, Shohei Sakaida, Ding Zhu, and A. Daniel Hill. 2020. "Diagnosing Multistage Fracture Treatments withDistributed Fiber-Optic Sensors." SPE Production & Operations 35 (04): 0852–64. https://onepetro.org/PO/article-abstract/35/04/0852/451069.

Park, H.Y., Datta-Gupta, A. and King, M.J. 2013. Handling Conflicting Multiple Objectives Using Pareto-based Evolutionary Algorithm During History Matching of Reservoir Performance. Presented at the SPE Reservoir Simulation Symposium, The Woodlands, Texas, USA, February 2013. https://doi.org/10.2118/163623-MS.

Pongratz, R., von Gijtenbeek, K., Kontarev, R., and B. W. McDaniel. (2007). Perforating for Fracturing—Best Practices and Case Histories. Paper presented at the SPE Hydraulic Fracturing Technology Conference, College Station, Texas, U.S.A., January 2007.

Robinson, S., Littleford, T., Luu, T., Wardynski, K., Evans, A., Horton, B., and M. Oman. (2020). Acoustic Imaging of Perforation Erosion in Hydraulically Fractured Wells for Optimizing Cluster Efficiency. Paper presented at the SPE Hydraulic Fracturing Technology Conference and Exhibition, The Woodlands, Texas, USA, February 2020. doi: https://doi.org/10.2118/199718-MS

Rost, S., and C. Thomas (2002). Array seismology: Methods and applications, Rev. Geophys. 40, no. 3, 2-1–2-27, doi: 10.1029/ 2000RG000100.

Rector, J. W., Lazaratos, S. K., Harris, J. M., and Schaack, M. V., 1995. High-resolution crosswell imaging of a west Texas carbonate reservoir: Part 3—Wavefield separation of reflections. GEOPHYSICS 60: 692-701. https://doi.org/10.1190/1.1443808

Sakaida, S., Zhu, D. and Hill, A.D., 2022, June. Development of Comprehensive and Efficient DTS Interpretation Method for Fracture Diagnosis. Presented at the SPWLA 63rd Annual Logging Symposium, Stavanger, Norway, June 2022. https://doi.org/10.30632/SPWLA-2022-0025.

Sakaida, Shohei, Hamanaka, Yasuyuki, Zhu, Ding, Hill, A. D., Kerr, Erich, Estrada, Erick, Scofield, Reid, and Andrew Johnson. "Evaluation of Fluid Containment and Perforation Erosion in Multistage Fracture Treatment." Paper presented at the SPE Annual Technical Conference and Exhibition, San Antonio, Texas, USA, October 2023. doi: https://doi-org.srv-proxy1.library.tamu.edu/10.2118/215165-MS

Sanghyun, L. and Stephen, K.D., 2018, March. Optimizing Automatic History Matching for Field Application Using Genetic Algorithm and Particle Swarm Optimization. Presented at the Offshore Technology Conference Asia, Kuala Lumpur, Malaysia, March 2018. https://doi.org/10.4043/28401-MS.

Sayers, C. M., & Kachanov, M. (1991). A simple technique for finding effective elastic constants of cracked solids for arbitrary crack orientation statistics. International Journal of Solids and Structures, 27(6), 671-680. https://doi.org/http://dx.doi.org/10.1016/0020-7683(91)90027-D

Sethian, J. A. 1999. Fast Marching Methods. SIAM Rev **41** (2): 199–235. https://doi.org/10.1137/S0036144598347059.

Schoenberg, M., & Protazio, J. (2005). "Zoeppritz" rationalized, and generalized to anisotropic media. The Journal of the Acoustical Society of America, 88(S1), S46-S46. https://doi.org/10.1121/1.2029011

Shapiro, S. A., O. S. Krüger, C. Dinske, and C. Langenbruch (2011). Magnitudes of induced earthquakes and geometric scales of fluid stimulated rock volumes, Geophysics 76, WC55–WC63.

Shearer, P. M. (2009). Introduction to seismology (2nd ed.), Cambridge University Press, p 261-262.

Sone, H., & Zoback, M. D. (2014). Viscous relaxation model for predicting least principal stress magnitudes in sedimentary rocks. *Journal of Petroleum Science and Engineering*, *124*, 416-431.

Sone, H., & Zoback, M. D. (2013). Mechanical properties of shale-gas reservoir rocks—Part 2: Ductile creep, brittle strength, and their relation to the elastic modulus. *Geophysics*, *78*(5), D393-D402.

Snee, J. L., and Zoback, M. D., 2022. State of stress in areas of active unconventional oil and gas development in North America. *AAPG Bulletin* 2022. 106 (2): 355–385. doi: https://doi.org/10.1306/08102120151

Snieder, R. (2002). General theory of elastic wave scattering. Acad. Press. https://books.google.com/books?id=XJ4C0AEACAAJ

Titov, A., Binder, G., Liu, Y., Jin, G., Simmons, J., Tura, A., Monk, D., Byerley, G., & Yates, M. (2021). Modeling and interpretation of scattered waves in interstage distributed acoustic sensing vertical seismic profiling survey. Geophysics, 86(2), D93-D102. https://doi.org/10.1190/geo2020-0293.1

Utah FORGE (2020). Utah FORGE induced seismicity mitigation plan, Report prepared for U.S. Department of Energy, Utah FORGE, University of Utah, Salt Lake City, Utah.

Vasco, D. W., Keers, H., and Karasaki, K. 2000. Estimation of Reservoir Properties Using Transient Pressure Data: An Asymptotic Approach. Water Resour Res **36** (12): 3447–3465. https://doi.org/10.1029/2000WR900179.

Yoshida, N., Hill, A.D., and Zhu, D. 2018. "Comprehensive Modeling of Downhole Temperature in a Horizontal Well with Multiple Fractures." SPE Journal 25 (05): 1580–1602. DOI: 10.2118/181812-PA

Weijers, L., de Pater, C. J., Owens, K. A., and H. H. Kogsbøll. (1994). Geometry of Hydraulic Fractures Induced From Horizontal Wellbores. *SPE Prod and Fac* 9, 87–92.
doi: https://doi.org/10.2118/25049-PA

Widess, M.B. (1973). How thin is a thin bed GEOPHYSICS 1973 38:6, 1176-1180

Wu, C., Harris, J. M., Nihei, K. T., & Nakagawa, S. (2005). Two-dimensional finite-difference seismic modeling of an open fluid-filled fracture: Comparison of thin-layer and linear-slip models. Geophysics, 70(4), T57-T62. https://doi.org/10.1190/1.1988187

Xue, X., Yang, C., Onishi, T., King, M.J. and Datta–Gupta, A. 2019. Modeling Hydraulically Fractured Shale Wells Using the Fast-Marching Method With Local Grid Refinements and an Embedded Discrete Fracture Model. SPE J. **24**: 2590–2608. https://doi.org/10.2118/193822-PAYilmaz, Ö., 1987. Seismic data processing. Investigations in geophysics. Houston: Society of exploration geophysicists.

Yilmaz, Ö., 2001. Seismic data analysis. Society of Exploration Geophysicists. Doi: 10.1190/1.9781560801580

Zhao, X., Willis, M. E., Inks, T., & Wilson, G. A. (2021). Quantifying hydraulically induced fracture height and density from rapid time-lapse distributed acoustic sensing vertical seismic profile data. Geophysics, 86(2), A15-A20. https://doi.org/10.1190/geo2020-0155.1

Zhou, C., Cai, W., Luo, Y., Schuster, G. T., and Hassanzadeh, S., 1995. Acoustic wave-equation travel time and waveform inversion of crosshole seismic data. GEOPHYSICS 60: 765-773. https://doi.org/10.1190/1.1443815

Zhu, X., Ajo-Franklin, J., Correa, J., Ma, Y., Saw, J., Luo, L., and Soga, K., 2023. Hydraulic Fracture Aperture Estimation Using Low-Frequency DAS and DSS in Austin Chalk and Eagle Ford Shale. IMAGE 2023.